Metalloenzyme-Catalyzed Radical Reactions Unknown or Uncommon in Native Enzymology

Wenzhen Fu,[1,†,‡] Liu-Peng Zhao,[1,‡] and Yang Yang[1,2,3]*

[1]Department of Chemistry and Biochemistry, University of California Santa Barbara, Santa Barbara, California 93106, United States;

[2]Biomolecular Science and Engineering (BMSE) Program, University of California Santa Barbara, Santa Barbara, California 93106, United States;

[3]Howard Hughes Medical Institute, University of California Santa Barbara, Santa Barbara, California 93106, United States

[‡]These authors contributed equally to this work.

Email: yang@chem.ucsb.edu

ABSTRACT. The past decade has witnessed groundbreaking developments in metalloenzyme-catalyzed free radical transformations which were previously unknown or uncommon in native metalloenzymology. Guided by mechanistic understandings from organic, organometallic and

biochemistry, an array of radical reactions has been developed using various metalloprotein catalysts based on first-row transition metal cofactors including Fe, Co and Cu. The structural and functional diversity and the readily tunable active-site environment of metalloproteins offer an excellent opportunity to solve the challenging chemo-, regio- and stereoselectivity problems in radical-mediated transformations facing synthetic chemists. In this Review, we summarize metalloprotein-catalyzed radical reactions based on the reactive intermediates involved, including carbon-centered radicals, nitrogen-centered radicals, oxygen-centered radicals, and metal carbenoids and nitrenoids with radical character. We further survey the reaction mechanism, enzyme engineering strategies, and substrate scope of these metalloprotein-catalyzed radical transformations, providing an overview of the current status of metalloenzymology unknown or uncommon in native biochemistry.

Table of Contents

1. Introduction

As reactive intermediates with unpaired electron(s), free radicals have long been recognized as versatile intermediates in organic synthesis.[1–6] However, challenges in taming these highly reactive intermediates for more efficient and selective transformations have hampered their broader adaption in synthetic chemistry. Over the past decade, free radical chemistry has experienced a renaissance, due to the exciting development of new strategies such as transition metal catalysis,[7–11] photoredox catalysis,[12–15] and electrochemistry,[16,17] allowing radicals to form under mild conditions in a controllable manner. However, due to the difficulties in maintaining tight association between the transiently formed radical intermediate and the chiral catalyst, inducing high levels of regio- and stereocontrol over radical-mediated transformations has remained a daunting task in asymmetric catalysis with small-molecule catalysts.[18–20]

As nature's privileged catalysts underlying the chemistry of life, enzymes are capable of facilitating challenging reactions with outstanding efficiency and selectivity,[21–23] including free radical-mediated processes. Natural radical enzymes, including anaerobic radical enzymes such as radical *S*-adenosylmethionine (SAM) enzymes[24–26] and cobalamin-dependent enzymes,[27,28] as well as aerobic enzymes such as heme[29–36] and nonheme oxygenases[37–40] and halogenases[41–44] use a plethora of interesting mechanisms to promote challenging open-shell processes. Over the past decade, by cross-pollinating ideas from synthetic chemistry and enzymology, mechanism-guided enzyme repurposing and engineering have greatly expanded the catalytic repertoire of naturally occurring enzyme systems. The excellent tunability of naturally occurring metalloprotein catalysts provides an opportunity to impose high degrees of stereocontrol over otherwise challenging radical reactions, thereby complementing the state-of-the-art chiral small-molecule catalysts designed to facilitate asymmetric radical transformations.[18–20] To date, using photochemistry to trigger radical

generation, natural enzymes based on diverse organic cofactors including nicotinamide,[45,46] flavin,[45–47] pyridoxal[48–54] and thiamine[55–59] have been reprogrammed to catalyze unnatural enantioselective reactions using a radical mechanism. Possessing a redox-active and catalytically versatile first-row transition-metal cofactor, metalloenzymes hold the potential of promoting free radical formation and transformation using a complementary metallocofactor-enabled redox mechanism. Furthermore, the unique reactivity of first-row transition metal elements holds the potential for challenging bond formation, allowing a range of unnatural asymmetric radical reactions to be advanced.

Prior to 2021, several carbene transfer and nitrene transfer reactions from the pioneering studies of Arnold and Fasan were proposed to proceed via Fe–C and Fe–N bond containing intermediates with substantial radical character on Fe-bound organic ligand.[60–63] In 2021, our group reported the first examples of unnatural stereoselective free radical reactions catalyzed by a repurposed natural P450 enzyme.[64] Since 2021, a range of metalloenzyme-catalyzed free radical reactions using various radical generation mechanisms have been developed. In this Review, we survey recent advances of natural metalloenzyme-catalyzed free radical transformations not found or uncommon in native enzymology, including their mechanism, enzyme engineering, and substrate scope. Based on different classes of radical intermediates involved, this Review is structured into five sections, including transformations involving carbon-centered radicals, transformations involving nitrogen-centered radicals, transformations involving oxygen-centered radicals, transformations involving metal nitrenoids with radical character on the nitrenoid nitrogen, and transformations involving metal carbenoids with radical character on the carbenoid carbon (Figure 1). As excellent earlier reviews have summarized metalloenzyme-catalyzed carbene transfer and nitrene transfer reactions published before 2021,[60–63] this review only covers

recent progress of carbene and nitrene transfer reactions involving radical intermediates published after 2021. Important related studies using artificial metalloenzymes (ArMs) are out of the scope of our review and we direct readers to outstanding recent reviews from experts in this field.[65–73]

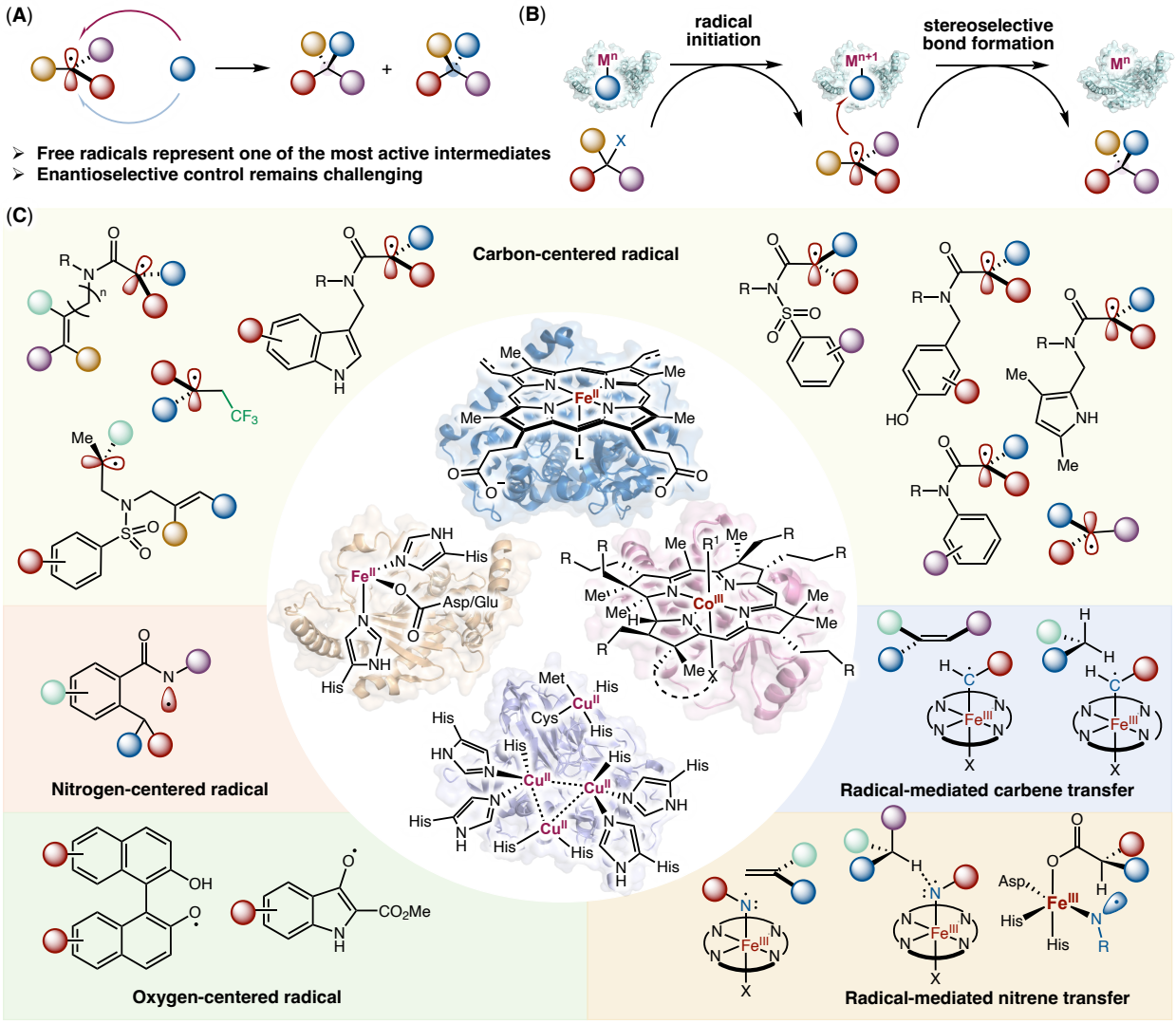

Figure 1. Summary of representative metalloenzymes and non-native radical intermediates. (A) General challenge for catalytic enantiocontrol over free radical-mediated transformations; (B) Metalloenzyme-catalyzed free radical transformations; (C) Summary of previously studied metalloenzymes and the radical intermediates involved in these transformations.

2. Transformations involving carbon-centered radicals

Carbon-centered radicals represent essential reactive intermediates in both synthetic methodology and natural product synthesis.[9,74–77] In native metalloenzymology, carbon-centered radicals are involved in various anaerobic and aerobic transformations. In this section, we review metalloenzyme-catalyzed unnatural transformations involving carbon-centered radicals that have been reported since 2021.

2.1 Addition of carbon-centered radical to alkenes

Alkene difunctionalization represents an important strategy to generate molecular complexity from easily available olefin building blocks.[78–80] Among these methods, radical-mediated stereoselective alkene difunctionalization processes triggered by the addition of a carbon-centered radical across the C=C double bond of an alkene could potentially enable the construction of multiple stereogenic centers in an efficient manner. In 2021, by capitalizing on the innate redox properties of the heme cofactor, our lab engineered cytochromes P450 to catalyze atom transfer radical cyclization (ATRC) reactions[81] with excellent diastereo- and enantioselectivity.[64] In the proposed catalytic cycle (Figure 2), through the halogen atom transfer between the α-haloamide substrate and the P450 enzyme in its ferrous state, a reactive α-carbonyl radical is generated, along with the formation of the ferric enzyme containing a Fe–Br bond. Within the enzyme's active site, the addition of this incipient α-carbonyl radical to the pendant alkene occurs in an enantioselective manner, giving rise to a new cyclized alkyl radical. Finally, through a halogen rebound mechanism involving the enzymatic Fe(III)–Br species, diastereoselective C–Br bond formation affords the final ATRC product and regenerates the ferrous protein catalyst.

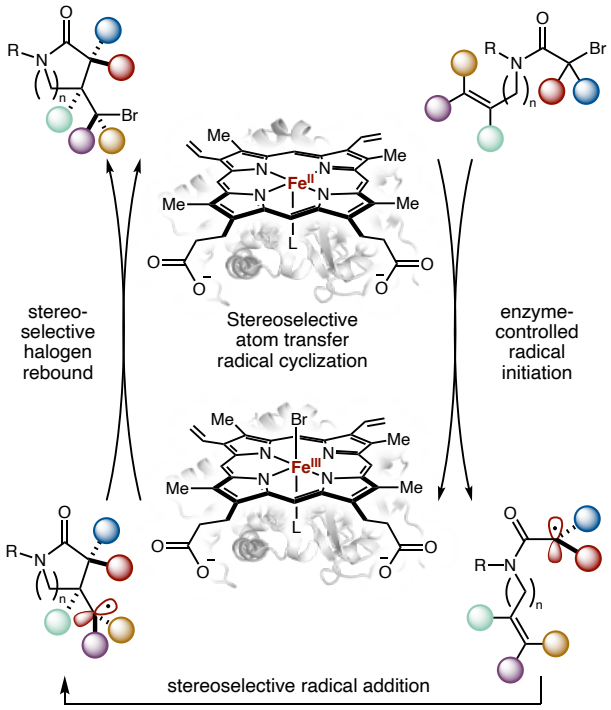

Figure 2. Proposed catalytic cycle for the biocatalytic stereoselective atom-transfer radical cyclization.

First, the evaluation of an in-house metalloenzyme collection led to the identification of two serine-ligated P450 variants, P411-CIS T438S ("P")[82] and $P411_{Diane2}$,[83] allowing either enantiomeric form of the ATRC product to be generated with promising enantioselectivity (Figure 3A–C). Subsequent directed evolution targeting active-site residues proximal to the heme cofactor furnished improved variants, including $P450_{ATRCase1}$ (P T327I I263Q L181F A82T H266T) and $P450_{ATRCase2}$ ($P411_{Diane2}$ P327C S400A L181V T438Q L436T). Using whole *E. coli* cells harboring $P450_{ATRCase1}$, the (*R*)-enantiomeric product formed in 8110 TTN and 97:3 e.r.. Using $P450_{ATRCase2}$, the (*S*)-enantiomer was generated in 3350 TTN and 9:91 e.r..

To gain further understanding of reaction mechanism and the origin of stereoselectivity in this P450-catalyzed atom transfer radical cyclization reaction, our group carried out computational

studies using molecular dynamics (MD) and quantum mechanics/molecular mechanics (QM/MM) simulations.[84] These studies revealed the role of beneficial mutation I263Q as a key hydrogen bond donor to engage the amide carbonyl group, facilitating bromine atom abstraction and enhancing radical cyclization enantiocontrol. Further QM/MM studies showed that due to the steric repulsion between the olefin and the heme, the (*Re*)-face-attack transition state has an activation energy 2.5 kcal/mol lower than of the (*Si*)-face attack transition state, leading to the (*R*)-enantiomeric cyclization product (Figure 3D). Substrates with different substituted benzyl group were tolerated, providing the corresponding ATRC products in TTNs of up to 8,110. Products bearing a *gem*-difluoromethyl moiety and contiguous quaternary stereocenters could also be prepared. δ-Lactams were also accessible with $P450_{ATRCase2}$ A330K (Figure 3E).

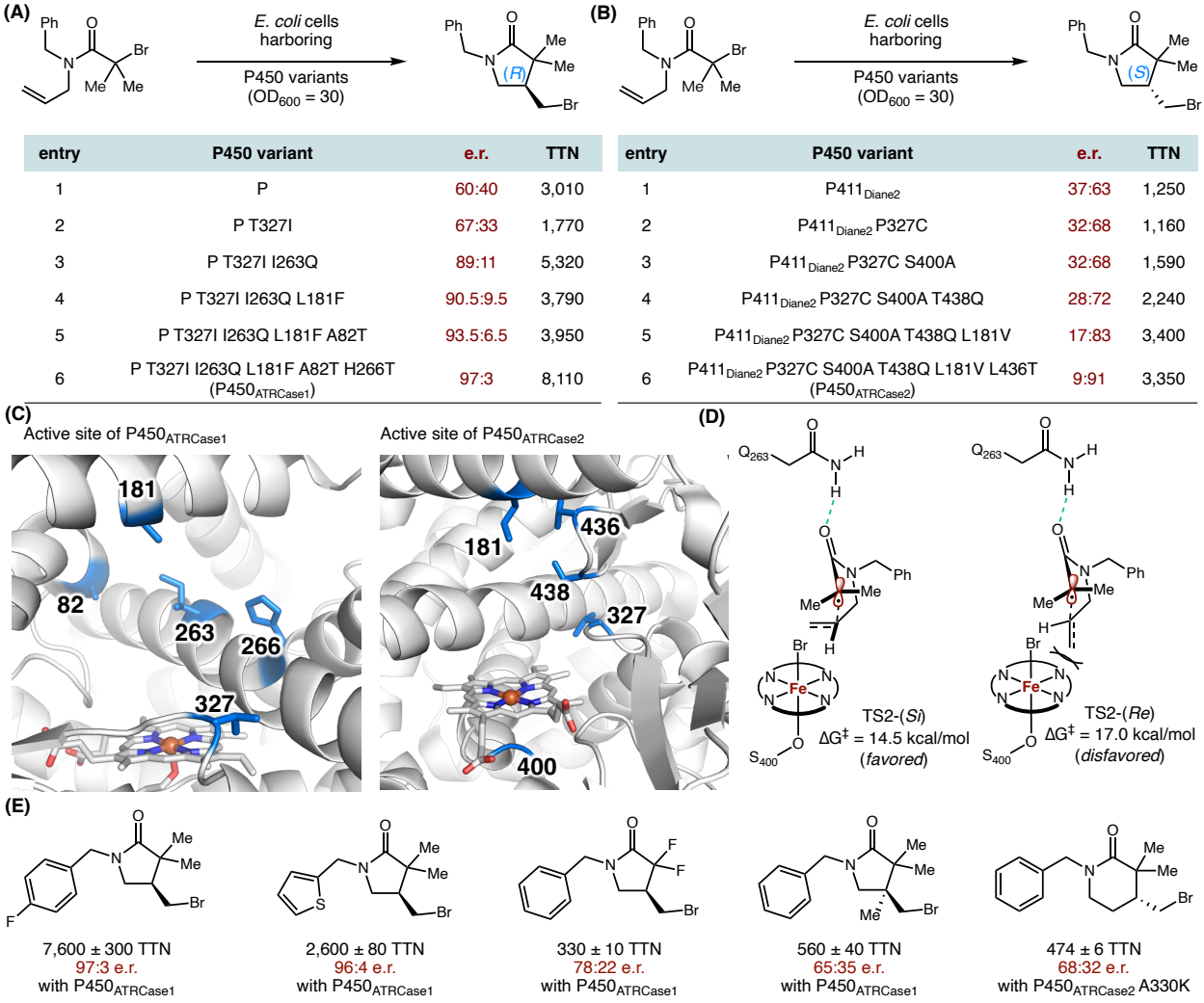

entry	P450 variant	e.r.	TTN
1	P	60:40	3,010
2	P T327I	67:33	1,770
3	P T327I I263Q	89:11	5,320
4	P T327I I263Q L181F	90.5:9.5	3,790
5	P T327I I263Q L181F A82T	93.5:6.5	3,950
6	P T327I I263Q L181F A82T H266T ($P450_{ATRCase1}$)	97:3	8,110

entry	P450 variant	e.r.	TTN
1	$P411_{Diane2}$	37:63	1,250
2	$P411_{Diane2}$ P327C	32:68	1,160
3	$P411_{Diane2}$ P327C S400A	32:68	1,590
4	$P411_{Diane2}$ P327C S400A T438Q	28:72	2,240
5	$P411_{Diane2}$ P327C S400A T438Q L181V	17:83	3,400
6	$P411_{Diane2}$ P327C S400A T438Q L181V L436T ($P450_{ATRCase2}$)	9:91	3,350

Figure 3. P450-catalyzed enantioselective atom transfer radical cyclization (ATRC). (A) Directed evolution of $P450_{ATRCase1}$; (B) Directed evolution of $P450_{ATRCase2}$; (C) The illustration of active sites: the left was made from 4H23 (PDB ID) and the right was made from 5UCW (PDB ID); (D) Probing the origin of enantioselectivity by QM/MM studies; (E) Selected ATRC products; reactions were carried out using whole *E. coli* cells overexpressing $P450_{ATRCase}$'s (OD_{600} = 5–30).

In 2022, Bruns and coworkers further demonstrated that heme-dependent myoglobin (Mb) was also capable of catalyzing atom transfer radical cyclization reactions for γ-lactam synthesis

(Figure 4A).[85] Replacing the Fe-bound histidine with a serine provided the Mb H93S variant with improved activity (Figure 4B). Similar or slightly improved total turnover numbers (TTNs) were observed with whole *E. coli* cells than those with purified protein.[64] Additionally, α,α,α-trichloroamide substrates were also transformed into the desired α,α-dichlorolactam. Radical clock studies using a substrate bearing a cyclopropyl moiety afforded the corresponding ring opening product, further confirming the radical-mediated nature of this myoglobin-catalyzed cyclization (Figure 4C). Despite extensive efforts, no enantioselectivity was observed in these myoglobin-catalyzed ATRC processes.

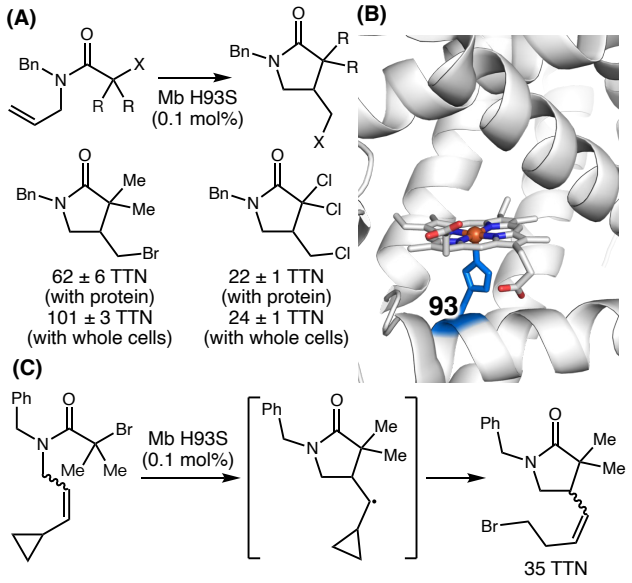

Figure 4. Mb H93S-catalyzed atom transfer radical cyclization. (A) Selected substrate scope; reactions were carried out using purified Mb H93S (0.1 mol%) or whole *E. coli* cells overexpressing Mb H93S (OD_{600} = 40); (B) The illustration of active site was made from the structure of 1WLA (PDB ID); (C) Radical clock experiment.

Nonheme Fe enzymes have also been reprogrammed to catalyze stereoselective radical transformations. Inspired by transition metal-catalyzed trifluoromethylazidation and related

processes,[86–90] the groups of Huang and Jia independently developed enantioselective styrene trifluoromethylazidation using nonheme Fe enzymes hydroxymandelate synthase (HMS) and quercetin 2,3-dioxygenase (QueD), respectively. In their proposed biocatalytic mechanism, Togni's reagent[89] is first reduced by Fe(II) to generate the trifluoromethyl radical. Subsequent addition of this trifluoromethyl radical to the styrene substrate leads to a new benzylic radical. Finally, enantioselective radical rebound with the Fe(III)–N_3 intermediate in the nonheme Fe enzyme's active site furnishes enantioenriched trifluoromethylazidation product (Figure 5A).

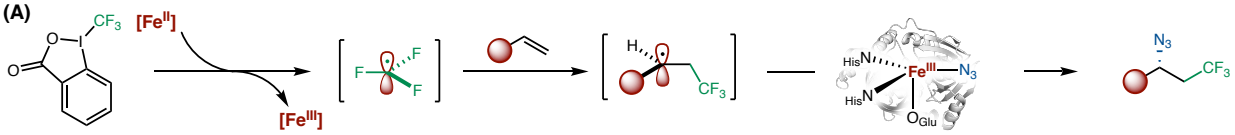

(B)

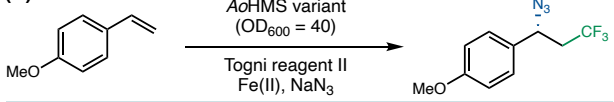

entry	*Ao*HMS variant	yield	e.r.
1	parent	34%	69:31
2	parent S201V	37%	70:30
3	parent S201V N334S	40%	81:19
4	parent S201V N334S E190D	35%	83:17
5	parent S201V N334S E190D L338A Y339V	29%	85:15
6	parent S201V N334S E190D L338A Y339V S332G	27%	89:11
7	parent S201V N334S E190D L338A Y339V S332G G328S	37%	91:9
8	parent S201V N334S E190D L338A Y339V S332G G328S P173L D228N A269T	35%	92:8
9	parent S201V N334S E190D L338A Y339V S332G G328S P173L D228N A269T V342A	52%	94:6
10	parent S201V N334S E190D L338A Y339V S332G G328S P173L D228N A269T V342A Q226P L303M (*Ao*HMS-CF_3)	53%	95:5

(C)

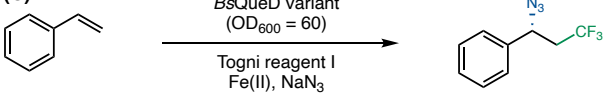

entry	*Bs*QueD variant	yield	e.r.
1	*Bs*QueD	0.4%	41:59
2	*Bs*QueD E241H	5.6%	47:53
3	*Bs*QueD E241H F295M	7.4%	70:30
4	*Bs*QueD E241H F295M L332I H239L L330Y	8.6%	80:20
5	*Bs*QueD E241H F295M L332I H239L L330Y N326D	9.1%	82:18
6	*Bs*QueD E241H F295M L332I H239L L330Y N326D L239P	7.3%	87:13
7	*Bs*QueD E241H F295M L332I H239L L330Y N326D L239P D233E	5.5%	89:11
8	*Bs*QueD E241H F295M L332I H239L L330Y N326D L239P D233E Y330F	6.3%	90:10
9	*Bs*QueD E241H F295M L332I H239L L330Y N326D L239P D233E Y330F Q203T	7.2%	91:9
10	*Bs*QueD E241H F295M L332I H239L L330Y N326D L239P D233E Y330F Q203T V239C (*Bs*QueD-CF_3)	4.8%	92:8

(D)

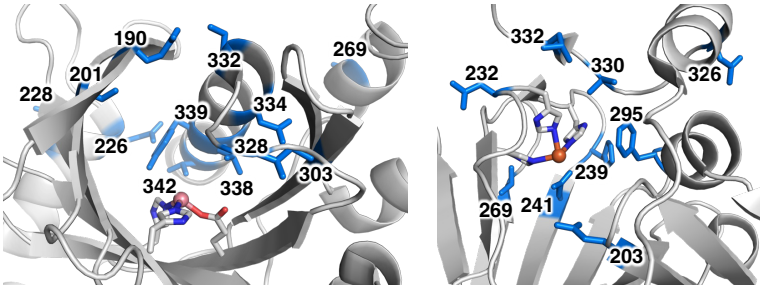

(E)

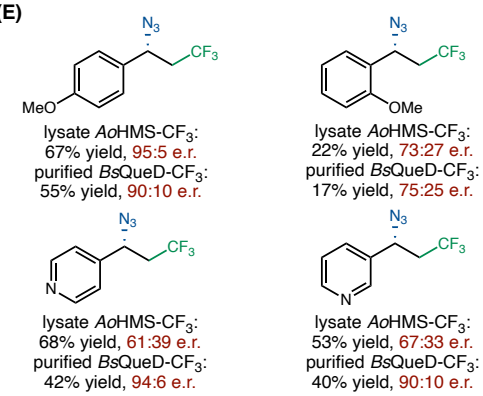

Figure 5. Nonheme Fe enzyme-catalyzed enantioselective trifluoromethylazidation of styrenes. (A) Proposed reaction mechanism; (B) Directed evolution of *Ao*HMS-CF_3; (C) Directed evolution of *Bs*QueD-CF_3; (D) The left illustration of active site was made from 2R5V (PDB ID); The right illustration was made from 1Y3T (PDB ID); (E) Selected substrate scope studies; reactions were

carried out using lysate of *Ao*HMS-CF_3 (OD_{600} = 40, 1.5 mol%) or purified *Bs*QueD-CF_3 (2 mol%).

Huang reported the use and engineering of nonheme Fe-dependent hydroxymandelate synthase from *Amycolatopsis orientalis* (*Ao*HMS)[91] to catalyze the enantioselective trifluoromethylazidation of styrenes.[92] To facilitate nonheme enzyme engineering for this unnatural radical reaction, the authors developed a high-throughput fluorescence screening assay using the Staudinger ligation of the organic azide products.[93] In each site-saturation mutagenesis (SSM) library, the top 15 hits based on enzyme activity from fluorescence assay were further evaluated based on enantioselectivity using chiral HPLC methods. With a sextuple mutant *Ao*HMS-QGHLYV (F188Q T214G Q305H F307L F330Y I335V) as the parent, iterative rounds of SSM and screening targeting residues close to the nonheme Fe catalytic triad resulted in *Ao*HMS-QGHLYV S201V N334S E190D L338A Y339V S332G G328S, which improved the enantioselectivity (91:9 e.r.) of the trifluoromethylazidation product. Additional random mutagenesis using error-prone PCR (epPCR)[94,95] introduced another three mutations including P173L, D228N, and A269T, which slightly improved product enantioselectivity (92:8 e.r.). Finally, three additional mutations V342A, Q226P, and L303M were introduced to furnish the final variant *Ao*HMS-CF_3, with an enantioselectivity of 95:5 e.r. (Figure 5B and 5D).

Jia engineered the nonheme Fe enzyme quercetin 2,3-dioxygenase from *Bacillus subtilis* (*Bs*QueD)[96,97] for trifluoromethylazidation.[98] Starting from wt *Bs*QueD, directed evolution via SSM and screening improved enzyme activity and enantioselectivity. Among the beneficial mutations identified, replacing the Fe-bound glutamate with a histidine (E241H) enhanced the yield and enantioselectivity of the trifluoromethylazidation product. Another mutation F295M was found to invert the enantioselectivity (70:30 e.r.). Further rounds of SSM and screening in an

iterative manner led to *Bs*QueD-CF_3 (*Bs*QueD E241H F295M L332I H239L L330Y N326D L239P D233E Y330F Q203T V269C), provided the product in 5% yield and 92:8 e.r. (Figure 5C, 5D). Further reaction condition optimization showed that using 2 mol% purified *Bs*QueD-CF_3 and 3 wt% TPGS-750-M,[99] the yield of the desired product could be further improved. The two extensively engineered nonheme systems independently developed by Huang and Jia shared a broad substrate scope using 1.5 mol% *Ao*HMS-CF_3 lysate and 2 mol% purified *Bs*QueD-CF_3 respectively (Figure 5E).

Metal substitution in nonheme enzymes allows the convenient replacement of the native catalytic center with alternative transition metals, giving rise to metalloenzymes with altered catalytic activities with broad synthetic applications.[100,101] Early pioneering studies by Kazlauskas,[102] Hartwig[103] and Simaan[104] replacing nonheme Fe with Cu and Rh explored metal-substituted nonheme enzymes in Lewis acid and hydroformylation chemistry. Recently, Huang reported the use of Cu-substituted nonheme enzyme SadA as Lewis acid catalysts to facilitate asymmetric Conia-ene reactions.[105] Inspired by these results and Buchwald's previously developed copper-catalyzed radical trifluoromethylation,[106–108] in 2025, Huang and coworkers reported the elegant use of Cu-substituted *Ao*HMS variants for the biocatalytic intramolecular alkene oxytrifluoromethylation.[109] In their proposed mechanism, Togni's reagent II is reduced by the Cu-substituted *Ao*HMS to generate the trifluoromethyl radical. Subsequent addition of this trifluoromethyl radical to the alkene leads to a new carbon-centered radical. Finally, enantioselective C–O bond formation mediated by the nonheme Cu center furnishes enantioenriched CF_3-substituted lactones.

Evaluation of Huang's engineered *Ao*HMS variants in the presence of Cu(II) led to Cu-substituted *Ao*HMS-V5 (*Ao*HMS-QGHLYV S201V N334S E190D L338A Y339V)[92] as an

excellent starting point, provided the product in 22% yield and 86:14 e.r. Directed evolution through five rounds of SSM and one round of random mutagenesis resulted in the final variant *Ao*HMS-AOT (*Ao*HMS-V5 A196T V203H A338V V339E D190E V335M H305R), providing the product in 37% yield and 97.5:2.5 e.r. (Figure 6A and 6B). Using 1.2 mol% cell-free lysate of *Ao*HMS-AOT, a range of substrates was tolerated, providing the corresponding products in up to 99% yields and 98:2 e.r.. Both β- and δ-lactones were also produced in an enantioenriched fashion, showcasing the synthetic versatility of the enzyme (Figure 6C).

(A)

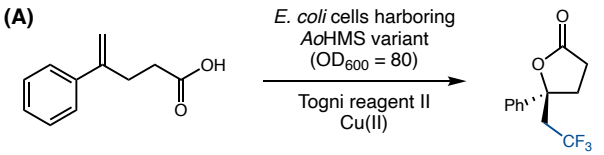

entry	*Ao*HMS variant	yield	e.r.
1	V5	22%	86:14
2	V5 A196T V203H A338T	24%	86.5:13.5
3	V5 A196T V203H A338T T338V	25%	90.5:9.5
4	V5 A196T V203H A338T T338V V339E	31%	90:10
5	V5 A196T V203H A338T T338V V339E D190E	30%	93:7
6	V5 A196T V203H A338T T338V V339E D190E V335M	35%	94:6
7	V5 A196T V203H A338T T338V V339E D190E V335M H305R (*Ao*HMS-AOT)	37%	97.5:2.5

(B)

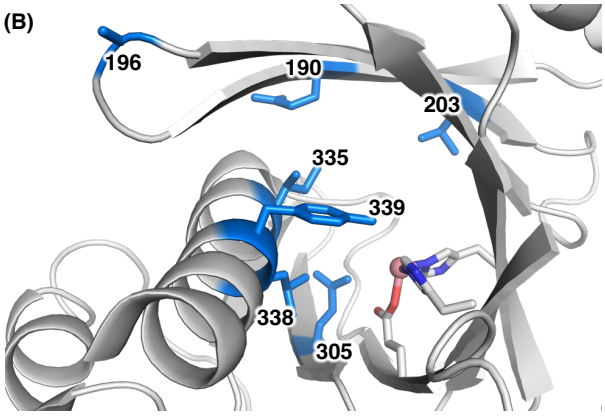

(C)

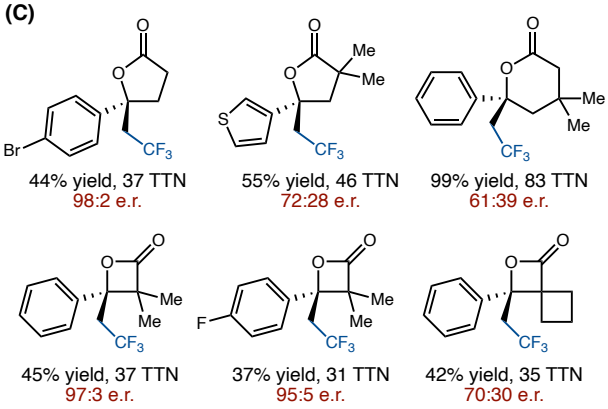

Figure 6. Cu-substituted *Ao*HMS-catalyzed enantioselective intramolecular alkene oxytrifluoromethylation. (A) Directed evolution of *Ao*HMS-AOT; (B) The illustration of active site was made from 2R5V (PDB ID); (C) Selected substrate scope studies; reactions were carried out using cell-free lysate of *Ao*HMS-AOT (OD_{600} = 80, 1.2 mol%).

B_{12}-dependent enzymes[110] such as adenosylcobalamin (AdoCbl)-dependent isomerases,[111] methyl-cobalamin (MeCbl)-dependent methyltransferases,[27] and dehalogenases[112] use cobalamin as the metallocofactor. The unique redox properties and diverse reactivity of the cobalamin cofactor provide an excellent opportunity for unnatural radical reactions to be advanced. In 2022, Lewis engineered transcription factor CarH[113] from *Thermus thermophilus* by fusing an *N*-terminal His_6-MBP tag to increase its solubility and introducing a H132G mutation to generate an open coordination site at Co center. The apo form of this CarH H132G construct was reconstituted with hydroxocobalamin (HOCbl),[114] which was termed as CarH* (MBP-*Tt*CarH H132G).[115] CarH* catalyzed C(sp^2)–H alkylation of styrenes using diazoacetate and diazoacetamide, displaying 2–6.5-fold higher yields relative to the free hydroxocobalamin cofactor (Figure 7A). In the proposed catalytic cycle, the hydroxocobalamin is first reduced to form the cob(I)alamin, which interacts with the diazoacetate substrate to generate a cob(III)alamin-alkyl complex upon electron transfer/proton transfer (ET/PT) events. This cob(III)alamin-alkyl complex is proposed to be in equilibration with cob(II)alamin and a carbon-center radical. The addition of this carbon-centered radical to styrene affords a new benzylic radical, which reacts with cob(II)alamin via β-H elimination to provide the alkylated styrene as the final product along with the cob(III)alamin hydride, which regenerates cob(I)alamin upon deprotonation and complete the catalytic cycle (Figure 7B).

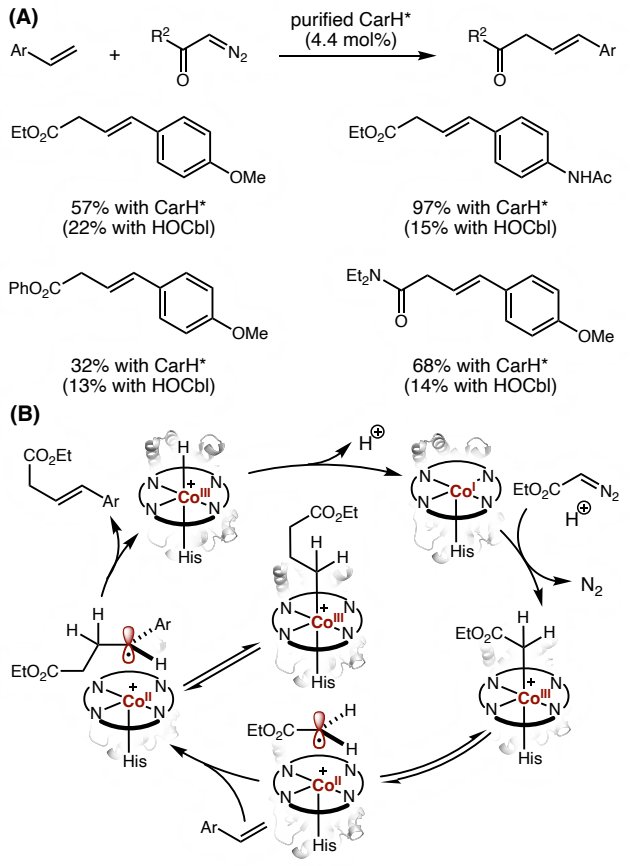

Figure 7. Styrene C–H alkylation catalyzed by CarH*. (A) Selected substrate scope; reactions were carried out using purified CarH* (4.4 mol%) or hydroxocobalamin (HOCbl, 4.4 mol%); (B) Proposed catalytic cycle.

Lewis further reported a CarH*-catalyzed radical cyclization for the synthesis of γ-lactams and δ-lactams (Figure 8).[116] Due to the unique ability of cobalamin to allow for β-H elimination, this CarH*-catalyzed radical cyclization exhibited a preference for olefin formation, thus complementing the reactivity of heme-based enzymes. Compared to free B_{12} cofactor, B_{12}-dependent protein CarH* showed improved catalytic activity and alkene/alkane chemoselectivity, further demonstrating the potential of protein catalysts to solve challenging chemoselectivity problems (Figure 8A). Mechanistically, the catalytic cycle is proposed to start via the reaction of

the α-chloro-α α-difluoroamide with Co(I) to form a Co(III)-alkyl complex. This Co(III)-alkyl complex readily equilibrates with the Co(II) alkyl radical form to allow radical cyclization to the pendant olefin, generating a new alkyl radical intermediate. β-H elimination from this radical species with Co(II) provides the cyclized alkene product and the Co(III)-H complex, which subsequently regenerates Co(I) via deprotonation. The cyclized alkane product is proposed to form via reduction of the corresponding alkyl radical intermediate (Figure 8B). In this CarH*-catalyzed radical cyclization, the α α-difluorocarbonyl moiety was proposed to play a key role in stabilizing the Co(III)–CF_2R species due to the more polar Co(III)–C bond with the *gem*-difluoro group. Enantioselective variants of this CarH*-catalyzed radical cyclization remained challenging.

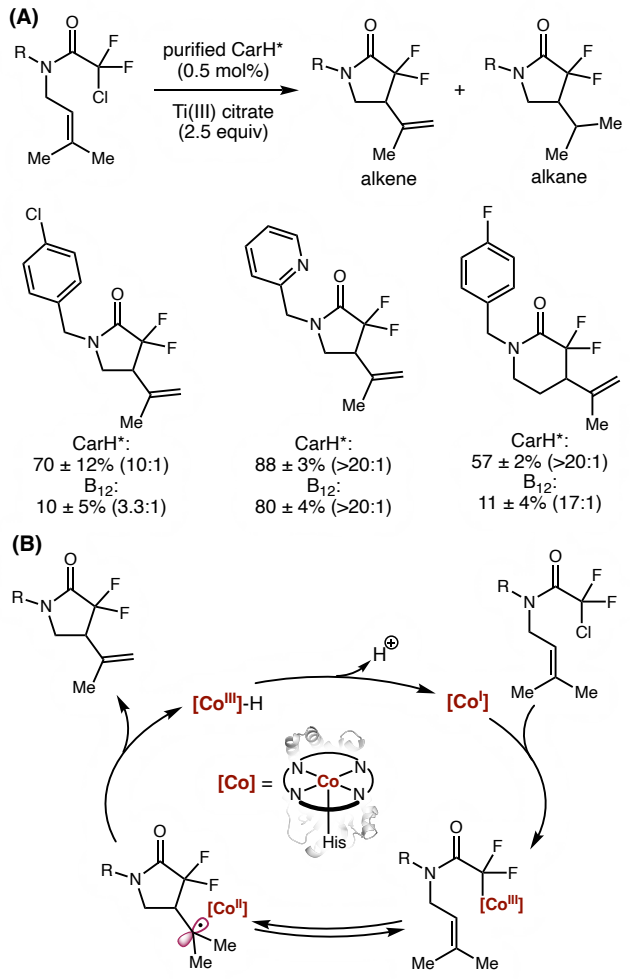

Figure 8. Radical cyclization catalyzed by CarH*. (A) Selected substrate scope, the alkene/alkane ratio in parenthesis refers to the yield of alkenes versus alkanes based on GC analysis; reactions were carried out using purified CarH* (0.5 mol%) or B_{12} (0.5 mol%); (B) Proposed catalytic cycle.

Transition-metal hydride intermediates play a critical role in the enzymology of naturally occurring [NiNi]-, [NiFe]-, and Fe-dependent hydrogenases.[117–119] In synthetic chemistry, first-row transition-metal hydride species based on Fe, Co, and Mn catalyzes a range of synthetically useful hydrofunctionalization of alkenes and alkynes[120–123] using a metal-hydride hydrogen atom transfer (MHAT) mechanism.[120,122] Inspired by this versatile MHAT catalytic manifold recently studied by the synthetic organic community, pioneering research has led to the successful repurposing of both nonheme Fe enzymes and heme enzymes to allow for unnatural enzymatic MHAT activities. Over the past several years, several hydrogen and hydride transfer reactions have been described with Zn- and Fe-dependent enzymes. In this review, we summarize processes where radical intermediates are likely involved. Elegant recent studies from Hartwig and Ji using Zn-dependent carbonic anhydrases[124–126] and Ward and Ji using Fe-dependent heme and nonheme enzymes[127,128] for metal hydride-mediated carbonyl reductions via a polar mechanism are out of the scope of this review.

In 2023, Chen, Chang, Guo and co-workers reported the use of Fe/αKG-dependent nonheme enzymes to catalyze the Mukaiyama hydration of olefins using a putative MHAT mechanism (Figure 9).[129] A range of styrenes was converted into the corresponding hydration products using nonheme Fe enzymes reconstituted from 0.2 mol% purified apo protein and 0.2 mol% Fe(II). Further studies suggested that the oxygen atom in the hydration product is derived from O_2. No enantioselectivity was observed for the hydration products. Deuterium incorporation studies using $NaBD_4$ showed 100% deuterium incorporation at the β-position and 15% deuterium incorporation

at the α-position of the hydration product (Figure 9B). EPR studies suggested that the ferric protein was reduced by $NaBH_4$ to the ferrous protein, which was re-oxidized to the ferric state in the presence of O_2. However, spectroscopic characterization of the putative Fe–H species remained difficult.

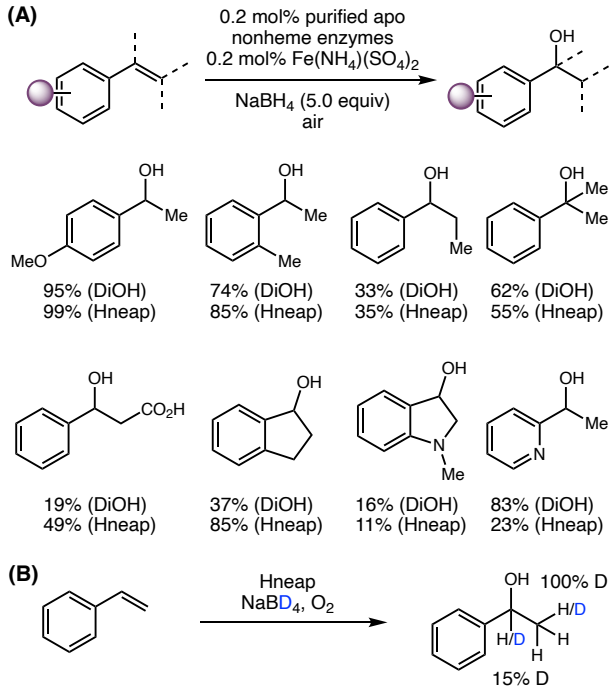

Figure 9. Biocatalytic Mukaiyama hydration of alkenes via MHAT. (A) Selected substrate scope; (B) The deuterium incorporation study.

In 2025, the Ward lab elegantly repurposed cytochromes P450 to catalyze asymmetric radical cyclization reactions via MHAT-generated carbon-centered radicals (Figure 10).[130] Wild-type $P450_{BM3}$[35] was found to catalyze this radical cyclization under MHAT conditions using $PhSiH_3$ as the hydrogen atom donor under air. The use of 1 mol% purified $P450_{BM3}$ provided the cyclized (*S*)-product in 13% yield with 13 TTN and 31:69 e.r.. Using 0.1 mol% purified CYP119,[131] the (*R*)-enantiomer of the cyclized product formed in 34% yield, 336 TTN and 64:36 e.r.. Three rounds

of directed evolution were carried out with $P450_{BM3}$, giving rise to a triple mutant $P450_{BM3}$ F87L A74Q I263Q ($P450_{BM3}$_LQQ) with improved activity and enantioselectivity (44% yield, 44 TTN and 6:94 e.r.) (Figure 10A). Similarly, iterative SSM and screening of CYP119 furnished CYP119 D77R T214V L205V T213 Q22H A209T I208S (CYP119 MHATase), providing the (*R*)-enantiomer in 30% yield, 305 TTN and 85:15 e.r. (Figure 10B). The addition of TPGS-750-M further improved the conversion of this biocatalytic reaction.[132] Using evolved P450 variants, substrates possessing a range of aryl sulfonamides and radical acceptors were successfully transformed using 0.05–0.1 mol% biocatalyst in the form of whole *E. coli* cells (Figure 10C).

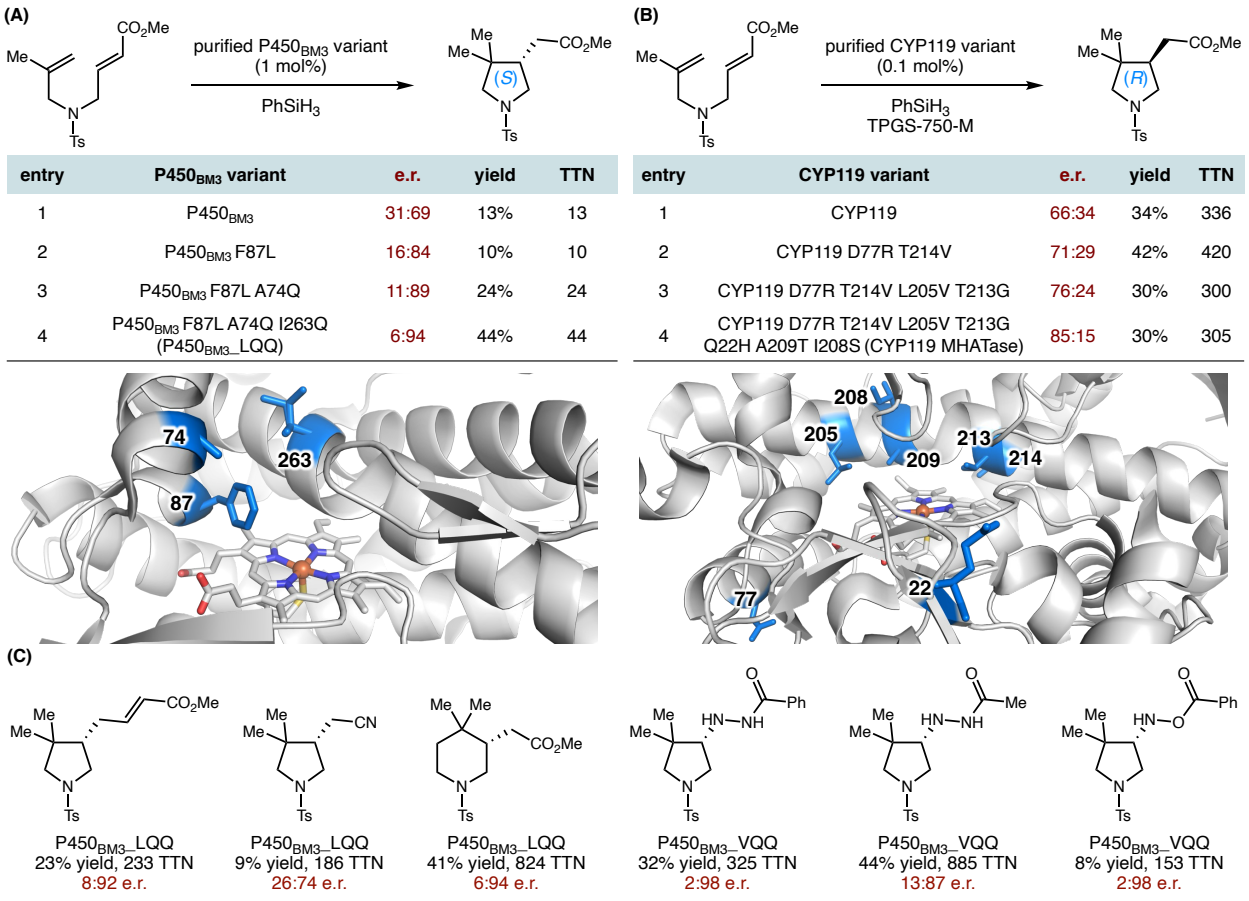

entry	$P450_{BM3}$ variant	e.r.	yield	TTN
1	$P450_{BM3}$	31:69	13%	13
2	$P450_{BM3}$ F87L	16:84	10%	10
3	$P450_{BM3}$ F87L A74Q	11:89	24%	24
4	$P450_{BM3}$ F87L A74Q I263Q ($P450_{BM3}$_LQQ)	6:94	44%	44

entry	CYP119 variant	e.r.	yield	TTN
1	CYP119	66:34	34%	336
2	CYP119 D77R T214V	71:29	42%	420
3	CYP119 D77R T214V L205V T213G	76:24	30%	300
4	CYP119 D77R T214V L205V T213G Q22H A209T I208S (CYP119 MHATase)	85:15	30%	305

Figure 10. P450-catatalyzed enantioselective radical cyclization via MHAT. (A) Directed evolution of $P450_{BM3}$_LQQ for (*S*)-product: the illustration of active site was made from 2IJ2

(PDB ID); (B) Directed evolution of CYP119 MHATase for (*R*)-product: the illustration of active site was made from 1IO7 (PDB ID); (C) Selected substrate scope; reactions were carried out using whole *E. coli* cells overexpressing $P450_{BM3}$_LQQ (0.05 mol%) or purified $P450_{BM3}$ F87V A74Q I263Q ($P450_{BM3}$_VQQ, 0.05–0.1 mol%).

Mechanistic studies revealed that the ferric P450 enzyme was reduced by $PhSiH_3$ to afford the ferrous enzyme, which is re-oxidized to the Fe(III) state by air. Deuterium labelling studies showed that the hydrosilane reagent was the hydrogen atom donor for MHAT and water served as the proton donor for the final protonation step. Based on these results, Ward proposed that in the plausible catalytic cycle, the Fe(III) P450 enzyme first reacts with $PhSiH_3$ to form an Fe(III)–H species, which undergoes MHAT with the alkene moiety to generate a carbon-centered radical and an Fe(II) species. Enzyme-controlled radical addition to the pendant α β-unsaturated carbonyl moiety forms a new carbon-centered radical, which undergoes concerted proton-coupled electron transfer (PCET) with water-bound P450–Fe(II) complex to afford the cyclized chiral product (Figure 11).

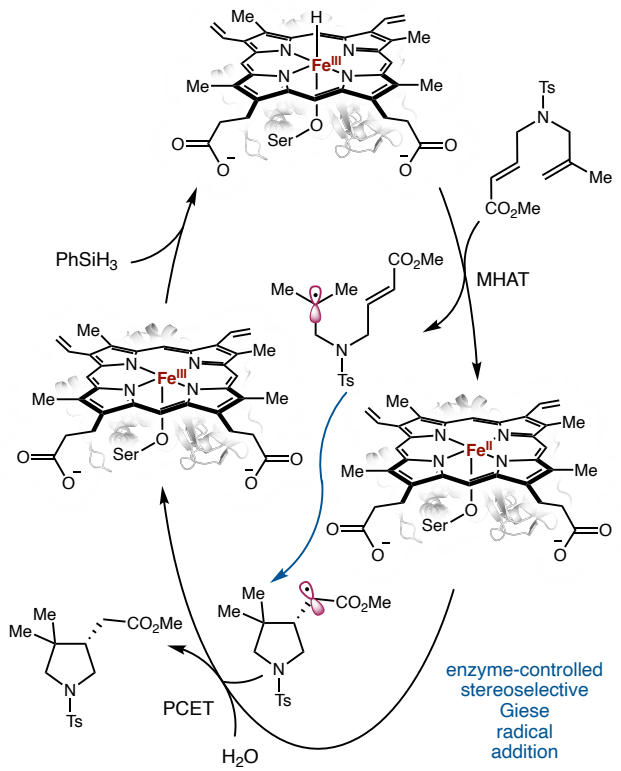

Figure 11. Proposed catalytic cycle for the P450-catalyzed asymmetric radical cyclization via MHAT.

In 2025, Athavale and co-workers elegantly engineered protoglobins for the asymmetric hydrogenation of unactivated olefins via a novel MHAT and HAT mechanism with active-site cysteine as the putative H atom donor.[133] Initial metalloprotein screening identified a protoglobin variant from *Aeropyrum pernix* (*Ape*Pgb C45G W59L Y60V V63R F145Q I149L, HAT_{OC}) as a promising candidate. To introduce an active-site cysteine as H atom donor,[134] several single cysteine mutants were generated by site-directed mutagenesis and HAT_{OC} V60C was found to deliver the asymmetric hydrogenation product in 3.8% yield and 91:9 e.r.. Directed evolution through an additional four rounds of SSM furnished the final variant HAT_R-5 (HATOC V60C Q145E L69N V89G L59M) with excellent activity and enantioselectivity. The asymmetric

hydrogenation reaction was carried out using whole *E. coli* cells overexpressing HAT_R-5 (OD_{600} = 50) and product was obtained in 44.8% yield and 98:2 e.r. (Figure 12A). The yield was further increased by using purified protein catalyst in the presence of TPGS-750-M. A range of 3-methylene piperidine, pyrrolidine, and azepine substrates with different *N*-protecting groups were tolerated, providing hydrogenation products in good yields and enantioselectivity (Figure 12B). Mechanistic studies were consistent with a stepwise radical pathway for this process. In the proposed catalytic cycle, the ferric heme protein reacts with phenylsilane to generate the Fe(III)–H species, which undergoes MHAT with the olefin substrate to generate a carbon-centered radical and the Fe(II) protein. The carbon-centered radical subsequently undergoes asymmetric hydrogen atom transfer with the active-site cysteine, delivering the asymmetric hydrogenation product and a thiyl radical. Final proton-coupled electron transfer (PCET) between the thiyl radical and Fe(II) center regenerates the ferric heme species and the cysteine thiol (Figure 12C).

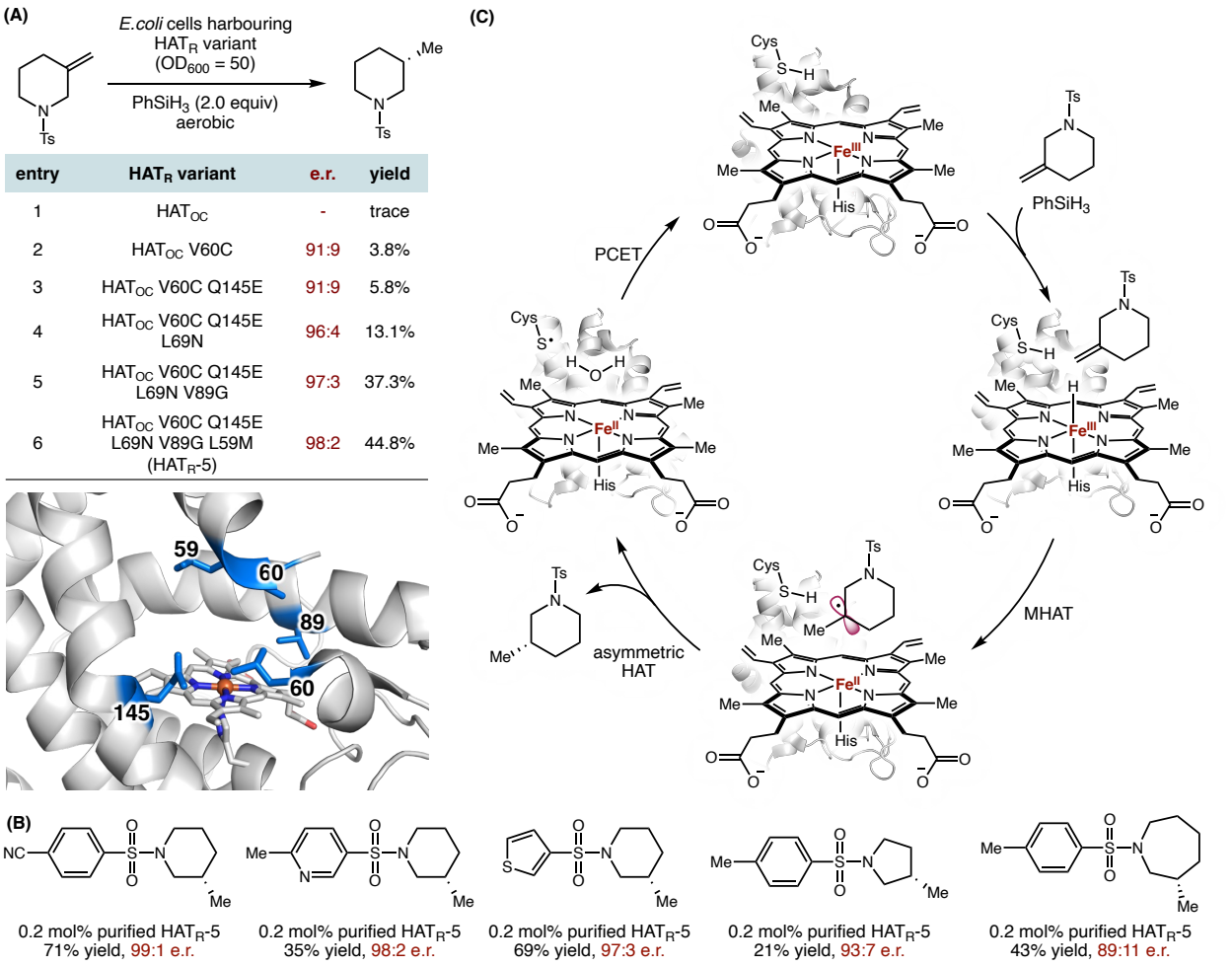

entry	HAT_R variant	e.r.	yield
1	HAT_{OC}	-	trace
2	HAT_{OC} V60C	91:9	3.8%
3	HAT_{OC} V60C Q145E	91:9	5.8%
4	HAT_{OC} V60C Q145E L69N	96:4	13.1%
5	HAT_{OC} V60C Q145E L69N V89G	97:3	37.3%
6	HAT_{OC} V60C Q145E L69N V89G L59M (HAT_R-5)	98:2	44.8%

Figure 12. Biocatalytic asymmetric hydrogenation of unactivated olefins. (A) Directed evolution of HAT_R-5: the illustration of active site was made from 8EUM (PDB ID); (B) Selected substrate scope; reactions were carried out using purified HAT_R-5 (0.2 mol%) in the presense of 6 wt% TPGS-750-M; (C) Proposed catalytic cycle for the biocatalytic asymmetric hydrogenation of olefins via MHAT and HAT.

2.2 Addition of carbon-centered radicals to arenes

Radical functionalization of arenes represents a powerful method to prepare substituted aromatic compounds.[135] In native enzymology, radical functionalization of aromatic substrates

often involve oxidative processes catalyzed by monooxygenases and dioxygenases.[136–138] Recent development of metalloenzyme-catalyzed unnatural radical functionalization of aromatic compounds would further expand the toolbox of arene functionalization and allow chiral aromatic scaffolds to be prepared in a highly enantioenriched fashion.

In 2023, our lab reported an enantioconvergent radical cyclization to arenes using engineered cytochromes P450 (Figure 13).[139] In our proposed catalytic cycle (Figure 13A), the P450 enzyme in its ferrous state first undergoes single-electron transfer to the 2-halo-1,3-dicarbonyl substrate, leading to a carbon-centered radical along with the oxidized ferric state enzyme. Subsequent addition of this nascent carbon-centered radical to the pendant aromatic ring within the enzyme active site occurs in an enantioselective fashion, furnishing a cyclized dearomatized radical intermediate. Further radical-polar crossover converts this radical to the enantioenriched 3,3-disubstituted oxindole product. Previous studies from Mayer[140] and our computational studies suggest the potential involvement of heme propionate in a proton-coupled electron transfer (PCET) mechanism for the oxidation of dearomatized radical intermediate.

In this study, evaluation of a collection of P450 variants led to the identification of $P411_{Diane2}$ and $P411_{Diane3}$,[83] providing the (*S*)- and (*R*)-enantiomeric products with 66:34 e.r. and 36:64 e.r., respectively. Subsequent iterative SSM and screening furnished two final variants, including $P450_{arc1}$ ($P411_{Diane2}$ W263Q L181M T438G H266L) and $P450_{arc2}$ ($P411_{Diane3}$ G437A V327P N70S A330F G74P) (Figure 13B). Using whole *E. coli* cells harboring $P450_{arc1}$, the (*S*)-product was obtained in 77% yield, 1,330 TTN and 96:4 e.r.. The (*R*)-product was obtained in 88% yield, 1,890 TTN and 12:88 e.r. using $P450_{arc2}$. Another closely-related variant $P450_{arc3}$ ($P450_{arc1}$ G438T L266H L78C V328E S332A) was found to catalyze the kinetic resolution of α-chloroamide substrate. At 55% conversion, the (*R*)-enantiomeric substrate was recovered in 45% yield and 94:6

e.r. (Figure 13C). These results further demonstrated the excellent tunability of P450 enzymes to allow for both enantioconvergent transformation and kinetic resolution through a common radical-based mechanism.

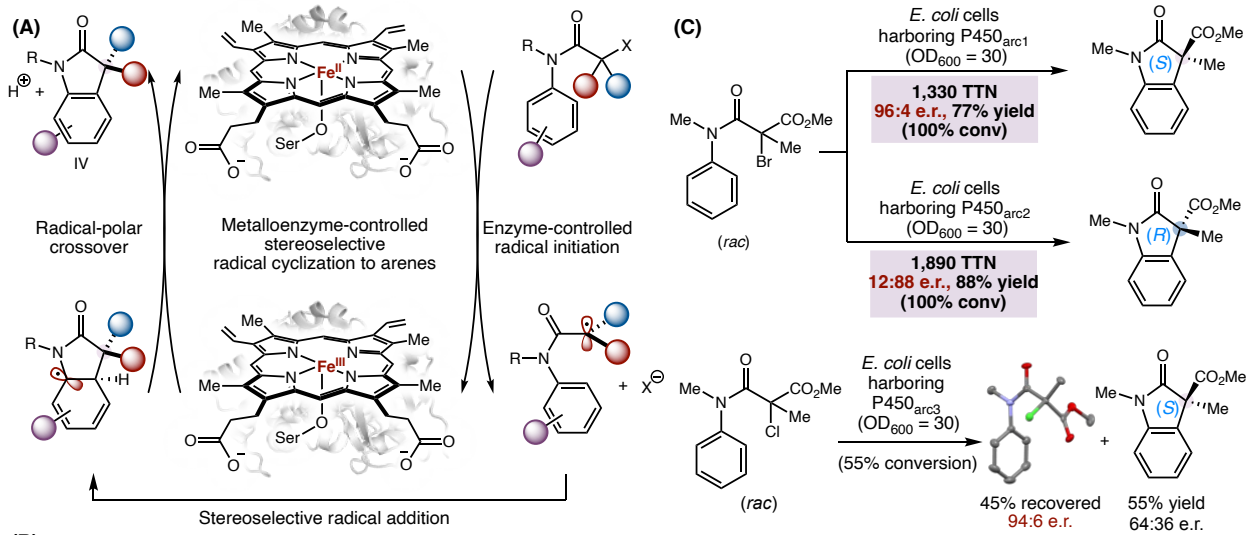

(B)

Directed evolution of $P450_{arc1}$

entry	P450 variant	e.r.	yield	TTN
1	$P450_{Diane2}$	66:34	53%	1,350
2	$P450_{Diane2}$ W263Q	80:20	90%	2,700
3	$P450_{Diane2}$ W263Q L181M	84:16	88%	1,810
4	$P450_{Diane2}$ W263Q L181M T438G	90:10	64%	1,450
5	$P450_{Diane2}$ W263Q L181M T438G H266L ($P450_{arc1}$)	96:4	77%	1,330

Directed evolution of $P450_{arc2}$

entry	P450 variant	e.r.	yield	TTN
1	$P450_{Diane3}$	36:64	49%	1,090
2	$P450_{Diane3}$ G437A	22:78	81%	2,230
3	$P450_{Diane3}$ G437A V327P	20:80	94%	2,460
4	$P450_{Diane3}$ G437A V327P N70S	15:85	97%	2,100
5	$P450_{Diane3}$ G437A V327P N70S A330F G74P ($P450_{arc2}$)	12:88	88%	1,890

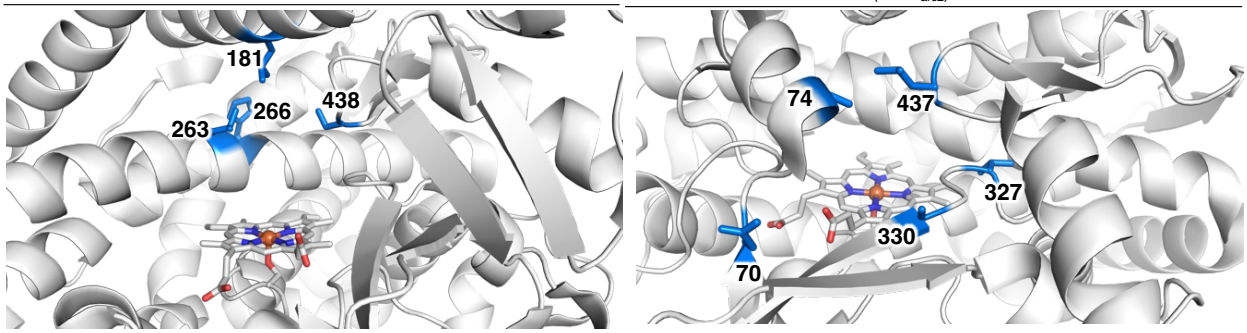

Figure 13. P450-catalyzed enantioconvergent radical cyclization to arenes. (A) Proposed catalytic cycle; (B) Directed evolution of $P450_{arc1}$ and $P450_{arc2}$: illustrations of active sites were made from

5UCW (PDB ID); (C) Enantiodivergent transformation and kinetic resolution in P450-catalyzed radical cyclization to arenes.

In 2024, our lab further expanded this P450-catalyzed radical arene functionalization to asymmetric radical dearomatization reactions.[132] Asymmetric dearomatization represent a valuable method to transform planar aromatic compounds into chiral three-dimensional products.[141–144] Despite recent development using other mechanisms for catalytic asymmetric dearomatization, free radical-mediated dearomatization has remained challenging in asymmetric catalysis.[145,146] Thus, the P450 radical dearomatases developed in our lab provided a solution to bridge this gap. In the proposed catalytic cycle (Figure 14), the α-carbonyl radical forms via single electron transfer between the α-halocarbonyl substrate and the ferrous P450 catalyst. Dearomative radical cyclization of this α-carbonyl radical to the pendant phenol affords a dearomatized radical intermediate. The oxidative radical-polar crossover finally provides the dearomatized spirocyclic product with contiguous quaternary centers in an enantioenriched manner. This electron transfer also regenerates the ferrous P450 and complete the catalytic cycle.

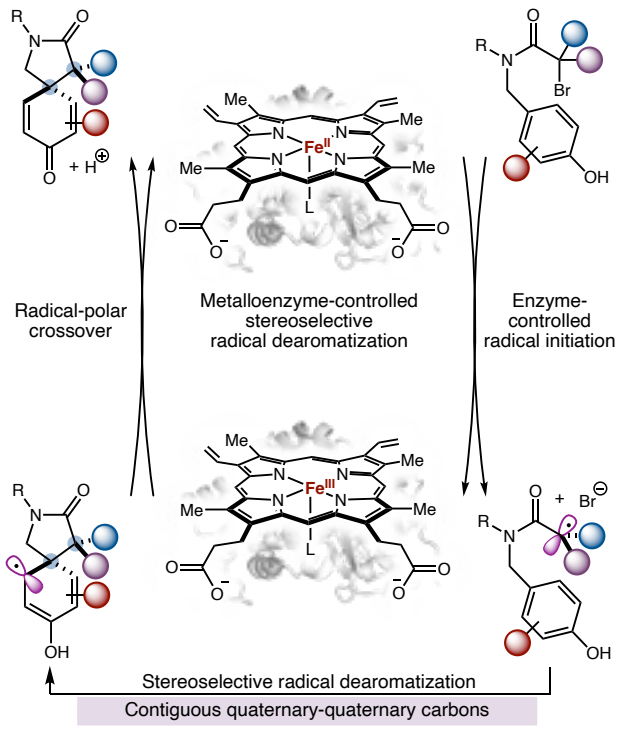

Figure 14. Proposed catalytic cycle for P450-catalyzed stereoselective radical dearomatization.

In enzyme evaluation, P411-CIS I263G L437F V87F P248T (P1) was found to promote the radical dearomatization of indole substrates, providing the corresponding spirocyclic product in 19% yield, 39 TTN and 83:17 e.r.. Three rounds of SSM and screening targeting active-site residues furnished a triple mutant P1 L181V A78C F437A ($P450_{rad1}$), providing the product in 90% yield, 182 TTN and 97:3 e.r. (Figure 15A). Enantioconvergent radical dearomatization of racemic phenol substrates was also achieved using P2 F437P L436A L75F G268P ($P450_{rad4}$), providing the product in 95% yield, 870 TTN and 91:9 e.r.. Improved enantioselectivity (94:6 e.r.) could be achieved with a higher loading of $P450_{rad4}$ (Figure 15B). Substrate scope studies showed that a range of indoles and phenols were accommodated by these evolved P450 radical dearomatases (Figure 15C). Biocatalytic enantiodivergent radical dearomatization of pyrroles could also be achieved with $P450_{rad2}$ (P411-CIS L75A L181A A82V) and $P450_{rad3}$ ($P411_{Diane2}$ W263I G268A

P327T V328A E267L), giving rise to either the (*R*)- (94% yield, 2,320 ± 30 TTN and 91:9 e.r.) or the (*S*)-product (76% yield, 3,230 ± 10 TTN and 8:92 e.r.) with good yield and enantioselectivity (Figure 15D). Upon the inclusion of 2 wt% TPGS-1000, the naphthol substrate with low solubility was also smoothly transformed in 84% yield, 1,510 ± 80 TTN and 97:3 e.r. using $P450_{rad5}$ (P411-CIS T438S)[82] (Figure 15E).

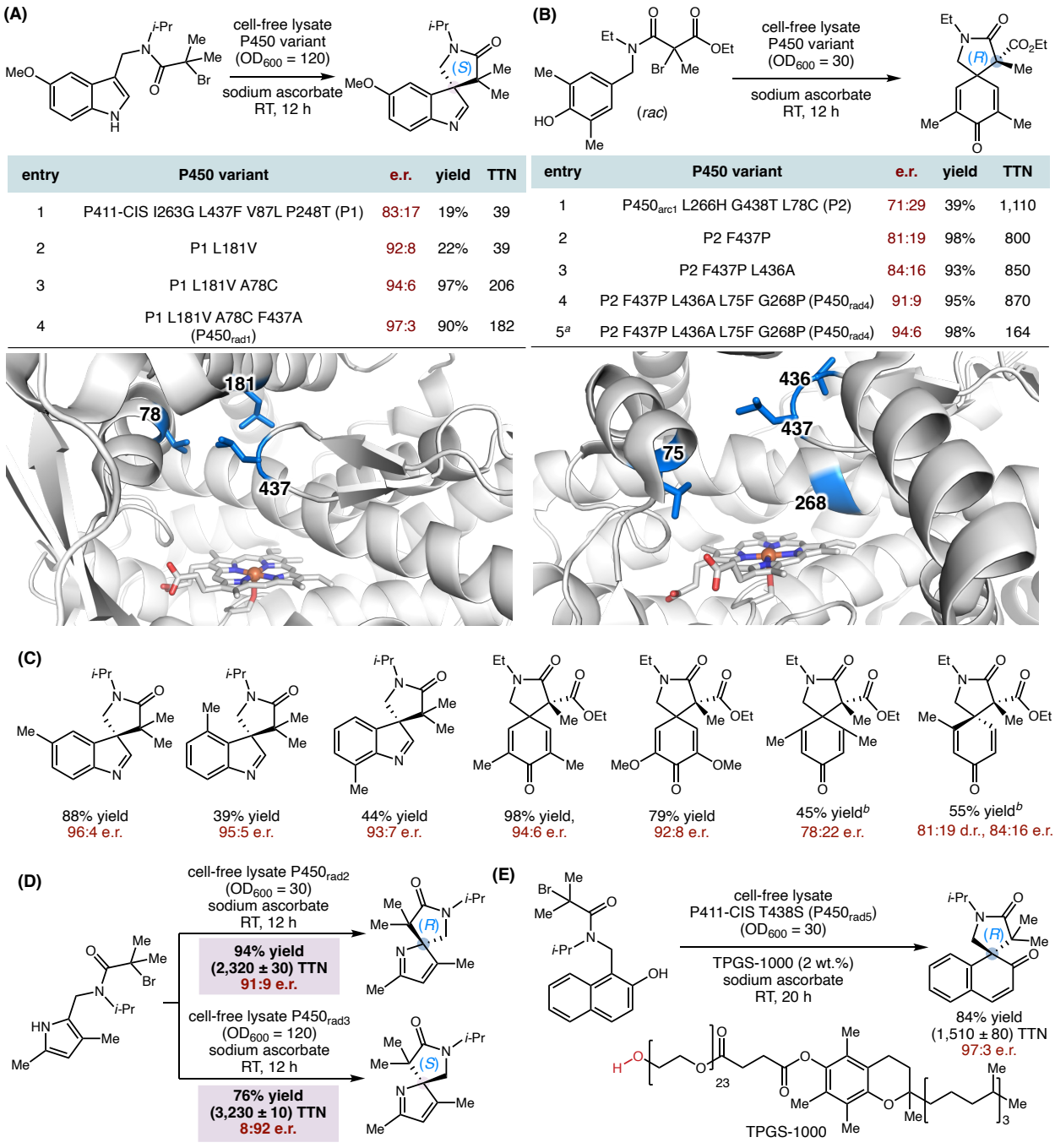

entry	P450 variant	e.r.	yield	TTN
1	P411-CIS I263G L437F V87L P248T (P1)	83:17	19%	39
2	P1 L181V	92:8	22%	39
3	P1 L181V A78C	94:6	97%	206
4	P1 L181V A78C F437A ($P450_{rad1}$)	97:3	90%	182

entry	P450 variant	e.r.	yield	TTN
1	$P450_{arc1}$ L266H G438T L78C (P2)	71:29	39%	1,110
2	P2 F437P	81:19	98%	800
3	P2 F437P L436A	84:16	93%	850
4	P2 F437P L436A L75F G268P ($P450_{rad4}$)	91:9	95%	870
5[a]	P2 F437P L436A L75F G268P ($P450_{rad4}$)	94:6	98%	164

Figure 15. P450-catalyzed enantioselective radical dearomatization. (A) Directed evolution of indole dearomatase $P450_{rad1}$: the illustration of active site was made from 5UCW (PDB ID); (B) Directed evolution of phenol dearomatase $P450_{rad4}$: the illustration of active site was made from 5UCW (PDB ID); (C) Selected substrate scope; reactions were carried out using cell-free lysate of

$P450_{rad1}$ (1 mol%) or $P450_{rad4}$ (0.6 mol%); [a]A higher P450 loading (OD_{600} = 120) was used; [b]Starting variant P2 was used; (D) P450-catalyzed enantiodivergent radical dearomatization of pyrroles; (E) P450-catalyzed enantioselective radical dearomatization of naphthol.

Lewis and coworkers reported that the B_{12}-dependent protein CarH* could catalyze reductive radical dearomatization in the presence of titanium (III) citrate, affording dearomatized spirocyclic products possessing a 1,3-cyclohexadiene (Figure 16).[116] This radical dearomatization follows an overall mechanism similar to that described in Figure 8. The α-chloro-α,α-difluoroamide substrate first reacts with the Co(I) protein to form a Co(III)-alkyl intermediate. This Co(III)-alkyl species readily generates an α,α-difluoro-α-carbonyl radical and a Co(II) species via homolytic cleavage of the Co(III)–C bond, allowing radical cyclization with the electron-deficient aromatic ring to provide a dearomatized radical intermediate. Single-electron reduction and protonation of this radical finally lead to the dearomatized product. Lewis and coworkers found that a range of arenes bearing an electron-withdrawing substituent could be converted, providing dearomatized products often with higher yields compared to free B_{12}. Heterocycles including a pyridine and a thiophene were also readily transformed under these conditions (Figure 16A). In addition to γ-lactams, δ-lactams could also be prepared from substrates bearing an extended linker, although a mixture of dearomatization product and C–H functionalization product were observed (Figure 16B). No enantioselectivity was observed for these CarH*-catalyzed radical dearomatization reactions.

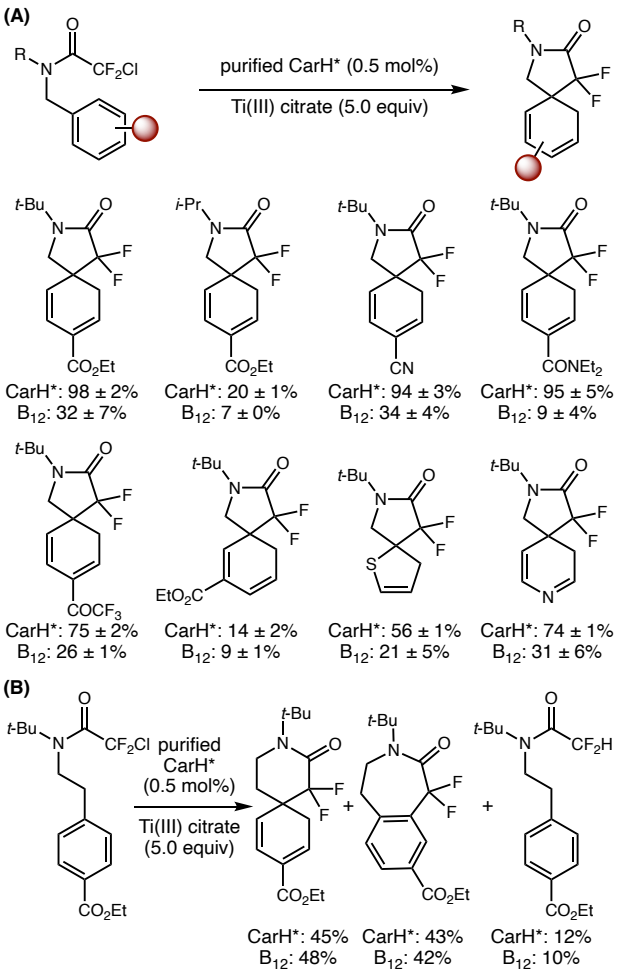

Figure 16. CarH*-catalyzed reductive radical dearomatization. (A) Selected substrate scope for γ-lactams; reactions were carried out using purified CarH* (0.5 mol%) or B_{12} (0.5 mol%); (B) δ-Lactam formation.

In 2025, our lab reported the first catalytic asymmetric Smiles rearrangement proceeding through the enantioselective addition of a carbon-centered radical to the *ipso*-carbon of the arylsulfonyl moiety (Figure 17).[147] In the proposed catalytic cycle, the racemic *N*-arylsulfonyl-α-chloroamide substrate is first reduced via single electron transfer from the ferrous P450 enzyme to generate an α-carbonyl radical. This radical then undergoes enantioselective radical cyclization to the *ipso*-carbon of the arylsulfonyl moiety to generate a dearomatized radical intermediate. SO_2

extrusion results in the formation of an amidyl radical, which undergoes a formal hydrogen atom transfer reaction to provide the acyclic amide product possessing a quaternary stereocenter. Alternatively, this amidyl radical may undergo a 5-*exo*-*trig* radical cyclization to the arene leading to the lactam product (Figure 17A).

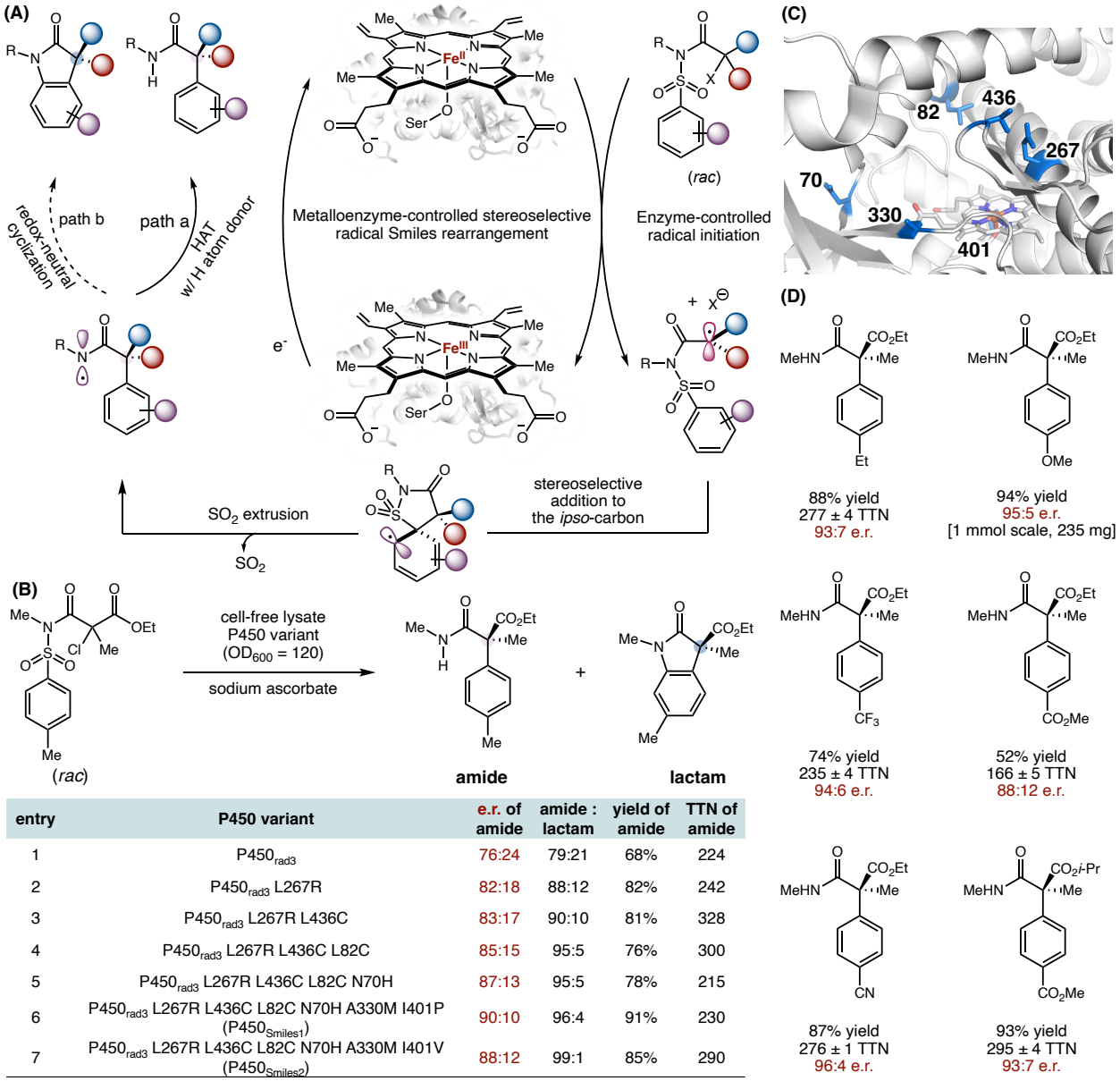

entry	P450 variant	e.r. of amide	amide : lactam	yield of amide	TTN of amide
1	$P450_{rad3}$	76:24	79:21	68%	224
2	$P450_{rad3}$ L267R	82:18	88:12	82%	242
3	$P450_{rad3}$ L267R L436C	83:17	90:10	81%	328
4	$P450_{rad3}$ L267R L436C L82C	85:15	95:5	76%	300
5	$P450_{rad3}$ L267R L436C L82C N70H	87:13	95:5	78%	215
6	$P450_{rad3}$ L267R L436C L82C N70H A330M I401P ($P450_{Smiles1}$)	90:10	96:4	91%	230
7	$P450_{rad3}$ L267R L436C L82C N70H A330M I401V ($P450_{Smiles2}$)	88:12	99:1	85%	290

Figure 17. Biocatalytic asymmetric radical Smiles rearrangement. (A) Proposed catalytic cycle; (B) Directed evolution of $P450_{Smiles}$; (C) The illustration of active site was made from the structure of 5UCW (PDB ID); (D) Selected substrate scope; reactions were carried out using cell-free lysate of $P450_{Smiles1}$ (OD_{600} = 120, 0.30–0.34 mol%).

Despite the multiple pathways available, our lab showed that both the chemoselectivity and enantioselectivity could be controlled through enzyme engineering. Initial evaluation of our P450 radical cyclase panel revealed that the previously engineered pyrrole dearomatase $P450_{rad3}$[132] catalyzed this radical Smiles rearrangement with the acyclic amide as the major product (amide:lactam = 79:21, 76:24 e.r.). Six rounds of directed evolution led to two final P450 aryl radical migratases, including $P450_{Smiles1}$ ($P450_{rad3}$ L267R L436C L82C N70H A330M I401P) and $P450_{Smiles2}$ ($P450_{rad3}$ L267R L436C L82C N70H A330M I401V). With $P450_{Smiles1}$, the acyclic amide was obtained in 91% yield with 230 TTN, 90:10 e.r. and an amide:lactam selectivity of 96:4. $P450_{Smiles2}$ allowed further improved chemoselectivity favoring the acyclic amide (85% yield, 290 TTN, 88:12 e.r. and an amide:lactam selectivity of 99:1) (Figure 17B and 17C). Classical molecular dynamics (MD) simulations of the amidyl radical intermediate in the final variant $P450_{Smiles2}$ revealed the importance of hydrogen bonding interactions with the L267R guanidium and C–H/π interactions in stabilizing the amidyl radical and disfavoring its cyclization. Both electron-rich or electron-deficient arenes were found to be compatible with this radical Smiles rearrangement, demonstrating this transformation is insensitive to the electronic properties of the arene (Figure 17D).

2.3 Functionalization of carbon-centered radicals via a rebound mechanism

The central mechanism in heme and nonheme Fe enzyme-catalyzed C–H hydroxylation and halogenation lies in the formation of a transient carbon-centered radical and subsequent radical rebound for C–O and C–X bond formation.[41,39,42,44] In this section, we review metalloenzyme-catalyzed functionalization reactions involving a radical rebound mechanism.

In nature, α-ketoglutarate-dependent (αKG) nonheme Fe halogenases catalyze diverse chlorination and bromination reactions via radical rebound with Fe(III)–X intermediates.[148–159] In the presence of exogenous anions such as azide and nitrate, promiscuous radical rebound activities including C–H azidation and C–H nitration have long been studied with a range of αKG-dependent halogenases (Figure 18). In 2014, Bollinger and coworkers reported that SyrB2 catalyzed C–H azidation and C–H nitration with modest activity of L-2-aminobutyrate loaded to the carrier protein SyrB1.[160] In 2019, Chang and coworkers found that *Sw*HalB catalyzed the δ-azidation of the amino acid substrate.[161] In 2020, Weng and coworkers reported that *Sa*DAH could catalyze the C–H azidation of dechloroacutumine.[162] In 2022, Buller and coworkers used engineered WelO5* for the C–H azidation and nitration of Soraphen A.[157] The chemoselectivity of C–H azidation over hydroxylation is often controlled by the positioning of the radical intermediate within the enzyme's active site. It remains a nontrivial task to generalize the chemoselectivity trend previously optimized to a broader range of substrates.

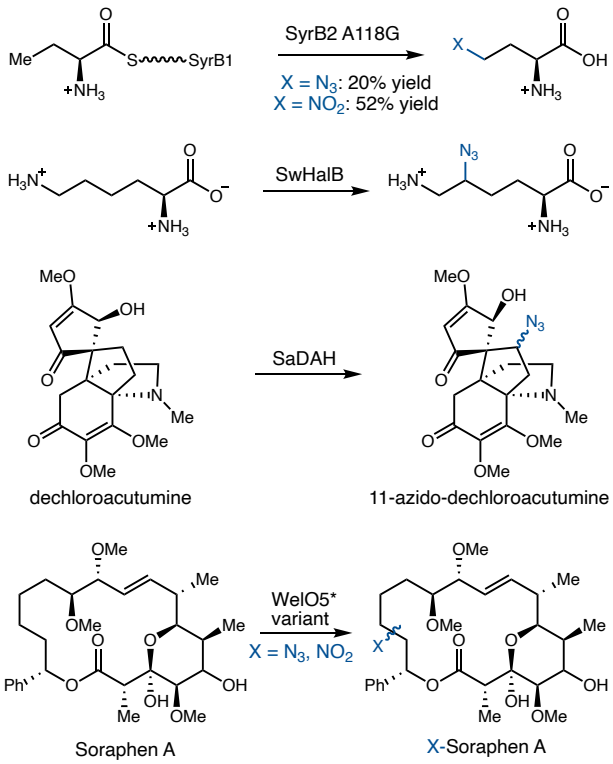

Figure 18. Promiscuous C–H azidation and C–H nitration activities with αKG-dependent nonheme Fe halogenases.

Very recently, in 2025, Tang discovered and characterized a novel dinuclear copper halogenase, ApnU, which performs selective C(sp^3)–H chlorination, bromination, iodination, azidation and thiocyanation through a distinct copper-based mechanism (Figure 19A).[163] Additionally, this enzymatic conversion in the absence of chloride showed markedly reduced activity and led to the formation of desaturation product, accompanied by trace amount of hydroxylation product (Figure 19B). This finding is in contrast to αKG-dependent nonheme Fe halogenases, where C–H hydroxylation often competes with halogenation. These results indicated that with these copper-dependent halogenases, chloride binding is likely important for both radical generation and hydroxyl rebound suppression. The pioneering studies from Tang further expands

the catalytic repertoire of enzymatic halogenation and highlights the diversity of natural metalloenzymes capable of effecting C(sp^3)–H functionalization.

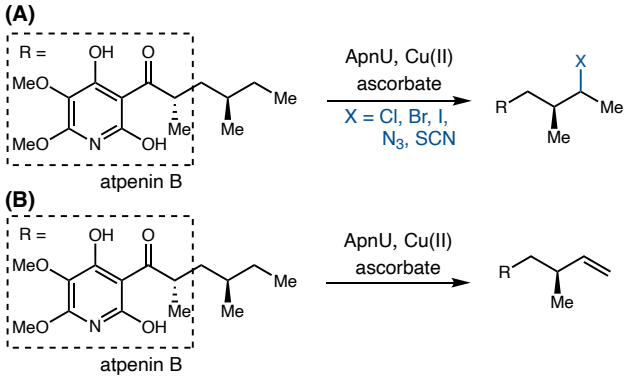

Figure 19. Copper enzyme ApnU-catalyzed C(sp^3)–H functionalization. (A) ApnU-catalyzed C(sp^3)–H chlorination, bromination, iodination, azidation and thiocyanation with different anions. (B) ApnU-catalyzed desaturation in the absence of halide anions.

The overall catalytic cycle of αKG-dependent halogenase-catalyzed C–H azidation is depicted in Figure 20A. Using α-ketoglutarate as the co-substrate and O_2 as the oxidant, a reactive Fe(IV)-oxo intermediate forms from the ferrous enzyme. This ferryl intermediate undergoes rapid hydrogen atom abstraction from the substrate, leading to a carbon-centered radical along with a ferric intermediate. Upon radical rebound with the Fe(III)–N_3 intermediate, the alkyl azide product forms and the ferrous enzyme is regenerated. If hydroxy rebound occurs with the Fe(III)(N_3)(OH) species, C–H hydroxylation product would form. Prior studies showed that natural Fe/αKG-dependent C–H hydroxylases typically feature a two-histidine-one-carboxylate facial triad, whereas Fe/αKG-dependent halogenases have a two-histidine facial dyad to allow for halogen anion binding.[148] Guided by these insights, in 2017, Boal and Liu successfully converted a Fe/αKG-dependent hydroxylase SadA into a halogenase by introducing a single D157G mutation to convert the Fe-binding aspartate to a glycine.[164] This SadA D157G single mutant transformed

its native substrate into a mixture of C–H chlorination and hydroxylation products, with the hydroxylated product accounting for 70% of combined products.[164] In 2021, Chang and coworkers used bioinformatic analysis, DNA shuffling and high-throughput enzyme engineering to convert a native C–H hydroxylase into a chlorinase Chi-14, achieving an excellent chlorination:hydroxylation selectivity of 92:8.[165]

In 2022, starting from SadA D157G (termed as SadX), Lewis reported the directed evolution of SadX to enable the C–H azidation of a broader range of substrates (Figure 20).[166] Four rounds of random mutagenesis using epPCR and screening furnished SadX 4-IC (SadX I71V R172H F152L I38V Q233R F261L V38I R48C), providing the azide product in 91% conversion with an improved azidation/hydroxylation selectivity (N_3/OH = 4.09) at 10 mol% SadX loading (Figure 20B).[167] Substrates bearing other substituents were also transformed into the azidation products with modest to good chemoselectivity (Figure 20C).

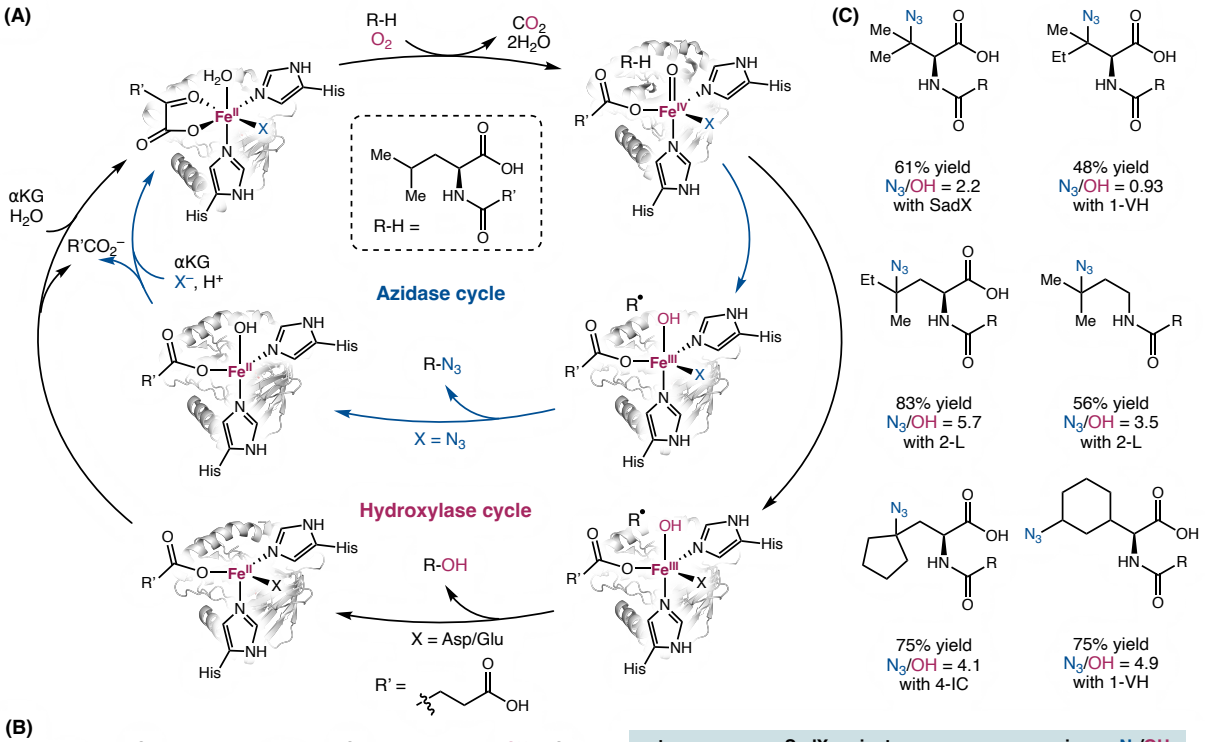

entry	SadX variant	conversion	N_3/OH
1	SadX	22%	0.46
2	SadX I71V R172H (1-VH)	20%	0.95
3	SadX I71V R172H F152L (2-L)	37%	1.03
4	SadX I71V R172H F152L I38V Q233R F261L (3-VRL)	49%	5.14
5	SadX I71V R172H F152L I38V Q233R F261L V38I R48C (4-IC)	91%	4.09

Figure 20. Biocatalytic C–H azidation catalyzed by SadA D157G. (A) Generally accepted catalytic cycle; (B) Directed evolution of SadA; (C) Selected substrate scope; reactions were carried out using purified SadX variants (10 mol%).

Recently, through cooperative catalysis using nonheme Fe enzymes and photoredox catalysts, our lab[168] and the Huang lab[169] independently developed enantioselective photobiocatalytic decarboxylative radical functionalization of *N*-hydroxyphthalimide (NHPI) esters derived from easily available carboxylic acids. Mechanistically, both groups proposed that the excited

photosensitizer (eosin Y[169] or fluorescein[168]) oxidizes the ferrous Fe center to form a ferric center along with the radical anion state of the photosensitizer (Figure 21A). The radical anion subsequently reduces the NHPI ester upon single-electron transfer, leading to a carbon-centered radical. This newly formed carbon-centered radical reacts with the nonheme Fe(III)–N_3 intermediate, affording the enantioenriched organic azide product via radical rebound (Figure 21B).

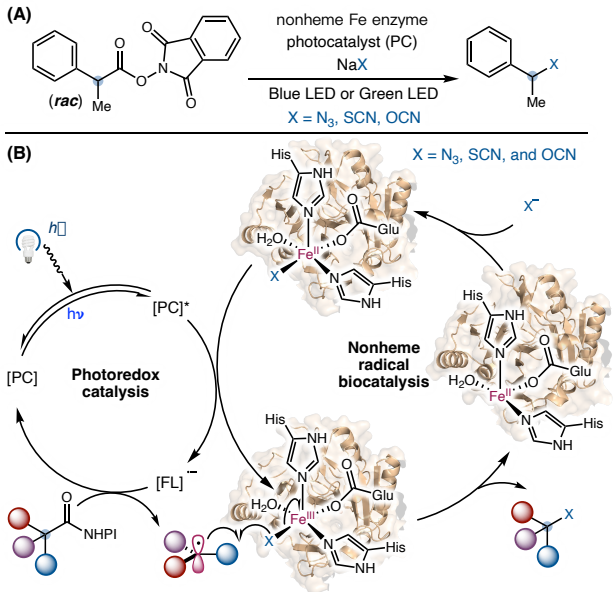

Figure 21. Enantioselective photobiocatalytic radical functionalization of *N*-hydroxyphthalimide (NHPI) esters. (A) Nonheme Fe enzyme-catalyzed decarboxylative azidation, thiocyanation, and isocyanation of redox-active esters. (B) Proposed dual catalytic cycle.

Using eosin Y as the photocatalyst and green LED irradiation, Huang engineered a 4-hydroxyphenylpyruvate dioxygenase from *Strptomyces avermitlis* (*Sav*HPPD)[170] to catalyze the enantioselective formation of C(sp^3)–N_3 and C(sp^3)–SCN bonds.[169] Directed evolution through SSM and screening targeting active-site residues resulted in a quadruple mutant *Sav*HPPD-PC (*Sav*HPPD V189A S230Y Q255A C188A, Figure 22A and 22B). Although this final variant only

showed a modest increase in activity, it significantly enhanced the enantioselectivity from 79:30 e.r. (wt *Sav*HPPD) to 94:6 e.r. (*Sav*HPPD-PC). With *Sav*HPPD-PC, thiocyanation using SCN^- also provided products in moderate yield and enantioselectivity (Figure 22F). In Huang's study, Stern-Volmer quenching suggested that Fe(II) with *Sav*HPPD-PC was an effective quencher of excited-state eosin Y. Huang proposed that active site of *Sav*HPPD-PC could accommodate the NHPI ester substrate, allowing efficient interception of the radical intermediate with the nonheme Fe center.

Parallel to Huang's study, our lab repurposed a nonheme Fe extrodiol dioxygenase, metapyrocatechase from *Pseudomonas putida* (*Pp*MPC),[171] which shares only 16% sequence identity with Huang's *Sav*HPPD, for enantioselective decarboxylative radical azidation, thiocyanation, and isocyanation. Directed evolution targeting substrate tunnel residues provided a final triple mutant *Pp*MPC azidase (*Pp*MPC I291L L155F F302Y), giving rise to the alkyl azide product in 74% yield and 99.5:0.5 e.r. with 1 mol% enzyme loading and irradiation at 440 nm. Further engineering and the reaction condition optimization for thiocyanation led to another triple mutant, *Pp*MPC I291L L155F I204L (*Pp*MPC thiocyanase), which delivered the corresponding thiocyanation product in 54% yield and 95:5 e.r. with irradiation at 525 nm (Figure 22C and 22D). The engineered enzymes tolerated a range of NHPI esters bearing electron-donating and electron-withdrawing groups. *Pp*MPC thiocyanase also catalyzed decarboxylative isocyanation using sodium isocyanate. The resulting isocyanate could be trapped *in situ* with aniline to provide the corresponding unsymmetrical urea in 20% yield and 98:2 e.r. (Figure 22E). Our lab noted a network of hydrophobic residues at the entrance of the substrate tunnel, including L155, V188, F191 I204, L248, L287, I291, F302, and M303, to serve as a hydrophobic lid to encapsulate the substrate binding pocket, potentially facilitating selective radical capture (Figure 22D). Based on

this finding and the limited active site volume, in contrast to Huang's report, our lab proposed that the carbon-centered radical forms outside the enzyme's active site and travels into the pocket.

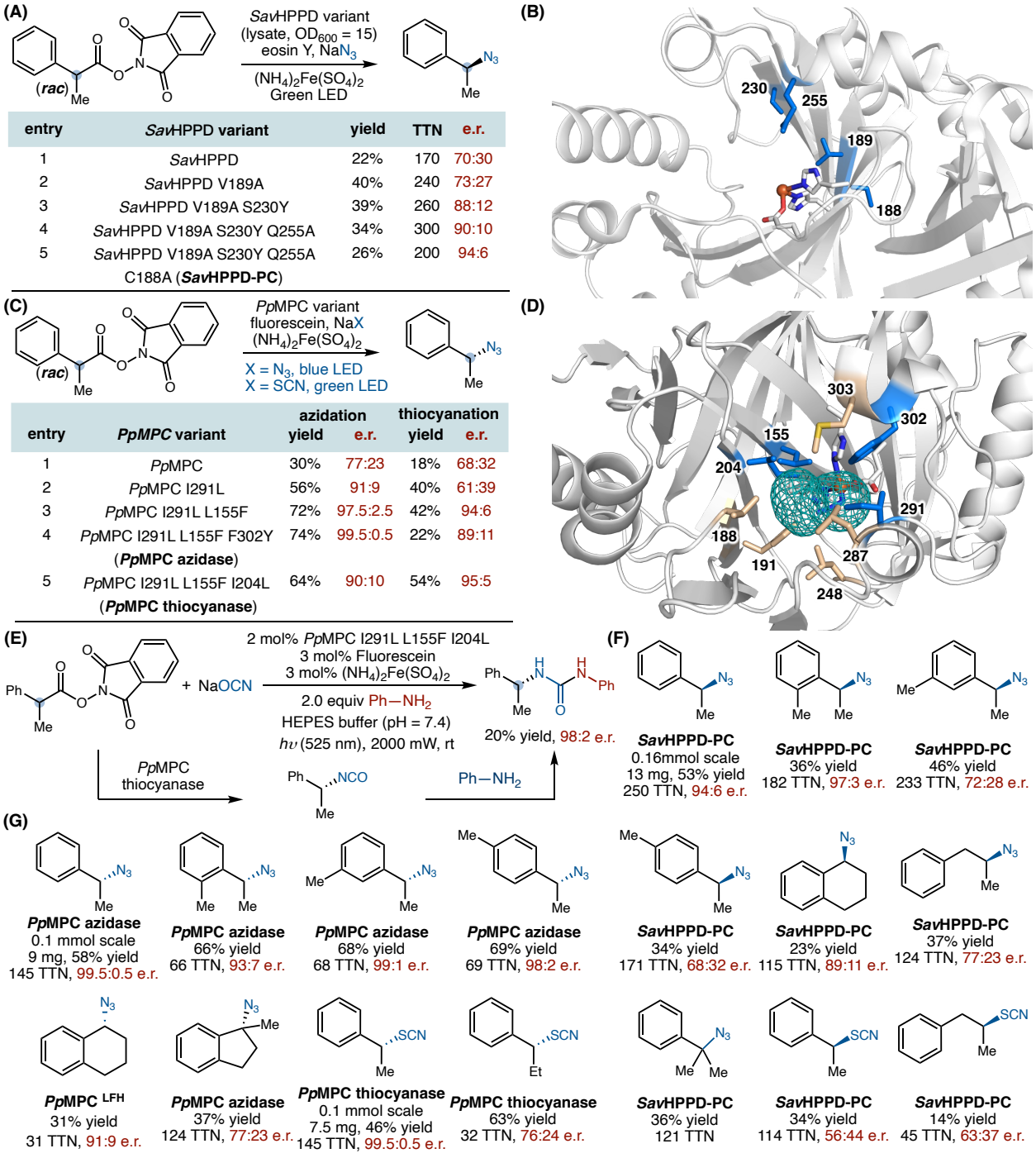

entry	*Sav*HPPD variant	yield	TTN	e.r.
1	*Sav*HPPD	22%	170	70:30
2	*Sav*HPPD V189A	40%	240	73:27
3	*Sav*HPPD V189A S230Y	39%	260	88:12
4	*Sav*HPPD V189A S230Y Q255A	34%	300	90:10
5	*Sav*HPPD V189A S230Y Q255A C188A (***Sav*HPPD-PC**)	26%	200	94:6

entry	***PpMPC* variant**	azidation yield	azidation e.r.	thiocyanation yield	thiocyanation e.r.
1	*Pp*MPC	30%	77:23	18%	68:32
2	*Pp*MPC I291L	56%	91:9	40%	61:39
3	*Pp*MPC I291L L155F	72%	97.5:2.5	42%	94:6
4	*Pp*MPC I291L L155F F302Y (***Pp*MPC azidase**)	74%	99.5:0.5	22%	89:11
5	*Pp*MPC I291L L155F I204L (***Pp*MPC thiocyanase**)	64%	90:10	54%	95:5

Figure 22. Nonheme Fe enzyme-catalyzed enantioselective decarboxylative azidation, thiocyanation and isocyantion. (A) Directed evolution of *Sav*HPPD-PC for enantioselective decarboxylative azidation. (B) The illustration of active site was made from 1T47 (PDB ID). (C) Directed evolution of *Pp*MPC azidase and *Pp*MPC thiocyanase for enantioselective decarboxylative azidation and thicyanation; the azidation reaction was conducted using 1 mol% purified *Pp*MPC whereas the thiocyanation reaction was conducted using 2 mol% purified *Pp*MPC. (D) The illustration of active site was made from 1MPY (PDB ID). (E) *Pp*MPC thiocyanase-catalyzed decarboxylative isocyanation. (F) Selected substrate scope of *Sav*HPPD-PC; Reactions were carried out with 0.2 mol% purified *Sav*HPPD-PC. (G) Selected substrate scope of *Pp*MPC azidase and *Pp*MPC thiocyanase; reactions were carried out with 1 mol% purified *Pp*MPC azidase or 2 mol% *Pp*MPC thiocyanase; *Pp*MPC^{LFH} = *Pp*MPC I291L L155F Y255H.

Inspired by decarboxylative C(sp^3)–N coupling via synergetic copper and photoredox catalysis developed by the Hu group,[172] in 2025, Huang and coworkers developed a biocatalytic decarboxylative C(sp^3)–N coupling with *N*-hydroxyphthalimide (NHPI) esters and anilines through cooperative catalysis using rhodamine B (RhB) as the photoredox catalyst and copper-substituted phenylalanine hydroxylase (PAH) from *Chromobacterium violaceum* (*Cv*PAH)[173] as the biocatalyst.[174] In the photoredox cycle, RhB$^{\bullet-}$ reduces the NHPI ester via single-electron transfer, leading to a carbon-centered radical. This newly formed carbon-centered radical reacts with the Cu(II)-amide intermediate within the enzyme active site, affording the enantioenriched C(sp^3)–N coupling product (Figure 23).

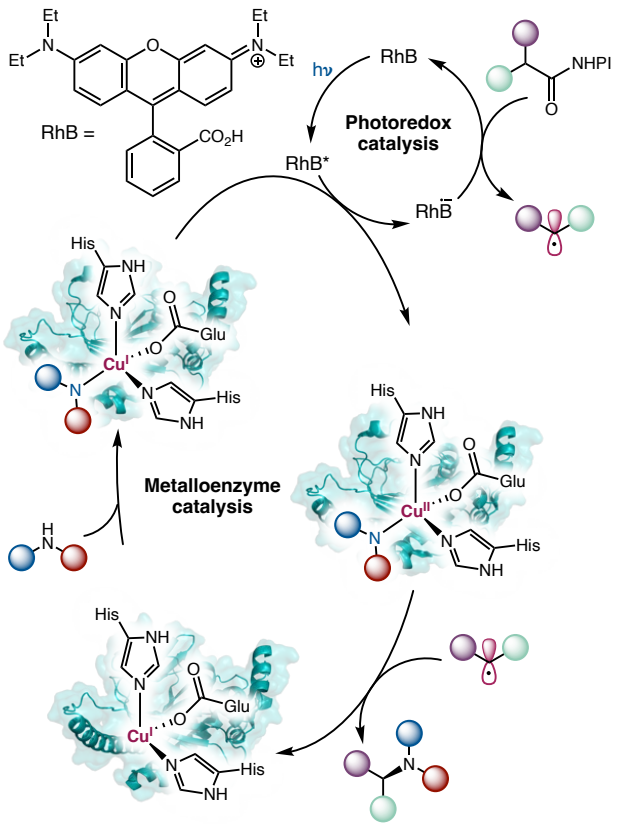

Figure 23. Proposed dual catalytic cycle for the enantioselective photobiocatalytic radical decarboxylative C(sp^3)–N coupling of *N*-hydroxyphthalimide (NHPI) esters and anilines.

Initial evaluation of wild type *Cv*PAH with copper as the catalytic center led to the desired coupling product in 1.5% yield and 16% ee. Directed evolution of *Cv*PAH through SSM targeting active-site residues furnished a quintuple mutant, *Cv*PAH F107L Y130S W180A P134L Y179W (*Cv*PAH-aminase), which produced the product in 19% yield and 94% ee (Figure 24A and 24B). By using an excess of NHPI ester (4.5 equiv), the yield of C–N coupling product was increased to 92% with the enantioselectivity unaffected. With 1.0–1.3 mol% cell-free lysate of *Cv*PAH-aminase, a range of racemic NHPI esters and anilines were tolerated and transformed into the enantioconvergent C(sp^3)–N coupling products in moderate to high yields and enantioselectivities

(Figure 24C). Mechanistic studies confirmed the formation of the carbon-centered radical and the essential role of copper catalytic center.

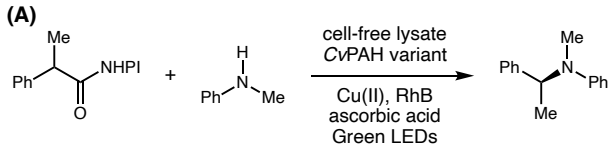

entry	*Cv*PAH variant	yield	TTN	ee
1	wt-*Cv*PAH	1.5%	4.1	16%
2	*Cv*PAH F107L Y130P	1.8%	2.3	66%
3	*Cv*PAH F107L Y130S	1.3%	1.4	85%
4	*Cv*PAH F107L Y130S W180A	8.8%	18	89%
5	*Cv*PAH F107L Y130S W180A P134L	6.2%	10	90%
6	*Cv*PAH F107L Y130S W180A P134L Y179W (*Cv*PAH-aminase)	19%	22	94%

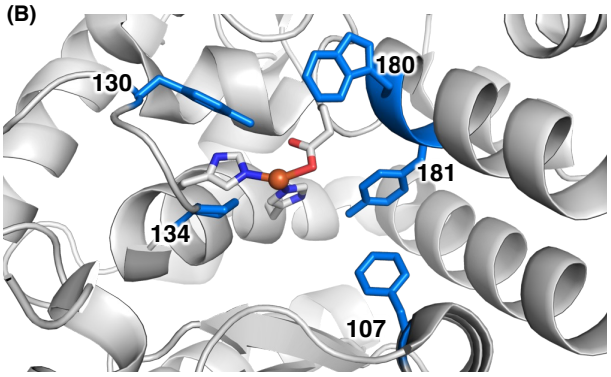

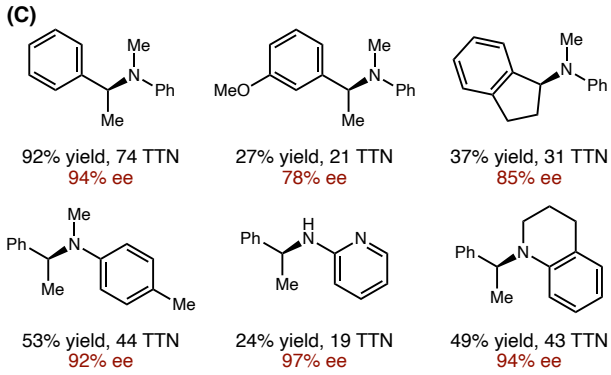

Figure 24. Cu-substituted *Cv*PAH-catalyzed enantioselective photobiocatalytic radical decarboxylative C(sp^3)–N coupling of *N*-hydroxyphthalimide (NHPI) esters and anilines. (A) Directed evolution of *Cv*PAH-aminase. (B) The illustration of active site was made from 1LTV

(PDB ID). (C) Selected substrate scope; reactions were carried out with 1.0–1.3 mol% cell-free lysate of *Cv*PAH-aminase.

2.4 Anti-Markovnikov oxidation of alkenes

P450-catalyzed oxidation of alkenes proceeding through Fe=O intermediates typically provides epoxidation products.[175] In contrast, P450-catalyzed anti-Markovnikov oxidation (aMOx) of alkenes leading to carbonyl products with an anti-Markovnikov site selectivity is rare, although such products were previously observed with biosynthetic P450 enzymes.[176] Using cytochrome P450 from the rhodobacterium *Labrenzia Aggregata* ($P450_{LA1}$),[177] Arnold and Hammer engineered P450 anti-Markovnikov oxidases (aMOx) as a biocatalytic solution to the challenging anti-Markovnikov alkene hydrofunctionalization problem (Figure 25).[178] In the proposed catalytic cycle, the highly reactive compound I reacts with the styrene substrate to form a short-lived carbon-centered radical. In the conventional epoxidation pathway, rapid C–O bond formation from this intermediate delivers the epoxide product. In the unusual anti-Markovnikov oxidation pathway, this short-lived carbon-centered radical undergoes an intramolecular single electron transfer from the carbon-centered radical to the Fe center, which would provide the carbon cation intermediate. Subsequent 1,2-hydride migration furnishes the anti-Markovnikov carbonyl product and the ferric P450 enzyme to complete the catalytic cycle.[179]

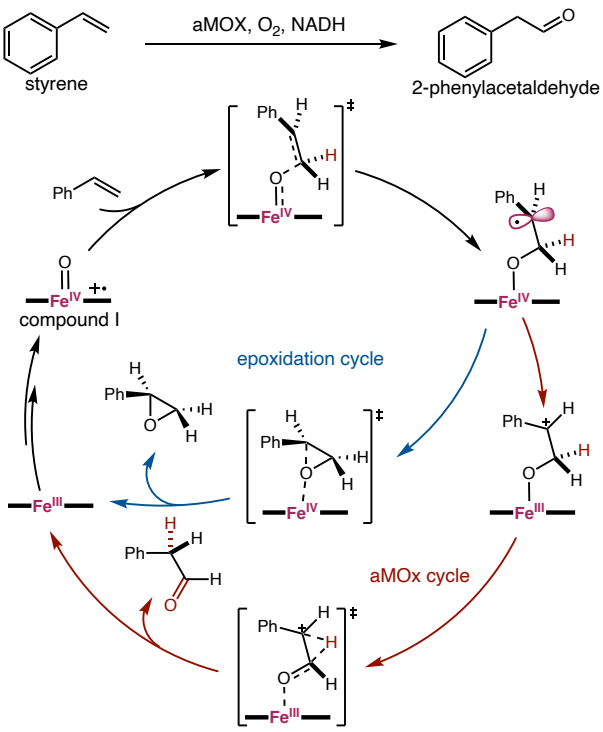

Figure 25. Proposed catalytic cycle for biocatalytic anti-Markovnikov oxidation of alkenes.

Directed evolution of $P450_{LA1}$ allowed substantial improvement in the catalytic activity and selectivity towards the anti-Markovnikov carbonyl product. Four random mutated libraries created by epPCR targeting the heme domain were screened using a high-throughput colorimetric method using Purpald,[180] leading to a quintuple mutant $P450_{LA1}$ T121A N201K N209S Y385H E418G with increased TTN and aMOx selectivity. An additional six rounds of SSM and screening using HPLC furnished the final variant aMOx with eight additional mutations, further improving the TTN and aMOx selectivity (Figure 26A). Use of an alcohol dehydrogenase (ADH) allowed the conversion of aldehyde products to the corresponding alcohols to avoid undesired side reactions of aldehydes. Various substituted styrene substrates were transformed with TTNs ranging from 730 to 4,500 in an anti-Markovnikov fashion using the combination of aMOx and ADH in a lysate form. The 1,2-hydride migration was found to be a stereospecific process, allowing (*S*)-2-

phenylpropan-1-ol product to form in 93:7 e.r. from the corresponding substrate. Internal alkenes were also tolerated by this first generation aMOx enzyme. The resulting ketones were reduced by ADH to form the corresponding enantioenriched alcohols with excellent enantioselectivity and moderate aMOx selectivity (Figure 26B). Hammer and Garcia-Borràs further studied the origin of the aMOx selectivity.[179] It was found that the final variant aMOx exerted conformational control over the carbon-centered radical intermediate, facilitating the intramolecular SET process and the rapid succeeding 1,2-hydride migration.

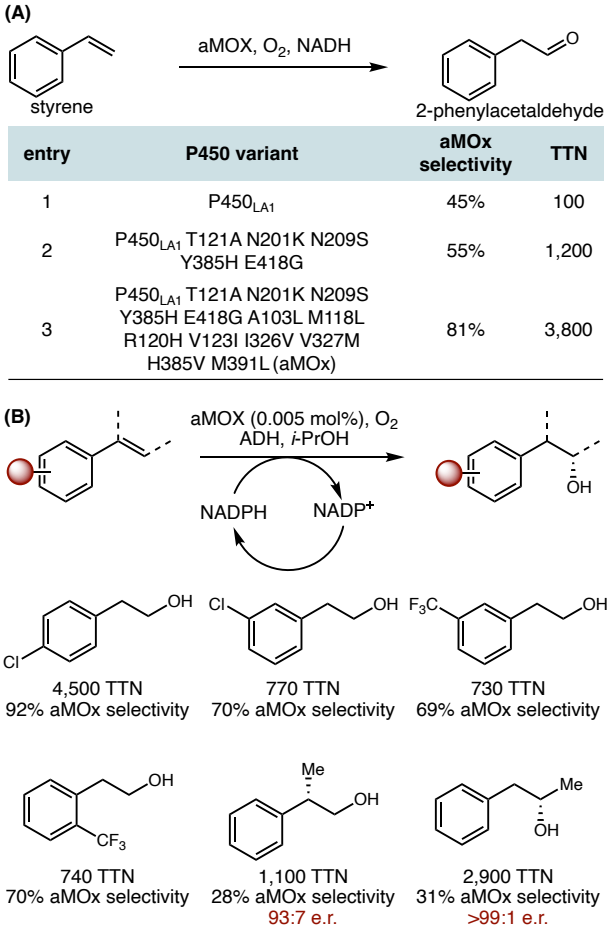

entry	P450 variant	aMOx selectivity	TTN
1	$P450_{LA1}$	45%	100
2	$P450_{LA1}$ T121A N201K N209S Y385H E418G	55%	1,200
3	$P450_{LA1}$ T121A N201K N209S Y385H E418G A103L M118L R120H V123I I326V V327M H385V M391L (aMOx)	81%	3,800

Figure 26. P450-catalyzed anti-Markovnikov oxidation of alkenes. (A) Directed evolution of aMOx; (B) Selected substrate scope; reactions were carried out with 0.005 mol% cell-free lysate of aMOx and 10 U ADH.

Hammer and coworkers further evolved aMOx activity to allow internal alkenes to be converted to ketone products.[181] A starting variant $P450_{LA1}$ P7E ($P450_{LA1}$ T121A V123I N201K H206W N209S I326V Y385H E418G) was selected from the initial screening. 12 new mutations from 11 rounds of SSM and screening led to the final ketone synthase (KS) variant, providing the ketone product in 2,600 TTN and 75% chemoselectivity using cell-free lysate (Figure 27A). The final KS variant showed good catalytic activities and chemoselectivities towards a range of substrates. An α-chiral ketone was obtained in 87:13 e.r., although with reduced activity and chemoselectivity (Figure 27B). Computational studies revealed that rigidification of the active site by these newly introduced mutations led to improved catalytic activity and chemoselectivity.

(A)

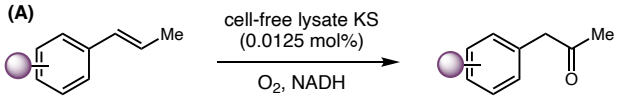

entry	P450 variant	ketone selectivity	TTN
1	$P450_{LA1}$	20%	72
2	$P450_{LA1}$ P7E	31%	225
3	$P450_{LA1}$ P7E W206A T210V	44%	660
4	$P450_{LA1}$ P7E W206A T210V E282D R120Q	51%	1,600
5	$P450_{LA1}$ P7E W206A T210V E282D R120Q V210I K393L V208Q A117Q L111Y	61%	3,000
6	$P450_{LA1}$ P7E W206A T210V E282D R120Q V210I K393L V208Q A117Q L111Y V204H L424W	68%	2,090
7	$P450_{LA1}$ P7E W206A T210V E282D R120Q V210I K393L V208Q A117Q L111Y V204H L424W A121V I210V M274F (KS)	75%	2,600

(B)

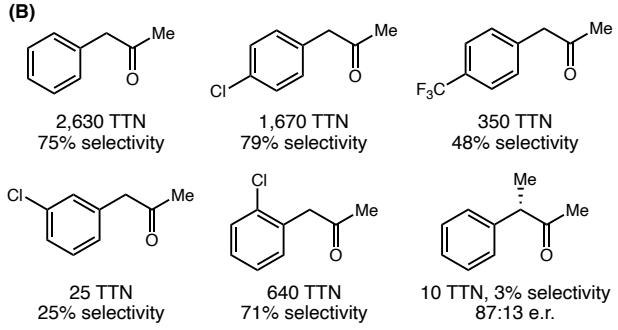

Figure 27. Biocatalytic anti-Markovnikov oxidation of internal alkenes (A) Directed evolution of ketone synthase; (B) Selected substrate scope; reactions were carried out with 0.0125 mol% cell-free lysate of KS.

2.5 Intermolecular radical C–C coupling

Designing new metalloenzyme mechanisms for radical-mediated C–C bond formation remains an ongoing challenge. In 2025, Huang and coworkers developed a photobiocatalytic enantioselective α-alkylation of 2-acyl imidazoles, affording α-chiral ketones in excellent enantioselectivity.[182] Using cupin proteins previously investigated by Itoh featuring a Lewis acidic Cu center,[183–185] Huang and coworkers found that *Thermotoga maritima* cupin variants[186,187] *Tm*1287-E68A and *Tm*1459-H52A produced opposite enantiomers of the C–C bond forming products (Figure 28A, entry 1 and 5). Subsequent site-directed mutagenesis of residues within 6 Å of the metal center led to optimized mutants *Tm*1287 E68A R23Y M22F and *Tm*1459 H52G F104V (Figure 28B amd 28D), allowing enantiodivergent C–C bond formation. A range of substituted 2-acyl imidazoles and phenacyl chlorides were well tolerated, furnishing products with excellent stereocontrol (Figure 28C).

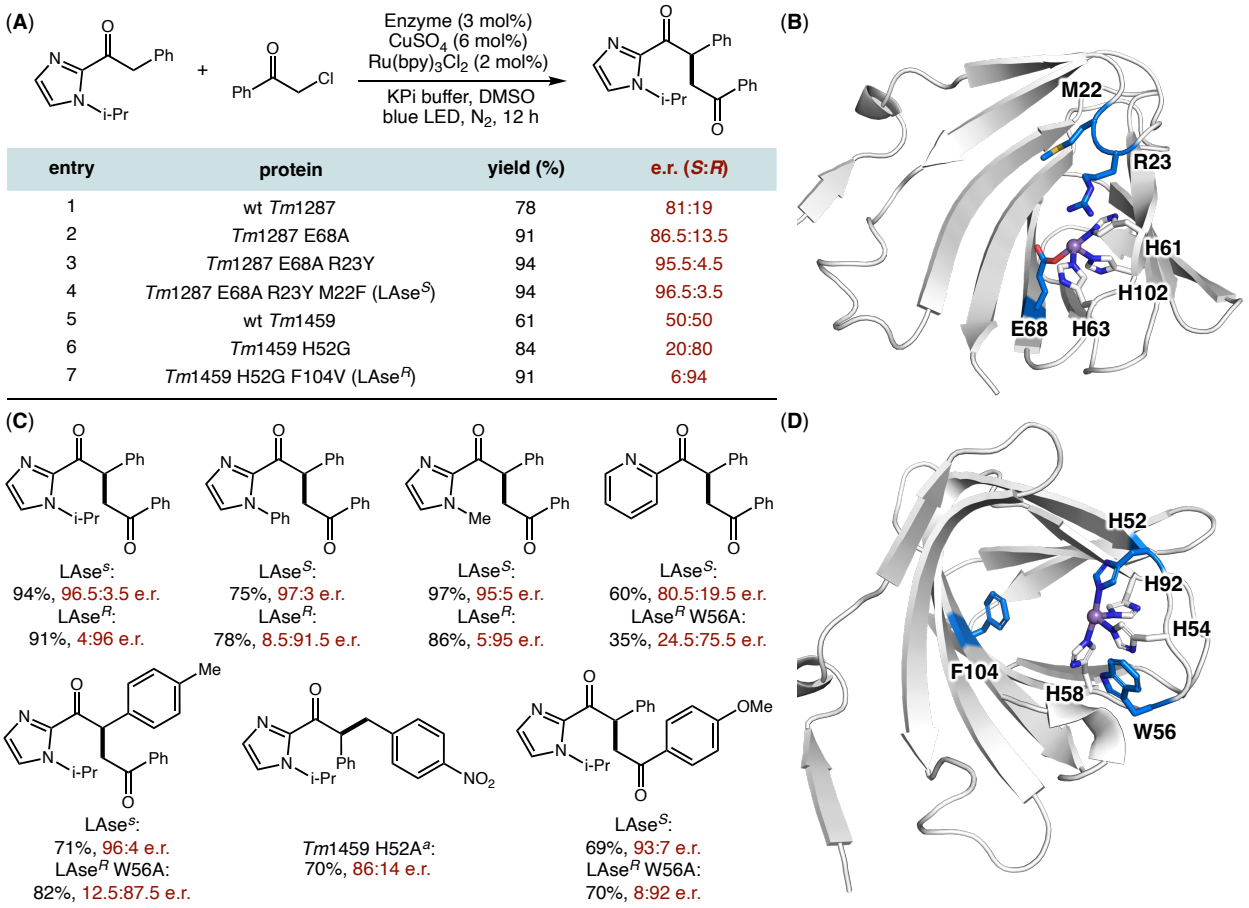

entry	protein	yield (%)	e.r. (*S*:*R*)
1	wt *Tm*1287	78	81:19
2	*Tm*1287 E68A	91	86.5:13.5
3	*Tm*1287 E68A R23Y	94	95.5:4.5
4	*Tm*1287 E68A R23Y M22F (LAse^S)	94	96.5:3.5
5	wt *Tm*1459	61	50:50
6	*Tm*1459 H52G	84	20:80
7	*Tm*1459 H52G F104V (LAse^R)	91	6:94

Figure 28. Enantiodivergent photobiocatalytic alkylation using Lewis acidic cupin protein. (A) Directed evolution of LAse^S and LAse^R; (B) The active-site illustration of *Tm*1287 was made from 1O4T (PDB ID); (C) Selected substrate scope, reaction conditions: 2-acyl imidazole (0.004 mmol), phenacyl chloride (0.012 mmol), enzyme (3 mol%), $CuSO_4$ (6 mol%), $Ru(bpy)_3Cl_2$ (2 mol%), and 8% v/v DMSO in KPi buffer (20 mM, pH 8.0) were stirred for 12 h at room temperature under an N_2 atmosphere with the illumination of 450–460 nm LEDs, total volume of the reaction was 0.8 mL, [a]4-nitrobenzyl bromide was used; (D) The active-site illustration of *Tm*1459 was made from 1VJ2 (PDB ID).

In 2025, by interfacing photoredox chemistry with enzymatic Fe carbenoid chemistry, our group developed a formal metal carbenoid-radical coupling process to enable the diastereo- and

enantioselective intermolecular C–C bond formation (Figure 29).[188] In the proposed photoredox catalytic cycle, single-electron oxidation of the organoboron by the excited photocatalyst (EB*) provides a carbon-centered radical along with the reduced radical anion form of the photocatalyst. Concurrent to the photoredox cycle, using an appropriate heme protein catalyst, reaction between the diazo compound and the heme Fe center leads to an open-shell singlet Fe carbenoid[189] with substantial radical character on the carbon center. This open-shell Fe carbenoid undergoes single electron reduction with the photocatalyst radical anion followed by enantioselective proton transfer to provide an Fe(III)-alkyl intermediate. This newly formed Fe(III)-alkyl complex undergoes a stereoinvertive biomolecular homolytic substitution (S_H2)[190] with the photoredox-derived carbon-centered radical resulting in radical C–C coupling product.

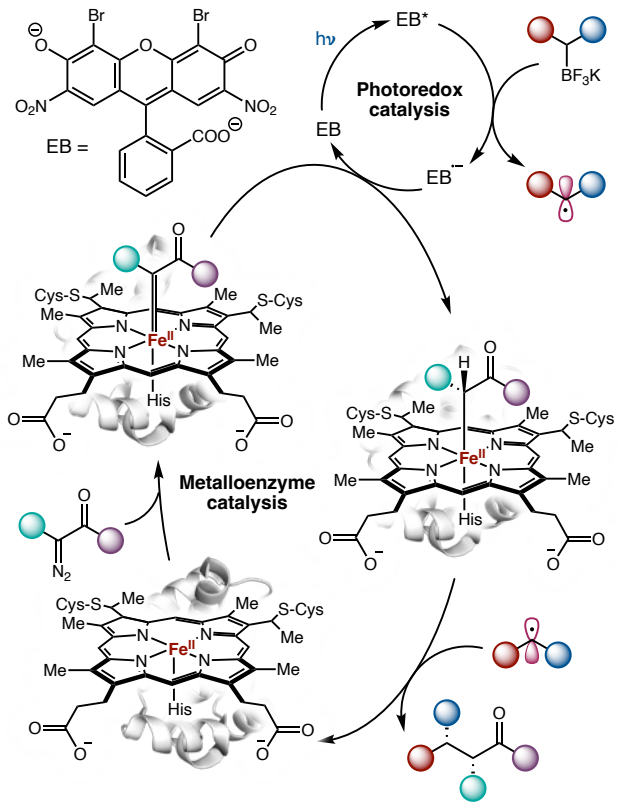

Figure 29. Proposed catalytic cycle for the biocatalytic asymmetric radical cross-coupling.

Using eosin B as the photoredox catalyst, metalloprotein catalyst evaluation revealed a variant of *Rhodothermus marinus*[191]cytochrome *c* (*Rma* cyt *c* V75R M100D M103T) was capable of catalyzing this intermolecular radical coupling in 53% yield and 88:12 e.r. (Figure 30). Four rounds of directed evolution furnished a sextuple mutant *Rma* cyt *c* V75R M76L M99R M100D T101G M103E (termed as *Rma* cyt $c^{RLRDGDE}$), allowing the C–C coupling product to form in 75% yield and 94.5:5.5 e.r. (Figure 30A). Furthermore, our lab found that this new intermolecular radical coupling strategy allowed for stereoselective secondary alkyl-secondary alkyl coupling. To engineer an effective heme protein catalyst for the enantioconvergent transformation of racemic secondary alkyltrifluoroborates, the generation and evaluation of a combinatorial library simultaneously mutating loop residues 99–103 proved critical, leading to *Rma* cyt *c* V75R M76I M99K M100C T101G D102P M103F (*Rma* cyt $c^{RIKCGPF}$), allowing the alkyl-alkyl coupling product to form with excellent diastereo- and enantioselectivity (78% yield, 96:4 d.r., and 93:7 e.r., Figure 30B and 30C). It was found that a range of organoboron substrates and diazo compounds could be transformed with excellent stereoselectivities (Figure 30D). Our mechanistic and computational studies suggested that an active-site proton donor residue (R75) may play a role in enhanced enzyme activity and proton transfer enantioselectivity.

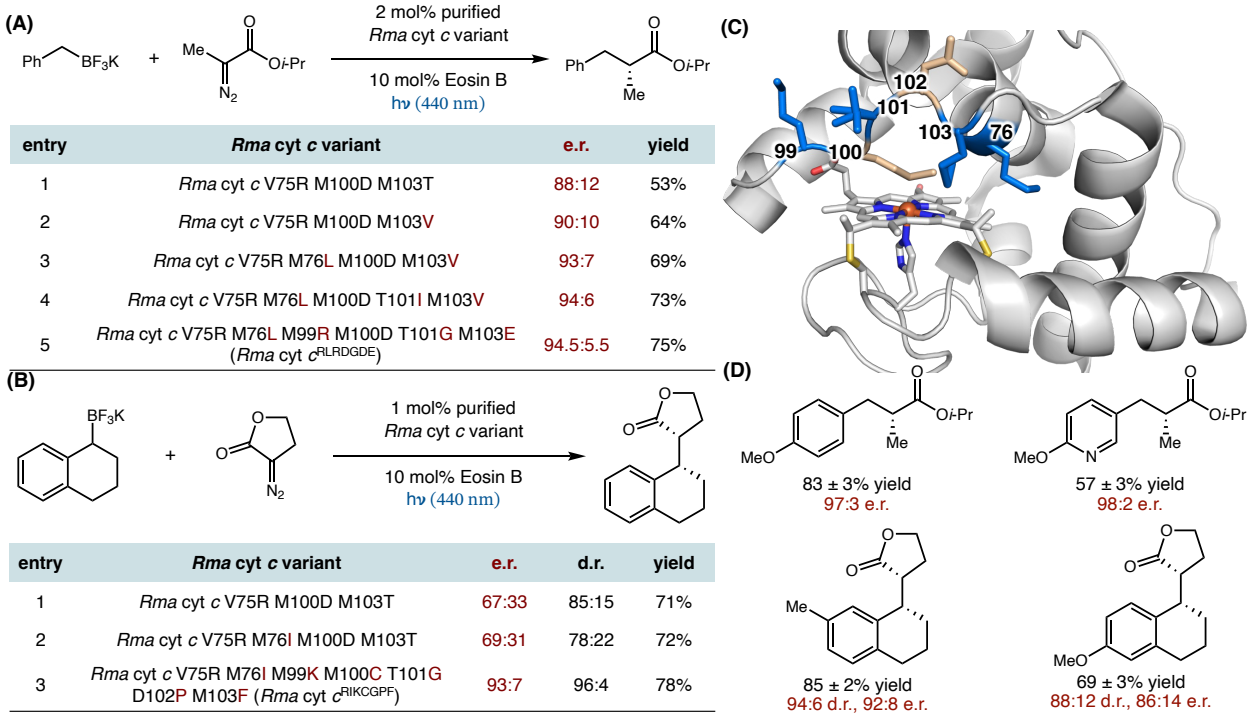

entry	*Rma* cyt *c* variant	e.r.	yield
1	*Rma* cyt *c* V75R M100D M103T	88:12	53%
2	*Rma* cyt *c* V75R M100D M103V	90:10	64%
3	*Rma* cyt *c* V75R M76L M100D M103V	93:7	69%
4	*Rma* cyt *c* V75R M76L M100D T101I M103V	94:6	73%
5	*Rma* cyt *c* V75R M76L M99R M100D T101G M103E (*Rma* cyt $c^{RLRDGDE}$)	94.5:5.5	75%

entry	*Rma* cyt *c* variant	e.r.	d.r.	yield
1	*Rma* cyt *c* V75R M100D M103T	67:33	85:15	71%
2	*Rma* cyt *c* V75R M76I M100D M103T	69:31	78:22	72%
3	*Rma* cyt *c* V75R M76I M99K M100C T101G D102P M103F (*Rma* cyt $c^{RIKCGPF}$)	93:7	96:4	78%

Figure 30. Biocatalytic asymmetric radical cross-coupling. (A) Directed evolution of *Rma* cyt *c* variant for the radical coupling with benzyl trifluoroborate salt; (B) Directed evolution of *Rma* cyt *c* variant for the radical coupling with secondary alkyltrifluoroborates; (C) The illustration of active site was made from 3CP5 (PDB ID); (D) Selected substrate scope; reactions were carried out with 2 mol% purified *Rma* cyt $c^{RLRDGDE}$ or 1 mol% purified *Rma* cyt $c^{RIKCGPF}$.

2.6 Miscellaneous

In 2015, Carrera discovered that toluene dioxygenase (TDO)[192] catalyzed the conversion of benzyl azide to benzonitrile, which could be further oxidized to produce a *cis*-diol product (Figure 31).[193,194] The final nitrile product was obtained at a titer of 1.2 g/L culture media from a 5 L bioreactor cultivating *E. coli* JM109 (pDTG601). The azido diol was obtained at a titer of 1.6 g/L, which came from the double [3,3]-sigmatropic rearrangement of allylazide (Figure 31A).[193] Studies[194] showed that the TDO-catalyzed benzylic C–H hydroxylation of benzyl azide occurred

to generate an α-hydroxy benzylazide. Through the intermediacy of a Fe nitrenoid intermediate, a benzaldoxime species forms, which undergoes dehydration to afford the nitrile product (Figure 31B and 31C).

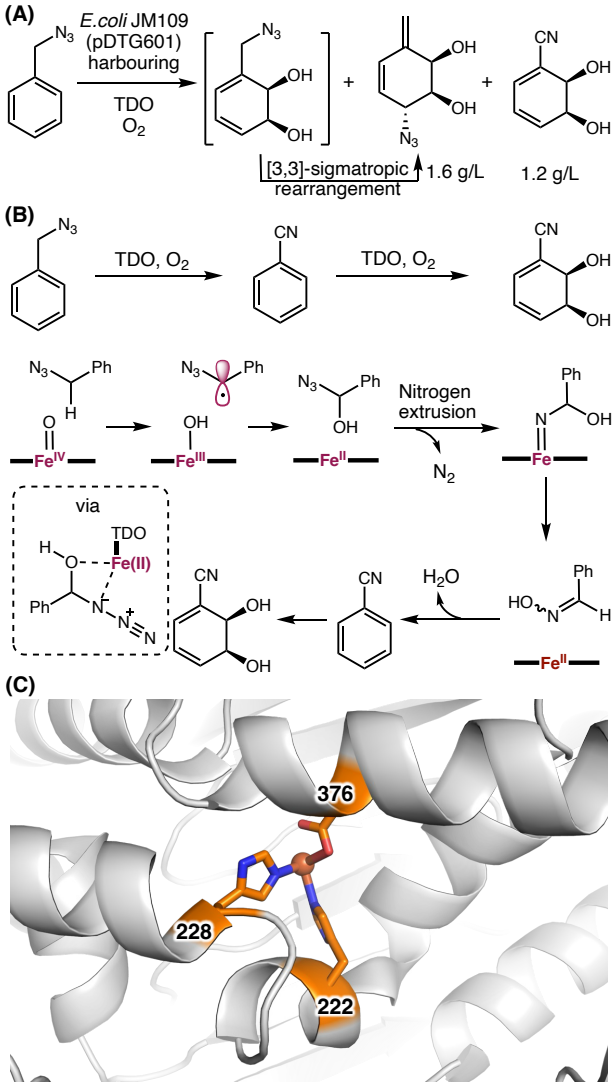

Figure 31. Toluene dioxygenase (TDO)-catalyzed oxidation of benzyl azide to benzonitrile. (A) TDO-catalyzed oxidation of benzyl azide; (B) Proposed mechanism in benzonitrile formation; (C) The illustration of active site of wt TDO was made from 3EN1 (PDB ID).

In 2019, Chang and Guo reported that other nonheme Fe enzymes including LdoA and PoIL could also catalyze this oxidative conversion of alkyl azides to the corresponding nitriles (Figure 32).[195] They found that L-leucine-5-hydroxylase (LdoA)[196] and polyoxin dihydroxylase (PoIL)[197] catalyzed the conversion of amino acids with a terminal azido group to the corresponding cyano-containing amino acid products. Using 0.24 mol% purified LdoA, (*S*)-2-amino-5-azidopentanoic acid was converted to the corresponding nitrile product with 150 TTN. Similarly, using 0.24 mol% purified PoIL, (*S*)-2-amino-4-azidobutanoic acid was converted with 180 TTN (Figure 32A). A similar mechanism as that proposed by Carrera is likely operative with LdoA and PoIL-catalyzed alkyl azide conversions (Figure 32B).

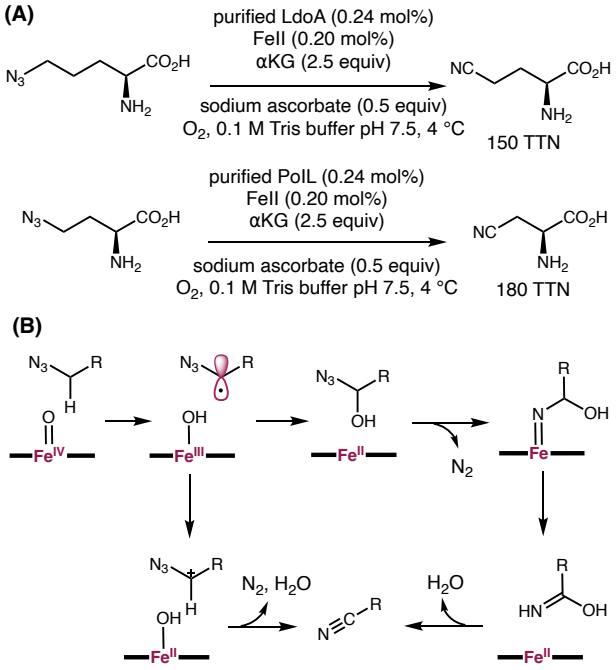

Figure 32. Biocatalytic azide-directed nitrile synthesis. (A) Successful substrates and products; (B) Proposed reaction pathway.

3. Transformations involving nitrogen-centered radicals

Advances in nitrogen-centered radical chemistry has opened up new avenues for the synthesis of diverse nitrogen-containing compounds.[198] Additionally, nitrogen-centered radicals also play an important role in the biosynthesis of complex natural products.[199] In recent years, a range of reactions involving nitrogen-centered radicals, including intramolecular addition to π-systems,[200] intermolecular addition to π-systems,[201–203] and 1,5-hydrogen-atom transfer (1,5-HAT) with nitrogen-centered radicals, have been harnessed for the development of new-to-nature biocatalytic reactions. These results underscored the synthetic potential of nitrogen-centered radicals, particularly when combined with enzymatic platforms capable of finely tuning their high reactivity and selectivity.

Remote C–H functionalization via nitrogen-centered radical-mediated 1,5-HAT is a powerful strategy for the construction of complex molecules.[204] This concept can be traced back over a century to the classical Hofmann–Löffler–Freytag (HLF) reaction.[205] In 2016, Cook and co-workers developed a fluorine atom transfer reaction using fluoroamides as substrates to achieve C(sp^3)–H bond fluorination, proceeding through an iron-mediated amidyl radical intermediate.[206] In 2022, Huang and co-workers reprogrammed a nonheme Fe enzyme, (4-hydroxyphenyl)pyruvate dioxygenase from *Streptomyces avermitilis* (*Sav*HppD),[170] to catalyze an unnatural C(sp^3)–H azidation reaction via amidyl radical intermediates (Figure 33).[207] Using *N*-fluoroamide as the model substrate, the use of wild-type *Sav*HppD afforded the desired azidation product with 250 TTN, 63:37 e.r., and a 9:1 azidation:fluorination selectivity. Using a newly developed high-throughput screening assay based on copper-catalyzed azide-alkyne cycloaddition, Huang evaluated more than 5,000 clones generated from epPCR and site-saturation mutagenesis.[208] These efforts resulted in a sextuple mutant *Sav*HppD V189A F216A P243A N245Q Q255A L367I

(*Sav*HppD Az1), catalyzing the enantioselective C–H azidation with 1,340 TTN and 87:13 e.r.. To further improve the enantioselectivity of the reaction, Huang reevaluated their in-house collection of *Sav*HppD variants and performed additional rounds of directed evolution using chromatography-based screening. This led to a new septuple mutant *Sav*HppD V189A N191A S230L P24N245F Q255P L367I (SavHppD Az2), providing the product with a slightly lower activity (490 TTN) but excellent enantiocontrol (96:4 e.r., Figure 33A).

Michaelis-Menten kinetic analyses of *Sav*HppD Az1, *Sav*HppD Az2 and the wild-type *Sav*HppD showed that the k_{cat}/K_M value of both *Sav*HppD Az1 and *Sav*HppD Az2 increased by approximately 2-fold compared to wt *Sav*HppD. Specifically, the *Sav*HppD Az1 variant showed a 4.1-fold increase in k_{cat} (29.4 min^{-1} (*Sav*HppD Az1) versus 7.20 min^{-1} (wt *Sav*HppD)). However, The K_M of *Sav*HppD Az1 was 1.7-fold higher (790 mM) than that of wt *Sav*HppD (470 mM), indicating weaker substrate binding. In contrast, *Sav*HppD Az2 exhibited a roughly 9-fold decrease in k_{cat} (3.39 min^{-1}) but a 6.6-fold smaller K_M (120 mM) relative to wt *Sav*HppD, suggesting a slower catalytic rate but tighter substrate binding. This is consistent with the observation that *Sav*HppD Az2 generally exhibited higher enantioselectivity but lower activity than *Sav*HppD Az1 across a range of *N*-fluoroamide substrates (Figure 33B). DFT and MD analyses[209] suggested that the azide ligand (N_3^-) is positioned *trans* to the carboxylate ligand, which facilitates the activation of substrate with the nonheme Fe center for efficient N–F bond activation. DFT calculations[207] suggest that the initial N–F activation is the rate-determining step with an activation free energy ($\Delta G^{\ddagger}$) of 17.2 kcal/mol. This fluorine atom abstraction is followed by a rapid 1,5-HAT step with a much lower barrier ($\Delta G^{\ddagger}$ = 3.9 kcal/mol) to generate a carbon-centered radical (Int-III), which is positioned to undergo selective azide rebound with a low energy barrier ($\Delta G^{\ddagger}$ = 4.4 kcal/mol) (Figure 33C). Although the fluorine rebound pathway also exhibits a low intrinsic barrier ($\Delta G^{\ddagger}$ =

5.0 kcal/mol), it is disfavored due to conformational constraints within the enzyme active site that hinder the necessary substrate repositioning. This finding showcased the ability of enzymes to control chemoselectivity through reactive intermediate positioning.

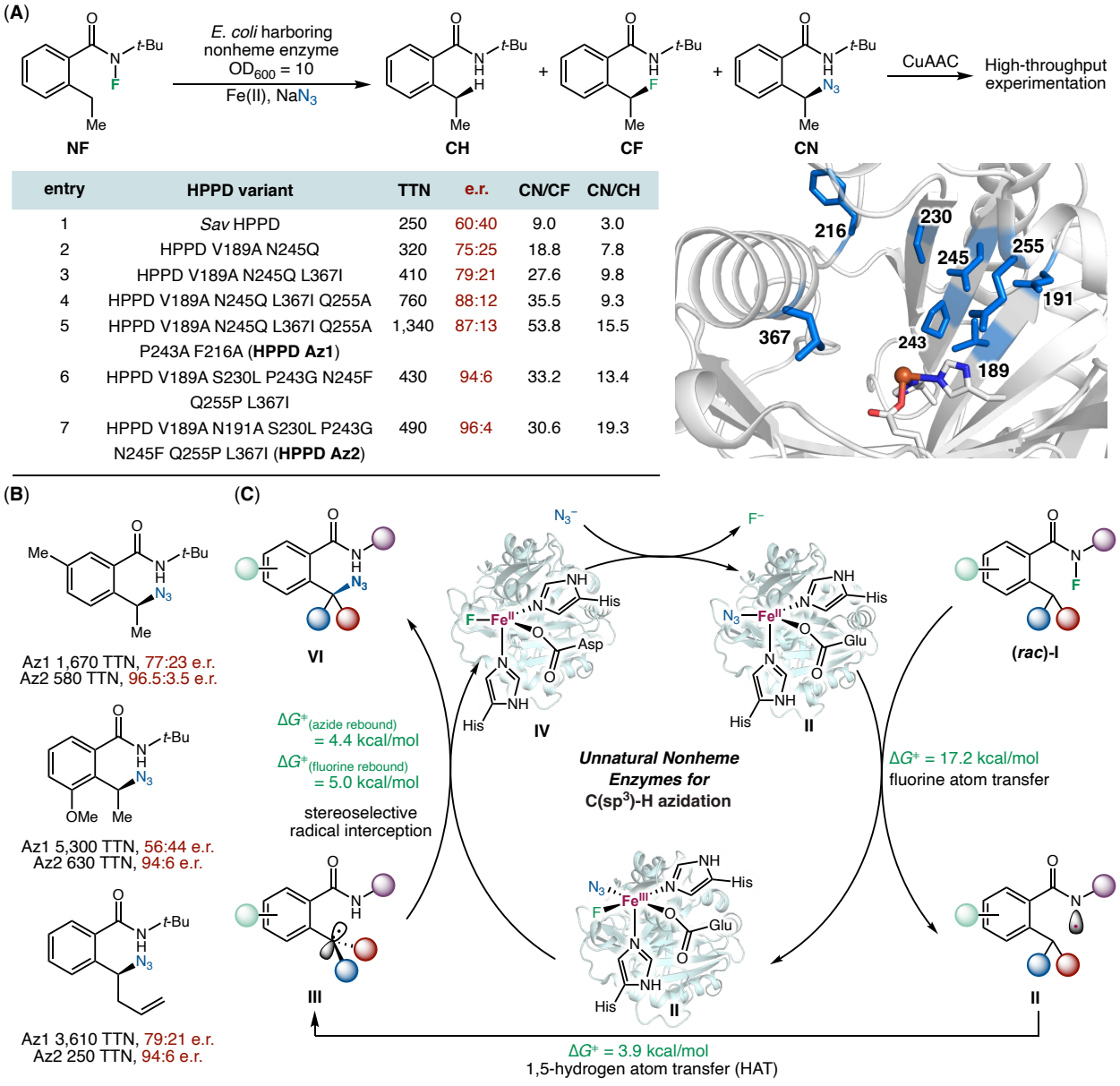

entry	HPDD variant	TTN	e.r.	CN/CF	CN/CH
1	*Sav* HPPD	250	60:40	9.0	3.0
2	HPPD V189A N245Q	320	75:25	18.8	7.8
3	HPPD V189A N245Q L367I	410	79:21	27.6	9.8
4	HPPD V189A N245Q L367I Q255A	760	88:12	35.5	9.3
5	HPPD V189A N245Q L367I Q255A P243A F216A (**HPPD Az1**)	1,340	87:13	53.8	15.5
6	HPPD V189A S230L P243G N245F Q255P L367I	430	94:6	33.2	13.4
7	HPPD V189A N191A S230L P243G N245F Q255P L367I (**HPPD Az2**)	490	96:4	30.6	19.3

Figure 33. Nonheme Fe enzyme catalyzed enantioselective C(sp^3)–H azidation of *N*-fluoroamides. (A) Directed evolution of *Sav*HppD as azidases, the illustration of active site was made from the

structure of 1T47 (PDB ID); (B) Selected substrate scope of *Sav*HppD Az1 and *Sav*HppD Az2; (C) Proposed catalytic cycle.

In 2024, our lab[210] and the Huang lab[211] contemporaneously reported nonheme Fe enzyme-catalyzed enantioselective C(sp^3)–F bond formation via C(sp^3)–H functionalization. Organofluorine compounds are ubiquitous in the pharmaceutical,[212] materials,[213] and agrochemical industries[214] due to their unique chemical, physical, and biological properties. However, to date, there is only a single naturally occurring fluorinase that catalyzes C(sp^3)–F bond formation in the conversion of *S*-adenosylmethionine to 5'-fluoro-5'-deoxyadenosine via a bimolecular nucleophilic substitution (S_N2) mechanism.[215] Although numerous α-ketoglutarate-dependent nonheme iron enzymes has been discovered and engineered to catalyze C–H bond functionalization, including halogenation,[44] azidation,[160,166,167] and nitration,[160] biocatalytic enantioselective C(sp^3)–H fluorination via an analogous radical-mediated fluorine rebound mechanism were not known prior to 2024 (Figure 34).

In Huang's work, a triple mutant of (*S*)-2-hydroxypropylphosphonate epoxidase from *Streptomyces viridochromogenes*[216] (*Sv*HppE-Fluor) was engineered to obtain the (*R*)-benzylfluoride product (150 TTN, 96.5:3.5 e.r. and 2.2:1 fluorination:reduction selectivity (Figure 34A and 34B). The Fe-binding glutamate was mutated to aspartate to generate additional space in the active site to accommodate the substrate. Parallel to Huang's work, our lab engineered a sextuple mutant of 1-aminocyclopropane-1-carboxylic acid oxidase from *Petunia hybrida* ($ACCO_{CHF}$)[217,218] allowing the (*S*)-benzylfluoride product to form in 601 TTN, 95:5 e.r. and an excellent fluorination:reduction selectivity of 98:2. With the exception of I184A, all the beneficial mutations identified from directed evolution are distal to the Fe center, indicating the potential importance of substrate tunnel engineering (Figure 34C and 34D). The excellent chemoselectivity

favoring fluorination over reduction with $ACCO_{CHF}$ allowed enantioenriched organofluorine compounds to be prepared on a gram scale. Together, $ACCO_{CHF}$ and *Sv*HppE-Fluor allowed the enantiodivergent synthesis of organofluorine products (Figure 34E).

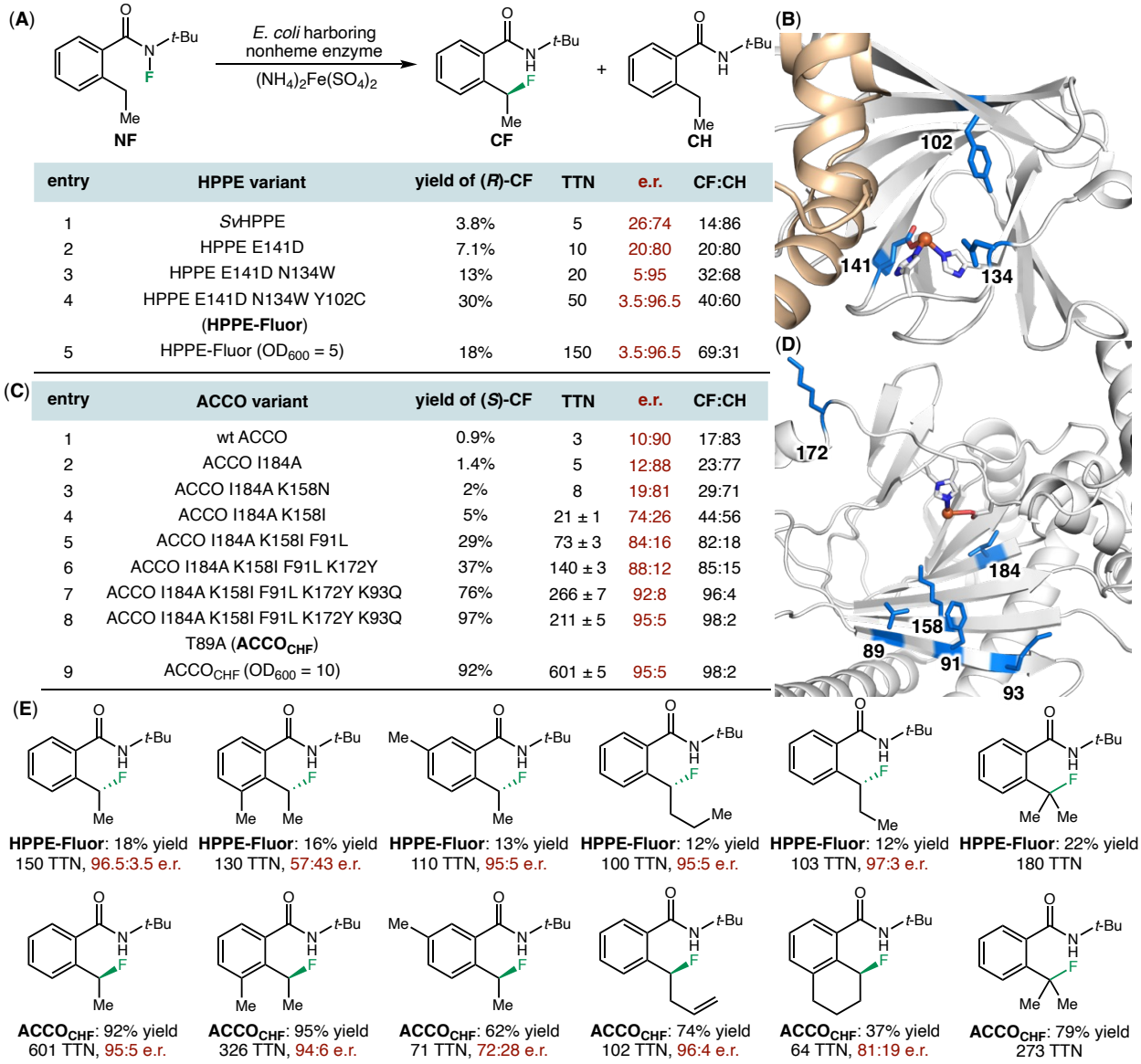

entry	HPPE variant	yield of (*R*)-CF	TTN	e.r.	CF:CH
1	*Sv*HPPE	3.8%	5	26:74	14:86
2	HPPE E141D	7.1%	10	20:80	20:80
3	HPPE E141D N134W	13%	20	5:95	32:68
4	HPPE E141D N134W Y102C (**HPPE-Fluor**)	30%	50	3.5:96.5	40:60
5	HPPE-Fluor (OD_{600} = 5)	18%	150	3.5:96.5	69:31

entry	ACCO variant	yield of (*S*)-CF	TTN	e.r.	CF:CH
1	wt ACCO	0.9%	3	10:90	17:83
2	ACCO I184A	1.4%	5	12:88	23:77
3	ACCO I184A K158N	2%	8	19:81	29:71
4	ACCO I184A K158I	5%	21 ± 1	74:26	44:56
5	ACCO I184A K158I F91L	29%	73 ± 3	84:16	82:18
6	ACCO I184A K158I F91L K172Y	37%	140 ± 3	88:12	85:15
7	ACCO I184A K158I F91L K172Y K93Q	76%	266 ± 7	92:8	96:4
8	ACCO I184A K158I F91L K172Y K93Q T89A (**$ACCO_{CHF}$**)	97%	211 ± 5	95:5	98:2
9	$ACCO_{CHF}$ (OD_{600} = 10)	92%	601 ± 5	95:5	98:2

Figure 34. Nonheme Fe enzyme-catalyzed enantioselective C(sp^3)–H fluorination. (A) Directed evolution of HPPE-Fluor, reactions were carried out using whole *E. coli* cells overexpressing *Sv*HPPE (OD_{600} = 40); (B) The active-site illustration of HPPE was made from 4J1X (PDB ID);

(C) Directed evolution of $ACCO_{CHF}$, reactions were carried out using whole *E. coli* cells overexpressing ACCO (OD_{600} = 30); (D) The active-site illustration of ACCO was made from 1W9Y (PDB ID); (E) Selected substrate scope of HPPE-Fluor and $ACCO_{CHF}$, reactions were carried out using whole *E. coli* cells overexpressing HPPE-Fluor (OD_{600} = 5) and $ACCO_{CHF}$ (OD_{600} = 10).

DFT calculations from our lab and the Huang lab showed that the activation barrier for N–F bond activation is 17.0 kcal/mol with HPPE and 11.8 kcal/mol with ACCO, indicating that this fluorine atom abstraction is likely the rate-determination step of this transformation. Moreover, a low activation barrier was observed for the radical rebound step (5.6 kcal/mol for HPPE, 3.4 kcal/mol for ACCO), suggesting that this rebound process is kinetically facile (Figure 35). Classical molecular dynamics (MD) simulations of wt ACCO and $ACCO_{CHF}$ show that the key mutations K158I, F91L and T89A widen the substrate entrance tunnel. This structural insight aligns with Michaelis-Menten kinetic experiments, which shows the enhanced enzymatic activity resulting from the improved substrate binding enabled by the substrate tunnel engineering.

To investigate the mechanism of the chemoselectivity of the radical rebound step, Huang examined the effect of additional azide anion on fluorine atom transfer. Using *Sv*HppE-Fluor, the fluorination product remained the predominant product, with a fluorination : azidation ratio of 17:1. This is in contrast to their prior results in C–H azidation with *Sav*HPPD,[207] where azidation was favored over fluorination. DFT calculations[207] indicated that both azide rebound and fluorine rebound are kinetically facile, with each proceeding with a low activation energy barrier. Together, Huang proposed that with *Sav*HppD, the carbon-centered radical is positioned closer to the azide, promoting rapid azide rebound, whereas in *Sv*HppE, the radical is oriented closer to the fluorine,

enabling fluorine rebound. This positioning effect is also used to explain the selectivity of halogenation versus hydroxylation in native nonheme halogenase enzymology[44] (Figure 35).

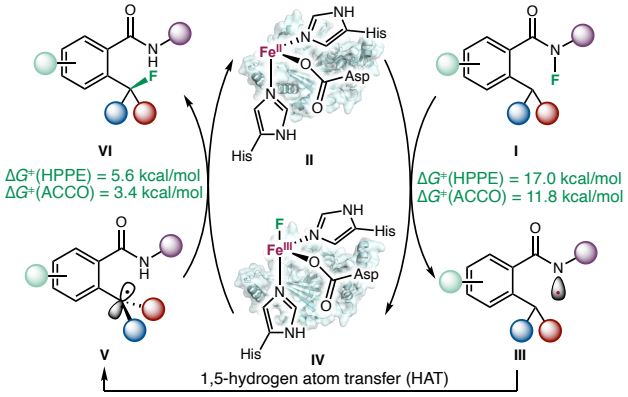

Figure 35. Proposed catalytic cycle of nonheme Fe enzyme-catalyzed enantioselective C(sp^3)–H fluorination.

4. Transformations involving oxygen-centered radicals

Oxygen-centered organic radicals such as alkoxy radicals and phenoxy radicals also represent versatile intermediates in organic synthesis.[219,220] In 2023, Zhong and coworkers reported a highly enantioselective oxidative coupling reactions between 3-hydroxyindole-2-carboxylates and various nucleophiles using copper efflux oxidase CueO[221] as the biocatalyst and H_2O_2 as the external oxidant (Figure 36).[222] Different types of nucleophiles, including indoles, pyrroles, electron-rich arenes and β-ketoesters, were compatible with this CueO-catalyzed process (Figure 36A). Based on radical trapping experiments,[223] Zhong proposed that this CueO-catalyzed reaction involves the formation of a phenoxyl radical and an oxidized 3-indolone ester as the intermediates. Isolation and characterization of this oxidized 3-indolone ester intermediate was unsuccessful, due to its high reactivity. Based on docking studies, Zhong proposed that this 3-indolone ester is bound

to CueO through hydrogen bonding interactions, allowing enantioinduction in the nucleophilic addition event (Figure 36B).

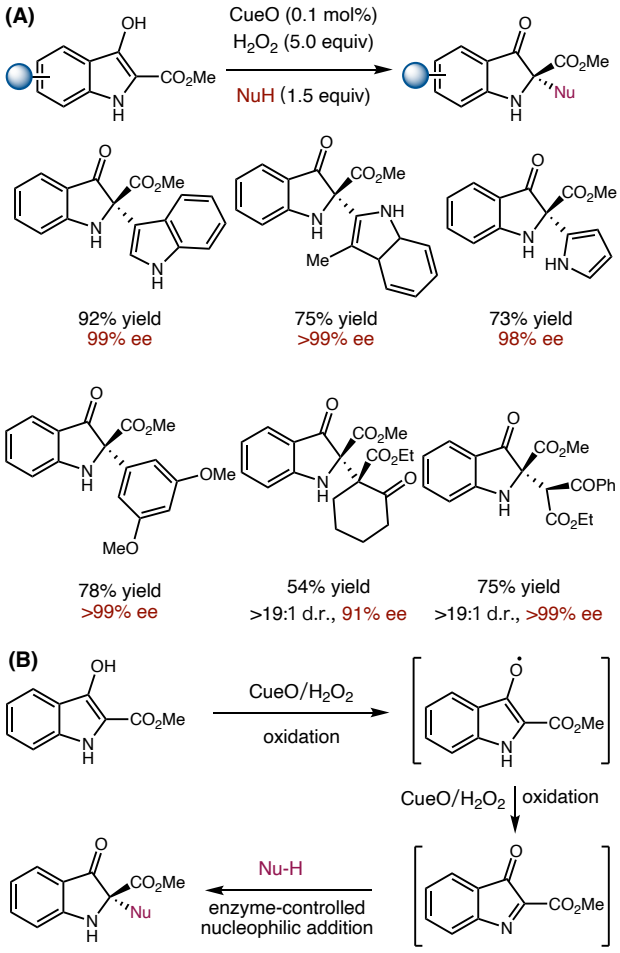

Figure 36. CueO-catalyzed enantioselective oxidative coupling of 3-hydroxyindole-2-carboxylates and other nucleophiles. (A) Selected substrate scope; reactions were carried out using 0.1 mol% cell-free lysate of CueO; (B) Proposed mechanism.

P450 enzymes could also induce the formation of oxygen-centered radical via single-electron oxidation of organic substrates using the highly reactive Fe=O intermediate.[224,225] In 2015, Müller reported that biosynthetic P450 enzymes including KtnC and DesC catalyzed C–C coupling providing biaryl natural products.[224] Based on these findings, in 2022, Narayan reported the

development of P450-catalyzed oxidative coupling of electron-rich aromatic compounds for the enantioselective synthesis of biaryl products.[225] In 2025, based on their previous studies, Narayan and coworkers further reported a biocatalytic deracemization of BINOL derivatives using cytochromes P450 (CYP158A2)[226], allowing access to enantioenriched atropisomers from racemic ones (Figure 37).[227] They proposed that this deracemization proceeds through the intermediacy of phenoxyl radicals following single-electron oxidation, allowing the rotation around the biaryl C–C bond. Upon further single-electron reduction, the biaryl compound is regenerated and enrichment in the major atropisomer occurred during this oxidation-reduction-based deracemization cycle (Figure 37A). Using 2 mol% purified CYP158A2, a wide range of binaphthol substrates were converted into enantioenriched form under these P450-catalyzed deracemization conditions (Figure 37B).

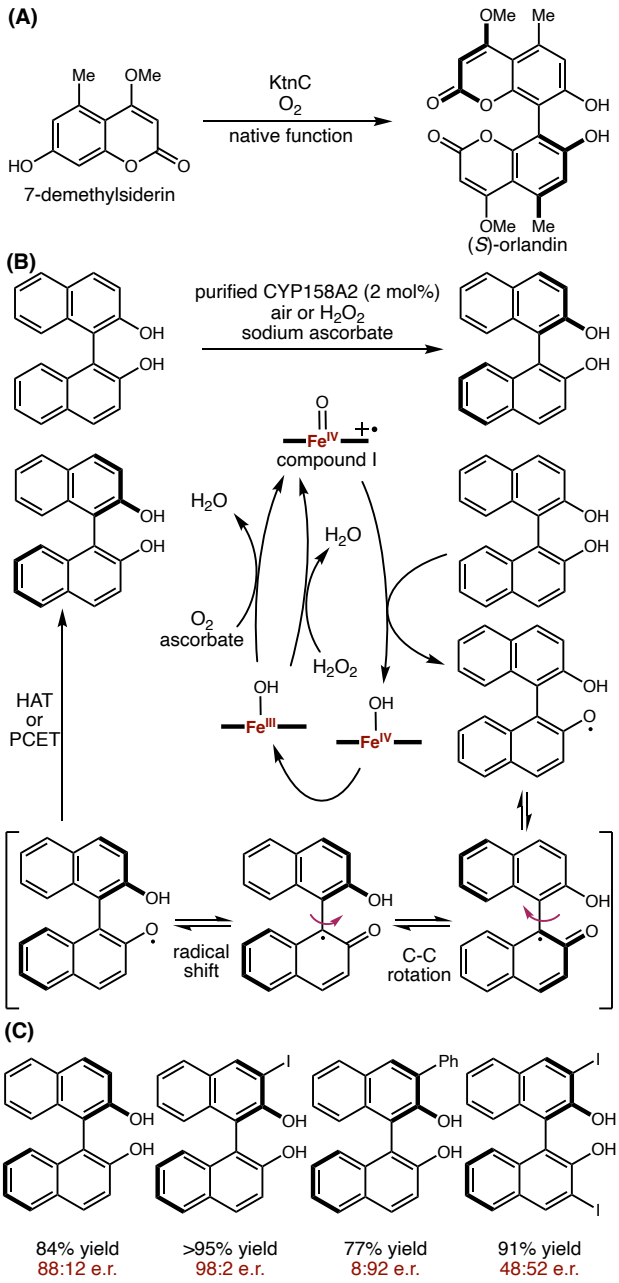

Figure 37. P450-catalyzed enantioselective deracemization of BINOLs. (A) The native function of KtnC, a biosynthetic P450 enzyme, is to catalyze the oxidative dimerization of 7-demethylsiderin to produce (*S*)-orlandin; (B) Proposed mechanism for the deracemization of binaphthol derivatives; (C) Selected substrate scope; reactions were carried out using 2 mol% purified CYP158A2.

5. Transformations involving metal nitrenoids with radical character on the nitrogen

Transition-metal nitrenoid-mediated reactions are useful tools for the construction of nitrogen-containing organic compounds. The use of metalloenzymes to catalyze unnatural nitrene transfer reactions dates back to 1985, when Dawson and Breslow reported the use of mammalian microsomal P450s to catalyze C–H amidation using iminoiodinanes as the nitrene precursor.[228] Despite this early report, the development of effective metalloprotein catalysts for stereoselective nitrene transfer reactions remained largely dormant until recently. In 2013, groundbreaking research from Arnold[82] and Fasan[229] led to P450-catalyzed enantioselective C–H amidation reactions using sulfonylazide substrates. Since then, a wide range of metalloenzyme-catalyzed nitrene transfer reactions, including intramolecular[83,230–232] and intermolecular C–H amination,[233] sulfidesimidation[234] and related [2,3]-sigmatropic rearrangement,[235] as well as aziridination,[236] have been rapidly advanced through the use of sulfamoyl azide or carbonazidates as the nitrene precursors. Nitrene transfer reactions have been extensively reviewed elsewhere.[60–63] Here, we review progress made after 2021 on metalloenzyme-catalyzed nitrene transfer reactions, where the metal nitrenoid intermediate features substantial radical characters on the nitrenoids nitrogen.

5.1 Metalloenzyme-catalyzed C–H amination

Since the groundbreaking work from Arnold and Fasan in 2013, organic azides have been widely used in heme protein-catalyzed nitrene transfer reactions.[62,63,237] Compared to sulfonyl azides and other organic azides bearing an electron-withdrawing group on the nitrogen, alkyl and aryl azides nitrenes have been largely underexplored in biocatalytic nitrene transfer processes.

In 2023, Arnold and co-workers developed a biocatalytic intramolecular C(sp^3)–H amination of alkyl and aryl azides using serine-ligated P450s (“P411s”) for the enantioselective synthesis of

nitrogen heterocycles (Figure 38).[238] A panel of engineered hemoproteins was evaluated, among which the previously engineered carbene transferase P411 M177L from the Arnold lab exhibited the highest initial activity, affording the pyrrolidine product in 4% yield and 82:18 e.r.. Through eight rounds of directed evolution, the final variant P411 M177L L75E Q437L A330Q M118V F77C S72W Q73A L436R (P411-PYS-5149) was identified, delivering the product in 66% yield and 91:9 e.r. (Figure 38A). P411-PYS-5149 not only showed an excellent scope for benzylic C(sp^3)–H amination but also exhibited initial activity toward the amination of unactivated C(sp^3)–H bonds (Figure 38B).

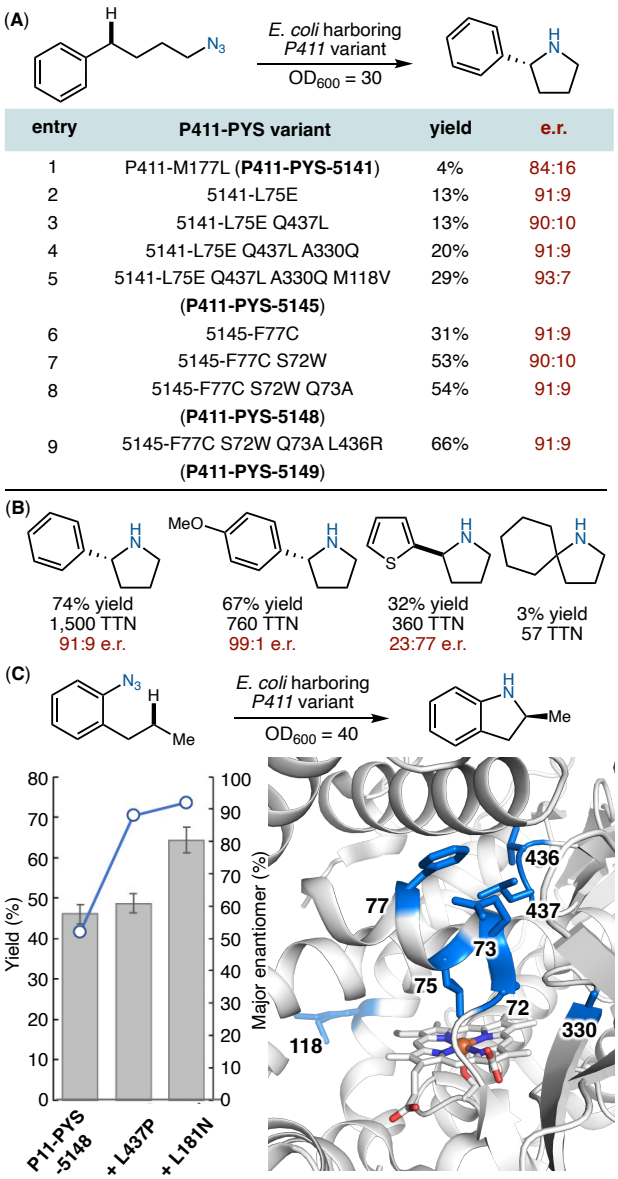

entry	P411-PYS variant	yield	e.r.
1	P411-M177L (**P411-PYS-5141**)	4%	84:16
2	5141-L75E	13%	91:9
3	5141-L75E Q437L	13%	90:10
4	5141-L75E Q437L A330Q	20%	91:9
5	5141-L75E Q437L A330Q M118V (**P411-PYS-5145**)	29%	93:7
6	5145-F77C	31%	91:9
7	5145-F77C S72W	53%	90:10
8	5145-F77C S72W Q73A (**P411-PYS-5148**)	54%	91:9
9	5145-F77C S72W Q73A L436R (**P411-PYS-5149**)	66%	91:9

Figure 38. 411 catalyzed nitrene transfer for enantiosynthesis of Chiral *N*-heterocyclic compounds. (A) Directed evolution of enantioselective alkyl nitrene transferase; (B) Selected substrate scope of enantioselective alkyl nitrene transfer, the experiments were conducted using suspensions of *E. coli* cells expressing P411-PYS-5149 (OD_{600} = 30); (C) Directed evolution of enantioselective aryl nitrene transferase, active-site illustration was made from the structure of 5UCW (PDB ID).

Arnold and coworkers found that an intermediate variant P411-PYS-5148 from this pyrrolidine synthase lineage exhibited promising activity for the synthesis of indolines, although with moderate enantioselectivity. Introduction of the L437P mutation improved this enantioselectivity. Ultimately, the triple mutant P411-PYS-5148 L437P L181N (P411-PYS-5151) delivered the methylindoline product in 64% yield and 92:8 e.r. (Figure 38C). DFT calculations were also carried out to understand the activity differences between alkyl and aryl nitrene intermediates. Based on DFT results, for alkyl azide substrates, Fe nitrenoid generation is the rate-limiting step in this C–H amination reaction. The activation barrier for nitrenoid formation (24.6 kcal/mol) is much higher than that of the subsequent HAT step (13.5 kcal/mol). In contrast, for aryl azide substrates, the HAT step has a higher barrier (20.8 kcal/mol) than the nitrogen extrusion step (18.0 kcal/mol), due to the increased stability of the *N*-aryl-substituted Fe nitrenoid. Together, these results revealed the distinct activity of *N*-alkyl-substituted Fe nitrenoid intermediates, when compared to their *N*-sulfonyl and *N*-aryl congeners.

In heme protein-catalyzed nitrene transfer reactions, the competing reduction of nitrene precursors catalyzed by the same protein catalyst represents a key issue in the optimization of synthetically useful processes.[232] In 2024, Hilvert and co-workers investigated the myoglobin-catalyzed azide reduction reaction, showing that this process proceeds via a reactive anionic ferrous intermediate (Figure 39A).[239] Through combined UV-visible spectroscopy, Mössbauer spectroscopy, X-ray crystallography and computational studies, Hilvert shed light on this intermediate and proposed a catalytic cycle that diverges from the canonical nitrene transfer pathways (Figure 39B). They demonstrated that this azide reduction process is regulated by the amount of dithionite (Figure 39A). These findings highlight the importance of redox tuning of

heme proteins, further suggesting that modulating the reduction potential of myoglobin via protein engineering or cofactor modification could enhance its efficiency in nitrene transfer catalysis.

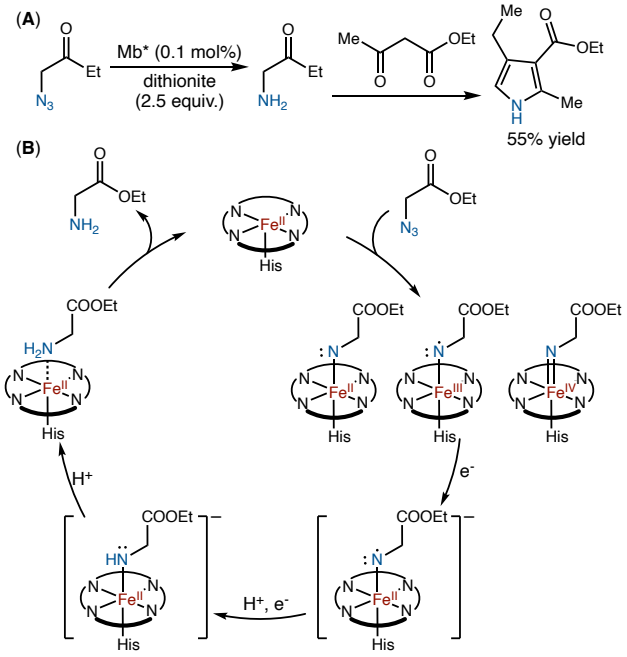

Figure 39. Myoglobin-catalyzed azide reduction. (A) Chemoenzymatic cascade for Knorr pyrrole synthesis; (B) Proposed catalytic cycle for azide reduction using myoglobin.

In addition to organic azides, hydroxylamine derivatives were also used as effective nitrene precursors in biocatalytic nitrene transfer reactions. In 2018, Ohnishi and co-workers discovered that a hydroxylamine ester is a key intermediate in natural biosynthetic pathways. They found that BezE, a cytochrome P450 from *Streptomyces sp.* RI18, facilitated the cyclization of geranylated *p*-acetoxyaminobenzoic acid via a nitrene transfer mechanism through N–O bond cleavage (Figure 40A).[240] In 2017, Ryan and co-workers reported that heme enzymes KtzT[241] and PipS[242] catalyzed N–N bond formation in the biosynthesis of piperazate natural products. Mechanistic studies suggested the involvement of a Fe nitrenoid intermediate generated from a hydroxylamine precursor (Figure 40B).

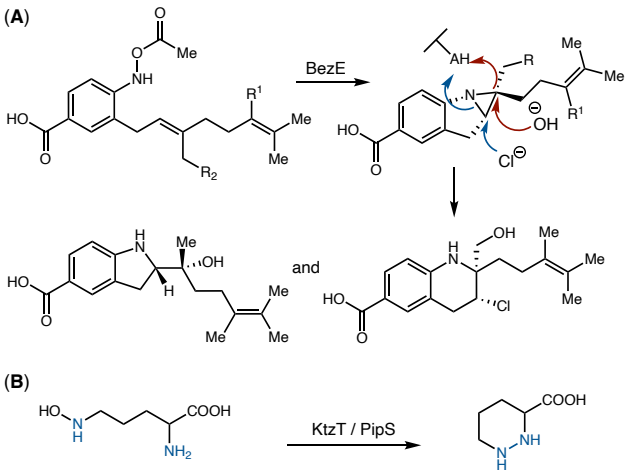

Figure 40. Biosynthetic processes involving heme-dependent enzyme-catalyzed nitrene transfer reactions starting from hydroxylamine derivatives. (A) Nitrene transferase BezE-catalyzed biosynthesis of benzastatin natural products; (B) Heme enzyme-catalyzed N–N bond formation in L-piperazic acid biosynthesis.

Prior to the discovery of biosynthetic nitrene transfer processes using hydroxylamine derivatives, in 2019, Arnold reported that engineered cytochrome *c* variants could catalyze the enantioselective aminohydroxylation of styrenes using *O*-pivaloylhydroxylamine as the nitrene precursor (Figure 41).[243] This work represents the first use of hydroxylamine derivatives as nitrene precursors in unnatural enzymatic amination reactions, demonstrating a wide range of new nitrene transfer reactions could be advanced using this class of nitrene precursors.

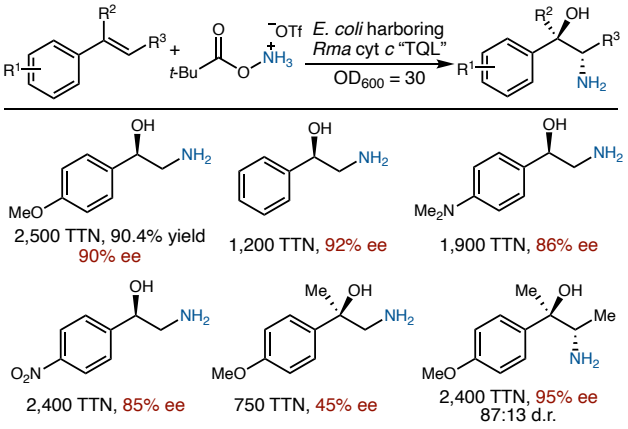

Figure 41. *Rma* cyt *c*-catalyzed enantioselective aminohydroxylation of styrenyl olefins.

Based on their previous studies on P411-catalyzed amination of benzylic and allylic C(sp^3)–H bonds,[244] in 2022, Arnold reported new P411 variants to allow for the asymmetric propargylic C(sp^3)–H amination *O*-pivaloylhydroxylamine triflic acid as the aminating reagent (Figure 42).[245] P411-B4 was chosen as the template for directed evolution of propargylic C(sp^3)–H aminating enzymes. Through eight rounds of iterative SSM and screening, beneficial mutations including E267D, N395C, G437Q, S72T, S438G, T269V, H266S and A74K were identified, culminating in PA-G8, which enabled the efficient enantioselective propargylic amination of 1-phenyl-1-butyne (Figure 42A and 42C). PA-G8 exhibited a broad substrate scope (>2,000 TTN, 82–96% ee). Propargylic substrates bearing a longer alkyl chain showed a slight decrease in catalytic activity but improved enantioselectivity (Figure 42B).

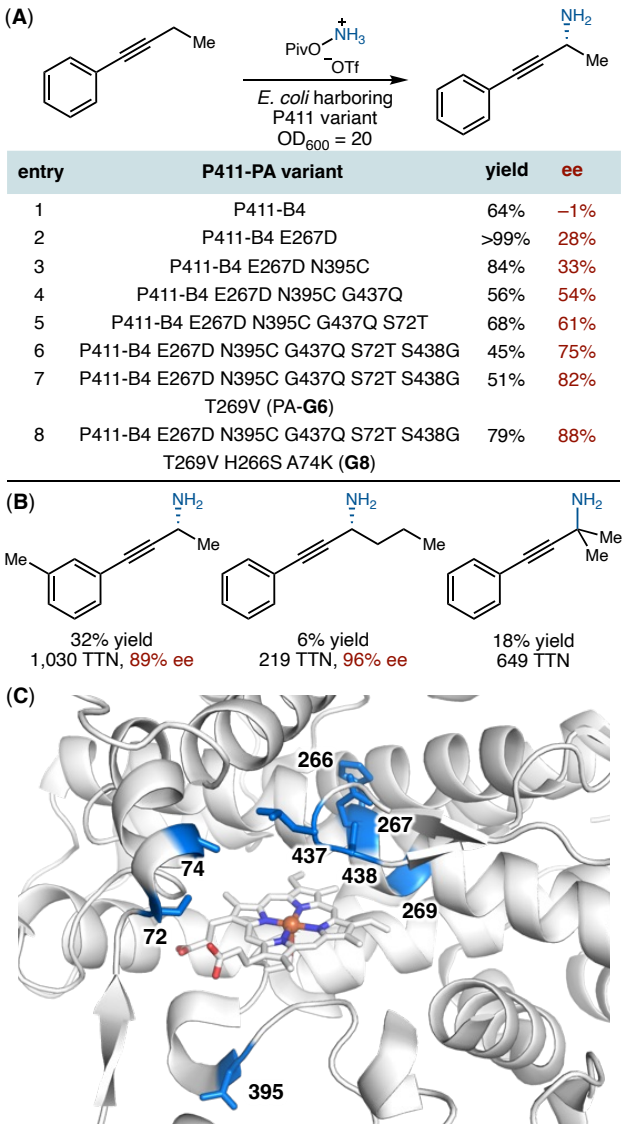

entry	P411-PA variant	yield	ee
1	P411-B4	64%	–1%
2	P411-B4 E267D	>99%	28%
3	P411-B4 E267D N395C	84%	33%
4	P411-B4 E267D N395C G437Q	56%	54%
5	P411-B4 E267D N395C G437Q S72T	68%	61%
6	P411-B4 E267D N395C G437Q S72T S438G	45%	75%
7	P411-B4 E267D N395C G437Q S72T S438G T269V (PA-**G6**)	51%	82%
8	P411-B4 E267D N395C G437Q S72T S438G T269V H266S A74K (**G8**)	79%	88%

Figure 42. P411-catalyzed enantioselective amination of propargylic C(sp^3)–H bonds. (A) Directed evolution of PA-G8; (B) Selected substrate scope of enantioselective propargylic C(sp^3)–H amination. Biocatalytic reactions were conducted using whole *E. coli* cells overexpressing P411-PYS-5149 (OD_{600} = 20). (C) The illustration of active site was made from 5UCW (PDB ID).

In 2022, the Arnold lab reported another breakthrough, allowing enantioselective C(sp^3)–H amination to be carried out with completely unactivated alkane substrates featuring C(sp^3)–H bonds with a high bond dissociation energy (BDE > 95 kcal/mol) (Figure 43).[246] Arnold selected

methylcyclohexane, a substrate structurally similar to toluene, as a model substrate to simultaneously evaluate C(sp^3)–H amination using *O*-pivaloyl-hydroxylammonium triflate and C(sp^3)–H amidation using *N*-acetyl-*O*-pivaloyl hydroxylamine. A previously evolved allylic C(sp^3)–H amination variant, APA6 (renamed uPA0),[244] was identified as the most active biocatalyst. In parallel, the previously evolved benzylic amidation variant, iAMD5-Y263V (renamed uAMD0),[247] exhibited the highest activity for C(sp^3)–H amidation. Through nine rounds of directed evolution using both SSM and epPCR, ten beneficial mutations M177L, M188Q, E409S, A330H, L740H, L780P, M263L, L333M, D251N and L188C were introduced, resulting in uPA9 (Figure 43A and 43C). uPA9 catalyzed enantioselective C(sp^3)–H amination with a nearly 20-fold higher activity, 86% site selectivity, 8:1 diastereoselectivity and 93:7 enantioselectivity, furnishing (1*R*,3*S*)-methylcyclohexylamine as the major product. Furthermore, nine rounds of directed evolution led to *uAMD9* carrying added beneficial mutations S438T, A74V, R226T, V74Q, S400A, G252V, M212V, N573T, S640E, Q74M, A388S, L233V, axial ligand mutation S400A and a premature stop codon I710Δ. *uAMD9* catalyzed the formation of (*1S*, *2R*)-2-methylcyclohexanamine acetate with 120 TTN, 91% site-selectivity, 7:1 d.r. and 85:15 e.r. (Figure 43B and 43C). All the mutants in *uAMD* evolutionary trajectory exhibited excellent oxygen tolerance, with minimal differences in activity and selectivity under aerobic and anaerobic conditions. Moreover, *uAMD9* was capable of amidating linear alkanes such as hexane and heptane, showing preferential regioselectivity for the C3 position, although with moderate enantioselectivity (Figure 43D).

(A)

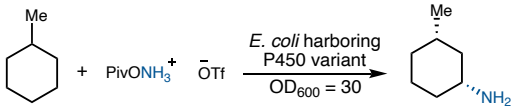

entry	P450 variant	TTN (yield) of amination
1	*APA6* (***uPA0***)	<5
2	*uPA0* M177L	10
3	*uPA0* M177L M118Q	15
4	*uPA0* M177L M118Q E409S	25
5	*uPA0* M177L M118Q E409S A330H	35
6	*uPA0* M177L M118Q E409S A330H L740H L780P (***uPA5***)	45
7	*uPA5* M263L L333M	65
8	*uPA5* M263L L333M D251N (***uPA8***)	65
9	*uPA5* M263L L333M D251N L188C (***uPA9***)	90 (12%)

(B)

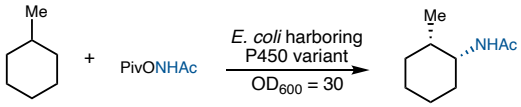

entry	P450 variant	TTN (yield) of amidation
1	*iAMD5* Y263V (***uAmD0***)	10
2	*uAmD0* S438T K861Δ	20
3	uA*mD0 S*438T K861Δ A74V	25
4	uAmD*0 S43*8T K861Δ V74Q R226T	30
5	uAmD0 *S438T* K861Δ A74Q R226T S400A	35
6	uAmD0 S4*38T K*861Δ A74Q R226T S400A G252V M212V N573T S640E I710Δ (***uAmD6***)	54
7	uAmD6 *Q74M* (***uAmD7***)	100
8	u*AmD6* Q74M A*399S*	100
9	uAmD6 Q74M A*399S* L233V (***uAmD9***)	120 (9%)

(C)

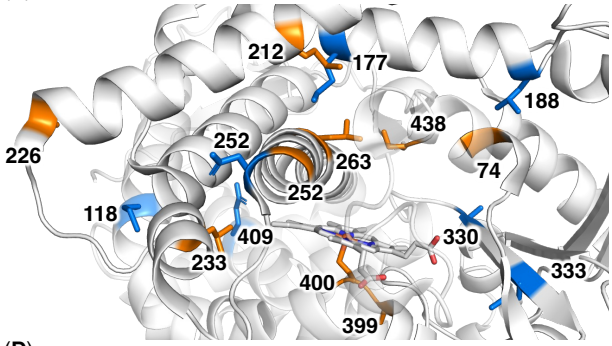

(D)

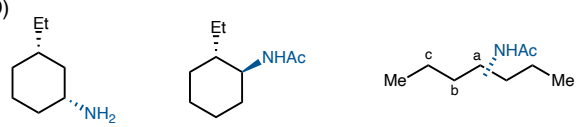

uPA9
100 TTN
> 99% s.s.
10.5:1 d.r.
98:2 *e.r.*

uAmD9
205 TTN
78% s.s.; 1:1 d.r.
cis: 98:2 *e.r.*
trans: 75:25 *e.r.*

***uAmD7* T438S**; 45 TTN
s.s. for a:b:c = 1.3:3.2:1
for b = 63:37 *e.r.*
for c = 53:47 *e.r.*

Figure 43. P411-catalyzed enantioselective amination and amidation of unactivated C(sp^3)–H bonds. (A) Directed evolution of uPA9 for the enantioselective amination of unactivated C(sp^3)–

H bonds; (B) Directed evolution of uAmD9 for the enantioselective amidation of unactivated C(sp^3)–H bonds; (C) The illustration of active site was made from 5UCW (PDB ID); (D) Selected substrate scope of enantioselective unactivated C(sp^3)–H amination and amidation.

DFT calculations using an Fe porphyrin model complex revealed a higher energy barrier ($\Delta G^{\ddagger}$ = 29.7 kcal/mol) for the HAT step in the amidation of unactivated C(sp^3)–H bonds compared to benzylic C(sp^3)–H systems ($\Delta G^{\ddagger}$ = 22.0 kcal/mol). These findings indicated that the newly P411 variants likely lowered the activation barrier for the challenging C(sp^3)–H functionalization. This is consistent with MD simulations in *u*AMD8, which revealed stabilizing dispersion interactions and hydrophobic interactions through directed evolution.

In 2024, Arnold and co-workers reported another P411-catalyzed enantioselective amination of tertiary C(sp^3)–H bonds, enabling the formation of α-tetrasubstituted carbinamines bearing a minimally differentiated methyl-ethyl stereocenter (Figure 44).[248] P411-TEA-5267 with three mutations (C324L, N395R, and G438V) relative to $P411_{BPA}$[244] was selected as the starting point for further engineering, furnishing the corresponding amine product with 20 TTN and 90% ee. Through iterative rounds of SSM and screening targeting active-site residues located on α-helices and flexible loops proximal to the heme cofactor, a septuple mutant P411-TEA-5267 M354E R395S A327V M177Y S72T Q403A S395V (P411-TEA-5274) was evolved, affording the desired product with 970 TTN and 92% ee. Interestingly, the S395V mutation located on the loop on the other side of the substrate binding pocket of the heme cofactor, led to a 4-fold increase in catalytic activity (Figure 44A and 44B).

(A)

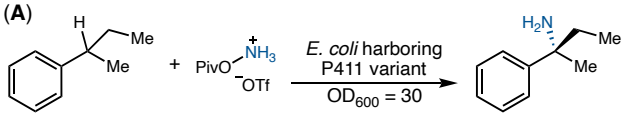

P411 variant	yield	TTN
P411-TEA-5267	1.0%	20
5267 M354E R395S	2.3%	35
5267 M354E R395S A327V	3.0%	64
5267 M354E R395S A327V M177Y A399G	5.8%	89
5267 M354E R395S A327V M177Y A399G S72T Q403A	17%	270
5267 M354E R395S A327V M177Y A399G S72T Q403A S395V (**P411-TEA-5274**)	26%	970

(B)

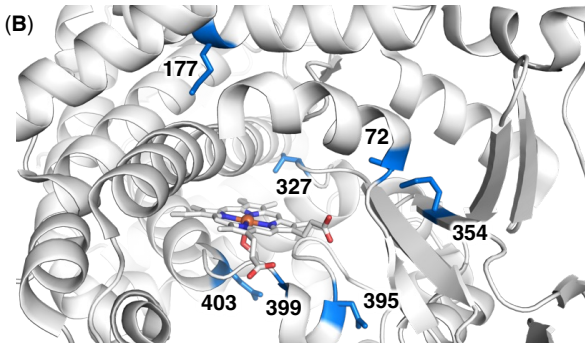

Figure 44. P411-catalyzed enantioselective amination of tertiary C(sp^3)–H bonds. (A) Directed evolution of tertiary C(sp^3)–H aminase P411-TEA-5274; (B) The illustration of active site was made from 5UCW (PDB ID).

P411-TEA-5274 also demonstrated excellent regioselectivity, enabling selective C(sp^3)–H amination over competing C(sp^2)–H amination and displaying preference for tertiary over primary C(sp^3)–H systems. In addition to benzylic substrates, P411-TEA-5274 was compatible with allylic (70 TTN, 90% ee) and propargylic substrates (120 TTN, 67% ee) (Figure 45A). Finally, reactions using enantiopure (*R*)-*sec*-butylbenzene and (*S*)-*sec*-butylbenzene led to products with retention of configuration, but markedly different reactivities, indicating that P411-TEA-5274 is a kinetic resolution catalyst that preferentially converts the (*R*)-enantiomer (Figure 45B).

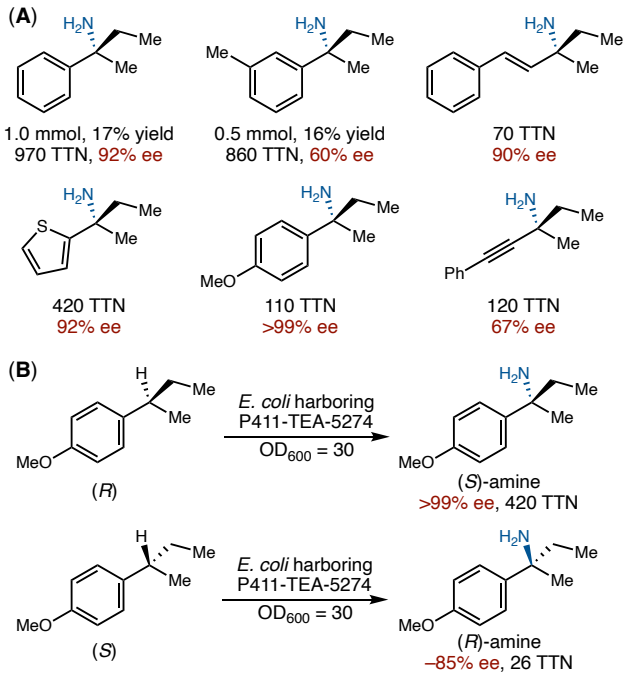

Figure 45. (A) Selected substrate scope; (B) P411-TEA-5274-catalyzed conversion of enantiopure (*R*)- or (*S*)-*sec*-butylbenzene.

In 2024, Arnold and co-workers further reported a biocatalytic enantioselective amination of α-C(sp^3)−H bonds of carboxylic acid esters using thermostable protoglobin variants (Figure 46).[249] Biocatalytic α-C–H amination using a heme protein-catalyzed nitrene transfer mechanism is hampered by the inherently slow hydrogen atom abstraction between the electrophilic metal-nitrenoid and C–H bonds adjacent to electro-withdrawing groups. Using a range of alkyl and benzylic carboxylic acid esters as the substrates, Arnold and coworkers evaluated an in-house collection of heme proteins, including 96 engineered P411 nitrene transferases and 60 small heme proteins (cytochromes *c* and globins), through high-throughput screening. A thermostable protoglobin from *Aeropyrum pernix* (*Ap*Pgb)[250] containing three mutations (W59A, Y60G, and F145G) was found to afford the desired (*S*)-amino ester product in 3% yield and 46% ee (Figure 46A). Subsequent rounds of epPCR and SSM led to the identification of nine beneficial mutations,

including F156L, I97T, F175L, I137T, T97V, H136N, K36E, C45A and K159E, resulting in a new α-ester aminase L-*Ap*Pgb-αEsA-G8, catalyzing the α-C−H amination of ethyl 2-(4-fluorophenyl)acetate in 41% yield and 84% ee. Further incorporation of three additional mutations, including F73W, R90G and G60S, provided L-*Ap*Pgb-αEsA-G11, allowing the desired product to form in 50% yield and 96% ee. Starting from L-*Ap*Pgb-αEsA-G8, introducing the F93A mutation led to a new biocatalyst to provide the product in 19% yield and inverted enantiopreference, allowing enantiodivergent C−H amination. Two additional rounds of SSM and screening provided D-*Ap*Pgb-αEsA-G2, which produced the (*R*)-enantiomer in 62% yield and 72% ee (Figure 46A and 46B). Both L-*Ap*Pgb-αEsA-G11 and D-*Ap*Pgb-αEsA-G2 displayed a broad substrate scope toward phenylacetic acid esters bearing various substituents, as well as α,α-disubstituted carboxylic acid esters. These evolved mutants also exhibited detectable initial activity toward aliphatic carboxylic esters (Figure 46C).

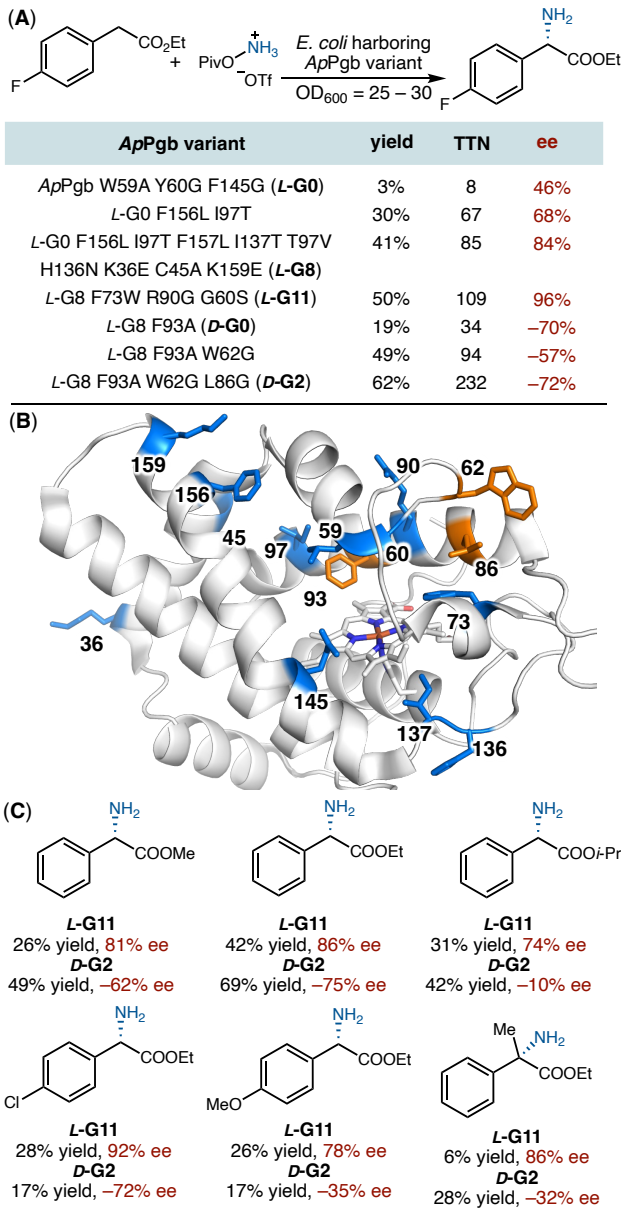

Figure 46. *Ap*Pgb catalyzed enantioselective amination of protic α-C(sp^3)–H bonds in carboxylic acid esters. (A) Directed evolution of L-*Ap*Pgb-αEsA and D-*Ap*Pgb-αEsA; (B) The illustration of active site was made from 7UTE (PDB ID); (C) Selected substrate scope; reactions were conducted using whole *E. coli* cells overexpressing *Ap*Pgb-αEsA (OD_{600} = 20 ± 3).

Despite advances in heme protein-catalyzed nitrene transfer using hydroxylamine esters, the use of the parent unsubstituted hydroxylamine as nitrene precursors has remained elusive,[251] in

part due to the high N–O bond dissociation energy of hydroxylamine. In 2023, Arnold and co-workers developed novel protoglobin nitrene transferases to allow for the use of hydroxylamine as the aminating reagent (Figure 47).[252] The protoglobin from *Pyrobaculum arsenaticum* (*Par*Pgb)[253] was engineered to catalyze benzylic C(sp^3)–H amination of 4-ethylanisole and aminohydroxylation of 4-vinylanisole using hydroxylammonium chloride. Starting from *Par*Pgb W59L V60Q (*Par*Pgb 5209), directed evolution using SSM, epPCR and staggered extension process (StEP) recombination[254] was carried out, leading to a new variant, *Par*Pgb-HYA-5213, which harbors seven beneficial mutations Y57D, W59L, V60Q, V85I, I149F, V175A and Q177R. *Par*Pgb-HYA-5213 exhibited a 160-fold improvement in yield compared to *Par*Pgb W59L V60Q (Figure 47A and 47B). Upon further optimization of reaction conditions, the desired product was obtained in 95% yield and >99% ee using 0.5 mol% biocatalyst. This newly evolved variant also proved efficient in the conversion of a range of ethylbenzene substrates and in the aminohydroxylation of styrenes (Figure 47C).

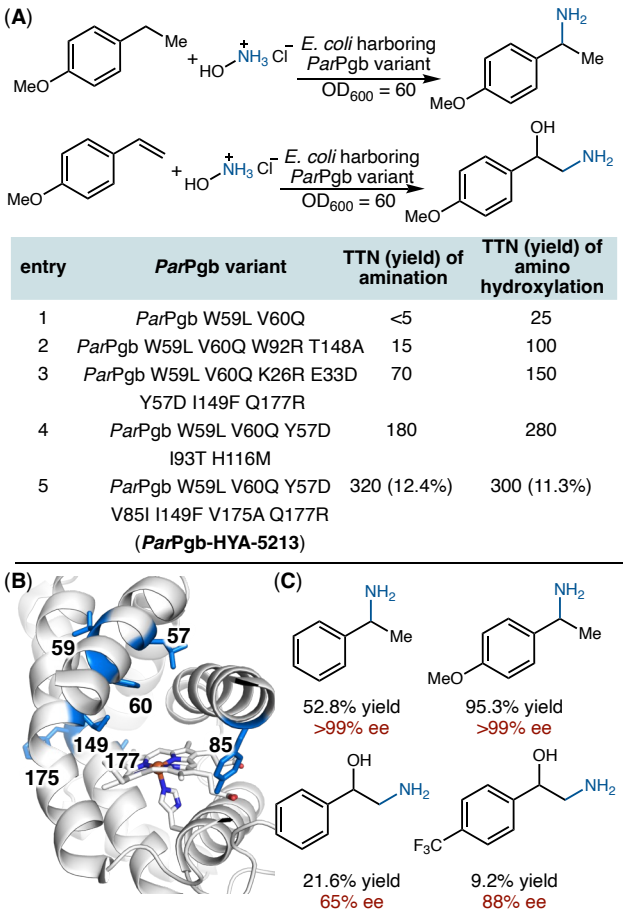

entry	*Par*Pgb variant	TTN (yield) of amination	TTN (yield) of amino hydroxylation
1	*Par*Pgb W59L V60Q	<5	25
2	*Par*Pgb W59L V60Q W92R T148A	15	100
3	*Par*Pgb W59L V60Q K26R E33D Y57D I149F Q177R	70	150
4	*Par*Pgb W59L V60Q Y57D I93T H116M	180	280
5	*Par*Pgb W59L V60Q Y57D V85I I149F V175A Q177R (***Par*Pgb-HYA-5213**)	320 (12.4%)	300 (11.3%)

Figure 47. *Par*Pgb-catalyzed enantioselective C(sp^3)–H amination and aminohydroxylation using hydroxylamine as a new aminating reagent in nitrene transfer. (A) Evolution trajectory of C–H aminase and promiscuity toward aminohydroxylation of 4-vinylanisole; (B) The illustration of active site was made from 2VEE (PDB ID); (C) Selected substrate scope of biocatalytic amination and aminohydroxylation. Reactions were conducted using 0.5 mol% purified *Par*Pgb-HYA-5213.

Michaelis-Menten kinetic studies of *Par*Pgb-HYA-5213 and *Par*Pgb-HYA-5209 were next carried out to further understand the mutational effects. These studies showed a 180-fold k_{cat} improvement of *Par*Pgb-HYA-5213 compared to the starting variant *Par*Pgb-HYA-5209. Furthermore, the K_M value for NH_2OH of *Par*Pgb-HYA-5213 dropped from 5.4 mM to 0.30 mM, representing a 180-fold improvement in apparent substrate affinity. Together, the k_{cat}/K_M value of

these variants increased from 0.1 mM^{-1} min^{-1} to 300 mM^{-1} min^{-1}, shedding light on the origin of enhanced catalytic efficiency in evolved protoglobin variants.

To elucidate the reaction mechanism, Arnold and coworkers conducted UV-vis spectroscopy using *Par*Pgb-HYA-5213 (Figure 48).[255] In the presence of a 200-fold excess of sodium dithionite, a prominent Soret band at 434 nm and a broad Q-band at 562 nm were observed, which were distinct from the resting state hemoprotein with bands at 413 nm and 543nm. Upon the addition of a 600-fold excess of hydroxylamine, a new UV-visible pattern with three characteristic bands at 425, 530, and 560 nm was observed, indicating the formation of a new species, E_{redHA}, from the reaction between E_{red} and NH_2OH (Figure 48B). E_{redHA} was found to decompose slowly to E_{ox} under ambient conditions. However, in the presence of a substrate bearing a benzylic $C(sp^3)$–H bond, E_{redHA} rapidly converted to E_{ox}, accompanied by the formation of the amination product (Figure 48C).

Further studies with alternative aminating reagents including nitrite (NO_2^-), nitric oxide (NO), and nitroxyl (HNO) revealed the generation of new UV-vis absorption bands at 422 nm and 568 nm, which are assigned to E_{red}. This E_{red} species decayed to E_{ox} within 100 min for NO_2^- and NO and 30 min for HNO. Additionally, EPR spectroscopy revealed that E_{red} exhibited identical signal peaks in the presence of different aminating regents, including NO_2^-, NO, HNO, and NH_2OH (Figure 48D). HR-ESI-MS analysis confirmed the formation of the desired aminated product when the spin-trapping regent DMPO was used (Figure 48E). Importantly, all the tested aminating reagents produced the aminated product with varying yields but consistently high enantioselectivity. Specifically, NH_2OH provided 90.7% yield, NO_2^- provided 26.25% yield, NO provided 17.8%, yield and HNO provided 89.8% yield (Figure 48F). These findings suggest the

involvement of a common iron-nitrosyl intermediate, which may further generate an iron-nitrenoid species within the enzyme active center to drive the amination reaction.

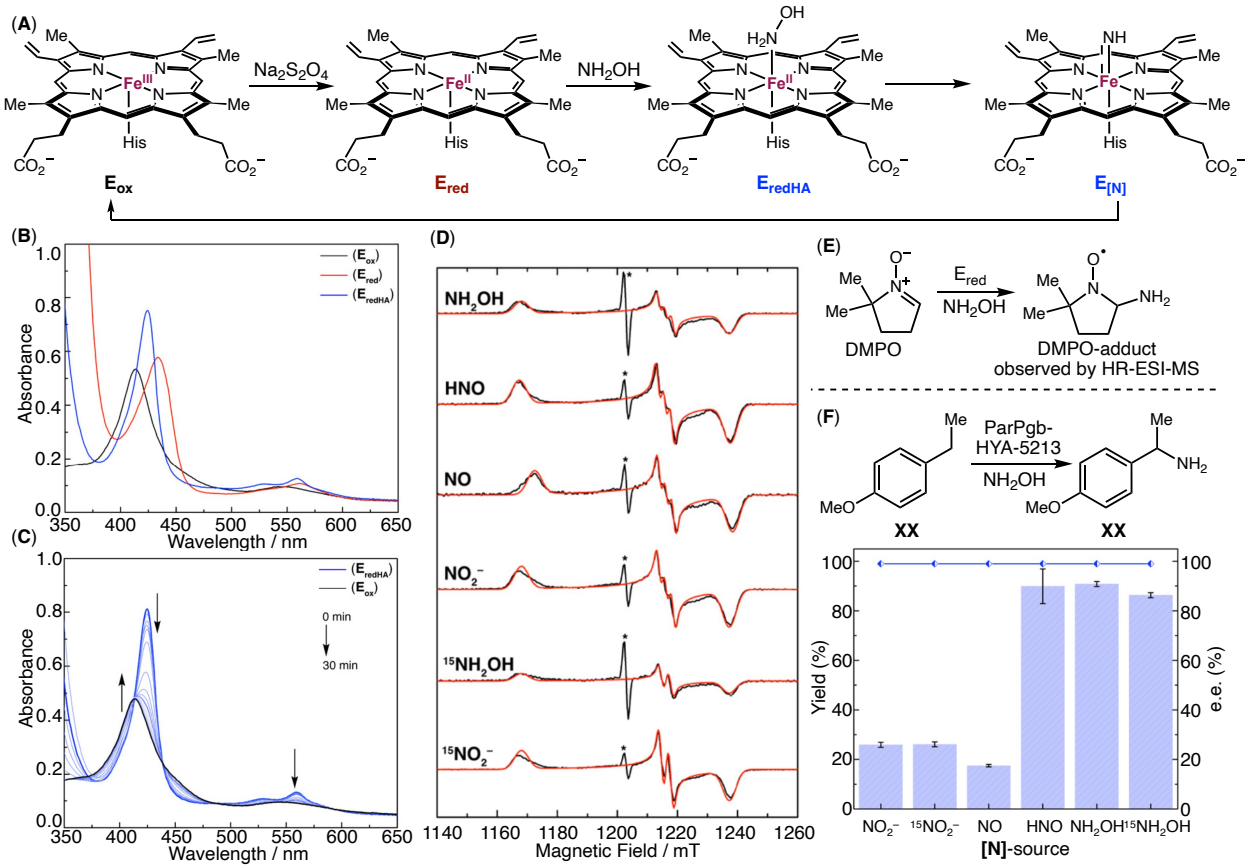

Figure 48. Spectroscopic and mechanistic studies. (A) Key intermediates in heme protein-catalyzed C(sp^3)–H amination; (B) UV-vis spectra of *Par*Pgb-HYA-5213 protein in its resting state (E_{ox}) and reduced state (E_{red}) and the hydroxylamine adduct of the reduced protein (E_{redHA}); (C) UV−vis spectra collected during the decomposition of E_{redHA} to E_{ox}, with isosbestic points at 438 and 572 nm; (D) Experimental (black line) and simulated (red line) Q-band pseudomodulated EPR spectra of the putative $\{FeNO\}^7$ species in a frozen solution at 15 K, obtained by mixing E_{red} with different aminating reagents including NH_2OH, NO_2^-, NO, HNO, $^{15}NH_2OH$, and $^{15}NO_2^-$. *Indicates a background signal from the resonator; (E) HR-ESI-MS spectra of DMPO adducts

obtained by treating E_{red} and DMPO with NH_2OH; (F) Biocatalytic nitrene transfer to the benzylic C−H bond of *p*-ethylanisole with different aminating sources using purified 0.5 mol% *Par*Pgb-HYA-5213. DMPO = 5,5-Dimethyl-1-pyrroline N-oxide. Adapted with permission from *J. Am. Chem. Soc.* **2024**, *146*, 20556–20562. Copyright 2024 American Chemical Society.

5.2 Metalloprotein-catalyzed C–H amidation

Compared to *N*-sulfonyl Fe nitrenoids and unprotected Fe nitrenoid, *N*-acyl Fe nitrenoids are prone to Curtius rearrangement and thus remain underexplored in biocatalytic nitrene transfer.[256,257] To address this challenge, in 2021, Arnold and co-workers developed an intermolecular benzylic C(sp^3)–H amidation by directed evolution and substrate walking, providing a series of P411 variants that catalyzed benzylic C(sp^3)–H amidation using acylnitrene precursors (Figure 49).[247] *i*AMD4 containing four beneficial mutations was evolved after four rounds of SSM and screening, enabling the benzylic amidation of 4-ethylanisole with 3-phenyl-*N*-(pivaloyloxy)nitrenoids in 475 TTN and 95:5 e.r. (Figure 49A, reaction I). Activity enhancement was mainly attributed to V328T near the heme cofactor. However, this variant exhibited very low activity for the benzylic amidation of ethylbenzene with *N*-(pivaloyloxy)acetamide (Figure 49A, entry 5). Subsequent introduction of C78L and S438Q mutations close to the heme cofactor provided *i*AMD6, which demonstrated a nearly 100-fold increase in activity toward reaction II. These mutations also abolished the activity for reaction I. Further engineering resulted in the final variant *i*AMD9, giving rise to the amide product in 57% yield, 1,580 TTN and >99% ee (Figure 49A). *i*AMD9 also showed a good substrate scope (Figure 49B). Using *i*AMD8, Arnold investigated the effect of different nitrene precursors, including *N*-hydroxyacetamide, *O*-pivaloyl, *O*-acetate, and dioxazolone using 4-ethylanisole as the model substrate (Figure 49C). Their results revealed that the *O*-pivaloylhydroxylamine exhibited a 2–4-fold higher reactivity compared to

other related nitrenoids precursors including the *O*-acetylhydroxylamine and dioxazolone, whereas the free *N*-hydroxyacetamide only provided a trace amount of product.

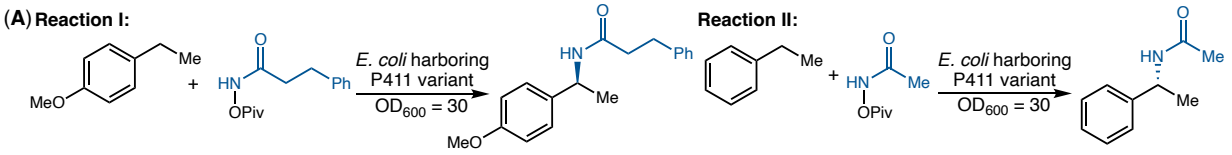

		reaction I		reaction II	
entry	P411 variant	TTN	e.r.	TTN (yield)	e.r.
1	*iAMD0*	N.D.	N.D.	N.D.	N.D.
2	*iAMD0* V78C	40	N.D.	<10	N.D.
3	*iAMD0* V78C V328T	440	85:15	<10	N.D.
4	*iAMD0* V78C V328T N70S	349	90:10	<10	N.D.
5	*iAMD0* V78C V328T N70S I401L (***iAMD4***)	475	95:5	<10	N.D.
6	*iAMD0* V78C V328T N70S I401L C78L (***iAMD5***)	445	83:17	153	N.D.
7	*iAMD4* C78L S438Q (***iAMD6***)	<10	N.D.	863	>99:1
8	*iAMD5* S438Q L82M			907	>99:1
9	*iAMD5* S438Q L82M L181Q (***iAMD8***)			1,096	>99:1
10	*iAMD5* S438Q L82M L437I (***iAMD8b***)			1,319	>99:1
11	*iAMD5* S438Q L82M L437I A74S (***iAMD9***)			1,581 (57%)	>99:1

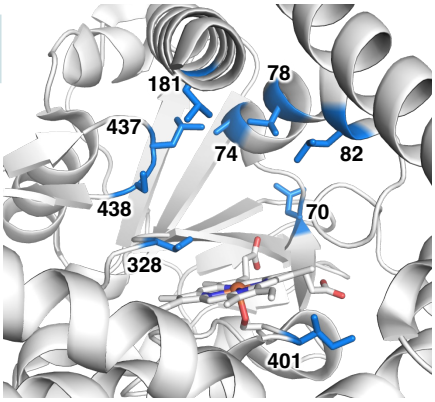

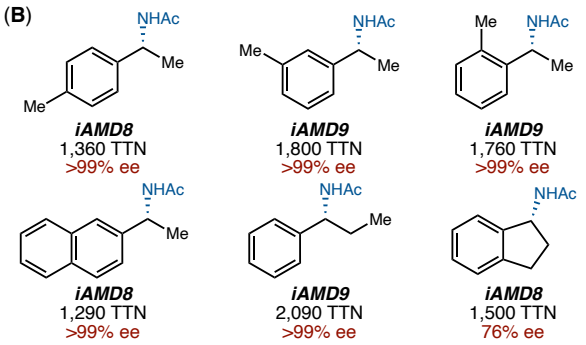

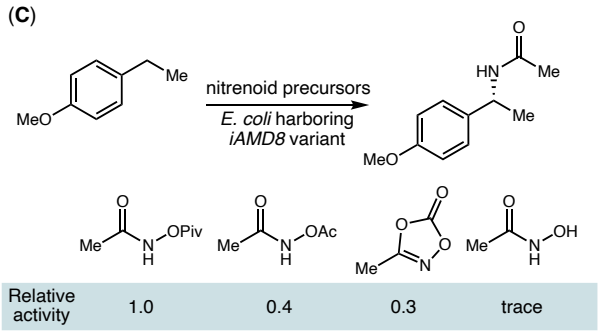

Relative activity	1.0	0.4	0.3	trace

Figure 49. P411-catalyzed enantioselective amidation of benzylic C(sp^3)–H bonds. (A) Directed evolution for C(sp^3)–H amidation using reactions I and II as the model system. Active-site illustration was made from 5UCW (PDB ID); (B) Selected substrate scope; (C) Relative activity of 4-ethylanisole in *i*AMD8-catalyzed C(sp^3)–H amidation with different nitrene precursors.

In 2023, Fasan and co-workers reported a myoglobin-catalyzed intramolecular C(sp^3)–H amidation mediated by *N*-acyl Fe nitrenoid species generated from dioxazolones, a class of easily accessible acyl nitrene precursor,[258,259] allowing the enantioselective synthesis of β–, γ–, and δ-

lactams (Figure 50).[260] Using 3-phenylpropyldioxazolone as the substrate, the sperm whale myoglobin H64V variant (Mb H64V) afforded the desired lactam product in 2% yield and 96% ee. In contrast, other heme proteins evaluated, including P450s, cytochromes *c*, peroxidases, and wt Mb exhibited no activity. Given the key effects of the H64 residue in carbene[261] and nitrene[229] transfer activity, Fasan and coworkers further evaluated their in-house collection of Mb variants bearing mutation at residue 64. Mb H64V V68A (Mb*) previously evolved by the same group from enantioselective carbene transfer,[261] was identified as the optimal biocatalyst, affording the lactam product in 50% yield and >99% ee, despite the formation of 40% reduced byproduct and 10% γ-lactone as side products. Additional variants bearing mutations at residues 64 and 68 were next studied. Mb H64A V68A conferred no enantioselectivity, indicating that the protein is highly sensitive to mutations at these sites (Figure 50A and 50B). Through further optimization of organic co-solvent and reaction buffer, the chemoselectivity was improved (75% yield and >99% ee). Screening of myoglobin variants bearing active-site mutations and one additional round of SSM afforded Mb L29T H64T V68L (Mb^{TTL}), providing the opposite enantiomer *ent*-lactam with 91% ee. Notably, both Mb* and Mb^{TTL} exhibited good substrate tolerance for the enantioselective synthesis of γ-lactams, while Mb* also showed high activity and selectivity in the formation of β- and δ-lactams. In γ-lactam formation, the newly evolved Mb* show higher activity for the substrates bearing an electron-donating group, whereas in β-lactam formation, a different trend was observed (Figure 50C).

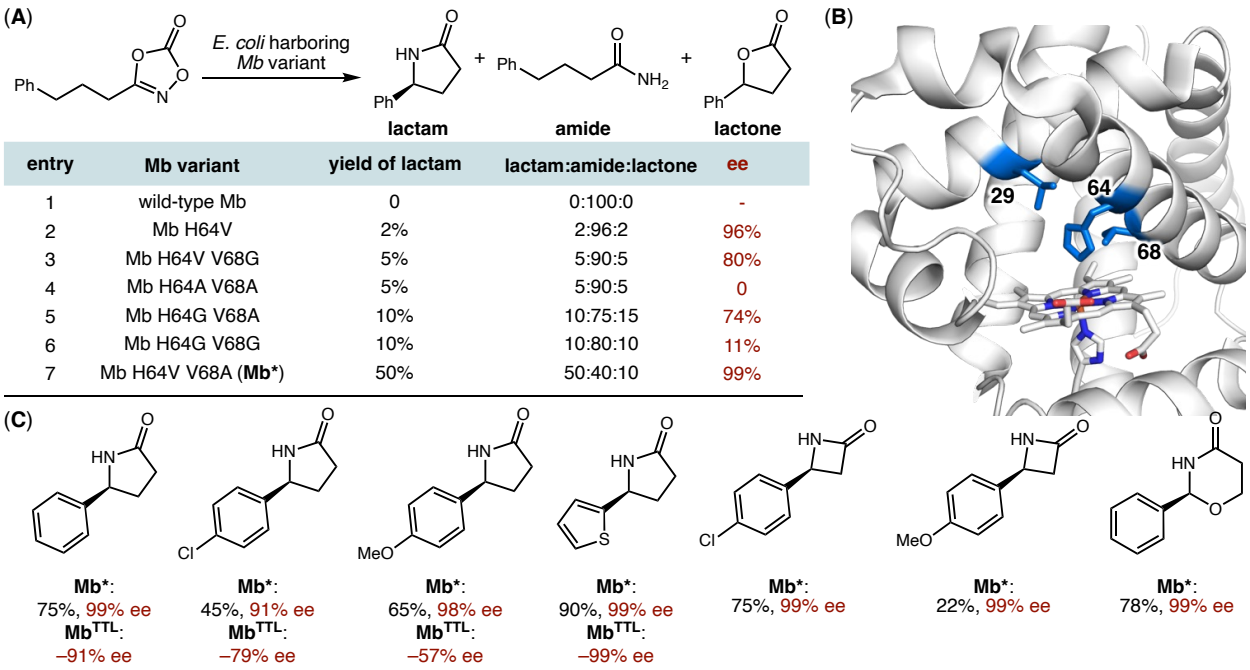

entry	Mb variant	yield of lactam	lactam:amide:lactone	ee
1	wild-type Mb	0	0:100:0	-
2	Mb H64V	2%	2:96:2	96%
3	Mb H64V V68G	5%	5:90:5	80%
4	Mb H64A V68A	5%	5:90:5	0
5	Mb H64G V68A	10%	10:75:15	74%
6	Mb H64G V68G	10%	10:80:10	11%
7	Mb H64V V68A (**Mb***)	50%	50:40:10	99%

Figure 50. Myoglobin-catalyzed enantioselective intramolecular C(sp^3)–H amidation using dioxazolones. (A) Directed evolution of Mb*; (B) The illustration of active site was made from 1JW8 (PDB ID); (C) Selected substrate scope for the biocatalytic amination for β-lactams, γ-lactams and δ-lactams; reactions were conducted using 2 mol% purified Mb variants.

In 2024, Arnold and co-workers extended their biocatalytic enantioselective C(sp^3)–H amidation to organosilane substrates (Figure 51).[262] A cytochrome P450 variant, uAmD5-5117, which was previously evolved for the amidation of unactivated C(sp^3)–H bonds,[246] was the only enzyme displaying initial activity in this enantioselective amidation of benzyltrimethylsilane, albeit with a very low activity (0.1% yield). Through four rounds of epPCR and recombination by staggered extension process (StEP), eight beneficial mutations, including T328A, N573D, E839G, R47H, E143K, F77S, F662C and K670I were introduced to uAmD5-5117, resulting in a 34-fold increase in activity. Although the simultaneous truncation of both the FAD and FMN reductase domains reduced enzyme activity, truncation of the FAD domain enhanced catalytic efficiency as

well as protein expression. By combining this truncation with the introduction of a key mutation T327P, a new variant, P411-SIA-5289 was obtained, delivering the product in 111 TTN and 99% ee. Finally, three additional beneficial mutations S70M, V263L, and T436A were introduced into P411-SIA-5289 to provide P411-SIA-5291, providing 34% yield and 99% ee. This represented a 430-fold improvement in catalytic activity (Figure 51A and 51C). P411-SIA-5291 tolerated a range of benzylsilane substrates. When substrate possessing an olefin moiety was applied, the P411-SIA-5291 catalyzed benzylic α-Si–C(sp^3)–H amidation preferentially over aziridination (Figure 51B).

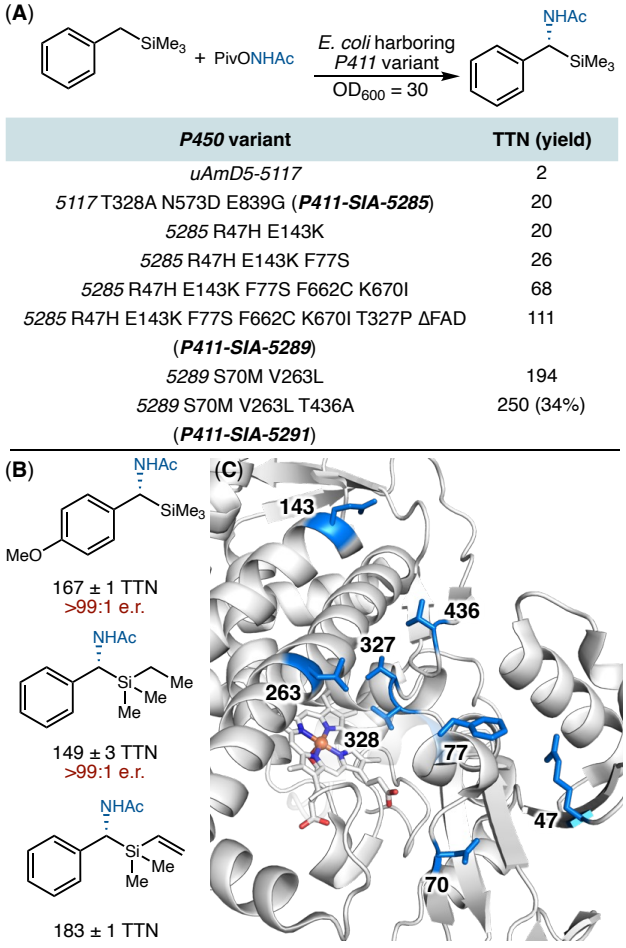

P450 variant	TTN (yield)
uAmD5-5117	2
5117 T328A N573D E839G (***P411-SIA-5285***)	20
5285 R47H E143K	20
5285 R47H E143K F77S	26
5285 R47H E143K F77S F662C K670I	68
5285 R47H E143K F77S F662C K670I T327P ΔFAD (***P411-SIA-5289***)	111
5289 S70M V263L	194
5289 S70M V263L T436A (***P411-SIA-5291***)	250 (34%)

Figure 51. P411-catalyzed enantioselective amination of α-Si–C(sp^3)–H bonds. (A) Directed evolution of P411-SIA-5291; Active-site illustration was made from 5UCW (PDB ID); (B) Selected substrate scope.

In 2025, Fasan and co-workers reported engineered myoglobins to catalyze the intramolecular C(sp^3)–H amination of carbamate derivatives, allowing the enantioselective construction of oxazolidinones (Figure 52).[263] Using Mb*, a range of phenyl ethyl carbamate substrates bearing different *N*-protecting groups, such as *N*-hydroxy, *N*-pivaloyl, *N*-benzoyl and *N*-tosyl were evaluated. All the tested substrates showed measurable initial activity and excellent enantioselectivity, within the *N*-benzoyl group providing the highest initial activity (Figure 52A). Screening of myoglobin variants led to a triple mutant Mb H64V V68A Y146F, delivering the desired product in 82% yield and 99:1 e.r.. On the other hand, Mb F43V I107E produced the opposite enantiomer in 48% yield and 92:8 e.r., allowing enantiodivergent access to oxazolidinones. Time course experiments using the model substrate were performed to compare Mb H64V V68A Y146F with Fasan's Mb H64V V68A variant (Mb*). These studies revealed improved chemoselectivity favoring the desired amidation product, indicating that the Y146F mutation suppresses unproductive electron transfer (Figure 52B).[232]

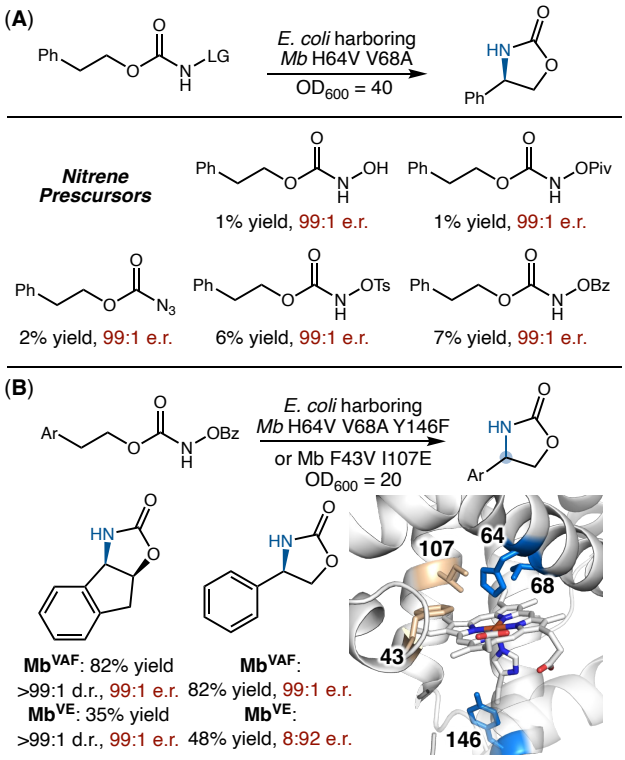

Figure 52. Mb-catalyzed intramolecular enantioselective amination of carbamate derivatives. (A) Evaluation of different carbamate derivatives; (B) Represent substrate scope of the biocatalytic enantiodivergent amination; Mb^{VAF} = Mb H64V V68A Y146F, Mb^{VE} = Mb F43V I107E; the illustration of active site was made from 1MBI (PDB ID).

In 2019, Arnold and co-workers engineered a nonheme ethylene-forming enzyme from *Pseudomonas savastanoi* (*Ps*EFE)[264] to perform nitrene transfer reactions. These results constitute the first examples of nonheme Fe enzyme catalyzed nitrene transfer (Figure 53).[265] They found the co-substrate 2-oxoglutarate in the native reaction could be replaced by *N*-oxalylglycine (NOG) and acetate in the unnatural aziridination reaction, leading to a 7.75-fold and 6.72-fold increase in activity, respectively (Figure 53A). Furthermore, a similar trend was also observed in *Ps*EFE-catalyzed intramolecular C(sp^3)–H amidation reaction (Figure 53B).

(A)

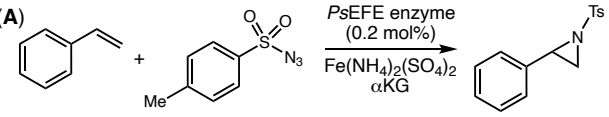

entry	deviation from standard conditions	relative activity
1	none	1.00
2	no αKG	0.52
3	acetate instead of αKG	6.72
4	NOG instead of αKG	7.75

(B)

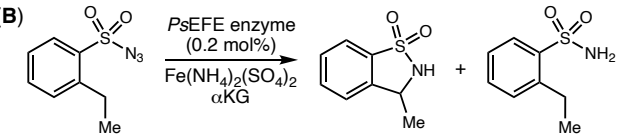

*Ps*EFE variant	deviation from standard conditions	TTN (yield)	ee	selectivity
wild type	acetate instead of αKG	12	n.d.	62%
*Ps*EFE^{VHMM}	none	31	61%	79%
*Ps*EFE^{VHMM}	no αKG	27	n.d.	77%
*Ps*EFE^{VHMM}	acetate instead of αKG	240	7.3%	97%
*Ps*EFE^{VHMM}	NOG instead of αKG	33	n.d.	80%
*Ps*EFE^{VMM}	none	130	n.d.	90%
*Ps*EFE^{VMM}	no αKG	25	n.d.	47%
*Ps*EFE^{VMM}	acetate instead of αKG	310	9.4%	96%
*Ps*EFE^{VMM}	NOG instead of αKG	450 (90%)	48%	>99%

(C)

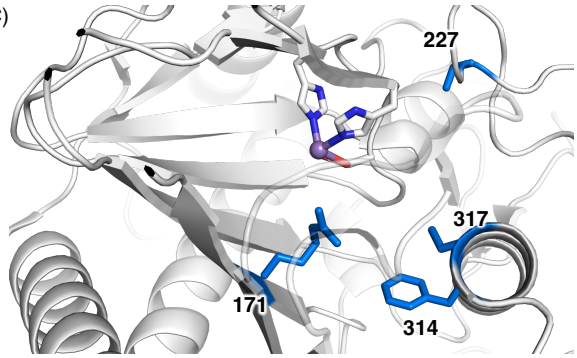

Figure 53. Ethylene forming enzyme (EFE)-catalyzed enantioselective nitrene transfer reaction. (A) *Ps*EFE-catalyzed aziridination; (B) *Ps*EFE-catalyzed intramolecular C(sp^3)–H amidation; *Ps*EFE^{VHMM} = *Ps*EFE R171V R227H F314M C317M, *Ps*EFE^{VMM} = *Ps*EFE R171V F314M C317M. (C) The illustration of active site was made from 6CBA (PDB ID).

Parallel to this study from the Arnold lab, in 2020, Fasan and coworkers reported the use of Rieske dioxygenases, including toluene dioxygenase (TDO),[266] naphthalene dioxygenase (NDO),[267,268] and chlorobenzene dioxygenase (CBDO),[269] for the intramolecular C(sp^3)–H amidation,[270] achieving good chemoselectivity of the desired amidation over other undesired pathways. Among these, NDO-catalyzed C–H amidation showed a good oxygen tolerance, affording 45% yield and over 90% selectivity on a one-gram scale for the conversion of 2,4,6-triisopro-pylbenzensulfonyl azide using *E. coli* JM109 (DE3) harboring NDO cells in a 5 L bioreactor.

Fasan and coworkers also evaluated various types of other nonheme iron enzymes, including Rieske and Fe/αKG-dependent dioxygenases and halogenases (Figure 54). They found that the presence of αKG had varying effects on the catalytic activity of αKG enzymes in this unnatural C(sp^3)–H amidation. Among these nonheme enzymes tested, H6H[271] and WelO5[272] exhibited detectable activity. These results demonstrated the potential nonheme Fe enzymes to facilitate these nitrene transfer reactions.

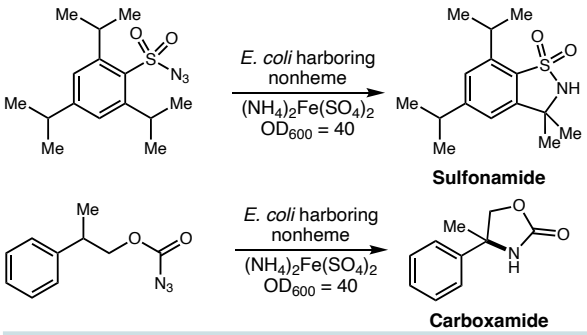

enzyme	condition	sulfonamide yield (selectivity)	carboxamide yield (selectivity)
TauD	A	27% (63%)	not active
TauD	B	13% (62%)	not active
AlkB	A	not active	2% (30%)
AlkB	B	not active	not active
Gab	A	14% (57%)	not active
Gab	B	13% (53%)	not active
AsqJ	A	24% (67%)	not active
AsqJ	B	12% (59%)	not active
H6H	A	13% (33%)	6% (27%)
H6H	B	not active	not active
WelO5	A	15% (58%)	not active
WelO5	B	13% (61%)	3% (80%)

Figure 54. Nonheme Fe enzyme-catalyzed intramolecular C(sp^3)–H amidation. Condition A: no additives, condition B: αKG, ascorbate and Fe salts were added.

In 2025, our lab reported the use of nonheme Fe enzymes for enantioselective non-canonical amino acid synthesis via a 1,3-nitrogen migration reaction (Figure 55).[273] Inspired by the important work from Meggers,[274,275] we capitalized on the availability of multiple open coordination sites of nonheme Fe to allow for the simultaneous binding of two substrate-derived fragments, allowing this nitrogen migration process to occur with excellent efficiency and enantioselectivity. In this proposed catalytic cycle, the activation of the azanyl ester substrate with nonheme Fe leads to an Fe nitrenoid with a bound carboxylate. This intermediate subsequently undergoes an intramolecular 1,5-hydrogen atom transfer, providing an iron bound α-carboxylate radical. Subsequent radical rebound between the Fe-bound nitrogen group species and the α-carboxylate radical facilitates the enantioselective C–N bond formation (Figure 55).

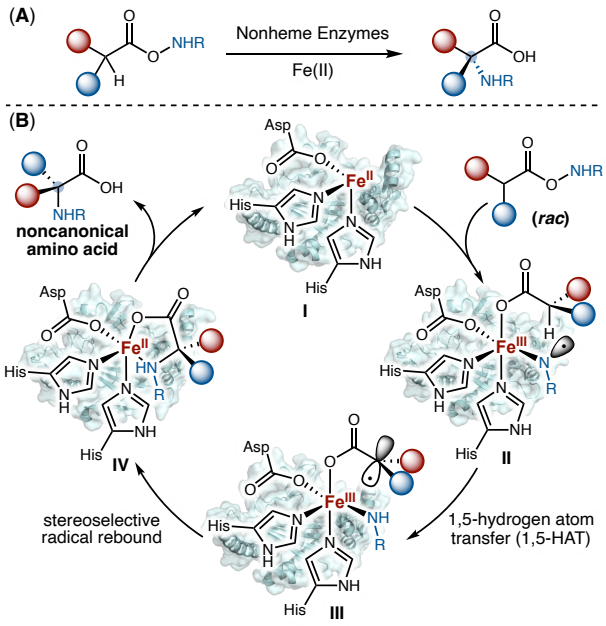

Figure 55. Nonheme Fe enzyme-catalyzed enantioselective 1,3-nitogen migration reaction. (A) Biocatalytic enantioselective synthesis of non-canonical amino acids; (B) Proposed catalytic cycle.

We found that 1-aminocyclopropane-1-carboxylic acid oxidase from *Petunia hybrida* (ACCO),[217] previously studied by our lab for enantioselective fluorine atom transfer,[210] resulted in the formation of *N*-Boc-L-phenylglycine in good initial activity and enantioselectivity. Furthermore, isopenicillin N synthase from *Emericella nidulans*,[276–278] sharing a similar overall structure and an evolutionarily related nonheme Fe enzyme with ACCO, enable a stereocomplementary synthesis of *N*-Boc-D-phenylglycine in 2.5% yield and 66:34 e.r. (Figure 56).[279,280] Directed evolution of ACCO and IPNS via iterative SSM and screening provided several highly efficient nonheme nitrogen migratases. Among these, $ACCO_{Nim1}$ (ACCO I184A K158T K172V L186V G156E R175P V236G G173R) and $IPNS_{Nim}$ (IPNS V185L I187V S102I R279H) catalyzed the enantioselective amination of prochiral substrates with complementary enantiopreference, enabling highly enantioselective synthesis of either D- or L- arylglycines.

$ACCO_{Nim2}$ (ACCO I184A K158T K172V L186V G156E R175P V236K G173V F250L) allowed the enantioconvergent conversion of racemic azanyl ester substrates with a tertiary C(sp^3)–H bond into α α-disubstituted α-amino acids which are challenging to synthesize via conventional biocatalysis methods based on reductive amination or transamination. $ACCO_{Nim3}$ ($ACCO_{Nim2}$ A248T S246F A180F G156T) catalyzed the asymmetric construction of challenging methyl-ethyl stereocenters via enantioconvergent C(sp^3)–H amination (Figure 56A). $ACCO_{Nim1}$, $IPNS_{Nim}$ and $ACCO_{Nim2}$ demonstrated a broad substrate scope for the enantioselective synthesis of α-monosubstituted and α α-disubstituted non-canonical amino acids. Moreover, this biocatalytic reaction could be carried out on a gram scale using cell-free lysate prepared from 0.5 L expression culture (Figure 56B).

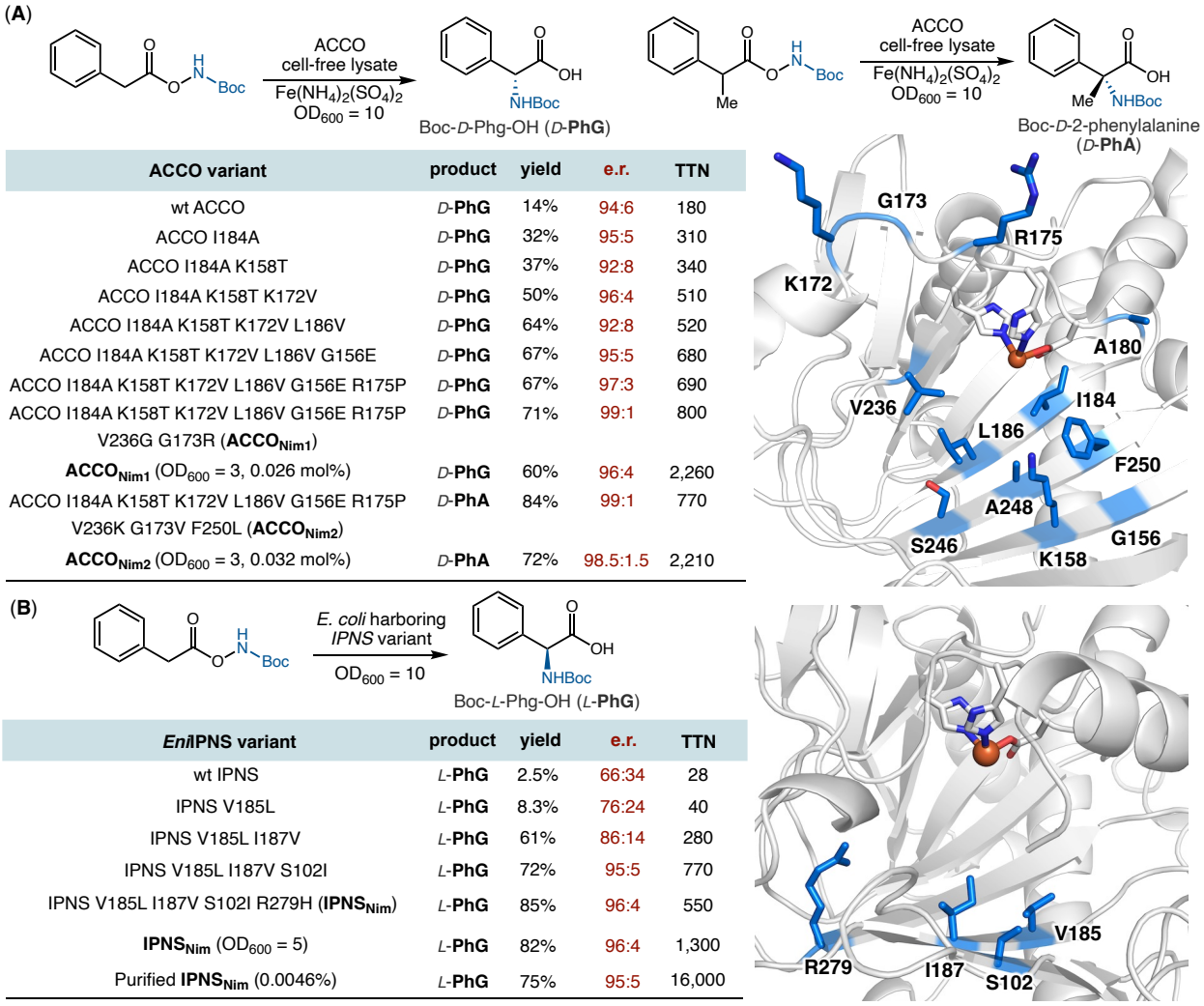

ACCO variant	product	yield	e.r.	TTN
wt ACCO	*D*-**PhG**	14%	94:6	180
ACCO I184A	*D*-**PhG**	32%	95:5	310
ACCO I184A K158T	*D*-**PhG**	37%	92:8	340
ACCO I184A K158T K172V	*D*-**PhG**	50%	96:4	510
ACCO I184A K158T K172V L186V	*D*-**PhG**	64%	92:8	520
ACCO I184A K158T K172V L186V G156E	*D*-**PhG**	67%	95:5	680
ACCO I184A K158T K172V L186V G156E R175P	*D*-**PhG**	67%	97:3	690
ACCO I184A K158T K172V L186V G156E R175P V236G G173R (**ACCO$_{Nim1}$**)	*D*-**PhG**	71%	99:1	800
ACCO$_{Nim1}$ (OD_{600} = 3, 0.026 mol%)	*D*-**PhG**	60%	96:4	2,260
ACCO I184A K158T K172V L186V G156E R175P V236K G173V F250L (**ACCO$_{Nim2}$**)	*D*-**PhA**	84%	99:1	770
ACCO$_{Nim2}$ (OD_{600} = 3, 0.032 mol%)	*D*-**PhA**	72%	98.5:1.5	2,210

*Eni*IPNS variant	product	yield	e.r.	TTN
wt IPNS	*L*-**PhG**	2.5%	66:34	28
IPNS V185L	*L*-**PhG**	8.3%	76:24	40
IPNS V185L I187V	*L*-**PhG**	61%	86:14	280
IPNS V185L I187V S102I	*L*-**PhG**	72%	95:5	770
IPNS V185L I187V S102I R279H (**IPNS$_{Nim}$**)	*L*-**PhG**	85%	96:4	550
IPNS$_{Nim}$ (OD_{600} = 5)	*L*-**PhG**	82%	96:4	1,300
Purified **IPNS$_{Nim}$** (0.0046%)	*L*-**PhG**	75%	95:5	16,000

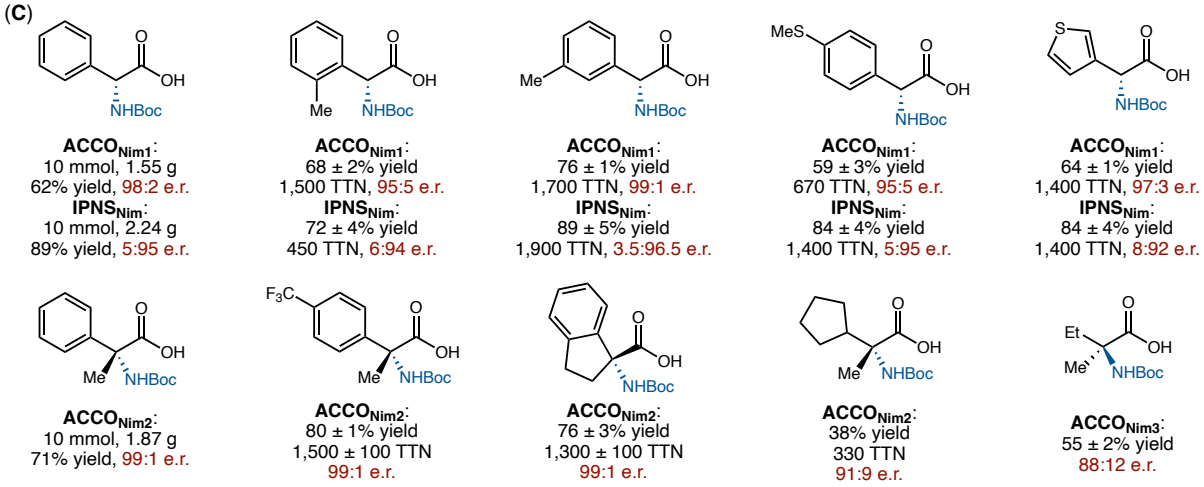

Figure 56. Nonheme Fe enzyme-catalyzed enantioselective 1,3-nitogen migration. (A) Directed evolution of 1,3-nitrogen migratase $ACCO_{Nim1}$ and $ACCO_{Nim2}$ for the enantioselective synthesis

of α-substituted and α α-disubstituted α-amino acids. The illustration of active site was made from 1WA6 (PDB ID); (B) Directed evolution of $IPNS_{Nim}$ for the enantiodivergent synthesis of arylglycines. The illustration of active site was made from 1BK0 (PDB ID); (C) Selected substrate scope of $ACCO_{Nim1}$, $ACCO_{Nim2}$, $ACCO_{Nim3}$ and $IPNS_{Nim}$. Reactions were conducted using cell-free lysate of ACCO (OD_{600} = 5–10) or whole *E. coli* cells overexpressing IPNS (OD_{600} = 5–10).

In our kinetic isotope effect (KIE) studies, for engineered $ACCO_{Nim1}$ a k_H/k_D value of (5.5 ± 0.3) was observed with azanyl ester and azanyl ester-d_2, indicating that the C(sp^3)–H cleavage via 1,5-hydrogen atom transfer is irreversible and is involved in the rate-determining step. By contrast, the engineered enantiopreference-switching migratase $IPNS_{Nim}$ gave a k_H/k_D value of (1.11 ± 0.09), suggesting a shift in rate-determining step between these two engineered nonheme Fe enzymes. (Figure 57A). Furthermore, intramolecular KIE studies with enantioenriched (*R*)-azanyl ester-d_1 and (*S*)-azanyl ester-d_1 were carried out using $ACCO_{Nim1}$, $IPNS_{Nim}$ and $ACCO_{Nim2}$. A similar k_H/k_D value was observed for the enantioselective nitrogen migratase $ACCO_{Nim1}$, providing a near-zero $\Delta G_{enantioselectivity}$ based on the free energy analysis of the HAT process (Figure 57B).[281] This finding suggests that $ACCO_{Nim1}$ evolved for the secondary C(sp^3)–H amination is almost non-enantioselective for hydrogen atom transfer. In contrast, for $ACCO_{Nim2}$, a large of k_H/k_D value of 9.3 ± 0.8 was observed for (*R*)-azanyl ester-d_1, whereas a smaller value of 2.1 ± 0.1 was detected for (*S*)-azanyl ester-d_1 (Figure 57C). This disparity corresponds to a modest $\Delta G_{enantioselectivity}$ and an e.r. of 67:33, suggesting a small degree of enantioselectivity during the HAT step. Strikingly, $IPNS_{Nim}$ showed a highly enantioselective HAT step, with a k_H/k_D value of 24 for (*R*)-azanyl ester-d_1 and only 0.11 for (*S*)-azanyl ester-$d_1$corresponding to a significant $\Delta G_{enantioselectivity}$ and an e.r. of 94:6 (Figure 57D). Computational studies using density functional theory (DFT) calculations and molecular dynamics (MD) simulations showed that IPNS and ACCO adopt two different substrate

binding modes, including a nitrene *trans*-to-His mode and a nitrene-*trans*-to-carboxylate mode, respectively. Classical MD simulations shed light on important interactions between the substrate and active-site residues that control the substrate binding mode and enantioselectivity. We note that important related studies from Pan using the streptavidin-biotin technology[282] has led to ArMs to allow for the same enantioselective nitrogen migration reactions.[283]

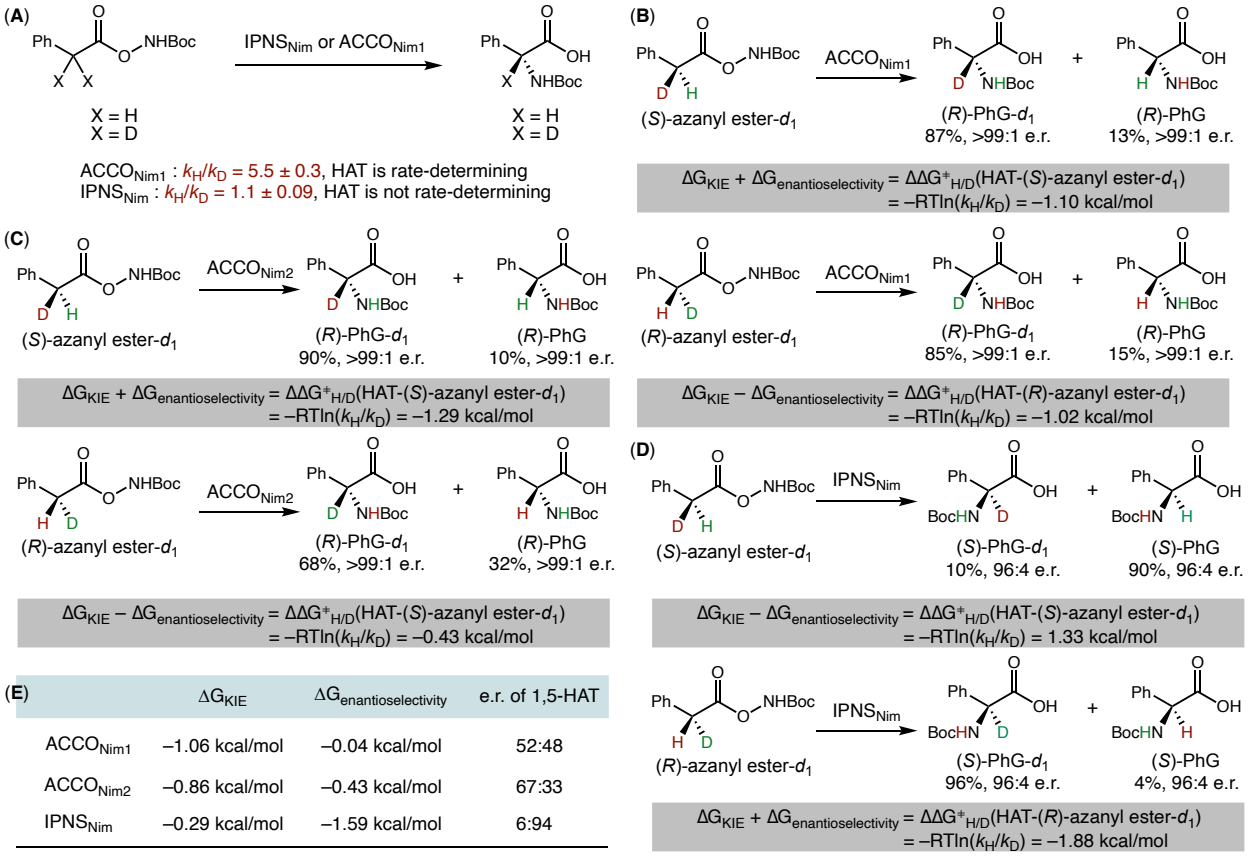

(E)

	ΔG_KIE	ΔG_enantioselectivity	e.r. of 1,5-HAT
ACCO_Nim1	–1.06 kcal/mol	–0.04 kcal/mol	52:48
ACCO_Nim2	–0.86 kcal/mol	–0.43 kcal/mol	67:33
IPNS_Nim	–0.29 kcal/mol	–1.59 kcal/mol	6:94

Figure 57. Mechanistic studies. (A) KIE determined by independently measured initial rates of **1a** and **1a**-d_2.; (B) Intramolecular KIE studies with enantiopure (*R*)-azanyl ester-d_1 and (*S*)-azanyl ester-d_1 using ACCO$_{Nim1}$; (C) Intramolecular KIE studies with enantiopure (*R*)-azanyl ester-d_1 and (*S*)-azanyl ester-d_1 using ACCO$_{Nim2}$; (C) Intramolecular KIE studies with enantiopure (*R*)-azanyl ester-d_1 and (*S*)-azanyl ester-d_1 using IPNS$_{Nim}$; (E) Dissecting the KIE and enzymatic enantio-induction effects by quantitative free energy analysis.

After our initial report,[279] Xiao/Huang[284] and Zhao[285] also reported nonheme Fe enzymes for nitrogen migration using azanyl esters with a different, methoxycarbonyl N-protecting group (Figure 58). In Xiao and Huang's work, a triple mutant of isopenicillin *N* synthase from *Aspergillus nidulans*[276–278] (*Ani*IPNS Y91G I187H T331V) was engineered to provide *N*-COOMe-D-phenylglycine in 72% yield and 98% ee with a TTN of 1281 (Figure 58A). In Zhao and Chen's work, a double mutant of leucoanthocyanidin dioxygenase from *Arabidopsis thaliana*[286] (*At*LDOX F304L T239S) was engineered to afford the same product in 81% yield and 97:3 e.r. with a TTN of 850 (Figure 58B). We also note that important related studies from Pan using the streptavidin-biotin technology[282] has led to ArMs to allow for the same enantioselective nitrogen migration reactions.[283] These excellent contributions further highlight the versatility of non-heme iron enzymes in enabling the non-native transformations.

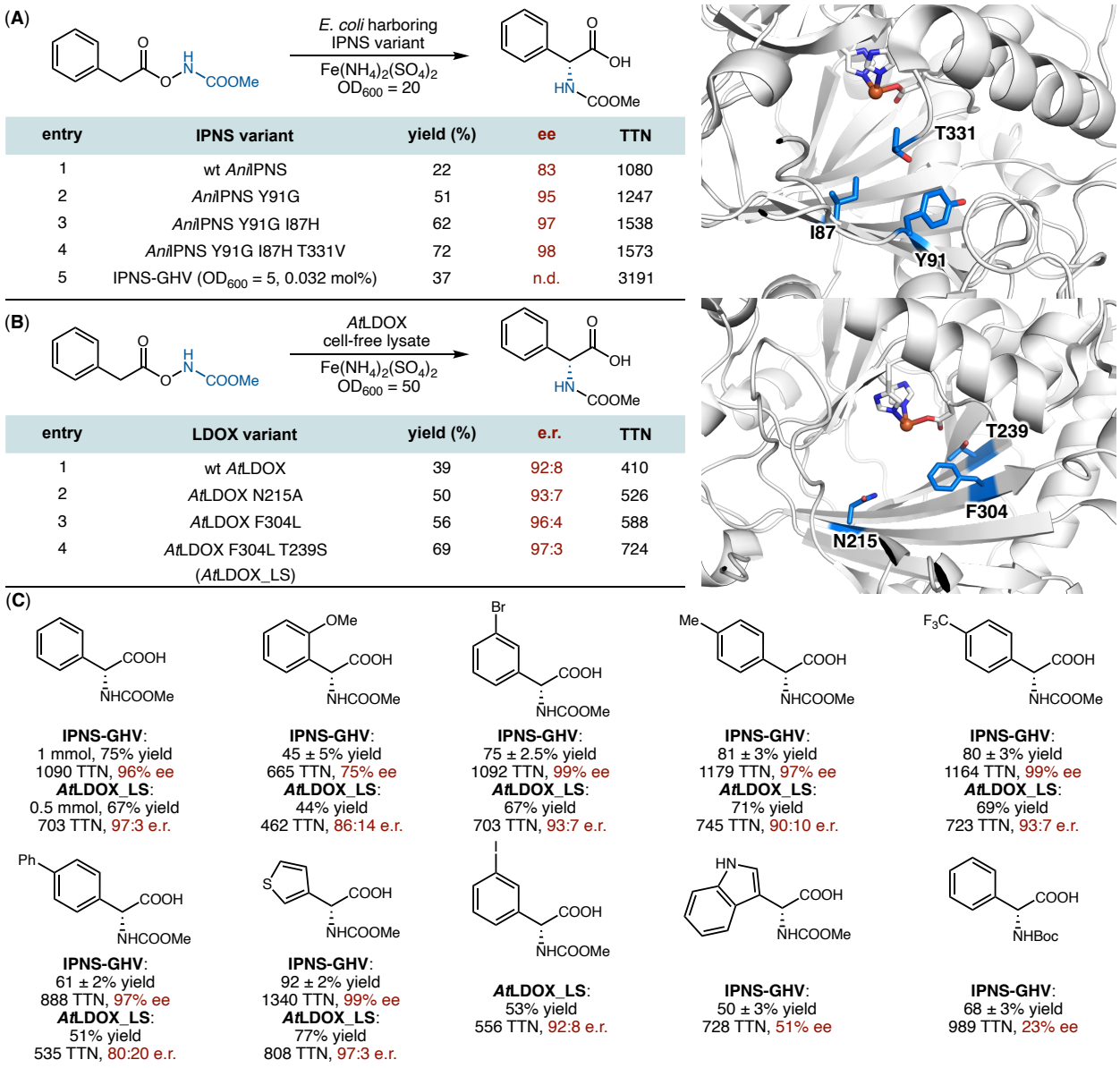

entry	IPNS variant	yield (%)	ee	TTN
1	wt *Ani*IPNS	22	83	1080
2	*Ani*IPNS Y91G	51	95	1247
3	*Ani*IPNS Y91G I87H	62	97	1538
4	*Ani*IPNS Y91G I87H T331V	72	98	1573
5	IPNS-GHV (OD_{600} = 5, 0.032 mol%)	37	n.d.	3191

entry	LDOX variant	yield (%)	e.r.	TTN
1	wt *At*LDOX	39	92:8	410
2	*At*LDOX N215A	50	93:7	526
3	*At*LDOX F304L	56	96:4	588
4	*At*LDOX F304L T239S (*At*LDOX_LS)	69	97:3	724

IPNS-GHV:
1 mmol, 75% yield
1090 TTN, 96% ee
***At*LDOX_LS**:
0.5 mmol, 67% yield
703 TTN, 97:3 e.r.

IPNS-GHV:
45 ± 5% yield
665 TTN, 75% ee
***At*LDOX_LS**:
44% yield
462 TTN, 86:14 e.r.

IPNS-GHV:
75 ± 2.5% yield
1092 TTN, 99% ee
***At*LDOX_LS**:
67% yield
703 TTN, 93:7 e.r.

IPNS-GHV:
81 ± 3% yield
1179 TTN, 97% ee
***At*LDOX_LS**:
71% yield
745 TTN, 90:10 e.r.

IPNS-GHV:
80 ± 3% yield
1164 TTN, 99% ee
***At*LDOX_LS**:
69% yield
723 TTN, 93:7 e.r.

IPNS-GHV:
61 ± 2% yield
888 TTN, 97% ee
***At*LDOX_LS**:
51% yield
535 TTN, 80:20 e.r.

IPNS-GHV:
92 ± 2% yield
1340 TTN, 99% ee
***At*LDOX_LS**:
77% yield
808 TTN, 97:3 e.r.

***At*LDOX_LS**:
53% yield
556 TTN, 92:8 e.r.

IPNS-GHV:
50 ± 3% yield
728 TTN, 51% ee

IPNS-GHV:
68 ± 3% yield
989 TTN, 23% ee

Figure 58. Nonheme Fe enzyme-catalyzed enantioselective 1,3-nitogen migration using methoxycarbonyl group protected azanyl esters. (A) Directed evolution of IPNS-GHV. The illustration of active site was made from 1W05 (PDB ID); (B) Directed evolution of *At*LDOX_LS. The illustration of active site was made from 1GP5 (PDB ID); (C) Selected substrate scope of IPNS-GHV and *At*LDOX_LS. Reactions were conducted using whole *E. coli* cells overexpressing IPNS (OD_{600} = 30) or cell-free lysate of *At*LDOX_LS (OD_{600} = 50).

Inspired by olefin difunctionalization using Fe-nitrene intermediates,[287–290] in 2025, Huang[291] and Jia[292] each reported nonheme Fe enzyme-catalyzed enantioselective aminoazidation of alkenes. In Huang's work, a septuple mutant of 4-hydroxymandelate synthase from *Amycolatopsis orientalis* (*Ao*HMS Q305H T214L L303A F330T V203C I335W G331W, denoted *Ao*HMS$_{AmAz}$) was engineered to afford the (*R*)-aminoazidation product in 44% yield and 95.5:4.5 e.r. using *p*-methoxystyrene as the substrate and *O*-pivaloylhydroxylamine triflic acid (PONT) as the nitrene precursor (Figure 59A). Jia engineered a quintuple mutant of *Bacillus subtilis* quercetin 2,3-dioxygenase (*Bs*QueD ΔK174 S116R T118A I71L L51V, denoted *Bs*QueD$_{AF}$), allowing (*S*)-2-aminoazidation product to form in 9.6% yield and 96:4 e.r. (Figure 59B). Upon further optimization of reaction conditions, whole-cell transformation afforded the product in 49%, 174 TTN and 97:3 e.r.. Engineered *Bs*QueD tolerated styrenes bearing electron-donating or electron-withdrawing substituents (Figure 59C and 59D). In addition, *Bs*QueD also catalyzed thiocyanation and isocyanation, with the resulting products being intramolecularly trapped by amines to furnish the corresponding chiral 2-aminothiazolines and 2-aminooxazolines (Figure 59E).

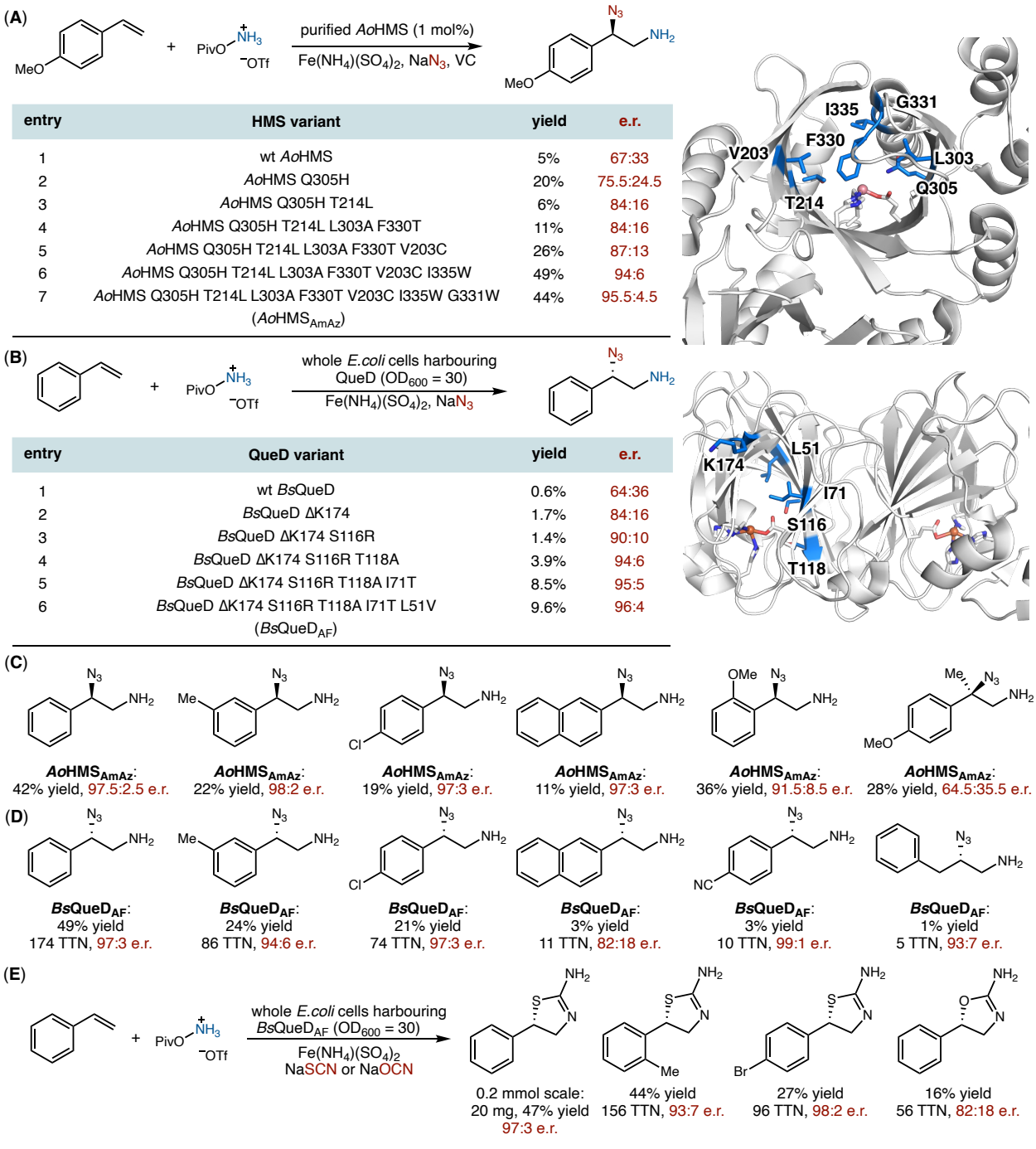

entry	HMS variant	yield	e.r.
1	wt *Ao*HMS	5%	67:33
2	*Ao*HMS Q305H	20%	75.5:24.5
3	*Ao*HMS Q305H T214L	6%	84:16
4	*Ao*HMS Q305H T214L L303A F330T	11%	84:16
5	*Ao*HMS Q305H T214L L303A F330T V203C	26%	87:13
6	*Ao*HMS Q305H T214L L303A F330T V203C I335W	49%	94:6
7	*Ao*HMS Q305H T214L L303A F330T V203C I335W G331W (*Ao*HMS$_{AmAz}$)	44%	95.5:4.5

entry	QueD variant	yield	e.r.
1	wt *Bs*QueD	0.6%	64:36
2	*Bs*QueD ΔK174	1.7%	84:16
3	*Bs*QueD ΔK174 S116R	1.4%	90:10
4	*Bs*QueD ΔK174 S116R T118A	3.9%	94:6
5	*Bs*QueD ΔK174 S116R T118A I71T	8.5%	95:5
6	*Bs*QueD ΔK174 S116R T118A I71T L51V (*Bs*QueD$_{AF}$)	9.6%	96:4

Figure 59. Nonheme Fe enzyme-catalyzed enantioselective aminative difunctionalization of alkenes. (A) Directed evolution of *Ao*HMS. The illustration of active site was made from 2R5V (PDB ID); (B) Directed evolution of *Bs*QueD. The illustration of active site was made from 1Y3T (PDB ID); (C) Selected substrate scope of *Ao*HMS$_{AmAz}$. Reactions were conducted using purified

enzymes (1–2 mol%); (D) Selected substrate scope for aminoazidation; reactions were conducted using whole *E. coli* cells overexpressing *Bs*QueD$_{AF}$ (OD_{600} = 32); (E) Selected substrate scope for synthesis of chiral 2-aminothiazolines and 2-aminooxazolines; reactions were conducted using whole *E. coli* cells overexpressing *Bs*QueD$_{AF}$ (OD_{600} = 32).

6. Transformations involving metal carbenoids with radical character on the carbenoid carbon

Transition-metal carbenoids represent versatile intermediates underlying a variety of synthetically useful transformations.[293–295] Since the pioneering work from the Arnold lab documented the first examples of heme protein-catalyzed cyclopropanation in 2013,[296] a wide range of heme protein catalysts have been developed to enable diverse carbene transfer reactions,[60–63] including C–H insertion,[297] N–H insertion,[298] Si–H insertion,[299] B–H insertion,[300] cyclopropanation,[301] cyclopropenation,[302] bicyclobutanation[303], and various rearrangement reactions.[304] These advances prior to 2020 have been comprehensively reviewed elsewhere.[60–63] Previous studies showed that these Fe carbenoid species can be described as Fe(III)-bound carbon-centered radical, as their open shell singlet (OSS) state were shown to be the most stable spin state. Herein, we review carbene transfer reactions proceeding through a stepwise radical mechanism, with an emphasis on recent studies that appeared after 2021. Carbene transfer reactions that are not proposed to proceed via a stepwise radical mechanism are not covered by this review, although it is also possible for these processes to involve radical intermediates. We refer our readers to other excellent recent reviews that focus on biocatalytic carbene transfer chemistry.[60–63]

6.1 Heme protein-catalyzed cyclopropanation

In 2022, Arnold and co-workers developed a biocatalytic carbene transfer using diazirines[305] as carbene precursors, expanding the scope of biocatalytic carbene transfer beyond the use of diazo compounds (Figure 60).[306] Using 3-phenyl-3H-diazirine lacking an electron-withdrawing α-substituent, a protoglobin variant *Ape*Pgb W59L Y60V F145Q catalyzed the enantioselective cyclopropanation of acrylate in <1% yield with a 2:1 *cis*:*trans* ratio. Subsequent directed evolution led to the introduction of seven beneficial mutations, including V63R, I149L, C45G, C102S, V60A, G61V and F175L, resulting in *Ape*Pgb GLAVRSQLL. This evolved *Ape*Pgb variant delivered the cyclopropane product in 28% yield, with a 6:1 d.r. and 86:14 e.r., representing a >150-fold improvement relative to *Ape*Pgb LVQ (Figure 60A and 60B). *Ape*Pgb GLAVRSQLL also catalyzed N–H insertion and Si–H insertion reactions with varying activities (Figure 60C).

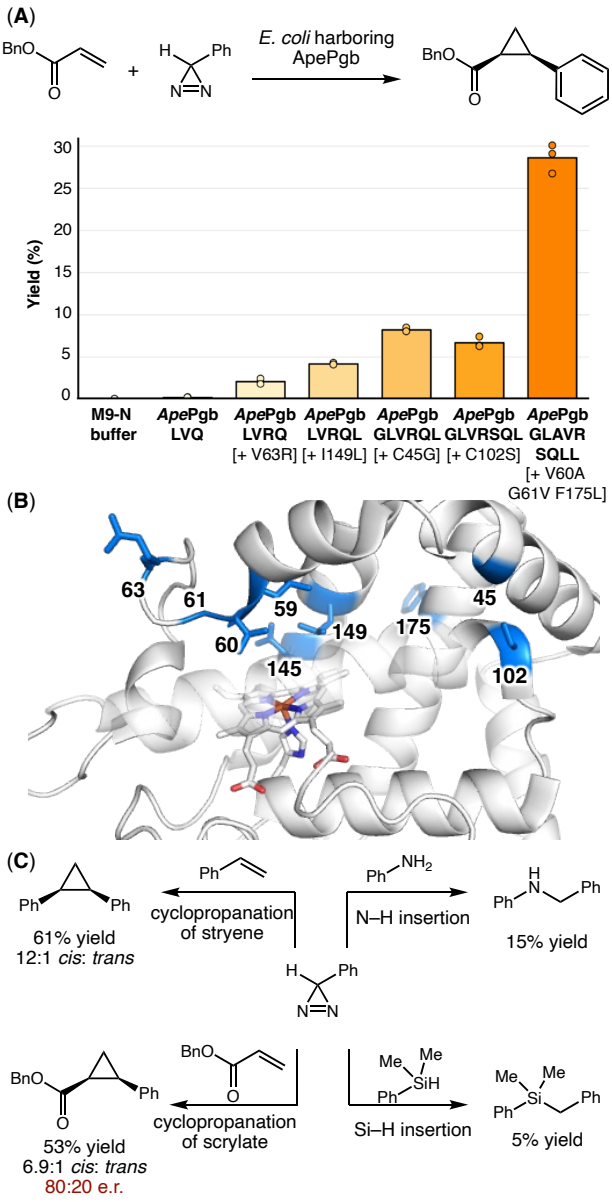

Figure 60. *Ape*Pgb-catalyzed enantioselective cyclopropanation using diazirines as the carbene precursors. (A) Evolution trajectory of *Ape*Pgb GLAVRSQLL for cyclopropanation; (B) The illustration of active site was made from 7UTE (PDB ID); (C) Substrate promiscuity of the new evolved *Ape*Pgb GLAVRSQLL variant using diazirine as the carbene precursor. Adapted with permission from *J. Am. Chem. Soc.* **2022**, *144*, 8892–8896. Copyright 2022 American Chemical Society.

Trapping experiments using dibenzocyclooctyne revealed that a [3+2] cycloaddition adduct[307] formed in the presence *Ape*Pgb GLAVRSQLL, suggesting that a diazo compound was likely generated in situ (Figure 61A). Computational studies[308] suggested that the diazo intermediate likely arises from an enzyme-catalyzed isomerization. Additionally, the cyclopropanation may proceed via a stepwise diradical mechanism (Figure 61B).

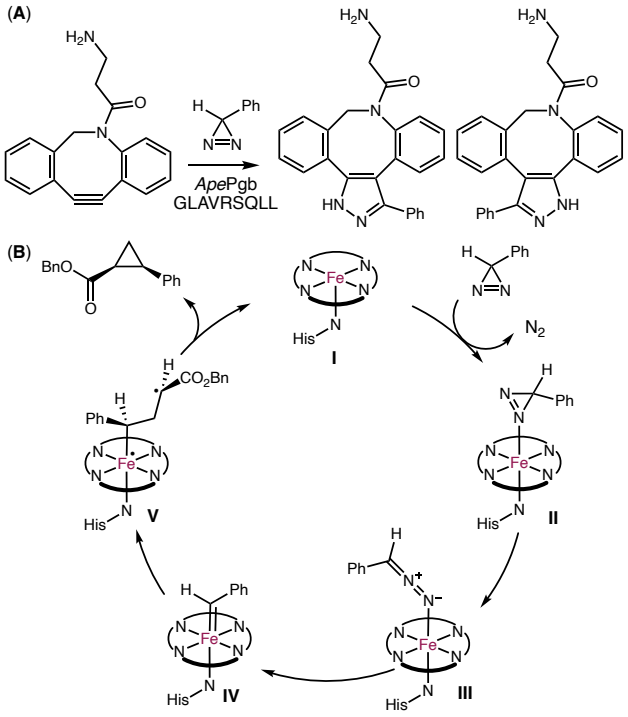

Figure 61. Mechanistic studies. (A) Reaction of dibenzocyclooctyne amine with phenyldiazomethane. (B) Proposed mechanism for the biocatalytic carbene transfer reaction using diazirines.

In 2023, Arnold, Huang and co-workers reported the biocatalytic enantioselective synthesis of *cis*-trifluoromethyl-substituted cyclopropanes using an engineered protoglobin,[309] complementing the existing method for *trans*-cyclopropane synthesis (Figure 62).[310] Building

upon the previous work from the Arnold lab on the synthesis of *cis*-cyclopropanes from unactivated alkanes and ethyl diazoacetate, a protoglobin from *Aeropyrnum pernix*[250] was found to catalyze the formation of *cis*-product with 110 TTN and 87:13 d.r.. Subsequent rounds of SSM and screening introduced two beneficial mutations, W59L and Y60Q, into *Ape*Pgb, resulted in a 3.8-fold improvement in activity. *Ape*Pgb Y60G F73W furnished *trans*-product with 20 TTN. The key mutations controlling stereoselectivity could be transferred to homologous proteins to allow similar diastereocontrol to be achieved. For example, a protoglobin from *Methanosarcina acetivorans* (*Ma*Pgb)[311,312] with 57% sequence identify of *Ape*Pgb showcased the utility of transfer of mutations. *Ma*Pgb LQ afforded the *cis*-product in 360 TTN and 98:2 d.r., while *Ma*Pgb GW produced the *trans*-product in 270 TTN and 92:8 d.r. (Figure 62A–C). *Ma*Pgb LQ catalyzed the cyclopropanation of diverse alkenes, including electron-rich and electron-deficient styrenes, unactivated alkenes and heteroatom-substituted alkenes (Figure 62D).

DFT calculations indicate that the reaction of benzyl acrylate and trifluorodiazoethane proceeds via a radical-mediated stepwise mechanism, due to the strong electron-withdrawing effects of the CF_3 group on the Fe carbenoid intermediate and the electron-deficient nature of acrylates used. C–C bond formation resulting from the addition of Fe carbenoid to the C=C double bond is rate-determining.

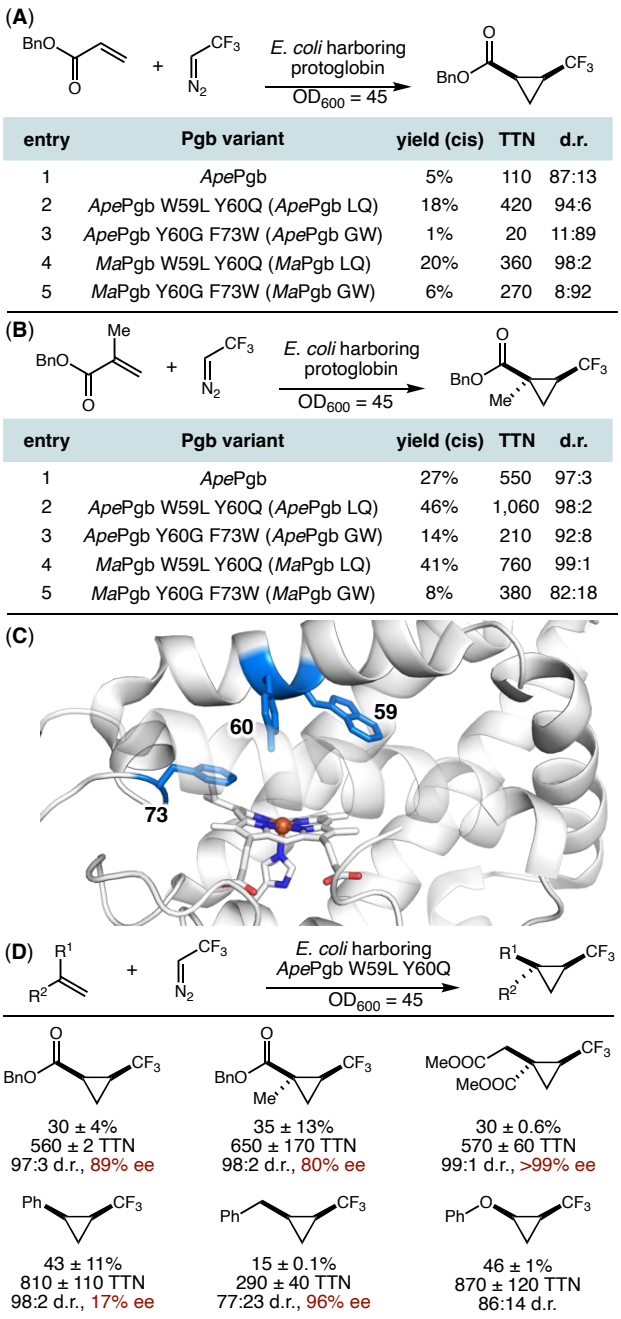

entry	Pgb variant	yield (cis)	TTN	d.r.
1	*Ape*Pgb	5%	110	87:13
2	*Ape*Pgb W59L Y60Q (*Ape*Pgb LQ)	18%	420	94:6
3	*Ape*Pgb Y60G F73W (*Ape*Pgb GW)	1%	20	11:89
4	*Ma*Pgb W59L Y60Q (*Ma*Pgb LQ)	20%	360	98:2
5	*Ma*Pgb Y60G F73W (*Ma*Pgb GW)	6%	270	8:92

entry	Pgb variant	yield (cis)	TTN	d.r.
1	*Ape*Pgb	27%	550	97:3
2	*Ape*Pgb W59L Y60Q (*Ape*Pgb LQ)	46%	1,060	98:2
3	*Ape*Pgb Y60G F73W (*Ape*Pgb GW)	14%	210	92:8
4	*Ma*Pgb W59L Y60Q (*Ma*Pgb LQ)	41%	760	99:1
5	*Ma*Pgb Y60G F73W (*Ma*Pgb GW)	8%	380	82:18

Figure 62. Protoglobin-catalyzed stereoselective cyclopropanation using α-trifluoromethyl diazo substrates. (A) Diastereo-divergent biocatalytic cyclopropanation of benzyl acrylate; (B) Cyclopropanation of benzyl methacrylate; (C) The illustration of active site of *Ma*Pgb was made from 2VEB (PDB ID). (D) Selected substrate scope of *Ape*Pgb LQ-catalyzed cyclopropanation

using α α α-trifluorodiazoethane. The absolute stereochemistry of cyclopropane products was not determined.

For benzyl methacrylate, all variants provided the *cis*-cyclopropane as the major product (Figure 62B). Restrained MD simulations in *Ma*Pgb LQ and GW variants suggest that key active-site residues control the orientation of the Fe carbenoid intermediate. For both benzyl acrylate and benzyl methacrylate, *Ma*Pgb LQ favored *pro-cis* near-attack conformations due to preorganization and steric constraints. In contrast, *Ma*Pgb GW adopted an alternative Fe carbenoid orientation with benzyl acrylate, leading to *trans*-selectivity. With the bulkier benzyl methacrylate, steric hindrance forced the GW variant to adopt *pro-cis* conformations, consistent with the observed shift in diastereoselectivity.

In 2024, Fasan and co-workers reported a myoglobin-catalyzed intramolecular cyclopropanation of benzothiophenes and related heterocycles to synthesize the sp^3-rich tetracyclic compounds (Figure 63).[313] A myoglobin variant bearing five beneficial mutations H64F V68G I107A F43I F46L ($Mb_{BTIC-C2}$) converted benzo[*b*]thiophen-2-ylmethyl 2-diazoacetate into the desired product in 75% yield and >99% ee. The introduction of H64V and V68G mutations improved the enantioselectivity, while I107A, F43I and F46L enhanced catalytic activity by approximately 20-fold (Figure 63A and 63C). Although $Mb_{BTIC-C2}$ demonstrated good substrate compatibility for the cyclopropanation of a C2-functionalized benzothiophene, it was ineffective in the transformation of C3-functionalized benzothiophene. Further Mb variant screening led to Mb H64V V68A, allowing the product to form in 23% yield and >99% ee. Further protein engineering provided Mb H64V V68A L29F I107L ($Mb_{BTIC-C3}$) as the optimal carbene transferase for the cyclopropanation of C3-functionalized benzothiophenes (Figure 63B and 63C). After further optimization of reaction conditions, 3-substituted thiophene derivatives were transformed

into tetracyclic products in 99% yield and >99% ee under 4 °C with slow addition of the substrate. Both $Mb_{BTIC\text{-}C2}$ and $Mb_{BTIC\text{-}C3}$ exhibited excellent enantioselectivity and functional group tolerance in the stereoselective cyclopropanation of benzothiophene or benzofuran substrates bearing diazo ester groups at the C2 or C3 position (Figure 63D).

(A)

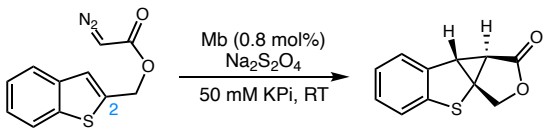

entry	Mb variant	yield	ee
1	wild-type **Mb**	0	-
2	Mb H64F	2%	61
3	Mb H64F V68G	4%	>99
4	Mb H64F V68G I107A	46%	>99
5	Mb H64F V68G I107A	75%	>99
6	F43I F46L (**BTIC-C2**)		
7	Mb H64F V68G I107A F43I	31%	>99
	Mb H64F V68G I107A F46L	35%	>99

(B)

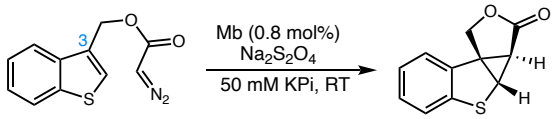

entry	Mb variant	yield	ee
1	wild-type **Mb**	0	-
2	**BTIC-C2**	0	-
3	Mb H64V	0	-
4	Mb V68G	0	-
5	Mb H64V V68A	23%	>99
6	Mb H64V V68A L29F	55%	>99
7	Mb H64V V68A L29F	60%	>99
	I107L (**BTIC-C3**)		

(C)

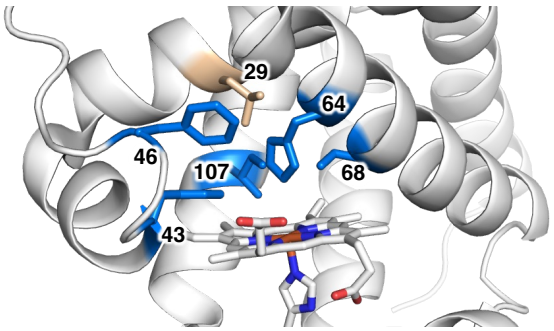

(D)

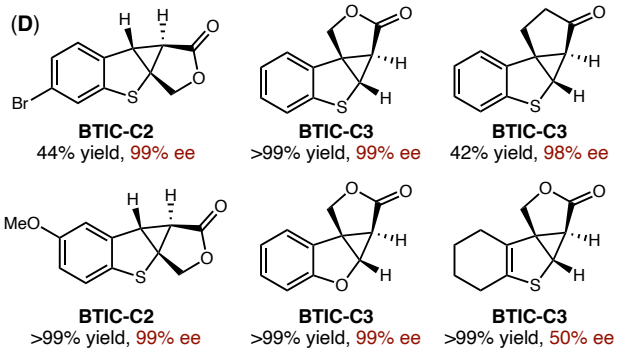

BTIC-C2
44% yield, 99% ee

BTIC-C3
>99% yield, 99% ee

BTIC-C3
42% yield, 98% ee

BTIC-C2
>99% yield, 99% ee

BTIC-C3
>99% yield, 99% ee

BTIC-C3
>99% yield, 50% ee

Figure 63. Myoglobin-catalyzed enantioselective intramolecular cyclopropanation of benzofurans and benzothiophenes. (A) Directed evolution of $Mb_{BTIC\text{-}C2}$ for cyclopropanation of C2-

functionalized benzothiophene; (B) Directed evolution of $Mb_{BTIC-C3}$ for cyclopropanation of C3-functionalized benzothiophene; (C) The illustration of active site was made from 1JW8 (PDB ID); (D) Selected substrate scope using 0.8 mol% purified enzyme.

In 2023, Arnold and co-workers reported a P411-catalyzed kinetic resolution cyclopropanation, enabling the stereoselective synthesis of 1,2,3-polysubstituted cyclopropanes and the recovery of (*E*)-enol acetates from a mixture of (*Z*/*E*)-olefins (Figure 64).[314] They initiated the reaction using a 1:1 mixture of (*Z*/*E*)-butyrophenone-derived enol acetate and α-diazoacetonitrile. A previously evolved variant for intramolecular C(sp^3)–H nitrene insertion, P411-INC-5182,[83] was identified as the best active biocatalyst in the initial screen, affording the cyclopropane product in 9% yield and 68 TTN. Further screening of the P411 variants led to the identification of P411-INC-5182 I327P Y263W, which provided the product in 33% yield and 230 TTN. Through iterative rounds of SSM and screening, two additional beneficial mutations, Q437V and N70S, were introduced, generating P411-INC-5185. This final variant delivered the cyclopropane product in 50% yield, 540 TTN, >99:1 d.r. and 95% ee, while the remaining olefin exhibited a *Z*/*E* ratio of 2:98 (Figure 64A and 64B).

(A)

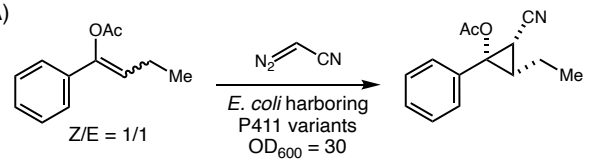

entry	P411 variant	yield	TTN
1	**P411-INC-5182**	9%	68
2	5182 I327P Y263W	33%	230
3	5182 I327P Y263W Q437V	49%	427
4	5182 I327P Y263W Q437V N70S (**P411-INC-5185**)	50%	536

(B)

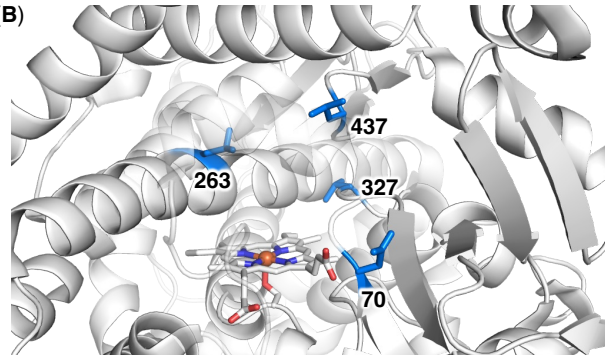

Figure 64. P411-catalyzed enantioselective synthesis of 1,2,3-polisubstituted cyclopropanes. (A) Directed evolution of cyclopropanase P411-INC-5185; (B) The illustration of active site was made from 5UCW (PDB ID).

When stereochemically pure (*Z*)-butyrophenone-derived enol acetate was used as the substrate, P411-INC-5185 catalyzed the reaction to afford the cyclopropane product in 89% yield, 840 TTN, >99:1 d.r. and 95% ee, whereas no conversion was observed for the (*E*)-substrate (Figure 65A). Arnold and coworkers discovered that the W263M mutant of P411-INC-5185 (P411-INC-5186) not only converted (*Z*)-butyrophenone-derived enol acetate into the corresponding cyclopropane but also the (*E*)-butyrophenone-derived enol acetate into α-alkylated ketone (Figure 65B).

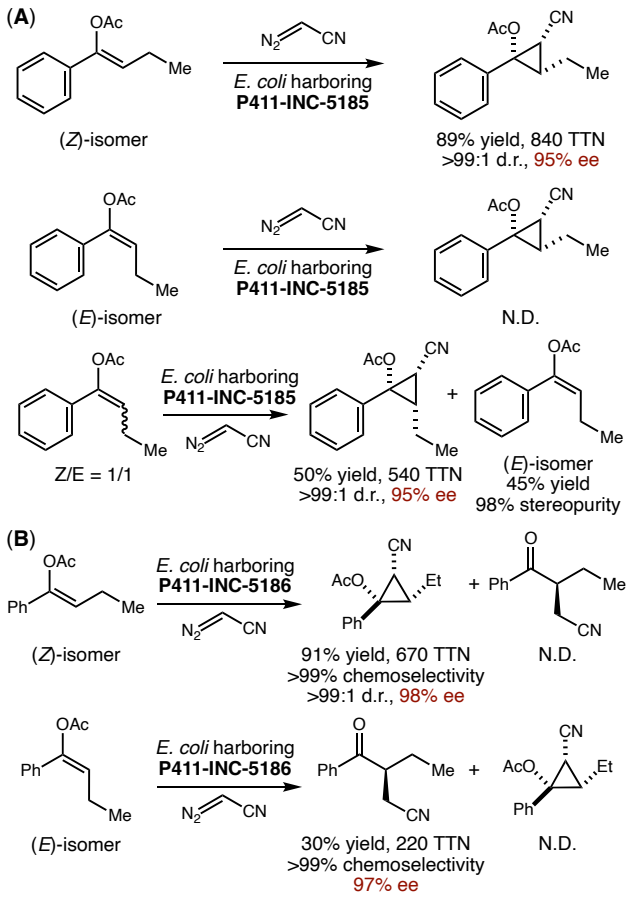

Figure 65. Mechanistic studies. (A) P411-INC-5185-catalyzed enantioselective cyclopropanation of a mixture of (*Z*/*E*)-butyrophenone-derived enol acetate. (B) P411-INC-5186-catalyzed cyclopropanation of (*Z*)-butyrophenone-derived enol acetate and α-alkylation of (*E*)-substrate.

DFT calculations suggest that the cyclopropanation reaction follows a radical-mediated stepwise mechanism. In this computed catalytic cycle, the Fe carbenoid intermediate (**Int-II**) is generated from the heme protein and the diazo substrate. The β-carbon of the electron-rich enol acetate subsequently interacts with the electrophilic carbenoid carbon to form the (*Z*)-Int-III or (*E*)-Int-III intermediate, depending on the specific (*Z*)- or (*E*)-enol acetate being used. The enantioselectivity of the reaction is determined by the formation of the first C–C bond, favoring

the (*S*)-configured stereocenter. (*E*)-Int-III is preferably converted to the α-alkylated product (Figure 66).

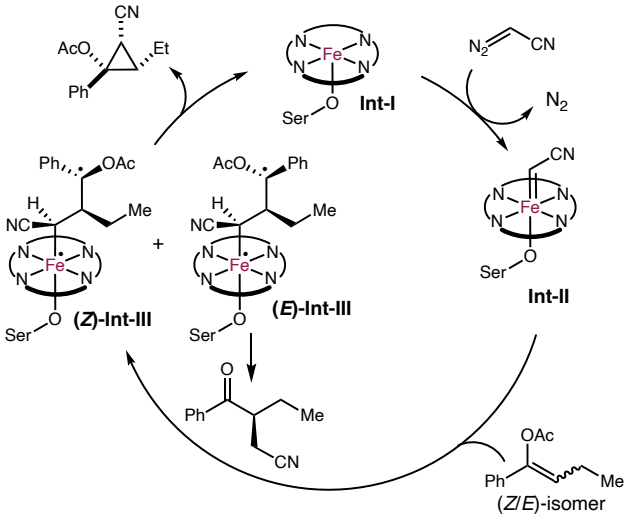

Figure 66. Proposed mechanism of P411-catalyzed enantioselective synthesis of 1,2,3-polisubstituted cyclopropanes.

6.2 C(sp^3)–H insertion

Biocatalytic C(sp^3)–H insertion reactions were first realized by the Arnold group in 2019 using serine-ligated P450 variants ("P411").[297] Since then, the development of P450-catalyzed stereoselective C(sp^3)–H insertion has provided a range of synthetically useful methods.[315–318] While the exact mechanism remains to be further elucidated, both concerted and stepwise mechanisms were proposed in previous reports.[319] In 2024, Fasan and coworkers reported a regiodivergent C–H insertion of indolines with ethyl diazoacetate (EDA) as the carbene precursor via a stepwise radical mechanism using engineered CYP119 variants (Figure 67).[320] A previously engineered mutant CYP119-137 (CYP119 F153G A209G T213G V254A C317S)[316] was found to promote the formation of C–H functionalization products at three different sites, along with other

demethylation/desaturation/N–H insertion products. Directed evolution of this starting variant furnished CYP119-168 (CYP119 F153G T213A V254W C317S) and CYP119-235 (CYP119 F153G L205W T213A V254A C317S), favoring the α- and β-C–H functionalization of the model substrate, respectively (Figure 67A and 67B). A range of indolines with different substituents were converted to the corresponding products with excellent TTN and enantioselectivities using intact *E. coli* cells harboring engineered CYP119. C–H insertion at the *N*-Me group was also observed with CYP119-235 for 5-methylated and 6-methylated indolines. Fasan and Zhang proposed a stepwise radical mechanism supported by DFT calculations. The formation of desaturation, demethylation and N–H insertion side products is also in accord with their proposed stepwise radical mechanism (Figure 67B).

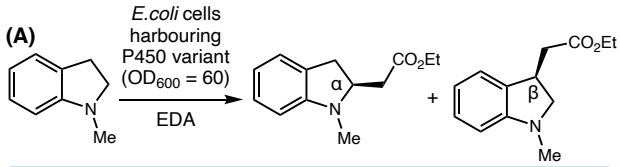

entry	CYP119 variant	e.r.	selectivity α-P:β-P	yield	TTN
1	CYP119 F153A A209G T213G V254A C317S (CYP119-137)	53:47 (α-P)	66:34	17% (α-P)	210 (α-P)
2	CYP119 F153G T213A V254W C317S (CYP119-168)	91:9 (α-P)	92:8	92% (α-P)	5,270 (α-P)
3	CYP119 F153G L205W T213A V254A C317S (CYP119-235)	94:6 (β-P)	16:84	78% (β-P)	5,380 (β-P)

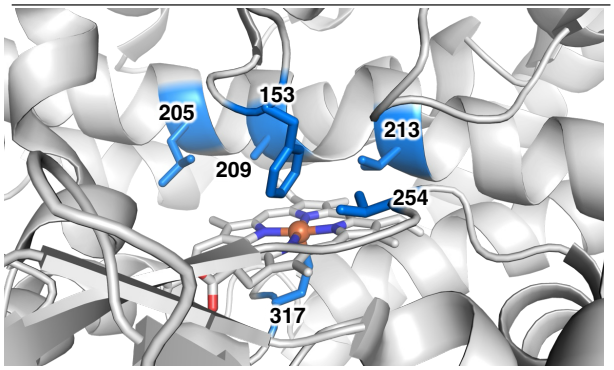

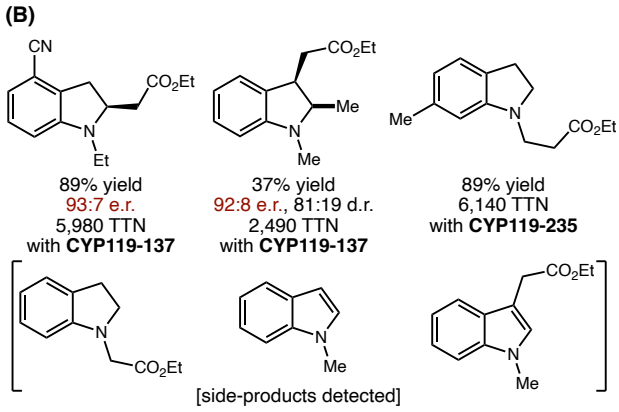

Figure 67. CYP119-catalyzed regio- and enantioselective C–H insertion reactions. (A) The site-selective C–H insertion and engineering of CYP119 variants. The illustration of active site was made from 1T07 (PDB ID); (B) Selected substrate scope and observed side products; reactions were carried out using whole *E. coli* cells overexpressing CYP119 variants (OD_{600} = 60).

7. Summary of recently engineered metalloenzymes for unnatural radical reactions

To date, a range of heme and nonheme enzymes have been used to develop unnatural radical reactions. Due to their excellent evolvability and synthetic versatility of the heme cofactor, cytochromes P450, particularly the self-sufficient $P450_{BM3}$ (CYP102A1) previously exploited for native oxidation chemistry,[33,35] have proven highly valuable in enzyme reprogramming, including the development of asymmetric radical transformations. CYP119 represents another widely used P450 enzymes for unnatural reaction development. Here, we summarize the latest results on P450 repurposing and engineering in the context of unnatural radical-mediated reactions (Table 1). As can be seen from Table 1, active site engineering remains an effective strategy to improve the catalytic activity and stereoselectivity of mechanistically diverse new-to-nature reactions. The fully encapsulated active site and the excellent evolvability of biotechnologically useful P450 enzymes allowed difficult stereocontrol to be readily achieved through active site tuning.

Other than P450s, smaller heme proteins including cytochromes *c* and various globins have also found use in stereoselective radical biocatalysis (Table 1). The thermostable *Rma* cytochrome *c* has been engineered for intermolecular C–C coupling, and key residues are located in the 75–77 α-helix and the 99–103 loop. Sperm whale myoglobin (Mb) and various thermophilic protoglobins are also widely used, particularly in carbene and nitrene transfer processes involving radical intermediates. Additionally, B_{12}-dependent proteins such as CarH* have also emerged as promising biocatalysts, although achieving enantioselective transformations have remained a challenge. Several Cu-dependent metalloenzymes, such as laccase CueO, halogenase ApnU, and cupin protein Lase, have also been found applications in radical-meditated asymmetric transformations through a promiscuous substrate binding activation.

Table 1. Summary of heme proteins and Co/Cu-dependent proteins used in asymmetric radical reactions

entry	engineered enzyme	wt enzyme (Uniprot ID)	developed reaction (Figure number)	mutations relative to wt protein	research group (ref.)
1	$P450_{ATRCase1}$	$P450_{BM3}$ (P14779)	atom transfer radical cyclization (Figure 3)	V78A, **A82T**, F87V, P142S, T175I, **L181F**, A184V, S226R, H236Q, E252G, **I263Q**, **H266T**, T268A, A290V, **T327I**, L353V, I366V, C400S, **T438S**, E442K	Yang[64]
2	$P450_{ATRCase2}$	$P450_{BM3}$ (P14779)	atom transfer radical cyclization (Figure 3)	A74G, V78L, A82L, F87A, P142S, T175I, M177L, **L181V**, A184V, S226R, H236Q, E252G, I263W, T268G, A290V, T**327C**, A328V, L353V, I366V, C**400A**, L437F, **T438Q**, E442K, ΔFAD	Yang[64]
3	$P450_{arc1}$	$P450_{BM3}$ (P14779)	radical cyclization to arenes (Figure 13)	A74G, V78L, A82L, F87A, P142S, T175I, M177L, **L181M**, A184V, S226R, H236Q, E252G, I**263Q**, **H266L**, T268G, A290V, T327P, A328V, L353V, I366V, C400S,	Yang[139]

				T436L, L437F, **T438G**, E442K, ΔFAD	
4	$P450_{arc2}$	$P450_{BM3}$ (P14779)	radical cyclization to arenes (Figure 13)	**N70S**, A**74P**, V**78A**, A82L, F**87G**, P142S, T175I, M177L, A184V, S226R, H236Q, E252G, I263Y, T268G, A290V, T**327P**, A328V, **A330F**, L353V, I366V, C400S, T436L, L**437A**, E442K, ΔFAD	Yang[139]
5	$P450_{arc3}$	$P450_{BM3}$ (P14779)	radical cyclization to arenes (Figure 13)	A74G, V**78C**, A82L, F87A, P142S, T175I, M177L, **L181M**, A184V, S226R, H236Q, E252G, I**263Q**, T268G, A290V, T327P, A**328E**, **S332A**, L353V, I366V, C400S, T436L, L437F, E442K, ΔFAD	Yang[139]
6	$P450_{rad1}$	$P450_{BM3}$ (P14779)	radical dearomatization of indoles (Figure 15)	V**78C**, F87L, P142S, T175I, **L181V**, A184V, S226R, H236Q, P248T, E252G, I263G, T268A, A290V, L353V, I366V, C400S, L**437A**, E442K	Yang[132]

7	$P450_{rad2}$	$P450_{BM3}$ (P14779)	radical dearomatization of pyrroles (Figure 15)	L75A, V78A, **A82V**, F87V, P142S, T175I, L181A, A184V, S226R, H236Q, E252G, T268A, A290V, L353V, I366V, C400S, E442K	Yang[132]
8	$P450_{rad3}$	$P450_{BM3}$ (P14779)	radical dearomatization of pyrroles (Figure 15)	A74G, V78L, A82L, F87A, P142S, T175I, M177L, A184V, S226R, H236Q, E252G, **E267L**, T268A, A290V, L353V, I366V, C400S, T436L, L437F, E442K, ΔFAD	Yang[132]
9	$P450_{rad4}$	$P450_{BM3}$ (P14779)	radical dearomatization of phenols (Figure 15)	A74G, **L75F**, V78C, A82L, F87A, P142S, T175I, M177L, L181M, A184V, S226R, H236Q, E252G, I263Q, T**268P**, A290V, T327P, A328V, L353V, I366V, C400S, T**436A**, L**437P**, E442K, ΔFAD	Yang[132]
10	$P450_{rad5}$	$P450_{BM3}$ (P14779)	radical dearomatization of 2-naphthols (Figure 15)	V78A, F87V, P142S, T175I, A184V, S226R, H236Q, E252G, T268A, A290V, L353V, I366V, C400S, T438S, E442K	Yang[132]

11	$P450_{Smiles1}$	$P450_{BM3}$ (P14779)	radical Smiles rearrangement (Figure 17)	**N70H**, A74G, V78L, A**82C**, F87A, P142S, T175I, M177L, A184V, S226R, H236Q, E252G, **E267R**, T268A, A290V, **A330M**, L353V, I366V, C400S, **I401P**, T**436C**, L437F, E442K, ΔFAD	Yang[147]
12	$P450_{Smiles2}$	$P450_{BM3}$ (P14779)	radical Smiles rearrangement (Figure 17)	**N70H**, A74G, V78L, A**82C**, F87A, P142S, T175I, M177L, A184V, S226R, H236Q, E252G, **E267R**, T268A, A290V, **A330M**, L353V, I366V, C400S, **I401V**, T**436C**, L437F, E442K, ΔFAD	Yang[147]
13	$P450_{BM3}$_LQQ	$P450_{BM3}$ (P14779)	metal-hydride H atom transfer (Figure 10)	**F87L**, **A74Q**, **I263Q**	Ward[130]
14	*i*AMD9	$P450_{BM3}$ (P14779)	intermolecular benzyl C(sp^3)–H amidation (Figure 49)	**N70S**, **A74S**, **V78L**, A**82M**, F87A, P142S, T175I, **L181Q**, A184V, S226R, H236Q, E252G, I263Y, T268G, A290V, A**328T**, L353V, I366V, C400S, **I401L**, **L437I**, T**438Q**, E442K	Arnold[247]

15	P411-SIA-5291	$P450_{BM3}$ (P14779)	intermolecular benzyl C(sp^3)–H amidation (Figure 51)	**R47H**, N**70M**, A74Q, **F77S**, V78L, A82L, F87A, P142S, **E143K**, T175I, A184V, S226T, H236Q, E252V, I**263L**, T268Q, A290V, **T327P**, L353V, I366V, C400A, I401L, **T436A**, E442K, **N573D**, **ΔFAD**	Arnold[262]
16	P411-PYS-5149	$P450_{BM3}$ (P14779)	intramolecular benzyl C(sp^3)–H amination (Figure 38)	**S72W**, **Q73A**, A74G, **L75E**, **F77C**, V78L, A82L, F87A, **M118V**, P142S, T175I, M177L, A184V, S226R, H236Q, E252G, I263Y, H266V, T268G, A290V, T327I, A328V, **A330Q**, L353V, I366V, C400S, T**436R**, E442K	Arnold[238]
17	P411-PYS-5151	$P450_{BM3}$ (P14779)	intramolecular aliphatic C(sp^3)–H amination (Figure 38)	S72W, Q73A, A74G, L75E, F77C, V78L, A82L, F87A, M118V, P142S, T175I, M177L, **L181N**, A184V, S226R, H236Q, E252G, I263Y, H266V, T268G, A290V, T327I, A328V, A330Q,	Arnold[238]

				L353V, I366V, C400S, T436L, **L437P**, E442K	
18	PA-G8	$P450_{BM3}$ (P14779)	propargylic C(sp^3)–H amination (Figure 42)	**S72T**, **A74K**, A78M, A82L, F87A, P142S, T175I, A184V, S226R, H236Q, E252G, I263M, **H266S**, **E267D**, T268P, **T269V**, A290V, A328V, L353V, I366V, **N395C**, C400S, L**437Q**, T**438G**, E442K	Arnold[245]
19	uPA9	$P450_{BM3}$ (P14779)	intermolecular amination of unactivated C(sp^3)–H bonds (Figure 43)	V78M, A82L, F87A, **M118Q**, P142S, T175I, **M177L**, A184V, **L188C**, S226R, H236Q, **D251N**, E252G, I**263L**, E267D, T268P, A290V, T327A, A328V, **A330H**, **L333M**, L353V, I366V, N395R, C400S, **E409S**, I437F, T438S, E442K, **L740H**, **L780P**	Arnold[246]
20	P411-TEA-5274	$P450_{BM3}$ (P14779)	intramolecular benzyl C(sp^3)–H amination (Figure 44)	**S72T**, V78M, A82L, F87A, P142S, T175I, **M177Y**, A184V, S226R, H236Q, E252G, I263M, E267D, T268P,	Arnold[248]

				A290V, T**327V**, A328V, L353V, **M354E**, I366V, N**395V**, **A399G**, C400S, **Q403A**, L437F, T438V, E442K	
21	*u*AMD9	$P450_{BM3}$ (P14779)	intermolecular amidation of unactivated C(sp^3)–H bonds (Figure 43)	N70S, **A74M**, L75Y, V78L, A82L, F87A, P142S, T175I, L181I, A184V, **M212V**, S**226T**, **L233V**, H236Q, E**252V**, I263V, T268G, A290V, A328T, L353V, I366V, **A399S**, C**400A**, I401L, L437F, E442K, **N573D**, **S640P**, **N706T**, **Y707M**, **E708K**, **G709E**, **I710Δ**	Arnold[246]
22	P411-INC-5185	$P450_{BM3}$ (P14779)	cyclopropanation of alkenes (Figure 64)	**N70S**, A74G, V78L, A82L, F87A, P142S, T175I, M177L, A184V, S226R, H236Q, E252G, I**263W**, T268G, A290V, T**327P**, A328V, L353V, I366V, C400S, T436L, L**437V**, E442K, ΔFAD	Arnold[314]
23	aMOx	$P450_{LA1}$ (A0P0F6)	anti-Markovnikov oxidation of alkenes	T121A, N201K, N209S, Y385H,	Arnold

			(Figure 25)	E418G, A103L, M118L, R120H, V123I, I326V, V327M, H385V, M391L	and Hammer[178]
24	KS	$P450_{LA1}$ (A0P0F6)	anti-Markovnikov oxidation of alkenes (Figure 27)	T121V, V123I, N201K, H206A, N209S, I326V, Y385H, E418G, T210V, E282D, R120Q, K393L, V208Q, A117Q, L111Y, V204H, L424W, M274F	Hammer[181]
25	CYP119 MHATase	CYP119 (Q55080)	metal-hydride H atom transfer (Figure 10)	D77R, T214V, L205V, T213G, Q22H, A209T, I208S	Ward[130]
26	CYP119-137	CYP119 (Q55080)	$C(sp^3)$–H insertion (Figure 67)	F153A, A209G, T213G, V254A, C317S	Fasan[320]
27	CYP119-168	CYP119 (Q55080)	$C(sp^3)$–H insertion (Figure 67)	F153G, T213A, V254W, C317S	Fasan[320]
28	CYP119-235	CYP119 (Q55080)	$C(sp^3)$–H insertion (Figure 67)	F153G, L205W, T213A, V254A, C317S	Fasan[320]
29	*Rma* cyt $c^{RLRDGDE}$	*Rma* cyt *c* (B3FQS5)	intermolecular radical C–C cross coupling (Figure 30)	V75R, M76L, M99R, M100D, T101G, M103E	Yang[188]
30	*Rma cyt* $c^{RIKCGPF}$	*Rma* cyt *c* (B3FQS5)	intermolecular radical C–C coupling (Figure 30)	V75R, M76I, M99K, M100C, T101G, D102P, M103F	Yang[188]

31	*Rma cyt c* "TQL"	*Rma* cyt *c* (B3FQS5)	aminohydroxylation of styrenyl olefins (Figure 41)	Y44T, M76Q, T98L, M99V, M100S, T101P, M103G	Arnold[243]
32	*Ap*Pgb *L*-G11	*Ape*Pgb (Q9YFF4)	intermolecular benzylic C(sp^3)–H amination (Figure 46)	W59A, Y60G, F145G, F156L, I97T, F157L, I327T, T97V, H136N, K36E, C45A, K159E, F73W, R90G, G60S	Arnold[249]
33	*Ap*Pgb *D*-G2	*Ape*Pgb (Q9YFF4)	intermolecular benzyl C(sp^3)–H amination (Figure 46)	W59A, Y60G, F145G, F156L, I97T, F157L, I327T, T97V, H136N, K36E, C45A, K159E, F93A, W62G, L86G	Arnold[249]
34	*Ape*Pgb GLAVRSQLL	*Ape*Pgb (Q9YFF4)	cyclopropanation of alkenes with a-CF_3 diazo substrate (Figure 60)	C35G, W59L, Y60A, G61V, V63R, C102S, F145Q, I149L, F175L	Arnold[306]
35	*Ape*Pgb LQ	*Ape*Pgb (Q9YFF4)	cyclopropanation of alkenes with a-CF_3 diazo substrate (Figure 62)	W59L, Y60Q	Arnold[309]
36	*Ape*Pgb GW	*Ape*Pgb (Q9YFF4)	cyclopropanation of alkenes with a-CF_3 diazo substrate (Figure 62)	Y60G, F73W	Arnold[309]
37	*Ma*Pgb LQ	*Ma*Pgb (Q8TLY9)	cyclopropanation with a-CF_3 diazo substrate (Figure 62)	W59L, Y60Q	Arnold and Huang[309]
38	*Ma*Pgb GW	*Ma*Pgb (Q8TLY9)	cyclopropanation with a-CF_3 diazo substrate (Figure 62)	Y60G, F73W	Arnold and Huang[309]

39	*Par*Pgb-HYA-5213	*Par*Pgb (A4WIC7)	intermolecular benzyl C(sp^3)–H amination and aminohydroxylation of styrenes (Figure 47)	Y57D, W59L, V60Q, V85I, I149F, V175A, Q177R	Arnold[252]
40	Mb H93S	Mb (P68082)	atom transfer radical cyclization (Figure 4)	H93S	Bruns[85]
41	Mb H64V V68A (Mb*)	Mb (P68082)	intramolecular benzylic C(sp^3)–H amidation (Figure 50)	H64V, V68A	Fasan[260]
42	Mb^{VAF}	Mb (P68082)	intramolecular benzylic C(sp^3)–H amidation (Figure 52)	H64V, V68A, Y146F	Fasan[263]
43	Mb^{VE}	Mb (P68082)	intramolecular benzylic C(sp^3)–H amidation (Figure 52)	F43V, I107E	Fasan[263]
44	$Mb_{BTIC\text{-}C2}$	Mb (P68082)	intramolecular cyclopropanation of benzothiophenes (Figure 63)	H64F, V68G, I107A, F43I, F46L	Fasan[313]
45	$Mb_{BTIC\text{-}C3}$	Mb (P68082)	intramolecular cyclopropanation of benzothiophenes (Figure 63)	H64V, V68A, L29F, I107L	Fasan[313]
46	HAT_R-5	*Ape*Pgb (Q9YFF4)	biocatalytic asymmetric hydrogenation of olefins (Figure 12)	C45G W59L Y60V V63R F145Q I149L Q145E L69N V89G L59M	Athavale[133]
47	CarH*	CarH (Q746J7)	C(sp^2)–H alkylation of styrenes/intramolecular radical cyclization (Figure 8 and 16)	Apo H132G + N-terminal His_6-MBP tag with hydroxocobalami	Lewis[115,116]

48	CueO	CueO (P36649)	oxidative cross coupling (Figure 36)	-	Zhong[222]
49	ApnU	ApnU (S8B5U1)	$C(sp^3)$–H chlorination, bromination, iodination, azidation and thiocyanation (Figure 19)	-	Tang[163]
50	$LAse^S$	*Tm*1287 (Q9X113)	enantiodivergent radical alkylation (Figure 28)	E68A R23Y M22F	Huang[182]
51	$LAse^R$	*Tm*1459 (Q9X1H0)	enantiodivergent radical alkylation (Figure 28)	H52G F104V	Huang[182]

The past five years have witnessed exciting progress in developing nonheme enzymes-catalyzed stereoselective radical reactions that were previously unknown in nature (Table 2). Compared with heme enzymes, nonheme enzymes offer more diverse coordination chemistry, multiple open coordination sites, and greater flexibility in metal ion substitution. Given the short history of engineering nonheme enzymes for synthetically valuable transformations, substantial advances are likely in the coming decade. Interestingly, in recently developed radical rebound reactions forming C–F, C–N_3, C–NCS, C–NCO, and C–SCN bonds, highly active nonheme Fe enzymes including ACCO, HPPE, HPPD, HMS, QueD and MPC are not αKG dependent in their native function. This suggests that certain structural features of these enzymes could be exploited for the discovery of new nonheme biocatalysts for unnatural transformations.

Table 2. Summary of nonheme Fe enzyme variants used in asymmetric radical reactions.

entry	engineered enzyme (Figure number)	wt enzyme (Uniprot ID)	native function (metal center)	coordinated residues	Developed reaction (metal center)	research group (ref.)
1	$ACCO_{CHF}$ (Figure 34)	ACCO (Q08506)	1-Aminocyclopropane-1-carboxylic acid oxidase (Fe)	H177, D179, H234	$C(sp^3)$–H fluorination (Fe)	Yang[210]
2	$ACCO_{Nim}$ (Figure 56)	ACCO (Q08506)	1-aminocyclopropane-1-carboxylic acid oxidase (Fe)	H177, D179, H234	1,3-nitrogen migration (Fe)	Yang[273]
3	$IPNS_{Nim}$ (Figure 56)	IPNS (P05326)	isopenicillin N synthase (Fe)	H214, D216, H270	1,3-nitrogen migration (Fe)	Yang[280]
4	IPNS-GHV (Figure 57)	IPNS (P05326)	isopenicillin N synthase (Fe)	H214, D216, H270	1,3-nitrogen migration (Fe)	Xiao[284]
5	*At*LDOX_LS (Figure 57)	LDOX (Q963232)	leucoanthocyanidin dioxygenase (Fe)	H232, D234, H288	1,3-nitrogen migration (Fe)	Zhao[285]
6	*Pp*MPC azidase (Figure 22)	*Pp*MPC (P06622)	Metapyrocatechase (Fe)	H153, H214, E265	decarboxylative radical azidation (Fe)	Yang[168]
7	*Pp*MPC thiocyanase (Figure 22)	*Pp*MPC (P06622)	Metapyrocatechase (Fe)	H153, H214, E265	decarboxylative radical thiocyanation, and isocyanation (Fe)	Yang[168]
8	*Ao*HMS-CF_3 (Figure 5)	*Ao*HMS (O52791)	hydroxymandelate synthase (Fe)	H161, H241, E320	trifluoromethylazidation of alkenes (Fe)	Huang[92]

9	*Ao*HMS$_{AmAz}$ (Figure 59)	*Ao*HMS (O52791)	hydroxymandelate synthase (Fe)	H161, H241, E320	aminoazidation of alkenes (Fe)	Huang[291]
10	*Ao*HMS-AOT (Figure 6)	*Ao*HMS (O52791)	hydroxymandelate synthase (Fe)	H161, H241, E320	aminoazidation of alkenes (Fe)	Huang[109]
11	*Bs*QueD-CF_3 (Figure 5)	*Bs*QueD (P42106)	quercetin 2,3-dioxygenase (Fe)	H62, H64, E69, H103	trifluoromethylazidation of alkenes (Fe)	Jia[98]
12	*Bs*QueD$_{AF}$ (Figure 59)	*Bs*QueD (P42106)	quercetin 2,3-dioxygenase (Fe)	H62, H64, E69, H103	aminative difubctionalization of alkenes (Fe)	Jia[292]
13	*Sav*HPPD-PC (Figure 22)	*Sav*HPPD (Q53586)	4-hydroxyphenylpyruvate dioxygenase (Fe)	H187, H270, E349	decarboxylative azidation and thiocyanation (Fe)	Huang[169]
14	*Sav*HPPD Az (Figure 33)	*Sav*HPPD (Q53586)	4-hydroxyphenylpyruvate dioxygenase (Fe)	H187, H270, E349	C(sp^3)–H azidation (Fe)	Huang[207]
15	*Sv*HppE-Fluor (Figure 34)	*Sv*HPPE (Q56185)	(*S*)-2-hydroxypropylphosphonate epoxidase (Fe)	H137, E141, H179	C(sp^3)–H fluorination (Fe)	Huang[211]
16	*Cv*PAH-aminase (Figure 24)	*Cv*PAH (P30967)	phenylalanine hydroxylase (Fe)	H138, H143, E184	decarboxylative radical amination (Cu)	Huang[174]
17	*Ps*EFE^{VHMM} (Figure 53)	*Ps*EFE (P32021)	ethylene-forming enzyme (Fe)	H189, D191, H268	aziridination/ intramolecular benzylic C(sp^3)–H amidation	Arnold[265]

					(Fe)	
18	TDO (Figure 31)	TDO (A5W4F1)	toluene dioxygenase (Fe)	H222, H228, D376	oxidation of benzyl azide to benzonitrile (Fe)	Carrera[192]
19	NDO	NDO (P0A110)	naphthalene dioxygenase (Fe)	H208, H213, D362	intramolecular benzylic C(sp^3)–H amidation (Fe)	Fasan[270]
20	SadX 4-IC (Figure 20)	SadA (Q0B2N4)	prolyl 4-hydroxylase (Fe)	H155 D157 H246	C–H azidation (Fe)	Lewis[167]

8. Conclusions

Over the past five years, metalloenzyme-catalyzed free radical transformations that are rare or absent in native enzymology have expanded rapidly. These unnatural reactions engage an array of reactive radical species, including carbon-, nitrogen-, and oxygen-centered radicals, as well as transition-metal nitrenoids and carbenoids with radical character. By leveraging the redox properties of first-row transition metals, radical initiation strategies have been broadened. In particular, single-electron transfer (SET) oxidation or reduction of radical precursors has proven effective for generating radicals directly within metalloenzyme active sites, enabling diverse stereoselective transformations. Highly reactive radical species can also be formed through photoredox catalytic cycles, either inside or proximal to the enzyme active site, and subsequently diffuse into the pocket to couple with other reaction partners. The integration of exogenous photocatalysts with metalloenzymes allows for the controlled generation of radical intermediates independent of the intrinsic redox potential of the metallocofactor, opening new avenues for

designing unnatural biocatalytic radical transformations. Critically, the malleable chiral pockets of enzymes now enable high levels of enantioselectivity to be achieved in free radical–mediated transformations, which was long considered a challenge in asymmetric catalysis. Furthermore, emerging technologies, including high-throughput screening,[321,322] machine learning–guided directed evolution,[323–326] and AI-assisted de novo protein design,[327–331] promise to accelerate the development of protein catalysts. Together with mechanism-guided reaction design, these advances are poised to expand the scope of metalloenzyme-catalyzed radical reactions in the years ahead.

AUTHOR INFORMATION

Corresponding Author

*yang@chem.ucsb.edu

Present Address

†Department of Medicinal Chemistry, School of Pharmacy, China Pharmaceutical University, Nanjing 210009, P. R. China.

Author Contributions

The manuscript was written through contributions of all authors. All authors have given approval to the final version of the manuscript.

‡These authors contributed equally.

Biographies

Wenzhen Fu received his B.S. degree in Chemistry from Zhengzhou University in 2012. He carried out graduate study at the Shanghai Institute of Organic Chemistry under the guidance of Prof. Wenjun Tang, focusing on transition-metal-catalyzed asymmetric reductive coupling and ligand design. After receiving his Ph.D. in Organic Chemistry in 2018, Wenzhen performed postdoctoral studies with Prof. James Turkson and Prof. Marcus A. Tius at the University of Hawaii Cancer Center. From 2020–2024, he continued his postdoctoral training under the direction of Prof. Yang Yang at the University of California Santa Barbara, focusing on P450-catalyzed asymmetric radical cyclization to aromatic compounds. In 2025, Wenzhen started his independent career in the School of Pharmacy at China Pharmaceutical University in Nanjing, China.

Liu-Peng Zhao received his B.S. degree in Chemistry from Shandong University in 2017 and earned his Ph.D. in 2022 from the Shanghai Institute of Organic Chemistry under the guidance of Prof. Yong Tang. During his doctoral studies, Liu-Peng developed [2+2+2] cascade cyclization strategies for the synthesis of natural indole alkaloids. In 2022, Liu-Peng started his postdoctoral training under the direction of Prof. Yang Yang at the University of California Santa Barbara, focusing on nonheme Fe enzyme-catalyzed asymmetric radical reactions.

Yang Yang obtained a B.S. in Chemistry in 2011 from Peking University, where he performed undergraduate research with Prof. Jianbo Wang. He also carried out summer research at the University of California Los Angeles with Prof. Neil Garg. He earned his Ph.D. in Organic Chemistry from the Massachusetts Institute of Technology in 2016 under the direction of Prof. Stephen Buchwald. Following graduate studies, he was an NIH Postdoctoral Fellow in the laboratory of Prof. Frances Arnold at the California Institute of Technology. In 2020, Yang started his independent career as an Assistant Professor in the Department of Chemistry and Biochemistry

at the University of California Santa Barbara. He was promoted to Associate Professor with Tenure in 2025. The Yang lab reprograms nature's biosynthetic machineries to access reaction space well beyond the native biochemical landscape. In recent years, Yang coined metalloredox radical biocatalysis (2021) and pyridoxal radical biocatalysis (2023) as general strategies to advance novel enzyme functions not previously known in nature, including those which are unknown in both chemistry and biology.

ACKNOWLEDGMENT

We are grateful to the National Institutes of Health (R35GM147387), National Science Foundation (CHE-2400087), Department of Energy (DE-SC0025389) and Army Research Office (W911NF-23-1-0182) and Howard Hughes Medical Institute for financial support. Y.Y. is an Alfred P. Sloan Research Fellow (FG-2024-22244), a Camille Dreyfus Teacher-Scholar Awardee (TC-25-084) and a David & Lucile Packard Fellow (2023-76169).

REFERENCES

(1) Yi, H.; Zhang, G.; Wang, H.; Huang, Z.; Wang, J.; Singh, A. K.; Lei, A. Recent Advances in Radical C–H Activation/Radical Cross-Coupling. *Chem. Rev.* **2017**, *117* (13), 9016–9085. https://doi.org/10.1021/acs.chemrev.6b00620.

(2) Plesniak, M. P.; Huang, H.-M.; Procter, D. J. Radical Cascade Reactions Triggered by Single Electron Transfer. *Nat. Rev. Chem.* **2017**, *1* (10), 0077. https://doi.org/10.1038/s41570-017-0077.

(3) Smith, J. M.; Harwood, S. J.; Baran, P. S. Radical Retrosynthesis. *Acc. Chem. Res.* **2018**, *51* (8), 1807–1817. https://doi.org/10.1021/acs.accounts.8b00209.

(4) Parsaee, F.; Senarathna, M. C.; Kannangara, P. B.; Alexander, S. N.; Arche, P. D. E.; Welin, E. R. Radical Philicity and Its Role in Selective Organic Transformations. *Nat. Rev. Chem.* **2021**, *5* (7), 486–499. https://doi.org/10.1038/s41570-021-00284-3.

(5) Golden, D. L.; Suh, S.-E.; Stahl, S. S. Radical C(sp^3)–H Functionalization and Cross-Coupling Reactions. *Nat. Rev. Chem.* **2022**, *6* (6), 405–427. https://doi.org/10.1038/s41570-022-00388-4.

(6) Garwood, J. J. A.; Chen, A. D.; Nagib, D. A. Radical Polarity. *J. Am. Chem. Soc.* **2024**, *146* (41), 28034–28059. https://doi.org/10.1021/jacs.4c06774.

(7) Toraya, T. Radical Catalysis in Coenzyme B_{12}-Dependent Isomerization (Eliminating) Reactions. *Chem. Rev.* **2003**, *103* (6), 2095–2128. https://doi.org/10.1021/cr020428b.

(8) Wang, F.; Chen, P.; Liu, G. Copper-Catalyzed Radical Relay for Asymmetric Radical Transformations. *Acc. Chem. Res.* **2018**, *51* (9), 2036–2046. https://doi.org/10.1021/acs.accounts.8b00265.

(9) Demarteau, J.; Debuigne, A.; Detrembleur, C. Organocobalt Complexes as Sources of Carbon-Centered Radicals for Organic and Polymer Chemistries. *Chem. Rev.* **2019**, *119* (12), 6906–6955. https://doi.org/10.1021/acs.chemrev.8b00715.

(10) Cheung, K. P. S.; Sarkar, S.; Gevorgyan, V. Visible Light-Induced Transition Metal Catalysis. *Chem. Rev.* **2022**, *122* (2), 1543–1625. https://doi.org/10.1021/acs.chemrev.1c00403.

(11) de Groot, L. H. M.; Ilic, A.; Schwarz, J.; Wärnmark, K. Iron Photoredox Catalysis–Past, Present, and Future. *J. Am. Chem. Soc.* **2023**, *145* (17), 9369–9388. https://doi.org/10.1021/jacs.3c01000.

(12) Narayanam, J. M. R.; Stephenson, C. R. J. Visible Light Photoredox Catalysis: Applications in Organic Synthesis. *Chem. Soc. Rev.* **2010**, *40* (1), 102–113. https://doi.org/10.1039/B913880N.

(13) Prier, C. K.; Rankic, D. A.; MacMillan, D. W. C. Visible Light Photoredox Catalysis with Transition Metal Complexes: Applications in Organic Synthesis. *Chem. Rev.* **2013**, *113* (7), 5322–5363. https://doi.org/10.1021/cr300503r.

(14) Romero, N. A.; Nicewicz, D. A. Organic Photoredox Catalysis. *Chem. Rev.* **2016**, *116* (17), 10075–10166. https://doi.org/10.1021/acs.chemrev.6b00057.

(15) Skubi, K. L.; Blum, T. R.; Yoon, T. P. Dual Catalysis Strategies in Photochemical Synthesis. *Chem. Rev.* **2016**, *116* (17), 10035–10074. https://doi.org/10.1021/acs.chemrev.6b00018.

(16) Yuan, Y.; Yang, J.; Lei, A. Recent Advances in Electrochemical Oxidative Cross-Coupling with Hydrogen Evolution Involving Radicals. *Chem. Soc. Rev.* **2021**, *50* (18), 10058–10086. https://doi.org/10.1039/D1CS00150G.

(17) Rein, J.; Zacate, S. B.; Mao, K.; Lin, S. A Tutorial on Asymmetric Electrocatalysis. *Chem. Soc. Rev.* **2023**, *52* (23), 8106–8125. https://doi.org/10.1039/D3CS00511A.

(18) Sibi, M. P.; Manyem, S.; Zimmerman, J. Enantioselective Radical Processes. *Chem. Rev.* **2003**, *103* (8), 3263–3296. https://doi.org/10.1021/cr020044l.

(19) Proctor, R. S. J.; Colgan, A. C.; Phipps, R. J. Exploiting Attractive Non-Covalent Interactions for the Enantioselective Catalysis of Reactions Involving Radical Intermediates. *Nat. Chem.* **2020**, *12* (11), 990–1004. https://doi.org/10.1038/s41557-020-00561-6.

(20) Mondal, S.; Dumur, F.; Gigmes, D.; Sibi, M. P.; Bertrand, M. P.; Nechab, M. Enantioselective Radical Reactions Using Chiral Catalysts. *Chem. Rev.* **2022**, *122* (6), 5842–5976. https://doi.org/10.1021/acs.chemrev.1c00582.

(21) Bornscheuer, U. T.; Huisman, G. W.; Kazlauskas, R. J.; Lutz, S.; Moore, J. C.; Robins, K. Engineering the Third Wave of Biocatalysis. *Nature* **2012**, *485* (7397), 185–194. https://doi.org/10.1038/nature11117.

(22) Wu, S.; Snajdrova, R.; Moore, J. C.; Baldenius, K.; Bornscheuer, U. T. Biocatalysis: Enzymatic Synthesis for Industrial Applications. *Angew. Chem. Int. Ed.* **2021**, *60* (1), 88–119. https://doi.org/10.1002/anie.202006648.

(23) Buller, R.; Lutz, S.; Kazlauskas, R. J.; Snajdrova, R.; Moore, J. C.; Bornscheuer, U. T. From Nature to Industry: Harnessing Enzymes for Biocatalysis. *Science* **2023**, *382* (6673), eadh8615. https://doi.org/10.1126/science.adh8615.

(24) Broderick, J. B.; Duffus, B. R.; Duschene, K. S.; Shepard, E. M. Radical S-Adenosylmethionine Enzymes. *Chem. Rev.* **2014**, *114* (8), 4229–4317. https://doi.org/10.1021/cr4004709.

(25) Landgraf, B. J.; McCarthy, E. L.; Booker, S. J. Radical S-Adenosylmethionine Enzymes in Human Health and Disease. *Annu. Rev. Biochem.* **2016**, *85*, 485–514. https://doi.org/10.1146/annurev-biochem-060713-035504.

(26) Hoffman, B. M.; Broderick, W. E.; Broderick, J. B. Mechanism of Radical Initiation in the Radical SAM Enzyme Superfamily. *Annu. Rev. Biochem.* **2023**, *92*, 333–349. https://doi.org/10.1146/annurev-biochem-052621-090638.

(27) Matthews, R. G. Cobalamin-Dependent Methyltransferases. *Acc. Chem. Res.* **2001**, *34* (8), 681–689. https://doi.org/10.1021/ar0000051.

(28) Brown, K. L. Chemistry and Enzymology of Vitamin B_{12}. *Chem. Rev.* **2005**, *105* (6), 2075–2150. https://doi.org/10.1021/cr030720z.

(29) Sono, M.; Roach, M. P.; Coulter, E. D.; Dawson, J. H. Heme-Containing Oxygenases. *Chem. Rev.* **1996**, *96* (7), 2841–2888. https://doi.org/10.1021/cr9500500.

(30) Denisov, I. G.; Makris, T. M.; Sligar, S. G.; Schlichting, I. Structure and Chemistry of Cytochrome P450. *Chem. Rev.* **2005**, *105* (6), 2253–2278. https://doi.org/10.1021/cr0307143.

(31) Ortiz de Montellano, P. R. Hydrocarbon Hydroxylation by Cytochrome P450 Enzymes. *Chem. Rev.* **2010**, *110* (2), 932–948. https://doi.org/10.1021/cr9002193.

(32) O'Reilly, E.; Köhler, V.; Flitsch, S. L.; Turner, N. J. Cytochromes P450 as Useful Biocatalysts: Addressing the Limitations. *Chem. Commun.* **2011**, *47* (9), 2490–2501. https://doi.org/10.1039/C0CC03165H.

(33) C. Whitehouse, C. J.; G. Bell, S.; Wong, L.-L. $P450_{BM3}$ (CYP102A1): Connecting the Dots. *Chem. Soc. Rev.* **2012**, *41* (3), 1218–1260. https://doi.org/10.1039/C1CS15192D.

(34) Poulos, T. L. Heme Enzyme Structure and Function. *Chem. Rev.* **2014**, *114* (7), 3919–3962. https://doi.org/10.1021/cr400415k.

(35) Fansher, D. J.; Besna, J. N.; Fendri, A.; Pelletier, J. N. Choose Your Own Adventure: A Comprehensive Database of Reactions Catalyzed by Cytochrome P450 BM3 Variants. *ACS Catal.* **2024**, *14* (8), 5560–5592. https://doi.org/10.1021/acscatal.4c00086.

(36) Pope, S. R.; McBride, M. J.; Nair, M. A.; Salas-Solá, X. E.; Krebs, C.; Bollinger, J. M.; Boal, A. K. Heme Oxygenase–Like Metalloenzymes. *Annu. Rev. Biochem.* **2025**, *94*, 59–88. https://doi.org/10.1146/annurev-biochem-030122-043608.

(37) Abu-Omar, M. M.; Loaiza, A.; Hontzeas, N. Reaction Mechanisms of Mononuclear Non-Heme Iron Oxygenases. *Chem. Rev.* **2005**, *105* (6), 2227–2252. https://doi.org/10.1021/cr040653o.

(38) Krebs, C.; Galonić Fujimori, D.; Walsh, C. T.; Bollinger, J. M. Jr. Non-Heme Fe(IV)–Oxo Intermediates. *Acc. Chem. Res.* **2007**, *40* (7), 484–492. https://doi.org/10.1021/ar700066p.

(39) Barry, S. M.; Challis, G. L. Mechanism and Catalytic Diversity of Rieske Non-Heme Iron-Dependent Oxygenases. *ACS Catal.* **2013**, *3* (10), 2362–2370. https://doi.org/10.1021/cs400087p.

(40) Jasniewski, A. J.; Que, L. Jr. Dioxygen Activation by Nonheme Diiron Enzymes: Diverse Dioxygen Adducts, High-Valent Intermediates, and Related Model Complexes. *Chem. Rev.* **2018**, *118* (5), 2554–2592. https://doi.org/10.1021/acs.chemrev.7b00457.

(41) Vaillancourt, F. H.; Yeh, E.; Vosburg, D. A.; Garneau-Tsodikova, S.; Walsh, C. T. Nature's Inventory of Halogenation Catalysts: Oxidative Strategies Predominate. *Chem. Rev.* **2006**, *106* (8), 3364–3378. https://doi.org/10.1021/cr050313i.

(42) Latham, J.; Brandenburger, E.; Shepherd, S. A.; Menon, B. R. K.; Micklefield, J. Development of Halogenase Enzymes for Use in Synthesis. *Chem. Rev.* **2018**, *118* (1), 232–269. https://doi.org/10.1021/acs.chemrev.7b00032.

(43) Crowe, C.; Molyneux, S.; V. Sharma, S.; Zhang, Y.; S. Gkotsi, D.; Connaris, H.; M. Goss, R. J. Halogenases: A Palette of Emerging Opportunities for Synthetic Biology–Synthetic Chemistry and C–H Functionalisation. *Chem. Soc. Rev.* **2021**, *50* (17), 9443–9481. https://doi.org/10.1039/D0CS01551B.

(44) Papadopoulou, A.; Meyer, F.; Buller, R. M. Engineering Fe(II)/α-Ketoglutarate-Dependent Halogenases and Desaturases. *Biochemistry* **2023**, *62* (2), 229–240. https://doi.org/10.1021/acs.biochem.2c00115.

(45) Harrison, W.; Huang, X.; Zhao, H. Photobiocatalysis for Abiological Transformations. *Acc. Chem. Res.* **2022**, *55* (8), 1087–1096. https://doi.org/10.1021/acs.accounts.1c00719.

(46) Emmanuel, M. A.; Bender, S. G.; Bilodeau, C.; Carceller, J. M.; DeHovitz, J. S.; Fu, H.; Liu, Y.; Nicholls, B. T.; Ouyang, Y.; Page, C. G.; Qiao, T.; Raps, F. C.; Sorigué, D. R.; Sun, S.-Z.; Turek-Herman, J.; Ye, Y.; Rivas-Souchet, A.; Cao, J.; Hyster, T. K. Photobiocatalytic Strategies for Organic Synthesis. *Chem. Rev.* **2023**, *123* (9), 5459–5520. https://doi.org/10.1021/acs.chemrev.2c00767.

(47) Fu, H.; Hyster, T. K. From Ground-State to Excited-State Activation Modes: Flavin-Dependent "Ene"-Reductases Catalyzed Non-Natural Radical Reactions. *Acc. Chem. Res.* **2024**, *57* (9), 1446–1457. https://doi.org/10.1021/acs.accounts.4c00129.

(48) Cheng, L.; Li, D.; Mai, B. K.; Bo, Z.; Cheng, L.; Liu, P.; Yang, Y. Stereoselective Amino Acid Synthesis by Synergistic Photoredox-Pyridoxal Radical Biocatalysis. *Science* **2023**, *381* (6656), 444–451. https://doi.org/10.1126/science.adg2420.

(49) Wang, T.-C.; Mai, B. K.; Zhang, Z.; Bo, Z.; Li, J.; Liu, P.; Yang, Y. Stereoselective Amino Acid Synthesis by Photobiocatalytic Oxidative Coupling. *Nature* **2024**, *629* (8010), 98–104. https://doi.org/10.1038/s41586-024-07284-5.

(50) Ouyang, Y.; Page, C. G.; Bilodeau, C.; Hyster, T. K. Synergistic Photoenzymatic Catalysis Enables Synthesis of A-Tertiary Amino Acids Using Threonine Aldolases. *J. Am. Chem. Soc.* **2024**, *146* (20), 13754–13759. https://doi.org/10.1021/jacs.4c04661.

(51) Wang, T.-C.; Zhang, Z.; Rao, G.; Li, J.; Shirah, J.; Britt, R. D.; Zhu, Q.; Yang, Y. Threonine Aldolase-Catalyzed Enantioselective α-Alkylation of Amino Acids through Unconventional Photoinduced Radical Initiation. *J. Am. Chem. Soc.* **2024**, *146* (32), 22476–22484. https://doi.org/10.1021/jacs.4c05949.

(52) Cheng, L.; Bo, Z.; Krohn-Hansen, B.; Yang, Y. Directed Evolution and Unusual Protonation Mechanism of Pyridoxal Radical C–C Coupling Enzymes for the Enantiodivergent

Photobiocatalytic Synthesis of Noncanonical Amino Acids. *J. Am. Chem. Soc.* **2025**, *147* (5), 4602–4612. https://doi.org/10.1021/jacs.4c16716.

(53) Zhang, C.; Zhou, J.; Xie, P.-P.; Rivera, S. M.; Alturaifi, T. M.; Finnigan, J.; Charnock, S.; Liu, P.; Yang, Y. Diversity-Oriented Photobiocatalytic Synthesis via Stereoselective Three-Component Radical Coupling. *Science* **2025**, *389* (6767), eadx2935. https://doi.org/10.1126/science.adx2935.

(54) Zhang, C.; Zhou, J.; Mai, B. K.; Qin, Z.; Finnigan, J.; Gittings, S.; Liu, P.; Yang, Y. A Pyridoxal Radical Carboligase and Imine Reductase Photobiocatalytic Cascade for Stereoselective Synthesis of Unnatural Prolines. *Nat. Chem.* **2025**, 1–8. https://doi.org/10.1038/s41557-025-01937-2.

(55) Xu, Y.; Chen, H.; Yu, L.; Peng, X.; Zhang, J.; Xing, Z.; Bao, Y.; Liu, A.; Zhao, Y.; Tian, C.; Liang, Y.; Huang, X. A Light-Driven Enzymatic Enantioselective Radical Acylation. *Nature* **2024**, *625* (7993), 74–78. https://doi.org/10.1038/s41586-023-06822-x.

(56) Liu, X.; Xu, S.; Chen, H.; Yang, Y. Unnatural Thiamine Radical Enzymes for Photobiocatalytic Asymmetric Alkylation of Benzaldehydes and α-Ketoacids. *ACS Catal.* **2024**, *14* (12), 9144–9150. https://doi.org/10.1021/acscatal.4c02752.

(57) Xing, Z.; Liu, F.; Feng, J.; Yu, L.; Wu, Z.; Zhao, B.; Chen, B.; Ping, H.; Xu, Y.; Liu, A.; Zhao, Y.; Wang, C.; Wang, B.; Huang, X. Synergistic Photobiocatalysis for Enantioselective Triple-Radical Sorting. *Nature* **2025**, *637* (8048), 1118–1123. https://doi.org/10.1038/s41586-024-08399-5.

(58) Zhao, B.; Xu, Y.; Zhu, Q.; Liu, A.; Peng, X.; Zhang, T.; Yu, L.; Zhang, Y.; Huang, X. Electricity-Driven Enzymatic Dynamic Kinetic Oxidation. *Nature* **2025**, *643* (8072), 699–704. https://doi.org/10.1038/s41586-025-09178-6.

(59) Peng, X.; Feng, J.; Liu, F.; Xie, W.-Z.; Sun, H.; Xu, Y.; Ming, Y.; Xing, Z.; Zheng, Y.; Wang, B.; Long, Y.-T.; Huang, X. Photobiocatalytic Benzylic C–H Acylation Enabled by the Synergy of a Thiamine-Dependent Enzyme, an Organophotocatalyst and Hydrogen-Atom Transfer. *Nat. Synth.* **2025**, 1–9. https://doi.org/10.1038/s44160-025-00866-9.

(60) Brandenberg, O. F.; Fasan, R.; Arnold, F. H. Exploiting and Engineering Hemoproteins for Abiological Carbene and Nitrene Transfer Reactions. *Curr. Opin. Biotechnol.* **2017**, *47*, 102–111. https://doi.org/10.1016/j.copbio.2017.06.005.

(61) Chen, K.; Arnold, F. H. Engineering New Catalytic Activities in Enzymes. *Nat. Catal.* **2020**, *3* (3), 203–213. https://doi.org/10.1038/s41929-019-0385-5.

(62) Yang, Y.; Arnold, F. H. Navigating the Unnatural Reaction Space: Directed Evolution of Heme Proteins for Selective Carbene and Nitrene Transfer. *Acc. Chem. Res.* **2021**, *54* (5), 1209–1225. https://doi.org/10.1021/acs.accounts.0c00591.

(63) Liu, Z.; Arnold, F. H. New-to-Nature Chemistry from Old Protein Machinery: Carbene and Nitrene Transferases. *Curr. Opin. Biotechnol.* **2021**, *69*, 43–51. https://doi.org/10.1016/j.copbio.2020.12.005.

(64) Zhou, Q.; Chin, M.; Fu, Y.; Liu, P.; Yang, Y. Stereodivergent Atom-Transfer Radical Cyclization by Engineered Cytochromes P450. *Science* **2021**, *374* (6575), 1612–1616. https://doi.org/10.1126/science.abk1603.

(65) Schwizer, F.; Okamoto, Y.; Heinisch, T.; Gu, Y.; Pellizzoni, M. M.; Lebrun, V.; Reuter, R.; Köhler, V.; Lewis, J. C.; Ward, T. R. Artificial Metalloenzymes: Reaction Scope and Optimization Strategies. *Chem. Rev.* **2018**, *118* (1), 142–231. https://doi.org/10.1021/acs.chemrev.7b00014.

(66) Reetz, M. T. Directed Evolution of Artificial Metalloenzymes: A Universal Means to Tune the Selectivity of Transition Metal Catalysts? *Acc. Chem. Res.* **2019**, *52* (2), 336–344. https://doi.org/10.1021/acs.accounts.8b00582.

(67) Natoli, S. N.; Hartwig, J. F. Noble−Metal Substitution in Hemoproteins: An Emerging Strategy for Abiological Catalysis. *Acc. Chem. Res.* **2019**, *52* (2), 326–335. https://doi.org/10.1021/acs.accounts.8b00586.

(68) Lewis, J. C. Beyond the Second Coordination Sphere: Engineering Dirhodium Artificial Metalloenzymes to Enable Protein Control of Transition Metal Catalysis. *Acc. Chem. Res.* **2019**, *52* (3), 576–584. https://doi.org/10.1021/acs.accounts.8b00625.

(69) Roelfes, G. LmrR: A Privileged Scaffold for Artificial Metalloenzymes. *Acc. Chem. Res.* **2019**, *52* (3), 545–556. https://doi.org/10.1021/acs.accounts.9b00004.

(70) Oohora, K.; Onoda, A.; Hayashi, T. Hemoproteins Reconstituted with Artificial Metal Complexes as Biohybrid Catalysts. *Acc. Chem. Res.* **2019**, *52* (4), 945–954. https://doi.org/10.1021/acs.accounts.8b00676.

(71) Treviño, R. E.; Shafaat, H. S. Protein-Based Models Offer Mechanistic Insight into Complex Nickel Metalloenzymes. *Curr. Opin. Chem. Biol.* **2022**, *67*, 102110. https://doi.org/10.1016/j.cbpa.2021.102110.

(72) Lovelock, S. L.; Crawshaw, R.; Basler, S.; Levy, C.; Baker, D.; Hilvert, D.; Green, A. P. The Road to Fully Programmable Protein Catalysis. *Nature* **2022**, *606* (7912), 49–58. https://doi.org/10.1038/s41586-022-04456-z.

(73) Van Stappen, C.; Deng, Y.; Liu, Y.; Heidari, H.; Wang, J.-X.; Zhou, Y.; Ledray, A. P.; Lu, Y. Designing Artificial Metalloenzymes by Tuning of the Environment beyond the Primary

Coordination Sphere. *Chem. Rev.* **2022**, *122* (14), 11974–12045. https://doi.org/10.1021/acs.chemrev.2c00106.

(74) Ollivier, C.; Renaud, P. Organoboranes as a Source of Radicals. *Chem. Rev.* **2001**, *101* (11), 3415–3434. https://doi.org/10.1021/cr010001p.

(75) Frey, P. A. Travels with Carbon-Centered Radicals. 5′-Deoxyadenosine and 5′-Deoxyadenosine-5′-Yl in Radical Enzymology. *Acc. Chem. Res.* **2014**, *47* (2), 540–549. https://doi.org/10.1021/ar400194k.

(76) Goddard, J.-P.; Ollivier, C.; Fensterbank, L. Photoredox Catalysis for the Generation of Carbon Centered Radicals. *Acc. Chem. Res.* **2016**, *49* (9), 1924–1936. https://doi.org/10.1021/acs.accounts.6b00288.

(77) Xiao, H.; Zhang, Z.; Fang, Y.; Zhu, L.; Li, C. Radical Trifluoromethylation. *Chem. Soc. Rev.* **2021**, *50* (11), 6308–6319. https://doi.org/10.1039/D1CS00200G.

(78) Sauer, G. S.; Lin, S. An Electrocatalytic Approach to the Radical Difunctionalization of Alkenes. *ACS Catal.* **2018**, *8* (6), 5175–5187. https://doi.org/10.1021/acscatal.8b01069.

(79) Li, Z.-L.; Fang, G.-C.; Gu, Q.-S.; Liu, X.-Y. Recent Advances in Copper-Catalysed Radical-Involved Asymmetric 1,2-Difunctionalization of Alkenes. *Chem. Soc. Rev.* **2020**, *49* (1), 32–48. https://doi.org/10.1039/C9CS00681H.

(80) Wu, X.; Zhu, C. Radical-Mediated Remote Functional Group Migration. *Acc. Chem. Res.* **2020**, *53* (8), 1620–1636. https://doi.org/10.1021/acs.accounts.0c00306.

(81) Eckenhoff, W. T.; Pintauer, T. Copper Catalyzed Atom Transfer Radical Addition (ATRA) and Cyclization (ATRC) Reactions in the Presence of Reducing Agents. *Catal. Rev.* **2010**, *52* (1), 1–59. https://doi.org/10.1080/01614940903238759.

(82) McIntosh, J. A.; Coelho, P. S.; Farwell, C. C.; Wang, Z. J.; Lewis, J. C.; Brown, T. R.; Arnold, F. H. Enantioselective Intramolecular C–H Amination Catalyzed by Engineered Cytochrome P450 Enzymes In Vitro and In Vivo. *Angew. Chem. Int. Ed.* **2013**, *52* (35), 9309–9312. https://doi.org/10.1002/anie.201304401.

(83) Yang, Y.; Cho, I.; Qi, X.; Liu, P.; Arnold, F. H. An Enzymatic Platform for the Asymmetric Amination of Primary, Secondary and Tertiary C(sp^3)–H Bonds. *Nat. Chem.* **2019**, *11* (11), 987–993. https://doi.org/10.1038/s41557-019-0343-5.

(84) Fu, Y.; Chen, H.; Fu, W.; Garcia-Borràs, M.; Yang, Y.; Liu, P. Engineered P450 Atom-Transfer Radical Cyclases Are Bifunctional Biocatalysts: Reaction Mechanism and Origin of Enantioselectivity. *J. Am. Chem. Soc.* **2022**, *144* (29), 13344–13355. https://doi.org/10.1021/jacs.2c04937.

(85) Lubskyy, A.; Guo, C.; Chadwick, R. J.; Petri-Fink, A.; Bruns, N.; Pellizzoni, M. M. Engineered Myoglobin as a Catalyst for Atom Transfer Radical Cyclisation. *Chem. Commun.* **2022**, *58* (78), 10989–10992. https://doi.org/10.1039/D2CC03227A.

(86) Wang, F.; Qi, X.; Liang, Z.; Chen, P.; Liu, G. Copper-Catalyzed Intermolecular Trifluoromethylazidation of Alkenes: Convenient Access to CF_3-Containing Alkyl Azides. *Angew. Chem. Int. Ed.* **2014**, *53* (7), 1881–1886. https://doi.org/10.1002/anie.201309991.

(87) Zhu, C.-L.; Wang, C.; Qin, Q.-X.; Yruegas, S.; Martin, C. D.; Xu, H. Iron(II)-Catalyzed Azidotrifluoromethylation of Olefins and N-Heterocycles for Expedient Vicinal Trifluoromethyl Amine Synthesis. *ACS Catal.* **2018**, *8* (6), 5032–5037. https://doi.org/10.1021/acscatal.8b01253.

(88) Furuya, T.; Kamlet, A. S.; Ritter, T. Catalysis for Fluorination and Trifluoromethylation. *Nature* **2011**, *473* (7348), 470–477. https://doi.org/10.1038/nature10108.

(89) Charpentier, J.; Früh, N.; Togni, A. Electrophilic Trifluoromethylation by Use of Hypervalent Iodine Reagents. *Chem. Rev.* **2015**, *115* (2), 650–682. https://doi.org/10.1021/cr500223h.

(90) Yang, X.; Wu, T.; Phipps, R. J.; Toste, F. D. Advances in Catalytic Enantioselective Fluorination, Mono-, Di-, and Trifluoromethylation, and Trifluoromethylthiolation Reactions. *Chem. Rev.* **2015**, *115* (2), 826–870. https://doi.org/10.1021/cr500277b.

(91) Brownlee, J.; He, P.; Moran, G. R.; Harrison, D. H. T. Two Roads Diverged: The Structure of Hydroxymandelate Synthase from Amycolatopsis Orientalis in Complex with 4-Hydroxymandelate,. *Biochemistry* **2008**, *47* (7), 2002–2013. https://doi.org/10.1021/bi701438r.

(92) Zhang, J. G.; Huls, A. J.; Palacios, P. M.; Guo, Y.; Huang, X. Biocatalytic Generation of Trifluoromethyl Radicals by Nonheme Iron Enzymes for Enantioselective Alkene Difunctionalization. *J. Am. Chem. Soc.* **2024**, *146* (50), 34878–34886. https://doi.org/10.1021/jacs.4c14310.

(93) Bednarek, C.; Wehl, I.; Jung, N.; Schepers, U.; Bräse, S. The Staudinger Ligation. *Chem. Rev.* **2020**, *120* (10), 4301–4354. https://doi.org/10.1021/acs.chemrev.9b00665.

(94) Leung, D. W.; Chen, E.; Goeddel, D. V. A Method for Random Mutagenesis of a Defined DNA Segment Using a Modified Polymerase Chain Reaction. *Technique* **1989**, *1*, 11–15.

(95) Cirino, P. C.; Mayer, K. M.; Umeno, D. Generating Mutant Libraries Using Error-Prone PCR. In *Directed Evolution Library Creation: Methods and Protocols*; Arnold, F. H., Georgiou, G., Eds.; Humana Press: Totowa, NJ, 2003; pp 3–9. https://doi.org/10.1385/1-59259-395-X:3.

(96) Barney, B. M.; Schaab, M. R.; LoBrutto, R.; Francisco, W. A. Evidence for a New Metal in a Known Active Site: Purification and Characterization of an Iron-Containing Quercetin 2,3-

Dioxygenase from *Bacillus Subtilis*. *Protein Expr. Purif.* **2004**, *35* (1), 131–141. https://doi.org/10.1016/j.pep.2004.01.005.

(97) Gopal, B.; Madan, L. L.; Betz, S. F.; Kossiakoff, A. A. The Crystal Structure of a Quercetin 2,3-Dioxygenase from Bacillus Subtilis Suggests Modulation of Enzyme Activity by a Change in the Metal Ion at the Active Site(s). *Biochemistry* **2005**, *44* (1), 193–201. https://doi.org/10.1021/bi0484421.

(98) He, H.; Yan, J.-X.; Zhu, J.-X.; Liu, S.-J.; Liu, X.-Q.; Chen, P.; Wang, X.; Jia, Z.-J. Enantioselective Trifluoromethylazidation of Styrenyl Olefins Catalyzed by an Engineered Nonheme Iron Enzyme. *Angew. Chem. Int. Ed.* **2025**, *137* (9), e202423507. https://doi.org/10.1002/ange.202423507.

(99) Lipshutz, B. H.; Ghorai, S.; Abela, A. R.; Moser, R.; Nishikata, T.; Duplais, C.; Krasovskiy, A.; Gaston, R. D.; Gadwood, R. C. TPGS-750-M: A Second-Generation Amphiphile for Metal-Catalyzed Cross-Couplings in Water at Room Temperature. *J. Org. Chem.* **2011**, *76* (11), 4379–4391. https://doi.org/10.1021/jo101974u.

(100) Pordea, A. Metal-Binding Promiscuity in Artificial Metalloenzyme Design. *Curr. Opin. Chem. Biol.* **2015**, *25*, 124–132. https://doi.org/10.1016/j.cbpa.2014.12.035.

(101) Eom, H.; Song, W. J. Emergence of Metal Selectivity and Promiscuity in Metalloenzymes. *J. Biol. Inorg. Chem.* **2019**, *24* (4), 517–531. https://doi.org/10.1007/s00775-019-01667-0.

(102) Jing, Q.; Kazlauskas, R. J. Regioselective Hydroformylation of Styrene Using Rhodium-Substituted Carbonic Anhydrase. *ChemCatChem* **2010**, *2* (8), 953–957. https://doi.org/10.1002/cctc.201000159.

(103) Key, H. M.; Clark, D. S.; Hartwig, J. F. Generation, Characterization, and Tunable Reactivity of Organometallic Fragments Bound to a Protein Ligand. *J. Am. Chem. Soc.* **2015**, *137* (25), 8261–8268. https://doi.org/10.1021/jacs.5b04431.

(104) Ghattas, W.; Dubosclard, V.; Tachon, S.; Beaumet, M.; Guillot, R.; Réglier, M.; Simaan, A. J.; Mahy, J.-P. CuII-Containing 1-Aminocyclopropane Carboxylic Acid Oxidase Is an Efficient Stereospecific Diels–Alderase. *Angew. Chem. Int. Ed.* **2019**, *58* (41), 14605–14609. https://doi.org/10.1002/anie.201909407.

(105) Mu, X.; Ji, X.; Chen, X.; Wu, H.; Rui, J.; Hong, X.; Worth, M. M.; Reitz, A. D.; Goldberg, L. T. M.; Garcia-Borràs, M.; Michel, S. L. J.; Yang, Y.; Huang, X. Unlocking Lewis Acid Catalysis in Non-Haem Enzymes for an Abiotic Ene Reaction. *Nat. Catal.* **2025**, *8* (7), 635–644. https://doi.org/10.1038/s41929-025-01350-5.

(106) Zhu, R.; Buchwald, S. L. Copper-Catalyzed Oxytrifluoromethylation of Unactivated Alkenes. *J. Am. Chem. Soc.* **2012**, *134* (30), 12462–12465. https://doi.org/10.1021/ja305840g.

(107) Zhu, R.; Buchwald, S. L. Enantioselective Functionalization of Radical Intermediates in Redox Catalysis: Copper-Catalyzed Asymmetric Oxytrifluoromethylation of Alkenes. *Angew. Chem. Int. Ed.* **2013**, *52* (48), 12655–12658. https://doi.org/10.1002/anie.201307790.

(108) Zhu, R.; Buchwald, S. L. Versatile Enantioselective Synthesis of Functionalized Lactones via Copper-Catalyzed Radical Oxyfunctionalization of Alkenes. *J. Am. Chem. Soc.* **2015**, *137* (25), 8069–8077. https://doi.org/10.1021/jacs.5b04821.

(109) Zhang, J. G.; Huang, X. Directed Evolution of Copper-Substituted Nonheme Enzymes for Enantioselective Alkene Oxytrifluoromethylation. *J. Am. Chem. Soc.* **2025**, *147* (33), 29624–29630. https://doi.org/10.1021/jacs.4c18532.

(110) Banerjee, R.; Ragsdale, S. W. The Many Faces of Vitamin B_{12}: Catalysis by Cobalamin-Dependent Enzymes1. *Annu. Rev. Biochem.* **2003**, *72*, 209–247. https://doi.org/10.1146/annurev.biochem.72.121801.161828.

(111) Marsh, E. N. G.; Drennan, C. L. Adenosylcobalamin-Dependent Isomerases: New Insights into Structure and Mechanism. *Curr. Opin. Chem. Biol.* **2001**, *5* (5), 499–505. https://doi.org/10.1016/S1367-5931(00)00238-6.

(112) Payne, K. A. P.; Quezada, C. P.; Fisher, K.; Dunstan, M. S.; Collins, F. A.; Sjuts, H.; Levy, C.; Hay, S.; Rigby, S. E. J.; Leys, D. Reductive Dehalogenase Structure Suggests a Mechanism for B_{12}-Dependent Dehalogenation. *Nature* **2015**, *517* (7535), 513–516. https://doi.org/10.1038/nature13901.

(113) Ortiz-Guerrero, J. M.; Polanco, M. C.; Murillo, F. J.; Padmanabhan, S.; Elías-Arnanz, M. Light-Dependent Gene Regulation by a Coenzyme B_{12}-Based Photoreceptor. *Proc. Natl. Acad. Sci.* **2011**, *108* (18), 7565–7570. https://doi.org/10.1073/pnas.1018972108.

(114) Kutta, R. J.; Hardman, S. J. O.; Johannissen, L. O.; Bellina, B.; Messiha, H. L.; Ortiz-Guerrero, J. M.; Elías-Arnanz, M.; Padmanabhan, S.; Barran, P.; Scrutton, N. S.; Jones, A. R. The Photochemical Mechanism of a B_{12}-Dependent Photoreceptor Protein. *Nat. Commun.* **2015**, *6* (1), 7907. https://doi.org/10.1038/ncomms8907.

(115) Yang, X.; Gerroll, B. H. R.; Jiang, Y.; Kumar, A.; Zubi, Y. S.; Baker, L. A.; Lewis, J. C. Controlling Non-Native Cobalamin Reactivity and Catalysis in the Transcription Factor CarH. *ACS Catal.* **2022**, *12* (2), 935–942. https://doi.org/10.1021/acscatal.1c04748.

(116) Li, J.; Kumar, A.; Lewis, J. C. Non-Native Intramolecular Radical Cyclization Catalyzed by a B_{12}-Dependent Enzyme. *Angew. Chem.* **2023**, *135* (51), e202312893. https://doi.org/10.1002/ange.202312893.

(117) Fontecilla-Camps, J. C.; Volbeda, A.; Cavazza, C.; Nicolet, Y. Structure/Function Relationships of [NiFe]- and [FeFe]-Hydrogenases. *Chem. Rev.* **2007**, *107* (10), 4273–4303. https://doi.org/10.1021/cr050195z.

(118) Shima, S.; Pilak, O.; Vogt, S.; Schick, M.; Stagni, M. S.; Meyer-Klaucke, W.; Warkentin, E.; Thauer, R. K.; Ermler, U. The Crystal Structure of [Fe]-Hydrogenase Reveals the Geometry of the Active Site. *Science* **2008**, *321* (5888), 572–575. https://doi.org/10.1126/science.1158978.

(119) Schilter, D.; Camara, J. M.; Huynh, M. T.; Hammes-Schiffer, S.; Rauchfuss, T. B. Hydrogenase Enzymes and Their Synthetic Models: The Role of Metal Hydrides. *Chem. Rev.* **2016**, *116* (15), 8693–8749. https://doi.org/10.1021/acs.chemrev.6b00180.

(120) Crossley, S. W. M.; Obradors, C.; Martinez, R. M.; Shenvi, R. A. Mn-, Fe-, and Co-Catalyzed Radical Hydrofunctionalizations of Olefins. *Chem. Rev.* **2016**, *116* (15), 8912–9000. https://doi.org/10.1021/acs.chemrev.6b00334.

(121) Ai, W.; Zhong, R.; Liu, X.; Liu, Q. Hydride Transfer Reactions Catalyzed by Cobalt Complexes. *Chem. Rev.* **2019**, *119* (4), 2876–2953. https://doi.org/10.1021/acs.chemrev.8b00404.

(122) L. Shevick, S.; V. Wilson, C.; Kotesova, S.; Kim, D.; L. Holland, P.; A. Shenvi, R. Catalytic Hydrogen Atom Transfer to Alkenes: A Roadmap for Metal Hydrides and Radicals. *Chem. Sci.* **2020**, *11* (46), 12401–12422. https://doi.org/10.1039/D0SC04112B.

(123) Guo, J.; Cheng, Z.; Chen, J.; Chen, X.; Lu, Z. Iron- and Cobalt-Catalyzed Asymmetric Hydrofunctionalization of Alkenes and Alkynes. *Acc. Chem. Res.* **2021**, *54* (11), 2701–2716. https://doi.org/10.1021/acs.accounts.1c00212.

(124) Ji, P.; Park, J.; Gu, Y.; Clark, D. S.; Hartwig, J. F. Abiotic Reduction of Ketones with Silanes Catalysed by Carbonic Anhydrase through an Enzymatic Zinc Hydride. *Nat. Chem.* **2021**, *13* (4), 312–318. https://doi.org/10.1038/s41557-020-00633-7.

(125) Chen, R.; Kayrouz, C. S.; McAmis, E.; Clark, D. S.; Hartwig, J. F. Carbonic Anhydrase Variants Catalyze the Reduction of Dialkyl Ketones with High Enantioselectivity. *Angew. Chem. Int. Ed.* **2024**, *63* (40), e202407111. https://doi.org/10.1002/anie.202407111.

(126) Bao, Y.; Li, Y.; Xie, Z.; Song, P.; Huang, J.; Zhang, X.; Ji, P. Designing γ-Carbonic Anhydrase as a Broad-Scope Metalloreductase with Ultrathermostability and Organic-Solvent Tolerance. *ACS Catal.* **2025**, *15* (10), 8036–8048. https://doi.org/10.1021/acscatal.5c02152.

(127) Zhang, X.; Chen, D.; Stropp, J.; Tachibana, R.; Zou, Z.; Klose, D.; Ward, T. R. Repurposing Myoglobin into an Abiological Asymmetric Ketoreductase. *Chem* **2024**, *10* (8), 2577–2589. https://doi.org/10.1016/j.chempr.2024.06.010.

(128) Wan, Z.; Zhang, X.; Zhuang, H.; Xie, Z.; Yu, L.; Fu, Z.; Sun, Y.; Wang, W.; Wu, R.; Ji, P. Stereoconvergent Reduction of Alkenes Using a Repurposed Iron-Based Dioxygenase. *Nat. Synth.* **2025**, *4* (8), 976–986. https://doi.org/10.1038/s44160-025-00788-6.

(129) Wang, B.; Lu, Y.; Cha, L.; Chen, T.-Y.; Palacios, P. M.; Li, L.; Guo, Y.; Chang, W.; Chen, C. Repurposing Iron- and 2-Oxoglutarate-Dependent Oxygenases to Catalyze Olefin Hydration. *Angew. Chem. Int. Ed.* **2023**, *62* (41), e202311099. https://doi.org/10.1002/anie.202311099.

(130) Zhang, X.; Chen, D.; Álvarez, M.; Ward, T. R. Repurposing Haemoproteins for Asymmetric Metal-Catalysed H Atom Transfer. *Nature* **2025**, *644* (8076), 381–390. https://doi.org/10.1038/s41586-025-09308-0.

(131) Park, S.-Y.; Yamane, K.; Adachi, S.; Shiro, Y.; Weiss, K. E.; Sligar, S. G. Crystallization and Preliminary X-Ray Diffraction Analysis of a Cytochrome P450 (CYP119) from Sulfolobus Solfataricus. *Acta Crystallogr., Sect. D: Biol. Crystallogr.* **2000**, *56* (9), 1173–1175. https://doi.org/10.1107/S0907444900008234.

(132) Fu, W.; Fu, Y.; Zhao, Y.; Wang, H.; Liu, P.; Yang, Y. A Metalloenzyme Platform for Catalytic Asymmetric Radical Dearomatization. *Nat. Chem.* **2024**, *16* (12), 1999–2008. https://doi.org/10.1038/s41557-024-01608-8.

(133) Vallapurackal, J.; Mandal, R.; Bossenbroek, J.; Rubio, A. V.; Poladian, E.; Collings, J. D.; Torres, C.; Hendrickson, M.; Morales, J.; Lyons, M. B.; Schultz, K.; Shafaat, H. S.; Houk, K. N.; Athavale, S. V. Biocatalytic, Asymmetric Radical Hydrogenation of Unactivated Alkenes. *Science* **2025**, *390* (6777), 1050–1056. https://doi.org/10.1126/science.aea4737.

(134) Kattamuri, P. V.; West, J. G. Hydrogenation of Alkenes via Cooperative Hydrogen Atom Transfer. *J. Am. Chem. Soc.* **2020**, *142* (45), 19316–19326. https://doi.org/10.1021/jacs.0c09544.

(135) Bellotti, P.; Huang, H.-M.; Faber, T.; Glorius, F. Photocatalytic Late-Stage C–H Functionalization. *Chem. Rev.* **2023**, *123* (8), 4237–4352. https://doi.org/10.1021/acs.chemrev.2c00478.

(136) Gibson, D. T.; Koch, J. R.; Kallio, R. E. Oxidative Degradation of Aromatic Hydrocarbons by Microorganisms. I. Enzymic Formation of Catechol from Benzene. *Biochemistry* **1968**, *7* (7), 2653–2662. https://doi.org/10.1021/bi00847a031.

(137) Boyd, D. R.; Bugg, T. D. H. Arene Cis-Dihydrodiol Formation: From Biology to Application. *Org. Biomol. Chem.* **2006**, *4* (2), 181–192. https://doi.org/10.1039/B513226F.

(138) Baker Dockrey, S. A.; Lukowski, A. L.; Becker, M. R.; Narayan, A. R. H. Biocatalytic Site- and Enantioselective Oxidative Dearomatization of Phenols. *Nat. Chem.* **2018**, *10* (2), 119–125. https://doi.org/10.1038/nchem.2879.

(139) Fu, W.; Neris, N. M.; Fu, Y.; Zhao, Y.; Krohn-Hansen, B.; Liu, P.; Yang, Y. Enzyme-Controlled Stereoselective Radical Cyclization to Arenes Enabled by Metalloredox Biocatalysis. *Nat. Catal.* **2023**, *6* (7), 628–636. https://doi.org/10.1038/s41929-023-00986-5.

(140) Warren, J. J.; Mayer, J. M. Proton-Coupled Electron Transfer Reactions at a Heme-Propionate in an Iron-Protoporphyrin-IX Model Compound. *J. Am. Chem. Soc.* **2011**, *133* (22), 8544–8551. https://doi.org/10.1021/ja201663p.

(141) Roche, S. P.; Porco Jr., J. A. Dearomatization Strategies in the Synthesis of Complex Natural Products. *Angew. Chem. Int. Ed.* **2011**, *50* (18), 4068–4093. https://doi.org/10.1002/anie.201006017.

(142) Zhuo, C.-X.; Zhang, W.; You, S.-L. Catalytic Asymmetric Dearomatization Reactions. *Angew. Chem. Int. Ed.* **2012**, *51* (51), 12662–12686. https://doi.org/10.1002/anie.201204822.

(143) C. Wertjes, W.; H. Southgate, E.; Sarlah, D. Recent Advances in Chemical Dearomatization of Nonactivated Arenes. *Chem. Soc. Rev.* **2018**, *47* (21), 7996–8017. https://doi.org/10.1039/C8CS00389K.

(144) Zheng, C.; You, S.-L. Advances in Catalytic Asymmetric Dearomatization. *ACS Cent. Sci.* **2021**, *7* (3), 432–444. https://doi.org/10.1021/acscentsci.0c01651.

(145) Wang, Y.; Zhang, W.-Y.; Yu, Z.-L.; Zheng, C.; You, S.-L. SmI_2-Mediated Enantioselective Reductive Dearomatization of Non-Activated Arenes. *Nat. Synth.* **2022**, *1* (5), 401–406. https://doi.org/10.1038/s44160-022-00065-w.

(146) Zhang, W.-Y.; Wang, H.-C.; Wang, Y.; Zheng, C.; You, S.-L. Enantioselective Dearomatization of Indoles via SmI_2-Mediated Intermolecular Reductive Coupling with Ketones. *J. Am. Chem. Soc.* **2023**, *145* (18), 10314–10321. https://doi.org/10.1021/jacs.3c01994.

(147) Fu, W.; Murcek, K.; Chen, J.; Liu, A.; Zhao, Y.; Liu, P.; Yang, Y. Catalytic Enantioselective Smiles Rearrangement Enabled by the Directed Evolution of P450 Radical Aryl Migratases. *J. Am. Chem. Soc.* **2025**, *147* (14), 12197–12205. https://doi.org/10.1021/jacs.5c01179.

(148) Vaillancourt, F. H.; Yin, J.; Walsh, C. T. SyrB2 in Syringomycin E Biosynthesis Is a Nonheme FeII α-Ketoglutarate- and O_2-Dependent Halogenase. *Proc. Natl. Acad. Sci.* **2005**, *102* (29), 10111–10116. https://doi.org/10.1073/pnas.0504412102.

(149) Blasiak, L. C.; Vaillancourt, F. H.; Walsh, C. T.; Drennan, C. L. Crystal Structure of the Non-Haem Iron Halogenase SyrB2 in Syringomycin Biosynthesis. *Nature* **2006**, *440* (7082), 368–371. https://doi.org/10.1038/nature04544.

(150) Hillwig, M. L.; Liu, X. A New Family of Iron-Dependent Halogenases Acts on Freestanding Substrates. *Nat. Chem. Biol.* **2014**, *10* (11), 921–923. https://doi.org/10.1038/nchembio.1625.

(151) Nakamura, H.; Schultz, E. E.; Balskus, E. P. A New Strategy for Aromatic Ring Alkylation in Cylindrocyclophane Biosynthesis. *Nat. Chem. Biol.* **2017**, *13* (8), 916–921. https://doi.org/10.1038/nchembio.2421.

(152) Hayashi, T.; Ligibel, M.; Sager, E.; Voss, M.; Hunziker, J.; Schroer, K.; Snajdrova, R.; Buller, R. Evolved Aliphatic Halogenases Enable Regiocomplementary C−H

Functionalization of a Pharmaceutically Relevant Compound. *Angew. Chem. Int. Ed.* **2019**, *58* (51), 18535–18539. https://doi.org/10.1002/anie.201907245.

(153) Marchand, J. A.; Neugebauer, M. E.; Ing, M. C.; Lin, C.-I.; Pelton, J. G.; Chang, M. C. Y. Discovery of a Pathway for Terminal-Alkyne Amino Acid Biosynthesis. *Nature* **2019**, *567* (7748), 420–424. https://doi.org/10.1038/s41586-019-1020-y.

(154) Zhao, C.; Yan, S.; Li, Q.; Zhu, H.; Zhong, Z.; Ye, Y.; Deng, Z.; Zhang, Y. An Fe^{2+}- and α-Ketoglutarate-Dependent Halogenase Acts on Nucleotide Substrates. *Angew. Chem. Int. Ed.* **2020**, *59* (24), 9478–9484. https://doi.org/10.1002/anie.201914994.

(155) Duewel, S.; Schmermund, L.; Faber, T.; Harms, K.; Srinivasan, V.; Meggers, E.; Hoebenreich, S. Directed Evolution of an FeII-Dependent Halogenase for Asymmetric $C(sp^3)$–H Chlorination. *ACS Catal.* **2020**, *10* (2), 1272–1277. https://doi.org/10.1021/acscatal.9b04691.

(156) Voss, M.; Hüppi, S.; Schaub, D.; Hayashi, T.; Ligibel, M.; Sager, E.; Schroer, K.; Snajdrova, R.; Buller, R. Enzyme Engineering Enables Inversion of Substrate Stereopreference of the Halogenase WelO5*. *ChemCatChem* **2022**, *14* (24), e202201115. https://doi.org/10.1002/cctc.202201115.

(157) Büchler, J.; Malca, S. H.; Patsch, D.; Voss, M.; Turner, N. J.; Bornscheuer, U. T.; Allemann, O.; Le Chapelain, C.; Lumbroso, A.; Loiseleur, O.; Buller, R. Algorithm-Aided Engineering of Aliphatic Halogenase WelO5* for the Asymmetric Late-Stage Functionalization of Soraphens. *Nat. Commun.* **2022**, *13* (1), 371. https://doi.org/10.1038/s41467-022-27999-1.

(158) Kissman, E. N.; Neugebauer, M. E.; Sumida, K. H.; Swenson, C. V.; Sambold, N. A.; Marchand, J. A.; Millar, D. C.; Chang, M. C. Y. Biocatalytic Control of Site-Selectivity and

Chain Length-Selectivity in Radical Amino Acid Halogenases. *Proc. Natl. Acad. Sci.* **2023**, *120* (12), e2214512120. https://doi.org/10.1073/pnas.2214512120.

(159) Wang, M. L.; Glasser, N. R.; Nair, M. A.; Krebs, C.; Martin Bollinger, J. Jr.; Balskus, E. P. Biochemical Studies of a Cyanobacterial Halogenase Support the Involvement of a Dimetal Cofactor. *Biochemistry* **2025**, *64* (10), 2173–2180. https://doi.org/10.1021/acs.biochem.4c00720.

(160) Matthews, M. L.; Chang, W.; Layne, A. P.; Miles, L. A.; Krebs, C.; Bollinger, J. M. Direct Nitration and Azidation of Aliphatic Carbons by an Iron-Dependent Halogenase. *Nat. Chem. Biol.* **2014**, *10* (3), 209–215. https://doi.org/10.1038/nchembio.1438.

(161) Neugebauer, M. E.; Sumida, K. H.; Pelton, J. G.; McMurry, J. L.; Marchand, J. A.; Chang, M. C. Y. A Family of Radical Halogenases for the Engineering of Amino-Acid-Based Products. *Nat. Chem. Biol.* **2019**, *15* (10), 1009–1016. https://doi.org/10.1038/s41589-019-0355-x.

(162) Kim, C. Y.; Mitchell, A. J.; Glinkerman, C. M.; Li, F.-S.; Pluskal, T.; Weng, J.-K. The Chloroalkaloid (−)-Acutumine Is Biosynthesized via a Fe(II)- and 2-Oxoglutarate-Dependent Halogenase in Menispermaceae Plants. *Nat. Commun.* **2020**, *11* (1), 1867. https://doi.org/10.1038/s41467-020-15777-w.

(163) Chiang, C.-Y.; Ohashi, M.; Le, J.; Chen, P.-P.; Zhou, Q.; Qu, S.; Bat-Erdene, U.; Hematian, S.; Rodriguez, J. A.; Houk, K. N.; Guo, Y.; Loo, J. A.; Tang, Y. Copper-Dependent Halogenase Catalyses Unactivated C−H Bond Functionalization. *Nature* **2025**, *638* (8049), 126–132. https://doi.org/10.1038/s41586-024-08362-4.

(164) Mitchell, A. J.; Dunham, N. P.; Bergman, J. A.; Wang, B.; Zhu, Q.; Chang, W.; Liu, X.; Boal, A. K. Structure-Guided Reprogramming of a Hydroxylase to Halogenate Its Small

Molecule Substrate. *Biochemistry* **2017**, *56* (3), 441–444. https://doi.org/10.1021/acs.biochem.6b01173.

(165) Neugebauer, M. E.; Kissman, E. N.; Marchand, J. A.; Pelton, J. G.; Sambold, N. A.; Millar, D. C.; Chang, M. C. Y. Reaction Pathway Engineering Converts a Radical Hydroxylase into a Halogenase. *Nat. Chem. Biol.* **2022**, *18* (2), 171–179. https://doi.org/10.1038/s41589-021-00944-x.

(166) Chan, N. H.; Gomez, C. A.; Vennelakanti, V.; Du, Q.; Kulik, H. J.; Lewis, J. C. Non-Native Anionic Ligand Binding and Reactivity in Engineered Variants of the Fe(II)- and α-Ketoglutarate-Dependent Oxygenase, SadA. *Inorg. Chem.* **2022**, *61* (36), 14477–14485. https://doi.org/10.1021/acs.inorgchem.2c02872.

(167) Gomez, C. A.; Mondal, D.; Du, Q.; Chan, N.; Lewis, J. C. Directed Evolution of an Iron(II)- and α-Ketoglutarate-Dependent Dioxygenase for Site-Selective Azidation of Unactivated Aliphatic C−H Bonds. *Angew. Chem. Int. Ed.* **2023**, *62* (15), e202301370. https://doi.org/10.1002/anie.202301370.

(168) Zhao, L.-P.; Lin, K.; Xie, P.-P.; Liu, H.; Xiang, H.; Liu, X.; Zhao, Y.; Liu, P.; Yang, Y. Cooperative Photometallobiocatalysis: Nonheme Fe Enzyme-Catalyzed Enantioconvergent Radical Decarboxylative Azidation, Thiocyanation, and Isocyanation of Redox-Active Esters. *Angew. Chem. Int. Ed.* **2025**, *64* (29), e202506361. https://doi.org/10.1002/anie.202506361.

(169) Rui, J.; Mu, X.; Soler, J.; Paris, J. C.; Guo, Y.; Garcia-Borràs, M.; Huang, X. Merging Photoredox with Metalloenzymatic Catalysis for Enantioselective Decarboxylative C(sp^3)–N_3 and C(sp^3)–SCN Bond Formation. *Nat. Catal.* **2024**, *7* (12), 1394–1403. https://doi.org/10.1038/s41929-024-01257-7.

(170) Brownlee, J. M.; Johnson-Winters, K.; Harrison, D. H. T.; Moran, G. R. Structure of the Ferrous Form of (4-Hydroxyphenyl)Pyruvate Dioxygenase from Streptomyces Avermitilis in Complex with the Therapeutic Herbicide, NTBC,. *Biochemistry* **2004**, *43* (21), 6370–6377. https://doi.org/10.1021/bi049317s.

(171) Kita, A.; Kita, S.; Fujisawa, I.; Inaka, K.; Ishida, T.; Horiike, K.; Nozaki, M.; Miki, K. An Archetypical Extradiol-Cleaving Catecholic Dioxygenase: The Crystal Structure of Catechol 2,3-Dioxygenase (Metapyrocatechase) from *Pseudomonas Putida* Mt-2. *Structure* **1999**, *7* (1), 25–34. https://doi.org/10.1016/S0969-2126(99)80006-9.

(172) Mao, R.; Frey, A.; Balon, J.; Hu, X. Decarboxylative C(sp^3)–N Cross-Coupling via Synergetic Photoredox and Copper Catalysis. *Nat. Catal.* **2018**, *1* (2), 120–126. https://doi.org/10.1038/s41929-017-0023-z.

(173) Erlandsen, H.; Kim, J. Y.; Patch, M. G.; Han, A.; Volner, A.; Abu-Omar, M. M.; Stevens, R. C. Structural Comparison of Bacterial and Human Iron-Dependent Phenylalanine Hydroxylases: Similar Fold, Different Stability and Reaction Rates. *J. Mol. Biol.* **2002**, *320* (3), 645–661. https://doi.org/10.1016/S0022-2836(02)00496-5.

(174) Shen, X.; Chen, X.; Xiao, Y.; Brown, J. B.; Zhang, J. G.; Ji, X.; Rui, J.; Garcia-Borràs, M.; Rao, Y.; Yang, Y.; Huang, X. Enantioconvergent Benzylic C(sp^3)–N Coupling with a Copper-Substituted Nonheme Enzyme. *Science* **2025**, *389* (6761), 741–746. https://doi.org/10.1126/science.adt5986.

(175) Ortiz de Montellano, P. R. Substrate Oxidation by Cytochrome P450 Enzymes. In *Cytochrome P450: Structure, Mechanism, and Biochemistry*; Ortiz de Montellano, P. R., Ed.; Springer International Publishing: Cham, 2015; pp 111–176. https://doi.org/10.1007/978-3-319-12108-6_4.

(176) de Visser, S. P.; Kumar, D.; Shaik, S. How Do Aldehyde Side Products Occur during Alkene Epoxidation by Cytochrome P450? Theory Reveals a State-Specific Multi-State Scenario Where the High-Spin Component Leads to All Side Products. *J. Inorg. Biochem.* **2004**, *98* (7), 1183–1193. https://doi.org/10.1016/j.jinorgbio.2004.01.015.

(177) Yin, Y.-C.; Yu, H.-L.; Luan, Z.-J.; Li, R.-J.; Ouyang, P.-F.; Liu, J.; Xu, J.-H. Unusually Broad Substrate Profile of Self-Sufficient Cytochrome P450 Monooxygenase CYP116B4 from Labrenzia Aggregata. *ChemBioChem* **2014**, *15* (16), 2443–2449. https://doi.org/10.1002/cbic.201402309.

(178) Hammer, S. C.; Kubik, G.; Watkins, E.; Huang, S.; Minges, H.; Arnold, F. H. Anti-Markovnikov Alkene Oxidation by Metal-Oxo–Mediated Enzyme Catalysis. *Science* **2017**, *358* (6360), 215–218. https://doi.org/10.1126/science.aao1482.

(179) Soler, J.; Gergel, S.; Klaus, C.; Hammer, S. C.; Garcia-Borràs, M. Enzymatic Control over Reactive Intermediates Enables Direct Oxidation of Alkenes to Carbonyls by a P450 Iron-Oxo Species. *J. Am. Chem. Soc.* **2022**, *144* (35), 15954–15968. https://doi.org/10.1021/jacs.2c02567.

(180) Harvey B. Hopps. Purpald®: A Reagent That Turns Aldehydes Purple! *Aldrichimica Acta* **2000**, *33* (1), 28–30. https://www.sigmaaldrich.cn/deepweb/assets/sigmaaldrich/marketing/global/documents/408/433/acta-vol33.pdf#page38.

(181) Gergel, S.; Soler, J.; Klein, A.; Schülke, K. H.; Hauer, B.; Garcia-Borràs, M.; Hammer, S. C. Engineered Cytochrome P450 for Direct Arylalkene-to-Ketone Oxidation via Highly Reactive Carbocation Intermediates. *Nat. Catal.* **2023**, *6* (7), 606–617. https://doi.org/10.1038/s41929-023-00979-4.

(182) Zhang, J.; Zhang, Q.; Ge, R.; Liu, A.; Chen, B.; Zhang, Z.; Zhao, B.; Yu, J.; Zhao, Y.; Yu, L.; Cao, M.; Wang, B.; Huang, X. Enantiodivergent Radical Alkylation by Synergistic Lewis-Acid-Enzyme and Photoredox Catalysis. *Angew. Chem. Int. Ed.* **2025**, *64* (25), e202500338. https://doi.org/10.1002/anie.202500338.

(183) Fujieda, N.; Nakano, T.; Taniguchi, Y.; Ichihashi, H.; Sugimoto, H.; Morimoto, Y.; Nishikawa, Y.; Kurisu, G.; Itoh, S. A Well-Defined Osmium–Cupin Complex: Hyperstable Artificial Osmium Peroxygenase. *J. Am. Chem. Soc.* **2017**, *139* (14), 5149–5155. https://doi.org/10.1021/jacs.7b00675.

(184) Fujieda, N.; Ichihashi, H.; Yuasa, M.; Nishikawa, Y.; Kurisu, G.; Itoh, S. Cupin Variants as a Macromolecular Ligand Library for Stereoselective Michael Addition of Nitroalkanes. *Angew. Chem. Int. Ed.* **2020**, *59* (20), 7717–7720. https://doi.org/10.1002/anie.202000129.

(185) Matsumoto, R.; Yoshioka, S.; Yuasa, M.; Morita, Y.; Kurisu, G.; Fujieda, N. An Artificial Metallolyase with Pliable 2-His-1-Carboxylate Facial Triad for Stereoselective Michael Addition. *Chem. Sci.* **2023**, *14* (14), 3932–3937. https://doi.org/10.1039/D2SC06809E.

(186) Jaroszewski, L.; Schwarzenbacher, R.; von Delft, F.; McMullan, D.; Brinen, L. S.; Canaves, J. M.; Dai, X.; Deacon, A. M.; DiDonato, M.; Elsliger, M.-A.; Eshagi, S.; Floyd, R.; Godzik, A.; Grittini, C.; Grzechnik, S. K.; Hampton, E.; Levin, I.; Karlak, C.; Klock, H. E.; Koesema, E.; Kovarik, J. S.; Kreusch, A.; Kuhn, P.; Lesley, S. A.; McPhillips, T. M.; Miller, M. D.; Morse, A.; Moy, K.; Ouyang, J.; Page, R.; Quijano, K.; Reyes, R.; Rezezadeh, F.; Robb, A.; Sims, E.; Spraggon, G.; Stevens, R. C.; van den Bedem, H.; Velasquez, J.; Vincent, J.; Wang, X.; West, B.; Wolf, G.; Xu, Q.; Hodgson, K. O.; Wooley, J.; Wilson, I. A. Crystal Structure of a Novel Manganese-Containing Cupin (TM1459) from Thermotoga

Maritima at 1.65 Å Resolution. *Proteins: Struct. Funct. Bioinform.* **2004**, *56* (3), 611–614. https://doi.org/10.1002/prot.20130.

(187) Schwarzenbacher, R.; von Delft, F.; Jaroszewski, L.; Abdubek, P.; Ambing, E.; Biorac, T.; Brinen, L. S.; Canaves, J. M.; Cambell, J.; Chiu, H.-J.; Dai, X.; Deacon, A. M.; DiDonato, M.; Elsliger, M.-A.; Eshagi, S.; Floyd, R.; Godzik, A.; Grittini, C.; Grzechnik, S. K.; Hampton, E.; Karlak, C.; Klock, H. E.; Koesema, E.; Kovarik, J. S.; Kreusch, A.; Kuhn, P.; Lesley, S. A.; Levin, I.; McMullan, D.; McPhillips, T. M.; Miller, M. D.; Morse, A.; Moy, K.; Ouyang, J.; Page, R.; Quijano, K.; Robb, A.; Spraggon, G.; Stevens, R. C.; van den Bedem, H.; Velasquez, J.; Vincent, J.; Wang, X.; West, B.; Wolf, G.; Xu, Q.; Hodgson, K. O.; Wooley, J.; Wilson, I. A. Crystal Structure of a Putative Oxalate Decarboxylase (TM1287) from Thermotoga Maritima at 1.95 Å Resolution. *Proteins: Struct. Funct. Bioinform.* **2004**, *56* (2), 392–395. https://doi.org/10.1002/prot.20016.

(188) Wang, H.; Mai, B. K.; Li, C.; Chen, X.-W.; Liu, P.; Yang, Y. Stereoselective Photometallobiocatalytic Radical C–C Coupling of Organoboron Reagents and Diazo Compounds via an Outer-Sphere Mechanism. ChemRxiv April 18, 2025. https://doi.org/10.26434/chemrxiv-2025-tkj0d. Accessed May 08, 2025.

(189) Lewis, R. D.; Garcia-Borràs, M.; Chalkley, M. J.; Buller, A. R.; Houk, K. N.; Kan, S. B. J.; Arnold, F. H. Catalytic Iron-Carbene Intermediate Revealed in a Cytochrome c Carbene Transferase. *Proc. Natl. Acad. Sci.* **2018**, *115* (28), 7308–7313. https://doi.org/10.1073/pnas.1807027115.

(190) Liu, W.; Lavagnino, M. N.; Gould, C. A.; Alcázar, J.; MacMillan, D. W. C. A Biomimetic SH2 Cross-Coupling Mechanism for Quaternary sp^3-Carbon Formation. *Science* **2021**, *374* (6572), 1258–1263. https://doi.org/10.1126/science.abl4322.

(191) Stelter, M.; Melo, A. M. P.; Pereira, M. M.; Gomes, C. M.; Hreggvidsson, G. O.; Hjorleifsdottir, S.; Saraiva, L. M.; Teixeira, M.; Archer, M. A Novel Type of Monoheme Cytochrome c: Biochemical and Structural Characterization at 1.23 Å Resolution of Rhodothermus Marinus Cytochrome c. *Biochemistry* **2008**, *47* (46), 11953–11963. https://doi.org/10.1021/bi800999g.

(192) Vila, M. A.; Brovetto, M.; Gamenara, D.; Bracco, P.; Zinola, G.; Seoane, G.; Rodríguez, S.; Carrera, I. Production of *Cis*-1,2-Dihydrocatechols of High Synthetic Value by Whole-Cell Fermentation Using *Escherichia Coli* JM109 (pDTG601): A Detailed Study. *J. Mol. Catal. B: Enzym.* **2013**, *96*, 14–20. https://doi.org/10.1016/j.molcatb.2013.06.003.

(193) Thevenet, N.; de la Sovera, V.; Vila, M. A.; Veiga, N.; Gonzalez, D.; Seoane, G.; Carrera, I. Double [3,3]-Sigmatropic Rearrangement in the Enzymatic Dioxygenation of Benzyl Azide: Preparation of Novel Synthetically Valuable Azido-Diols. *Org. Lett.* **2015**, *17* (3), 684–687. https://doi.org/10.1021/ol503708v.

(194) Vila, M. A.; Pazos, M.; Iglesias, C.; Veiga, N.; Seoane, G.; Carrera, I. Toluene Dioxygenase-Catalysed Oxidation of Benzyl Azide to Benzonitrile: Mechanistic Insights for an Unprecedented Enzymatic Transformation. *ChemBioChem* **2016**, *17* (4), 291–295. https://doi.org/10.1002/cbic.201500653.

(195) Davidson, M.; McNamee, M.; Fan, R.; Guo, Y.; Chang, W. Repurposing Nonheme Iron Hydroxylases To Enable Catalytic Nitrile Installation through an Azido Group Assistance. *J. Am. Chem. Soc.* **2019**, *141* (8), 3419–3423. https://doi.org/10.1021/jacs.8b13906.

(196) Hibi, M.; Kawashima, T.; Sokolov, P. M.; Smirnov, S. V.; Kodera, T.; Sugiyama, M.; Shimizu, S.; Yokozeki, K.; Ogawa, J. L-Leucine 5-Hydroxylase of Nostoc Punctiforme Is a Novel Type of Fe(II)/α-Ketoglutarate-Dependent Dioxygenase That Is Useful as a

Biocatalyst. *Appl. Microbiol. Biotechnol.* **2013**, *97* (6), 2467–2472. https://doi.org/10.1007/s00253-012-4136-7.

(197) Chen, W.; Dai, D.; Wang, C.; Huang, T.; Zhai, L.; Deng, Z. Genetic Dissection of the Polyoxin Building Block-Carbamoylpolyoxamic Acid Biosynthesis Revealing the "Pathway Redundancy" in Metabolic Networks. *Microb. Cell Fact.* **2013**, *12* (1), 121. https://doi.org/10.1186/1475-2859-12-121.

(198) Pratley, C.; Fenner, S.; Murphy, J. A. Nitrogen-Centered Radicals in Functionalization of Sp2 Systems: Generation, Reactivity, and Applications in Synthesis. *Chem. Rev.* **2022**, *122* (9), 8181–8260. https://doi.org/10.1021/acs.chemrev.1c00831.

(199) Ushimaru, R.; Abe, I. Nitrogen-Centered Radicals Driving Unusual Enzyme Reactions in Biosynthetic Pathways. *Chem. Soc. Rev.* **2025**. https://doi.org/10.1039/D5CS00342C.

(200) Ye, Y.; Cao, J.; Oblinsky, D. G.; Verma, D.; Prier, C. K.; Scholes, G. D.; Hyster, T. K. Using Enzymes to Tame Nitrogen-Centred Radicals for Enantioselective Hydroamination. *Nat. Chem.* **2023**, *15* (2), 206–212. https://doi.org/10.1038/s41557-022-01083-z.

(201) Shi, F.; Chen, B.; Yu, J.; Zhu, R.; Zheng, Y.; Huang, X. Enantioselective Biosynthesis of Vicinal Diamines Enabled by Synergistic Photo/Biocatalysis Consisting of an Ene-Reductase and a Green-Light-Excited Organic Dye. *Chin. J. Catal.* **2025**, *68*, 223–229. https://doi.org/10.1016/S1872-2067(24)60168-3.

(202) Harrison, W.; Jiang, G.; Zhang, Z.; Li, M.; Chen, H.; Zhao, H. Photoenzymatic Asymmetric Hydroamination for Chiral Alkyl Amine Synthesis. *J. Am. Chem. Soc.* **2024**, *146* (15), 10716–10722. https://doi.org/10.1021/jacs.4c00620.

(203) Zhang, Z.; Feng, J.; Yang, C.; Cui, H.; Harrison, W.; Zhong, D.; Wang, B.; Zhao, H. Photoenzymatic Enantioselective Intermolecular Radical Hydroamination. *Nat. Catal.* **2023**, *6* (8), 687–694. https://doi.org/10.1038/s41929-023-00994-5.

(204) Stateman, L. M.; Nakafuku, K. M.; Nagib, D. A. Remote C–H Functionalization via Selective Hydrogen Atom Transfer. *Synthesis* **2018**, *50*, 1569–1586. https://doi.org/10.1055/s-0036-1591930.

(205) Teng, X.; Yu, T.; Shi, J.; Huang, H.; Wang, R.; Peng, W.; Sun, K.; Yang, S.; Wang, X. Recent Advances in the Functionalization of Remote C−H Bonds by Hofmann-Löffler-Freytag-Type Reactions. *Adv. Synth. Catal.* **2023**, *365* (19), 3211–3226. https://doi.org/10.1002/adsc.202300718.

(206) Groendyke, B. J.; AbuSalim, D. I.; Cook, S. P. Iron-Catalyzed, Fluoroamide-Directed C–H Fluorination. *J. Am. Chem. Soc.* **2016**, *138* (39), 12771–12774. https://doi.org/10.1021/jacs.6b08171.

(207) Rui, J.; Zhao, Q.; Huls, A. J.; Soler, J.; Paris, J. C.; Chen, Z.; Reshetnikov, V.; Yang, Y.; Guo, Y.; Garcia-Borràs, M.; Huang, X. Directed Evolution of Nonheme Iron Enzymes to Access Abiological Radical-Relay C(sp^3)−H Azidation. *Science* **2022**, *376* (6595), 869–874. https://doi.org/10.1126/science.abj2830.

(208) Meldal, M.; Tornøe, C. W. Cu-Catalyzed Azide−Alkyne Cycloaddition. *Chem. Rev.* **2008**, *108* (8), 2952–3015. https://doi.org/10.1021/cr0783479.

(209) Liu, H.; Chen, X.; Wu, H.; She, Y.; Yang, Y.-F. Cluster Model Study of the Mechanism and Origins of Enantio- and Chemoselectivity in Non-Heme Iron Enzyme-Catalyzed C–H Azidation. *RSC Adv.* **2025**, *15* (12), 8931–8937. https://doi.org/10.1039/D5RA00632E.

(210) Zhao, L.-P.; Mai, B. K.; Cheng, L.; Gao, F.; Zhao, Y.; Guo, R.; Wu, H.; Zhang, Y.; Liu, P.; Yang, Y. Biocatalytic Enantioselective C(sp^3)–H Fluorination Enabled by Directed Evolution of Non-Haem Iron Enzymes. *Nat. Synth.* **2024**, *3* (8), 967–975. https://doi.org/10.1038/s44160-024-00536-2.

(211) Zhao, Q.; Chen, Z.; Soler, J.; Chen, X.; Rui, J.; Ji, N. T.; Yu, Q. E.; Yang, Y.; Garcia-Borràs, M.; Huang, X. Engineering Non-Haem Iron Enzymes for Enantioselective C(sp^3)–F Bond Formation via Radical Fluorine Transfer. *Nat. Synth.* **2024**, *3* (8), 958–966. https://doi.org/10.1038/s44160-024-00507-7.

(212) Zhou, Y.; Wang, J.; Gu, Z.; Wang, S.; Zhu, W.; Aceña, J. L.; Soloshonok, V. A.; Izawa, K.; Liu, H. Next Generation of Fluorine-Containing Pharmaceuticals, Compounds Currently in Phase II–III Clinical Trials of Major Pharmaceutical Companies: New Structural Trends and Therapeutic Areas. *Chem. Rev.* **2016**, *116* (2), 422–518. https://doi.org/10.1021/acs.chemrev.5b00392.

(213) Wang, Y.; Yang, X.; Meng, Y.; Wen, Z.; Han, R.; Hu, X.; Sun, B.; Kang, F.; Li, B.; Zhou, D.; Wang, C.; Wang, G. Fluorine Chemistry in Rechargeable Batteries: Challenges, Progress, and Perspectives. *Chem. Rev.* **2024**, *124* (6), 3494–3589. https://doi.org/10.1021/acs.chemrev.3c00826.

(214) Ogawa, Y.; Tokunaga, E.; Kobayashi, O.; Hirai, K.; Shibata, N. Current Contributions of Organofluorine Compounds to the Agrochemical Industry. *iScience* **2020**, *23* (9), 101467. https://doi.org/10.1016/j.isci.2020.101467.

(215) O'Hagan, D.; Schaffrath, C.; Cobb, S. L.; Hamilton, J. T. G.; Murphy, C. D. Biosynthesis of an Organofluorine Molecule. *Nature* **2002**, *416* (6878), 279–279. https://doi.org/10.1038/416279a.

(216) Wang, C.; Chang, W.; Guo, Y.; Huang, H.; Peck, S. C.; Pandelia, M. E.; Lin, G.; Liu, H.; Krebs, C.; Bollinger, J. M. Evidence That the Fosfomycin-Producing Epoxidase, HppE, Is a Non–Heme-Iron Peroxidase. *Science* **2013**, *342* (6161), 991–995. https://doi.org/10.1126/science.1240373.

(217) Zhang, Z.; Ren, J.-S.; Clifton, I. J.; Schofield, C. J. Crystal Structure and Mechanistic Implications of 1-Aminocyclopropane-1-Carboxylic Acid Oxidase—The Ethylene-Forming Enzyme. *Chem. Biol.* **2004**, *11* (10), 1383–1394. https://doi.org/10.1016/j.chembiol.2004.08.012.

(218) Houben, M.; Van de Poel, B. 1-Aminocyclopropane-1-Carboxylic Acid Oxidase (ACO): The Enzyme That Makes the Plant Hormone Ethylene. *Front. Plant Sci.* **2019**, *10*. https://doi.org/10.3389/fpls.2019.00695.

(219) Huang, X.; Groves, J. T. Oxygen Activation and Radical Transformations in Heme Proteins and Metalloporphyrins. *Chem. Rev.* **2018**, *118* (5), 2491–2553. https://doi.org/10.1021/acs.chemrev.7b00373.

(220) Chang, L.; An, Q.; Duan, L.; Feng, K.; Zuo, Z. Alkoxy Radicals See the Light: New Paradigms of Photochemical Synthesis. *Chem. Rev.* **2022**, *122* (2), 2429–2486. https://doi.org/10.1021/acs.chemrev.1c00256.

(221) Singh, S. K.; Roberts, S. A.; McDevitt, S. F.; Weichsel, A.; Wildner, G. F.; Grass, G. B.; Rensing, C.; Montfort, W. R. Crystal Structures of Multicopper Oxidase CueO Bound to Copper(I) and Silver(I): FUNCTIONAL ROLE OF A METHIONINE-RICH SEQUENCE*. *J. Biol. Chem.* **2011**, *286* (43), 37849–37857. https://doi.org/10.1074/jbc.M111.293589.

(222) Guo, H.; Sun, N.; Guo, J.; Zhou, T.-P.; Tang, L.; Zhang, W.; Deng, Y.; Liao, R.-Z.; Wu, Y.; Wu, G.; Zhong, F. Expanding the Promiscuity of a Copper-Dependent Oxidase for

Enantioselective Cross-Coupling of Indoles. *Angew. Chem. Int. Ed.* **2023**, *62* (16), e202219034. https://doi.org/10.1002/anie.202219034.

(223) Siegbahn, P. E. M. Theoretical Study of O_2 Reduction and Water Oxidation in Multicopper Oxidases. *J. Phys. Chem. A* **2020**, *124* (28), 5849–5855. https://doi.org/10.1021/acs.jpca.0c03385.

(224) Mazzaferro, L. S.; Hüttel, W.; Fries, A.; Müller, M. Cytochrome P450-Catalyzed Regio- and Stereoselective Phenol Coupling of Fungal Natural Products. *J. Am. Chem. Soc.* **2015**, *137* (38), 12289–12295. https://doi.org/10.1021/jacs.5b06776.

(225) Zetzsche, L. E.; Yazarians, J. A.; Chakrabarty, S.; Hinze, M. E.; Murray, L. A. M.; Lukowski, A. L.; Joyce, L. A.; Narayan, A. R. H. Biocatalytic Oxidative Cross-Coupling Reactions for Biaryl Bond Formation. *Nature* **2022**, *603* (7899), 79–85. https://doi.org/10.1038/s41586-021-04365-7.

(226) Zhao, B.; Guengerich, F. P.; Bellamine, A.; Lamb, D. C.; Izumikawa, M.; Lei, L.; Podust, L. M.; Sundaramoorthy, M.; Kalaitzis, J. A.; Reddy, L. M.; Kelly, S. L.; Moore, B. S.; Stec, D.; Voehler, M.; Falck, J. R.; Shimada, T.; Waterman, M. R. Binding of Two Flaviolin Substrate Molecules, Oxidative Coupling, and Crystal Structure of *Streptomyces Coelicolor* A3(2) Cytochrome P450 158A2*. *J. Biol. Chem.* **2005**, *280* (12), 11599–11607. https://doi.org/10.1074/jbc.M410933200.

(227) Roos, C. B.; Schulert, S. L.; Zetzsche, L. E.; McMinn, S. E.; Cheong, A. E.; Shim, E.; Kwan, E. E.; Narayan, A. R. H. Synthesis of Enantioenriched Atropisomers by Biocatalytic Deracemization. *Nature* **2025**, *647* (8090), 648–655. https://doi.org/10.1038/s41586-025-09738-w.

(228) Svastits, E. W.; Dawson, J. H.; Breslow, R.; Gellman, S. H. Functionalized Nitrogen Atom Transfer Catalyzed by Cytochrome P-450. *J. Am. Chem. Soc.* **1985**, *107* (22), 6427–6428. https://doi.org/10.1021/ja00308a064.

(229) Bordeaux, M.; Singh, R.; Fasan, R. Intramolecular C(sp^3)–H Amination of Arylsulfonyl Azides with Engineered and Artificial Myoglobin-Based Catalysts. *Bioorg. Med. Chem.* **2014**, *22* (20), 5697–5704. https://doi.org/10.1016/j.bmc.2014.05.015.

(230) Singh, R.; Bordeaux, M.; Fasan, R. P450-Catalyzed Intramolecular sp^3 C–H Amination with Arylsulfonyl Azide Substrates. *ACS Catal.* **2014**, *4* (2), 546–552. https://doi.org/10.1021/cs400893n.

(231) Singh, R.; Kolev, J. N.; Sutera, P. A.; Fasan, R. Enzymatic C(sp^3)-H Amination: P450-Catalyzed Conversion of Carbonazidates into Oxazolidinones. *ACS Catal.* **2015**, *5* (3), 1685–1691. https://doi.org/10.1021/cs5018612.

(232) Steck, V.; Kolev, J. N.; Ren, X.; Fasan, R. Mechanism-Guided Design and Discovery of Efficient Cytochrome P450-Derived C–H Amination Biocatalysts. *J. Am. Chem. Soc.* **2020**, *142* (23), 10343–10357. https://doi.org/10.1021/jacs.9b12859.

(233) Prier, C. K.; Zhang, R. K.; Buller, A. R.; Brinkmann-Chen, S.; Arnold, F. H. Enantioselective, Intermolecular Benzylic C–H Amination Catalysed by an Engineered Iron-Haem Enzyme. *Nat. Chem.* **2017**, *9* (7), 629–634. https://doi.org/10.1038/nchem.2783.

(234) Farwell, C. C.; McIntosh, J. A.; Hyster, T. K.; Wang, Z. J.; Arnold, F. H. Enantioselective Imidation of Sulfides via Enzyme-Catalyzed Intermolecular Nitrogen-Atom Transfer. *J. Am. Chem. Soc.* **2014**, *136* (24), 8766–8771. https://doi.org/10.1021/ja503593n.

(235) Prier, C. K.; Hyster, T. K.; Farwell, C. C.; Huang, A.; Arnold, F. H. Asymmetric Enzymatic Synthesis of Allylic Amines: A Sigmatropic Rearrangement Strategy. *Angew. Chem. Int. Ed.* **2016**, *55* (15), 4711–4715. https://doi.org/10.1002/anie.201601056.

(236) Farwell, C. C.; Zhang, R. K.; McIntosh, J. A.; Hyster, T. K.; Arnold, F. H. Enantioselective Enzyme-Catalyzed Aziridination Enabled by Active-Site Evolution of a Cytochrome P450. *ACS Cent. Sci.* **2015**, *1* (2), 89–93. https://doi.org/10.1021/acscentsci.5b00056.

(237) Xu, W.-N.; Gao, Y.-D.; Su, P.; Huang, L.; He, Z.-L.; Yang, L.-C. Progress in Enzyme-Catalyzed C(sp^3)–H Amination. *ACS Catal.* **2024**, *14* (18), 14139–14160. https://doi.org/10.1021/acscatal.4c04947.

(238) Qin, Z.-Y.; Gao, S.; Zou, Y.; Liu, Z.; Wang, J. B.; Houk, K. N.; Arnold, F. H. Biocatalytic Construction of Chiral Pyrrolidines and Indolines via Intramolecular C(sp^3)–H Amination. *ACS Cent. Sci.* **2023**, *9* (12), 2333–2338. https://doi.org/10.1021/acscentsci.3c00516.

(239) Tinzl, M.; Diedrich, J. V.; Mittl, P. R. E.; Clémancey, M.; Reiher, M.; Proppe, J.; Latour, J.-M.; Hilvert, D. Myoglobin-Catalyzed Azide Reduction Proceeds via an Anionic Metal Amide Intermediate. *J. Am. Chem. Soc.* **2024**, *146* (3), 1957–1966. https://doi.org/10.1021/jacs.3c09279.

(240) Tsutsumi, H.; Katsuyama, Y.; Izumikawa, M.; Takagi, M.; Fujie, M.; Satoh, N.; Shin-ya, K.; Ohnishi, Y. Unprecedented Cyclization Catalyzed by a Cytochrome P450 in Benzastatin Biosynthesis. *J. Am. Chem. Soc.* **2018**, *140* (21), 6631–6639. https://doi.org/10.1021/jacs.8b02769.

(241) Du, Y.-L.; He, H.-Y.; Higgins, M. A.; Ryan, K. S. A Heme-Dependent Enzyme Forms the Nitrogen–Nitrogen Bond in Piperazate. *Nat. Chem. Biol.* **2017**, *13* (8), 836–838. https://doi.org/10.1038/nchembio.2411.

(242) Higgins, M. A.; Shi, X.; Soler, J.; Harland, J. B.; Parkkila, T.; Lehnert, N.; Garcia-Borràs, M.; Du, Y.-L.; Ryan, K. S. Structure and Mechanism of Haem-Dependent Nitrogen–Nitrogen Bond Formation in Piperazate Synthase. *Nat. Catal.* **2025**, *8* (3), 207–217. https://doi.org/10.1038/s41929-024-01280-8.

(243) Cho, I.; Prier, C. K.; Jia, Z.-J.; Zhang, R. K.; Görbe, T.; Arnold, F. H. Enantioselective Aminohydroxylation of Styrenyl Olefins Catalyzed by an Engineered Hemoprotein. *Angew. Chem. Int. Ed.* **2019**, *58* (10), 3138–3142. https://doi.org/10.1002/anie.201812968.

(244) Jia, Z.-J.; Gao, S.; Arnold, F. H. Enzymatic Primary Amination of Benzylic and Allylic C(sp^3)–H Bonds. *J. Am. Chem. Soc.* **2020**, *142* (23), 10279–10283. https://doi.org/10.1021/jacs.0c03428.

(245) Liu, Z.; Qin, Z.-Y.; Zhu, L.; Athavale, S. V.; Sengupta, A.; Jia, Z.-J.; Garcia-Borràs, M.; Houk, K. N.; Arnold, F. H. An Enzymatic Platform for Primary Amination of 1-Aryl-2-Alkyl Alkynes. *J. Am. Chem. Soc.* **2022**, *144* (1), 80–85. https://doi.org/10.1021/jacs.1c11340.

(246) Athavale, S. V.; Gao, S.; Das, A.; Mallojjala, S. C.; Alfonzo, E.; Long, Y.; Hirschi, J. S.; Arnold, F. H. Enzymatic Nitrogen Insertion into Unactivated C–H Bonds. *J. Am. Chem. Soc.* **2022**, *144* (41), 19097–19105. https://doi.org/10.1021/jacs.2c08285.

(247) Athavale, S. V.; Gao, S.; Liu, Z.; Mallojjala, S. C.; Hirschi, J. S.; Arnold, F. H. Biocatalytic, Intermolecular C−H Bond Functionalization for the Synthesis of Enantioenriched Amides. *Angew. Chem. Int. Ed.* **2021**, *60* (47), 24864–24869. https://doi.org/10.1002/anie.202110873.

(248) Mao, R.; Gao, S.; Qin, Z.-Y.; Rogge, T.; Wu, S. J.; Li, Z.-Q.; Das, A.; Houk, K. N.; Arnold, F. H. Biocatalytic, Enantioenriched Primary Amination of Tertiary C–H Bonds. *Nat. Catal.* **2024**, *7* (5), 585–592. https://doi.org/10.1038/s41929-024-01149-w.

(249) Alfonzo, E.; Hanley, D.; Li, Z.-Q.; Sicinski, K. M.; Gao, S.; Arnold, F. H. Biocatalytic Synthesis of α-Amino Esters via Nitrene C–H Insertion. *J. Am. Chem. Soc.* **2024**, *146* (40), 27267–27273. https://doi.org/10.1021/jacs.4c09989.

(250) Freitas, T. A. K.; Hou, S.; Dioum, E. M.; Saito, J. A.; Newhouse, J.; Gonzalez, G.; Gilles-Gonzalez, M.-A.; Alam, M. Ancestral Hemoglobins in Archaea. *Proc. Natl. Acad. Sci.* **2004**, *101* (17), 6675–6680. https://doi.org/10.1073/pnas.0308657101.

(251) Bach, R. D.; Schlegel, H. B. The Bond Dissociation Energy of the N–O Bond. *J. Phys. Chem. A* **2021**, *125* (23), 5014–5021. https://doi.org/10.1021/acs.jpca.1c02741.

(252) Gao, S.; Das, A.; Alfonzo, E.; Sicinski, K. M.; Rieger, D.; Arnold, F. H. Enzymatic Nitrogen Incorporation Using Hydroxylamine. *J. Am. Chem. Soc.* **2023**, *145* (37), 20196–20201. https://doi.org/10.1021/jacs.3c08053.

(253) Pesce, A.; Bolognesi, M.; Nardini, M. Chapter Three - Protoglobin: Structure and Ligand-Binding Properties. In *Advances in Microbial Physiology*; Poole, R. K., Ed.; Microbial Globins - Status and Opportunities; Academic Press, 2013; Vol. 63, pp 79–96. https://doi.org/10.1016/B978-0-12-407693-8.00003-0.

(254) Zhao, H.; Giver, L.; Shao, Z.; Affholter, J. A.; Arnold, F. H. Molecular Evolution by Staggered Extension Process (StEP) in Vitro Recombination. *Nat. Biotechnol.* **1998**, *16* (3), 258–261. https://doi.org/10.1038/nbt0398-258.

(255) Das, A.; Gao, S.; Lal, R. G.; Hicks, M. H.; Oyala, P. H.; Arnold, F. H. Reaction Discovery Using Spectroscopic Insights from an Enzymatic C–H Amination Intermediate. *J. Am. Chem. Soc.* **2024**, *146* (30), 20556–20562. https://doi.org/10.1021/jacs.4c05761.

(256) Hong, S. Y.; Park, Y.; Hwang, Y.; Kim, Y. B.; Baik, M.-H.; Chang, S. Selective Formation of γ-Lactams via C–H Amidation Enabled by Tailored Iridium Catalysts. *Science* **2018**, *359* (6379), 1016–1021. https://doi.org/10.1126/science.aap7503.

(257) Zhou, Z.; Chen, S.; Hong, Y.; Winterling, E.; Tan, Y.; Hemming, M.; Harms, K.; Houk, K. N.; Meggers, E. Non-C2-Symmetric Chiral-at-Ruthenium Catalyst for Highly Efficient Enantioselective Intramolecular C(sp^3)–H Amidation. *J. Am. Chem. Soc.* **2019**, *141* (48), 19048–19057. https://doi.org/10.1021/jacs.9b09301.

(258) van Vliet, K. M.; de Bruin, B. Dioxazolones: Stable Substrates for the Catalytic Transfer of Acyl Nitrenes. *ACS Catal.* **2020**, *10* (8), 4751–4769. https://doi.org/10.1021/acscatal.0c00961.

(259) Kweon, J.; Chang, S. Highly Robust Iron Catalyst System for Intramolecular C(sp^3)−H Amidation Leading to γ-Lactams. *Angew. Chem. Int. Ed.* **2021**, *60* (6), 2909–2914. https://doi.org/10.1002/anie.202013499.

(260) Roy, S.; Vargas, D. A.; Ma, P.; Sengupta, A.; Zhu, L.; Houk, K. N.; Fasan, R. Stereoselective Construction of β-, γ- and δ-Lactam Rings via Enzymatic C–H Amidation. *Nat. Catal.* **2024**, *7* (1), 65–76. https://doi.org/10.1038/s41929-023-01068-2.

(261) Bordeaux, M.; Tyagi, V.; Fasan, R. Highly Diastereoselective and Enantioselective Olefin Cyclopropanation Using Engineered Myoglobin-Based Catalysts. *Angew. Chem. Int. Ed.* **2015**, *54* (6), 1744–1748. https://doi.org/10.1002/anie.201409928.

(262) Das, A.; Long, Y.; Maar, R. R.; Roberts, J. M.; Arnold, F. H. Expanding Biocatalysis for Organosilane Functionalization: Enantioselective Nitrene Transfer to Benzylic Si–C–H Bonds. *ACS Catal.* **2024**, *14* (1), 148–152. https://doi.org/10.1021/acscatal.3c05370.

(263) Majhi, J.; Roy, S.; Chattopadhyay, A.; Fasan, R. Highly Enantioselective Construction of Oxazolidinone Rings via Enzymatic C(sp^3)–H Amination. *ACS Catal.* **2025**, *15* (2), 809–816. https://doi.org/10.1021/acscatal.4c06066.

(264) Martinez, S.; Fellner, M.; Herr, C. Q.; Ritchie, A.; Hu, J.; Hausinger, R. P. Structures and Mechanisms of the Non-Heme Fe(II)- and 2-Oxoglutarate-Dependent Ethylene-Forming Enzyme: Substrate Binding Creates a Twist. *J. Am. Chem. Soc.* **2017**, *139* (34), 11980–11988. https://doi.org/10.1021/jacs.7b06186.

(265) Goldberg, N. W.; Knight, A. M.; Zhang, R. K.; Arnold, F. H. Nitrene Transfer Catalyzed by a Non-Heme Iron Enzyme and Enhanced by Non-Native Small-Molecule Ligands. *J. Am. Chem. Soc.* **2019**, *141* (50), 19585–19588. https://doi.org/10.1021/jacs.9b11608.

(266) Lewis, S. E. Applications of Biocatalytic Arene Ipso,Ortho Cis-Dihydroxylation in Synthesis. *Chem. Commun.* **2014**, *50* (22), 2821–2830. https://doi.org/10.1039/C3CC49694E.

(267) Parales, R. E.; Lee, K.; Resnick, S. M.; Jiang, H.; Lessner, D. J.; Gibson, D. T. Substrate Specificity of Naphthalene Dioxygenase: Effect of Specific Amino Acids at the Active Site of the Enzyme. *J. Bacteriol.* **2000**, *182* (6), 1641–1649. https://doi.org/10.1128/jb.182.6.1641-1649.2000.

(268) Ferraro, D. J.; Okerlund, A.; Brown, E.; Ramaswamy, S. One Enzyme, Many Reactions: Structural Basis for the Various Reactions Catalyzed by Naphthalene 1,2-Dioxygenase. *IUCrJ* **2017**, *4* (5), 648–656. https://doi.org/10.1107/S2052252517008223.

(269) Yildirim, S.; Franko, T. T.; Wohlgemuth, R.; Kohler, H.-P. E.; Witholt, B.; Schmid, A. Recombinant Chlorobenzene Dioxygenase from Pseudomonas Sp. P51: A Biocatalyst for

Regioselective Oxidation of Aromatic Nitriles. *Adv. Synth. Catal.* **2005**, *347* (7–8), 1060–1072. https://doi.org/10.1002/adsc.200505075.

(270) Vila, M. A.; Steck, V.; Rodriguez Giordano, S.; Carrera, I.; Fasan, R. C−H Amination via Nitrene Transfer Catalyzed by Mononuclear Non-Heme Iron-Dependent Enzymes. *ChemBioChem* **2020**, *21* (14), 1981–1987. https://doi.org/10.1002/cbic.201900783.

(271) Hashimoto, T.; Matsuda, J.; Yamada, Y. Two-Step Epoxidation of Hyoscyamine to Scopolamine Is Catalyzed by Bifunctional Hyoscyamine 6β-Hydroxylase. *FEBS Lett.* **1993**, *329* (1–2), 35–39. https://doi.org/10.1016/0014-5793(93)80187-Y.

(272) Mitchell, A. J.; Zhu, Q.; Maggiolo, A. O.; Ananth, N. R.; Hillwig, M. L.; Liu, X.; Boal, A. K. Structural Basis for Halogenation by Iron- and 2-Oxo-Glutarate-Dependent Enzyme WelO5. *Nat. Chem. Biol.* **2016**, *12* (8), 636–640. https://doi.org/10.1038/nchembio.2112.

(273) Zhao, L.-P.; Liu, H.; Mai, B. K.; Zhang, Y.; Cheng, L.; Liu, P.; Yang, Y. Nonheme Fe 1,3-Nitrogen Migratases for Asymmetric Noncanonical Amino Acid Synthesis. *Nat. Chem. Biol.* **2025**, 1–10. https://doi.org/10.1038/s41589-025-01953-w.

(274) Ye, C.-X.; Shen, X.; Chen, S.; Meggers, E. Stereocontrolled 1,3-Nitrogen Migration to Access Chiral α-Amino Acids. *Nat. Chem.* **2022**, *14* (5), 566–573. https://doi.org/10.1038/s41557-022-00895-3.

(275) Ye, C.-X.; Dansby, D. R.; Chen, S.; Meggers, E. Expedited Synthesis of α-Amino Acids by Single-Step Enantioselective α-Amination of Carboxylic Acids. *Nat. Synth.* **2023**, *2* (7), 645–652. https://doi.org/10.1038/s44160-023-00267-w.

(276) Roach, P. L.; Clifton, I. J.; Fülöp, V.; Harlos, K.; Barton, G. J.; Hajdu, J.; Andersson, I.; Schofield, C. J.; Baldwin, J. E. Crystal Structure of Isopenicillin N Synthase Is the First from

a New Structural Family of Enzymes. *Nature* **1995**, *375* (6533), 700–704. https://doi.org/10.1038/375700a0.

(277) Roach, P. L.; Clifton, I. J.; Hensgens, C. M. H.; Shibata, N.; Schofield, C. J.; Hajdu, J.; Baldwin, J. E. Structure of Isopenicillin N Synthase Complexed with Substrate and the Mechanism of Penicillin Formation. *Nature* **1997**, *387* (6635), 827–830. https://doi.org/10.1038/42990.

(278) Burzlaff, N. I.; Rutledge, P. J.; Clifton, I. J.; Hensgens, C. M. H.; Pickford, M.; Adlington, R. M.; Roach, P. L.; Baldwin, J. E. The Reaction Cycle of Isopenicillin N Synthase Observed by X-Ray Diffraction. *Nature* **1999**, *401* (6754), 721–724. https://doi.org/10.1038/44400.

(279) Zhao, L.-P.; Liu, H.; Mai, B. K.; Zhang, Y.; Cheng, L.; Liu, P.; Yang, Y. Nonheme Fe 1,3-Nitrogen Migratases for Asymmetric Noncanonical Amino Acid Synthesis. *Nat. Chem. Biol.* **2025**, *21* (11), 1773–1782. https://doi.org/10.1038/s41589-025-01953-w.

(280) Lin, K.; Zhao, L.-P.; Wang, S.; Liu, H.; Zhang, Y.; Mai, B. K.; Liu, P.; Yang, Y. Nonheme Fe Enzyme-Catalyzed Enantiodivergent Nitrogen Migration: Directed Evolution and Computational Study of Isopenicillin N Synthases for Biocatalytic Synthesis of Arylglycines. *Angew. Chem. Int. Ed.* **2025**, *64*, 10.1002/anie.202524718. https://doi.org/10.1002/anie.202524718.

(281) Mai, B. K.; Neris, N. M.; Yang, Y.; Liu, P. C–N Bond Forming Radical Rebound Is the Enantioselectivity-Determining Step in P411-Catalyzed Enantioselective C(sp^3)–H Amination: A Combined Computational and Experimental Investigation. *J. Am. Chem. Soc.* **2022**, *144* (25), 11215–11225. https://doi.org/10.1021/jacs.2c02283.

(282) Liang, A. D.; Serrano-Plana, J.; Peterson, R. L.; Ward, T. R. Artificial Metalloenzymes Based on the Biotin–Streptavidin Technology: Enzymatic Cascades and Directed Evolution. *Acc. Chem. Res.* **2019**, *52* (3), 585–595. https://doi.org/10.1021/acs.accounts.8b00618.

(283) Chen, Q.; Yu, J.; Li, S.; Wang, C.; Zheng, P.; Pan, H.-J. Stereocontrolled 1,3-Nitrogen Migration Catalyzed by Artificial Metalloenzymes Bearing Stereogenic Metal Centers. *ChemCatChem* **2025**, *17* (16), e00901. https://doi.org/10.1002/cctc.202500901.

(284) Yuan, T.; Zhang, M.; Cheng, L.; Zheng, X.; Jiang, S.; Huang, X.; Xiao, H. Biocatalytic Synthesis of N-Protected α-Amino Acids through 1,3-Nitrogen Migration by Nonheme Iron Enzymes. *J. Am. Chem. Soc.* **2025**, *147* (48), 44041–44047. https://doi.org/10.1021/jacs.5c11008.

(285) Cheng, M.; Li, T.; Gan, Y.; Zhang, W.; Chen, X.; Zhao, Q. Directed Evolution of a Nonheme Iron Enzyme to Access Chiral α-Amino Acid Derivatives by 1,3-Migratory Nitrene C(sp^3)─H Insertion. *Angew. Chem. Int. Ed. n/a* (n/a), e15741. https://doi.org/10.1002/anie.202515741.

(286) Pelletier, M. K.; Murrell, J. R.; Shirley, B. W. Characterization of Flavonol Synthase and Leucoanthocyanidin Dioxygenase Genes in Arabidopsis (Further Evidence for Differential Regulation of "Early" and "Late" Genes). *Plant Physiol.* **1997**, *113* (4), 1437–1445. https://doi.org/10.1104/pp.113.4.1437.

(287) Legnani, L.; Morandi, B. Direct Catalytic Synthesis of Unprotected 2-Amino-1-Phenylethanols from Alkenes by Using Iron(II) Phthalocyanine. *Angew. Chem. Int. Ed.* **2016**, *55* (6), 2248–2251. https://doi.org/10.1002/anie.201507630.

(288) Lu, D.-F.; Zhu, C.-L.; Sears, J. D.; Xu, H. Iron(II)-Catalyzed Intermolecular Aminofluorination of Unfunctionalized Olefins Using Fluoride Ion. *J. Am. Chem. Soc.* **2016**, *138* (35), 11360–11367. https://doi.org/10.1021/jacs.6b07221.

(289) Legnani, L.; Prina-Cerai, G.; Delcaillau, T.; Willems, S.; Morandi, B. Efficient Access to Unprotected Primary Amines by Iron-Catalyzed Aminochlorination of Alkenes. *Science* **2018**, *362* (6413), 434–439. https://doi.org/10.1126/science.aat3863.

(290) Makai, S.; Falk, E.; Morandi, B. Direct Synthesis of Unprotected 2-Azidoamines from Alkenes via an Iron-Catalyzed Difunctionalization Reaction. *J. Am. Chem. Soc.* **2020**, *142* (51), 21548–21555. https://doi.org/10.1021/jacs.0c11025.

(291) Huls, A. J.; Soler, J.; Su, Y.; Yang, Y.; Garcia-Borràs, M.; Huang, X. Biocatalytic Olefin Difunctionalization for Synthesis of Chiral 2-Azidoamines Using Nonheme Iron Enzymes. *Angew. Chem. Int. Ed.* **2025**, *64* (39), e202423403. https://doi.org/10.1002/anie.202423403.

(292) Liu, F.; Li, S.-Y.; Fan, Z.-S.; Luo, J.-H.; Zeng, X.; Wei, L.; Li, Y.; Li, J.-Y.; Zheng, Y.; Wang, X.; Zhang, C.; Chen, P.; Jia, Z.-J. Directed Evolution of Nonheme Iron Enzymes for Enantioselective Aminative Difunctionalization of Alkenes. *JACS Au* **2025**, *5* (9), 4472–4480. https://doi.org/10.1021/jacsau.5c00817.

(293) Davies, H. M. L.; Manning, J. R. Catalytic C–H Functionalization by Metal Carbenoid and Nitrenoid Insertion. *Nature* **2008**, *451* (7177), 417–424. https://doi.org/10.1038/nature06485.

(294) Doyle, M. P.; Duffy, R.; Ratnikov, M.; Zhou, L. Catalytic Carbene Insertion into C−H Bonds. *Chem. Rev.* **2010**, *110* (2), 704–724. https://doi.org/10.1021/cr900239n.

(295) He, Y.; Huang, Z.; Wu, K.; Ma, J.; Zhou, Y.-G.; Yu, Z. Recent Advances in Transition-Metal-Catalyzed Carbene Insertion to C–H Bonds. *Chem. Soc. Rev.* **2022**, *51* (7), 2759–2852. https://doi.org/10.1039/D1CS00895A.

(296) Coelho, P. S.; Brustad, E. M.; Kannan, A.; Arnold, F. H. Olefin Cyclopropanation via Carbene Transfer Catalyzed by Engineered Cytochrome P450 Enzymes. *Science* **2013**, *339* (6117), 307–310. https://doi.org/10.1126/science.1231434.

(297) Zhang, R. K.; Chen, K.; Huang, X.; Wohlschlager, L.; Renata, H.; Arnold, F. H. Enzymatic Assembly of Carbon–Carbon Bonds via Iron-Catalysed sp^3 C–H Functionalization. *Nature* **2019**, *565* (7737), 67–72. https://doi.org/10.1038/s41586-018-0808-5.

(298) Steck, V.; Carminati, D. M.; Johnson, N. R.; Fasan, R. Enantioselective Synthesis of Chiral Amines via Biocatalytic Carbene N–H Insertion. *ACS Catal.* **2020**, *10* (19), 10967–10977. https://doi.org/10.1021/acscatal.0c02794.

(299) Kan, S. B. J.; Lewis, R. D.; Chen, K.; Arnold, F. H. Directed Evolution of Cytochrome c for Carbon–Silicon Bond Formation: Bringing Silicon to Life. *Science* **2016**, *354* (6315), 1048–1051. https://doi.org/10.1126/science.aah6219.

(300) Huang, X.; Garcia-Borràs, M.; Miao, K.; Kan, S. B. J.; Zutshi, A.; Houk, K. N.; Arnold, F. H. A Biocatalytic Platform for Synthesis of Chiral α-Trifluoromethylated Organoborons. *ACS Cent. Sci.* **2019**, *5* (2), 270–276. https://doi.org/10.1021/acscentsci.8b00679.

(301) Bordeaux, M.; Tyagi, V.; Fasan, R. Highly Diastereoselective and Enantioselective Olefin Cyclopropanation Using Engineered Myoglobin-Based Catalysts. *Angew. Chem. Int. Ed.* **2015**, *54* (6), 1744–1748. https://doi.org/10.1002/anie.201409928.

(302) Chen, K.; Arnold, F. H. Engineering Cytochrome P450s for Enantioselective Cyclopropenation of Internal Alkynes. *J. Am. Chem. Soc.* **2020**, *142* (15), 6891–6895. https://doi.org/10.1021/jacs.0c01313.

(303) Chen, K.; Huang, X.; Kan, S. B. J.; Zhang, R. K.; Arnold, F. H. Enzymatic Construction of Highly Strained Carbocycles. *Science* **2018**, *360* (6384), 71–75. https://doi.org/10.1126/science.aar4239.

(304) Miller, D. C.; Lal, R. G.; Marchetti, L. A.; Arnold, F. H. Biocatalytic One-Carbon Ring Expansion of Aziridines to Azetidines via a Highly Enantioselective [1,2]-Stevens Rearrangement. *J. Am. Chem. Soc.* **2022**, *144* (11), 4739–4745. https://doi.org/10.1021/jacs.2c00251.

(305) Moss, R. A. Diazirines: Carbene Precursors Par Excellence. *Acc. Chem. Res.* **2006**, *39* (4), 267–272. https://doi.org/10.1021/ar050155h.

(306) Porter, N. J.; Danelius, E.; Gonen, T.; Arnold, F. H. Biocatalytic Carbene Transfer Using Diazirines. *J. Am. Chem. Soc.* **2022**, *144* (20), 8892–8896. https://doi.org/10.1021/jacs.2c02723.

(307) Moran, J.; McKay, C. S.; Pezacki, J. P. Strain-Promoted 1,3-Dipolar Cycloadditions of Diazo Compounds with Cyclooctynes. *Can. J. Chem.* **2011**, *89* (2), 148–151. https://doi.org/10.1139/V10-112.

(308) Rogge, T.; Zhou, Q.; Porter, N. J.; Arnold, F. H.; Houk, K. N. Iron Heme Enzyme-Catalyzed Cyclopropanations with Diazirines as Carbene Precursors: Computational Explorations of Diazirine Activation and Cyclopropanation Mechanism. *J. Am. Chem. Soc.* **2024**, *146* (5), 2959–2966. https://doi.org/10.1021/jacs.3c06030.

(309) Schaus, L.; Das, A.; Knight, A. M.; Jimenez-Osés, G.; Houk, K. N.; Garcia-Borràs, M.; Arnold, F. H.; Huang, X. Protoglobin-Catalyzed Formation of Cis-Trifluoromethyl-Substituted Cyclopropanes by Carbene Transfer. *Angew. Chem. Int. Ed.* **2023**, *62* (4), e202208936. https://doi.org/10.1002/anie.202208936.

(310) Tinoco, A.; Steck, V.; Tyagi, V.; Fasan, R. Highly Diastereo- and Enantioselective Synthesis of Trifluoromethyl-Substituted Cyclopropanes via Myoglobin-Catalyzed Transfer of Trifluoromethylcarbene. *J. Am. Chem. Soc.* **2017**, *139* (15), 5293–5296. https://doi.org/10.1021/jacs.7b00768.

(311) Pesce, A.; Tilleman, L.; Donné, J.; Aste, E.; Ascenzi, P.; Ciaccio, C.; Coletta, M.; Moens, L.; Viappiani, C.; Dewilde, S.; Bolognesi, M.; Nardini, M. Structure and Haem-Distal Site Plasticity in Methanosarcina Acetivorans Protoglobin. *PLoS One* **2013**, *8* (6), e66144. https://doi.org/10.1371/journal.pone.0066144.

(312) Tilleman, L.; Abbruzzetti, S.; Ciaccio, C.; Sanctis, G. D.; Nardini, M.; Pesce, A.; Desmet, F.; Moens, L.; Doorslaer, S. V.; Bruno, S.; Bolognesi, M.; Ascenzi, P.; Coletta, M.; Viappiani, C.; Dewilde, S. Structural Bases for the Regulation of CO Binding in the Archaeal Protoglobin from Methanosarcina Acetivorans. *PLoS One* **2015**, *10* (6), e0125959. https://doi.org/10.1371/journal.pone.0125959.

(313) Vargas, D. A.; Ren, X.; Sengupta, A.; Zhu, L.; Roy, S.; Garcia-Borràs, M.; Houk, K. N.; Fasan, R. Biocatalytic Strategy for the Construction of sp^3-Rich Polycyclic Compounds from Directed Evolution and Computational Modelling. *Nat. Chem.* **2024**, *16* (5), 817–826. https://doi.org/10.1038/s41557-023-01435-3.

(314) Mao, R.; Wackelin, D. J.; Jamieson, C. S.; Rogge, T.; Gao, S.; Das, A.; Taylor, D. M.; Houk, K. N.; Arnold, F. H. Enantio- and Diastereoenriched Enzymatic Synthesis of 1,2,3-Polysubstituted Cyclopropanes from (Z/E)-Trisubstituted Enol Acetates. *J. Am. Chem. Soc.* **2023**, *145* (29), 16176–16185. https://doi.org/10.1021/jacs.3c04870.

(315) Zhang, J.; Huang, X.; Zhang, R. K.; Arnold, F. H. Enantiodivergent α-Amino C–H Fluoroalkylation Catalyzed by Engineered Cytochrome P450s. *J. Am. Chem. Soc.* **2019**, *141* (25), 9798–9802. https://doi.org/10.1021/jacs.9b04344.

(316) Ren, X.; Couture, B. M.; Liu, N.; Lall, M. S.; Kohrt, J. T.; Fasan, R. Enantioselective Single and Dual α-C–H Bond Functionalization of Cyclic Amines via Enzymatic Carbene Transfer. *J. Am. Chem. Soc.* **2023**, *145* (1), 537–550. https://doi.org/10.1021/jacs.2c10775.

(317) Zhang, J.; Maggiolo, A. O.; Alfonzo, E.; Mao, R.; Porter, N. J.; Abney, N. M.; Arnold, F. H. Chemodivergent C(sp^3)–H and C(sp^2)–H Cyanomethylation Using Engineered Carbene Transferases. *Nat. Catal.* **2023**, *6* (2), 152–160. https://doi.org/10.1038/s41929-022-00908-x.

(318) Wackelin, D. J.; Mao, R.; Sicinski, K. M.; Zhao, Y.; Das, A.; Chen, K.; Arnold, F. H. Enzymatic Assembly of Diverse Lactone Structures: An Intramolecular C–H Functionalization Strategy. *J. Am. Chem. Soc.* **2024**, *146* (2), 1580–1587. https://doi.org/10.1021/jacs.3c11722.

(319) Epping, R. F. J.; Vesseur, D.; Zhou, M.; de Bruin, B. Carbene Radicals in Transition-Metal-Catalyzed Reactions. *ACS Catal.* **2023**, *13* (8), 5428–5448. https://doi.org/10.1021/acscatal.3c00591.

(320) Couture, B. M.; Cui, R.; Chu, J.-M.; Shen, Z.; Khare, S. D.; Zhang, Y.; Fasan, R. Radical-Mediated Regiodivergent C(sp^3)–H Functionalization of N-Substituted Indolines via Enzymatic Carbene Transfer. *Chem Catal.* **2024**, *4* (11). https://doi.org/10.1016/j.checat.2024.101133.

(321) Hecko, S.; Schiefer, A.; Badenhorst, C. P. S.; Fink, M. J.; Mihovilovic, M. D.; Bornscheuer, U. T.; Rudroff, F. Enlightening the Path to Protein Engineering:

Chemoselective Turn-On Probes for High-Throughput Screening of Enzymatic Activity. *Chem. Rev.* **2023**, *123* (6), 2832–2901. https://doi.org/10.1021/acs.chemrev.2c00304.

(322) Gantz, M.; Neun, S.; Medcalf, E. J.; van Vliet, L. D.; Hollfelder, F. Ultrahigh-Throughput Enzyme Engineering and Discovery in In Vitro Compartments. *Chem. Rev.* **2023**, *123* (9), 5571–5611. https://doi.org/10.1021/acs.chemrev.2c00910.

(323) Yang, K. K.; Wu, Z.; Arnold, F. H. Machine-Learning-Guided Directed Evolution for Protein Engineering. *Nat. Methods* **2019**, *16* (8), 687–694. https://doi.org/10.1038/s41592-019-0496-6.

(324) Ding, K.; Chin, M.; Zhao, Y.; Huang, W.; Mai, B. K.; Wang, H.; Liu, P.; Yang, Y.; Luo, Y. Machine Learning-Guided Co-Optimization of Fitness and Diversity Facilitates Combinatorial Library Design in Enzyme Engineering. *Nat. Commun.* **2024**, *15* (1), 6392. https://doi.org/10.1038/s41467-024-50698-y.

(325) Yang, J.; Lal, R. G.; Bowden, J. C.; Astudillo, R.; Hameedi, M. A.; Kaur, S.; Hill, M.; Yue, Y.; Arnold, F. H. Active Learning-Assisted Directed Evolution. *Nat. Commun.* **2025**, *16* (1), 714. https://doi.org/10.1038/s41467-025-55987-8.

(326) Singh, N.; Lane, S.; Yu, T.; Lu, J.; Ramos, A.; Cui, H.; Zhao, H. A Generalized Platform for Artificial Intelligence-Powered Autonomous Enzyme Engineering. *Nat. Commun.* **2025**, *16* (1), 5648. https://doi.org/10.1038/s41467-025-61209-y.

(327) Huang, P.-S.; Boyken, S. E.; Baker, D. The Coming of Age of de Novo Protein Design. *Nature* **2016**, *537* (7620), 320–327. https://doi.org/10.1038/nature19946.

(328) Dawson, W. M.; Rhys, G. G.; Woolfson, D. N. Towards Functional *de Novo* Designed Proteins. *Curr. Opin. Chem. Biol.* **2019**, *52*, 102–111. https://doi.org/10.1016/j.cbpa.2019.06.011.

(329) Chalkley, M. J.; Mann, S. I.; DeGrado, W. F. De Novo Metalloprotein Design. *Nat. Rev. Chem.* **2022**, *6* (1), 31–50. https://doi.org/10.1038/s41570-021-00339-5.

(330) Chu, A. E.; Lu, T.; Huang, P.-S. Sparks of Function by de Novo Protein Design. *Nat. Biotechnol.* **2024**, *42* (2), 203–215. https://doi.org/10.1038/s41587-024-02133-2.

(331) Kortemme, T. De Novo Protein Design—From New Structures to Programmable Functions. *Cell* **2024**, *187* (3), 526–544. https://doi.org/10.1016/j.cell.2023.12.028.

TOC: